Micro-Ultrasound Molecular Imaging

Verya Daeichin

2015

This research was performed within the framework of CTMM, the center for Translational Molecular Medicine, project PARISk, and supported by the Dutch Heart Foundation (DHF-2008T094). Financial support by the Dutch Heart Foundation for the publication of this thesis is gratefully acknowledged.

Financial support for publication of this thesis was provided by:
Erasmus Medical Center
FUJIFILM VisualSonics, Inc.
Dutch Heart Foundation
Bracco Suisse SA

Cover design by:
Marieke Broertjes

Printed by:
Gildeprint, Enschede, the Netherlands

ISBN: 978-94-6108-890-1

Micro-Ultrasound Molecular Imaging

Moleculaire beeldvorming met micro-ultrageluid

Thesis

to obtain the degree of Doctor from the
Erasmus University Rotterdam
by command of the Rector Magnificus

Prof.dr. H.A.P. Pols

and in accordance with the decision of the Doctorate Board

The public defense shall be held on
Wednesday 21st of January at 15.30 hours
by

Verya Daeichin
born in Kermanshah, Iran

Doctoral Committee

Promoters:	Prof.dr.ir. A.F.W. van der Steen
	Prof.dr.ir. N. de Jong
Other members:	Dr. J. Essers
	Prof.dr. F. S. Foster
	Prof.dr.ir J. F. Verzijlbergen
Copromoter:	Dr. J.G. Bosch

تا خاک مرا به قالب آمیخته اند
بس فتنه که از خاک بر انگیخته اند
من بهتر از این نمی توانم بودن
کز بوته مرا چنین برون ریخته اند

تقدیم به:
مرضیه، جهانبخش، شیدا و شاهین

Contents

Abbreviations

AFM: atomic force microscopy
AM: amplitude-modulation
ApoE$^{-/-}$: apolipoprotein E-deficient
BM: block matching
b-MB: bound microbubble
CAR: contrast-to-artifact ratio
CTR: contrast-to-tissue ratio
DICOM: digital imaging and communications in medicine
DOPE: 1,2-dioleoyl-sn-glycero-3-phosphoethanolamine
DPPA: 1,2-dipalmitoyl-sn-glycero-3-phosphate
DPPC: 1,2-dipalmitoyl-sn-glycero-3-phosphocholine
DSPC: 1,2-distearoyl-sn-glycero-3-phosphocholine
DSPE: 1,2-distearoyl-sn-glycero-3-phosphoethanolamine
EGFR: epidermal growth factor receptor
EPR : enhanced permeability and retention
GFP: green fluorescent protein
GP: glycoprotein
HE: Hematoxylin and Eosin
HFU: high frequency ultrasound
HIFU: high intensity focused ultrasound
HUVEC: human umbilical vein endothelial cell
Hz: Hertz
ICAM-1: intracellular adhesion molecule 1
KZK : Khokhlov, Zabolotskaya, and Kuznetsov
MB: microbubble
MDP: multidimensional dynamic programming
MI : mechanical index
MinIP: minimum intensity projection
MIP: maximum intensity projection
MMP-2: matrix metalloproteinase-2
MSB: Martius Scarlet Blue
NCC: normalized correlation coefficients
NF: nonlinear-fundamental
PAA: poly acrylic acid
PC : phosphatidylcholine

PEG :polyethylene glycol spacer
PerIP: percentile intensity projection
PFA: paraformaldehyde
PI: pulse-inversion
PIAM: pulse-inversion combined with amplitude-modulation
PLA: poly(l-lactic acid)
PRF: pulse repetition frequency
PS: phosphatidylserine
PVA: polyvinyl alcohol
RBC: red blood cell
RES: reticuloendothelial system
ROI: regions of interest
S-D: self-demodulation
SFRP2: secreted frizzled related protein 2
SH: subharmonic
SNR: signal-to-noise ratio
StemBells: stem cells conjugated with targeted microbubbles
TACS: thrombin aptamer crosslinking strand
TIC: time intensity curves
tMB: targeted microbubble
TMM: tissue mimicking material
TMP: tissue mimicking phantom
UCA: ultrasound contrast agent
UH: ultraharmonic
UMI: ultrasound molecular imaging
UMMD: ultrasound and microbubble mediated drug delivery
UMTD : ultrasound and microbubble targeted drug delivery
u-MB: unbound microbubble
UtMMD : ultrasound and targeted microbubble mediated drug delivery
VCAM-1: vascular cell adhesion molecule 1
VEGF: vascular endothelial growth factor
VEGFR2: vascular endothelial growth factor receptor 2
2D: two dimensional
3D: three dimensional

Introduction

01

Perhaps using sound to identify objects, those which remained mysterious to sight and touch senses, is one of the very early diagnostic tools mankind has ever used. We all can distinguish the sound of a plastic cup from one made of glass when tapped by a finger nail no matter how similar they look. The sounds that we hear and those that we don't, are mechanical vibrations (acoustic waves) traveling through a compressible and expandable (elastic) medium such as air or water. We can recognize the sound of a glass cup from a plastic one because of the fact that such mechanical vibrations of the particles of materials with dissimilar properties are unlike. Perhaps the most characteristic properties of an acoustic wave are its amplitude and its pitch (frequency). The amplitude of a sound determines how loud the sound is. The frequency of a sound is an indicator of how fast are the mechanical vibrations of the medium substances. The frequency of an acoustic wave is measured in cycles per second or Hertz (Hz) which is named after the German physicist Heinrich Hertz. The faster the vibration of the medium substances the higher the frequency or the pitch of the acoustic wave will be. For instance, imagine the strings of a guitar, the tighter the string the faster it will vibrate when picked and the higher the pitch of the sound it makes. Our devices for generating sound (e.g. string of a guitar) and detecting it (e.g. human ear) are limited to a certain frequency range. For instance, there is a limit to the pitch you can achieve by tightening a guitar string before breaking the string, and a normal healthy human ear can detect frequencies in the range of 20 to 20,000 Hz (20 kHz). Based on such frequency dependent limitation or better to say abilities, the sound can be categorized into three regimes: sonic, ultrasonic and infrasonic. Sonic (20 to 20 kHz) is the range where human ears operate. Ultrasound refers to sound with frequencies higher than 20 kHz and infrasound relates to those with frequencies below 20 Hz.

Diagnostic ultrasound

Interestingly, the sound itself can not only be heard or detected but it can also be used as a tool for inducing and creating new sounds. Remember that a sound or an acoustic wave is nothing but mechanical vibrations of the medium. Each vibrating particle in the medium transfers part of its energy into the neighboring particles and makes them vibrate. This is how an acoustical wave is traveling (propagating) though a medium. When such an acoustic wave reaches a new medium, it not only induces acoustic waves in the new medium but also is reflected at the interface of the media. Consequently, this reflected acoustic wave propagates back to the original medium (so called reflected acoustic wave or echo). The principle of the propagation and reflection of an acoustic wave (imagine a short loud scream in front of two walls) is depicted in Figure 1. A short acoustic wave (wave 1) with amplitude of A_1, is propagating through the medium (in this case air) and hits the first wall (reflector) which is located at the distance D_1 from the source. Part of this wave is reflected backwards (wave 2 with amplitude A_2) and the rest propagates through and passes the first wall (wave 3 with amplitude A_3). Then, this wave hits the next wall. Again part of the wave is reflected (wave 4 with amplitude A_4). Amplitudes (loudness) of the reflected waves (A_2 and A_4) indicate how strong the walls can reflect the sound depending on their material properties. The location of the walls (D_1 and D_2) can be estimated by measuring the time it takes for the sounds to travel from the source to the walls and back to the source (T_1 and T_2): since the speed of sound in the medium is known (speed of sound in air is about 330 meters per second (m/s)) the distances D_1 and D_2 are proportional to T_1 and T_2. The amplitude of the echoes on the other hand can reveal some information about the differences in the material of the walls. Such information is used in diagnostic ultrasound to map the different tissue types and their locations in an image.

This is the principle of medical diagnostic ultrasound imaging or sonography: sending sounds (in the ultrasound frequency range) to hit media (tissues) with different properties and listen to (detect) the different echoes they make. Such a transmission and detection of acoustic waves are done with a part of an ultrasound imaging device called transducer or probe (Figure 2A). These detected ultrasound waves are usually converted into images for better interpretation especially when dealing with two dimensional (2D) and three dimensional (3D) configurations. The principle of diagnostic ultrasound imaging reconstruction is very simple. Let's assume a 2D configuration with some simplifications. The ultrasound probe transmits thin beam of sound into tissue one after each other

along its length and receives the echo signals from the tissue. Tissue never is homogeneous and small variations in the density and compressibility will scatter the acoustic waves differently, producing echoes that are different in amplitude and maybe also in frequency. Thanks to the almost constant speed of sound in soft tissue (~ 1540 m/s), the time that it takes for the echo signals to reach the ultrasound probe determines the locations (depth) of the different tissue types reflecting the sound. A conventional 2D ultrasound image (Bmode image) is created by repeatedly transmitting a thin beam of sound along the ultrasound probe into the tissue and receiving the echo signals. Then the amplitude of each thin echo beam is detected and converted into intensities for displaying (Figure 2B). This way, the stronger the echo signals from a particular tissue the brighter that tissue appears on the ultrasound Bmode image. This principle is illustrated in Figure 1B where a kidney of a mouse has been imaged with a high frequency ultrasound imaging platform in Figure 2A. The 2D Bmode image is reconstructed from the amplitude of 256 thin ultrasound beams where one of them is highlighted by a yellow box and enlarged in Figure 2B. Each of these gray scale lines are reconstructed from detected amplitude of an echo beam. An example of such an echo signal corresponding to the yellow box is shown in Figure 2B (blue signal). The detected amplitude of such an echo signal is overlaid on the echo signal in red in Figure 2B.

Thanks to the technological development in the past decades, reconstruction of the ultrasound images are performed very rapidly resulting in almost real-time imaging of the target. With fast reconstruction methods, it is possible to monitor moving structures such as a pumping heart in real-time. Various types of ultrasound images can be formed using current medical ultrasound instruments. Although the most well-known types are B-mode image and images of moving organs, other types of ultrasound imaging can display blood flow, the location of blood pools, the presence of specific molecules, the stiffness of tissue, or the anatomy of a three-dimensional region. Ultrasound can also be used therapeutically, to break up gallstones and kidney stones or to heat and destroy diseased or cancerous tissue.

The resolution of an ultrasound image along the direction of the acoustic wave (axial direction) depends on the length of the acoustic wave (wavelength) transmitted by the probe. The resolution in the other direction (lateral resolution) is determined by the narrowness of the wave transmitted. Both of these resolutions in a 2D ultrasound image generally are related to the frequency of the transmitted acoustic wave. The frequency range used in clinical ultrasonography ranges from 1 to 10 MHz resulting in pixel resolution in the range of 1 – 0.1 mm^2. In the preclinical applications (imaging small animals such as mice and rats) higher resolutions are preferable since the anatomical structures are much smaller than in humans. Therefore, higher frequencies (>15 MHz) are used for preclinical applications. Although increasing the frequency improves the resolution of the acquired ultrasound images, the penetration depth of the acoustic waves in the tissue and therefore the depth of the ultrasound images decreases. This is due to the fact that the absorption of ultrasound energy by the medium increases by increasing the frequency. With the frequencies used in clinical applications the image depth can be up to 10 cm whereas this depth is usually below 2 cm for preclinical applications with high frequency ultrasound.

Contrast in ultrasound images depends generally on the amplitude of the echo signals corresponding to each location. Stiffer tissues backscatter the ultrasound signal stronger than the other softer tissues and they appear brighter in the image. Blood in the other hand is a weak scatterer. Therefore it appears darker than other tissues in an ultrasound image. Imaging of blood supply in the body has high diagnostic value. For instance, blood supply through very small vessels (microvasculature) in an atherosclerotic plaque can predict the risk of rupture for such a plaque. Rupture of an atherosclerotic plaque in the arteries is one of the main causes of heart attack and stroke. Also, presence or absence of blood can reveal crucial information for detecting a tumor and whether a tumor is benign or malignant. Therefore imaging blood throughout the different carrying structure in the body is of great importance in the medical field. In order to be able to image blood with ultrasound with good enough contrast, exogenous scatterers, so called ultrasound contrast agents (UCAs) are required.

Ultrasound contrast agent

The origin of UCA was an accidental discovery by Gramiak and colleagues in 1968. During ultrasonography examination, they observed that the injection of agitated saline in the blood circulation resulted in strong echoes from that part of the blood containing the agitated saline. The gas introduced by agitation appeared as bright scatterers on the ultrasound images. The reason for such strong echoes was the micron-size air bubbles (microbubbles) in the saline produced by agitation. Generally, gas has higher compressibility than surrounding liquid and tissue, therefore acting as stronger scatterers than the surrounding medium. The modern UCA are still gas-filled microbubbles (MBs) with shells made of lipids, polymer or proteins for both stabilization of the MB and biocompatibility. Also gases heavier than air are used (e.g. C_4f_{10}) to improve the life-time of the MB in the physiological conditions. The size of commonly used UCA (e.g. SonoVue®, MicroMarker®) ranges between approximately 1-8 μm in diameter. This is very comparable to size of human red blood cells which have disk diameters of approximately 6.2–8.2 μm and thicknesses of 2–2.5 μm. UCA is generally administered by intravenous injection (mostly via tail veins in small animals such as mice, Figure 2A). Small sizes of the MBs allow them to flow in the circulation system after being injected. Before entering the systemic circulation, MBs have to pass through the lung capillaries. The small size of pulmonary capillaries filters out the larger MBs (> 5 μm). The injected dose of the UCA compared to the blood volume is very low (less than 3 mL of UCA compared to average 5 L of blood in human). However, due to the large number of MBs (in the order of 1.10^9 per mL), the signal from the blood pool is considerably enhanced. Few minutes after injecting the MBs, they are deteriorating by: passing the lungs and capillary beds; being taken up by physiological mechanism such as macrophages in liver; or just being deflated. The total volume of gas that the injected MBs contain, is very small (in the order of 0.4 mL) and is ultimately exhaled (note that the volume of gasses exhaled in a single regular breathe is about 500 mL).

The increase in the application of UCA arises from extensive fundamental research on the behavior of MBs in an ultrasound field. MBs behavior can be investigated individually using an acoustical and/or an optical experimental setup. The departments of Biomedical Engineering at Erasmus Medical Center in Rotterdam and Physics of Fluids at University of Twente have developed and built a high-speed camera called Brandaris 128. Brandaris 128 is capable of recording 128 frames as fast as 25 million frame per second. This gives the opportunity to capture the oscillation of MBs even when they vibrate as fast as 10 million times

per second (10 MHz). An example of such optical investigation of microbubble oscillation with Brandaris 128 camera is depicted in Figure 3. Both the acoustical and optical investigations on MBs show that their behavior when insonified with high intensity ultrasound waves is nonlinear. For instance if you insonify a MB with an ultrasound wave which has an amplitude A and record the echo signal from the MB (let's call it Echo1) and then repeat the experiment with an ultrasound wave with double the amplitude (2×A) and again record the echo from the MB (Echo2), the amplitude of Echo2 is most probably not two times the amplitude of Echo1. Even sometimes if you insonify the same MB two times with exactly the same ultrasound wave the echo signals can be different. Such nonlinearity in the MB response is not only in the amplitude of the echo signals but also can occur in the phase information. The nonlinear behavior of MBs is the key feature employed by most of the techniques used for imaging the UCA in medical ultrasound applications. Interestingly, the response of tissue to the ultrasound, in the moderate amplitude rage, is rather linear. Therefore, with techniques capable of exploiting the nonlinear component of the echo signals, UCA signals can be separated from the tissue signals. Moreover, UCA can be destroyed with ultrasound waves with high enough amplitude. This controlled temporary presence of UCA can also be utilized for detecting and visualizing them. For instance, in one ultrasound image the UCA in the blood pool surrounded by the tissue is imaged, then a high intensity ultrasound is applied to burst the MBs and then the same location is imaged again. The subtraction of these two images results in an image containing only the destroyed UCA, since the tissue signals in both images are the same and therefore canceled out by subtraction. An example of so called contrast mode images exploiting the nonlinear responses of the UCA are depicted in Figure 2C and 2D. Figure 2B is the corresponding contrast mode image of a mouse kidney before injection of the UCA. Ideally this image should be completely black, but there are always some artifact signals due to imperfect cancelation of the tissue signals. In this example the artifact signal is mainly coming from the skin interface which is a very strong reflector for ultrasound. However the tissue signal from the kidney itself is suppressed very well. Figure 2D shows exactly the same location but after injecting the UCA. The UCA in the kidney is detected and well visualized.

The UCA are widely used in clinical and preclinical applications and they have been shown to be safe compared to other non-ultrasound diagnostic contrast agents, and the merits are high [1-5]. Besides being strong reflectors of ultrasound signals and enhancing the contrast of the blood pool, MBs are used for other interesting applications among which are sonoporation and drug delivery and molecular imaging.

Sonoporation and drug delivery

Sonoporation is a method which utilizes ultrasound to modify the permeability of the cell's membrane. The exact mechanism of sonoporation is still under investigation. However, MBs seem to be able to massage the membrane of the cell while they are oscillating or breaking when ultrasound is applied. This way, large molecules such as DNA can be transferred into the cell. Also, efficiency of delivering drugs into the cells can be improved with this technique. Another interesting application of MBs is drug delivery which is usually combined with sonoporation. Different drugs can be loaded, in the core, into the shell or attached to the shell of MBs. When reaching the diseased cells, drugs carried by the MBs can be released locally with applying high intensity ultrasound to disrupt the drug loaded MBs. This method of delivering drug benefits from the sonoporation effect since the MBs are attached to or close to the target cells.

Ultrasound molecular imaging

Molecular imaging using high frequency ultrasound (micro-ultrasound) and UCA is the main topic of this research and will be addressed extensively throughout this manuscript. Briefly, molecular imaging is a method to better understand fundamental molecular pathways inside organisms and diseases in a noninvasive manner. Generally, with progression of any disease the normal physiological pathways can be disturbed. Signs and indicators of a particular disease state or some other physiological state of an organism are known as biomarkers. Utilizing the MBs, different type of ligands can be attached to their shell. These ligands can target a specific biomarker of a particular disease. For instance antibodies which can bind to a particular biomarker can be attached to the polyethylene glycol spacer (PEG) arms which are embedded in the lipid shell of the MBs via a streptavidin biotin bounding (Figure 4D). Imaging targeted MBs (tMBs) which are attached to biomarkers of a disease can reveal information about the disease at the molecular level. It's a rather new technique, started in late 90s where MBs that were decorated with ligands targeting specific biomarkers were used to indicate malignancy of various tumor types. Ultrasouns molecular imaging can also be combined with sonoporotion and drug delivery technologies. The drug-loaded MBs can be targeted in a way to find the site of a particular disease through blood circulation. Ultrasound molecular imaging can be divided into

three major phases: Manufacturing and characterization of the tMBs; targeting and imaging the tMBs attached to the diseased biomarker; and quantification of the attached tMBs representing the diseased molecular signals. These crucial steps will be addressed extensively through the chapters of this manuscript.
Because of the size of the MBs (similar to red blood cells) these agents are confined to the blood pool. Therefore, they are perfect agents for targeting the biomarkers expressed on interior surface of blood vessels (endothelium). The physiological process of new blood vessels growing from the pre-existing ones (so called angiogenesis) is an important step in growth and development, as well as in vital mechanism such as wound healing. However, angiogenesis is also a fundamental step in progression of diseases: malignancy of tumors and vulnerability of atherosclerosis plaques are among those which together are the major cause of mortality in developed and developing countries.

Atherosclerosis

Atherosclerosis is a disease in which an artery wall thickens as a result of accumulation of materials such as white blood cells, cholesterol, triglycerides, eventually calcium and other crystallized materials. The accumulated materials within the artery wall are referred to as atherosclerotic lesions, or atherosclerotic plaques (Figure 4B). Atherosclerosis is a chronic disease that can exist without being noticed for decades meaning that one can live with a stable form of the disease without noticing it for his/her entire life. Chronically expanding atherosclerotic lesions can eventually cause complete closure of the lumen leading to death of the tissues fed by that artery. Apart from such slow atherosclerosis progress, a faster mechanism called plaque rupture can occur in more advanced stage of the disease (Figure 4C). The unstable (also called vulnerable) atherosclerosis plaque can rupture and expose its thrombogenic content to the blood circulation and induce acute thrombus formation in the lumen of arteries (Figure 4C). In some cases such thrombi can occlude arteries outright, or detach and move into the blood circulation and eventually occluding smaller downstream branches, leading to death of the tissues fed by the artery in approximately five minutes. This catastrophic event is called an infarction. When such an event happens in the arteries feeding the heart muscles (coronary arteries) one of the deadliest scenarios is occurred, causing myocardial infarction (a heart attack). Similar process can happen in an artery feeding the brain (carotid arteries) causing stroke.

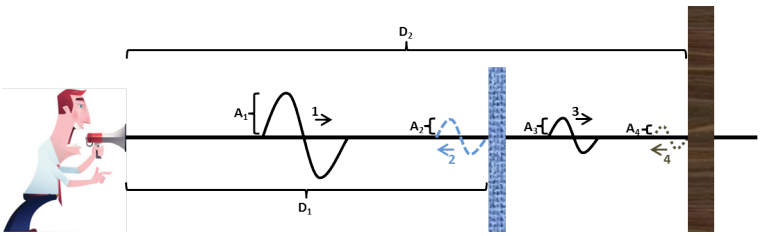

Figure 1
Simplified principle of propagation and reflection of sound. A short acoustic signal (wave 1) is generated and propagated through air hitting two walls (reflectors) on its way. Part of wave 1 is reflected by the first wall (wave 2) and the rest passes through (wave 3) and hits the second wall. Second wall also reflects part of the acoustic wave (wave 4). The amplitude of the waves (A_1 to A_4) show the strength of the acoustic waves and the location of the walls (D_1 and D_2) can be calculated assuming a fixed and known speed of sound in the medium and measuring the time it takes for the echo signals to travel back to the source.

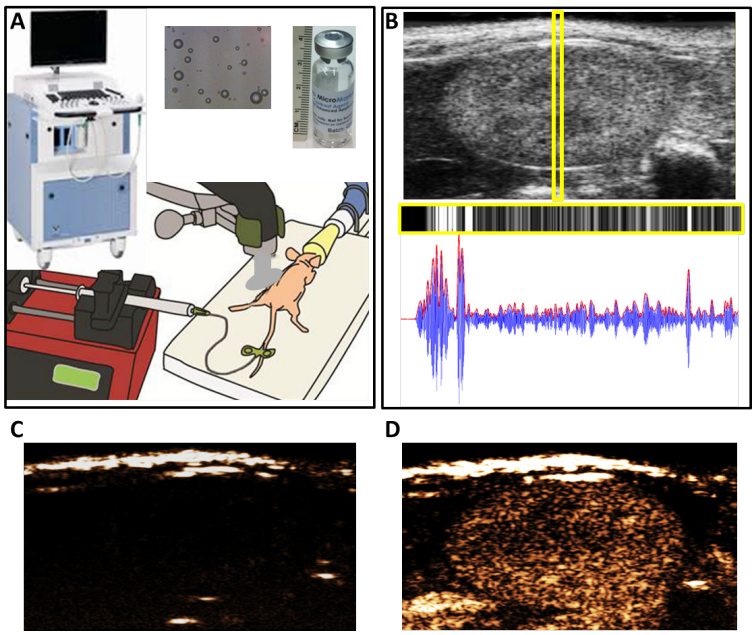

Figure 2
Principles of medical ultrasound imaging and image reconstruction in Bmode and contrast mode:
A) Clockwise from top left: an example of a micro-ultrasound imaging platform (Vevo 2100, VisualSonics Inc.); a microscopic image of microbubbles with 400 times magnification; a picture of MicroMarker ultrasound contrast agent vial; a cartoon of a mouse laying on a pad which is warm to keep the animal at the appropriate temperature, has sensors to monitor the physiological signals (ECG, temperature and breathing) of the animal and a mask connected to anesthetic gasses to keep the animal unconscious if needed; a schematic of an ultrasound imaging probe with a holder for positioning the probe; a butterfly needle and a syringe mounted on a microinjection pump for injecting the ultrasound contrast agent into animal blood circulation via the tail vein.
B) A conventional 2D Bmode ultrasound image of a kidney of a mouse acquired with Vevo 2100 high frequency ultrasound system and MS250 probe; this image is reconstructed from thin ultrasound beams converted to grayscale images and stacked up to make a 2D image, an example of such a grayscale image and the recorded backscattered wave with its detected amplitude is depicted in this Figure as well.
C) A contrast mode image of the same kidney before injection of microbubbles, ideally this image should be completely black but there are always some artifacts due to imperfect cancelation of tissue signals.
D) Contrast mode image after injection of the microbubbles where only the microbubbles are imaged (as well as the tissue artifacts in panel C).

Figure 3
Optical investigation of microbubble oscillation with Brandaris 128 camera. The microbubble is placed in an OptiCell at the focus of an ultrasound transducer. Brandaris camera starts recording 128 frames at the same time the microbubble is excited by the acoustic wave shot by the ultrasound transducer. An example of 128 frames of a microbubble oscillation captured by Brandaris is showne in the top part of the Figure. Note that the Brandaris 128 camera is almost 2 meters long and 2 meters wide where the microbubble diameter is about 5 micrometer.

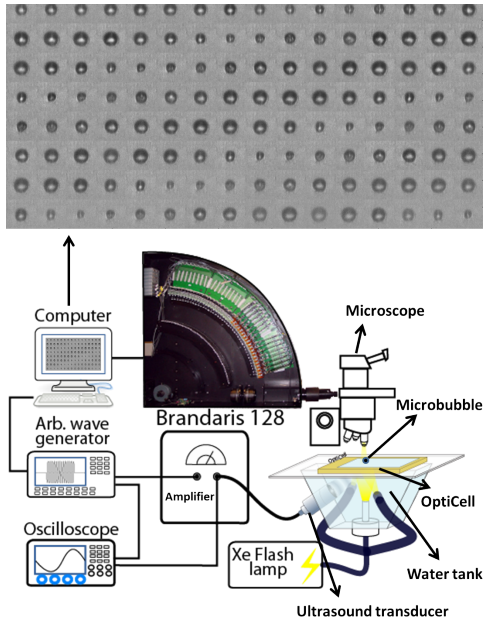

Figure 4
Atherosclerosis and targeted microbubbles.
A) A healthy artery with an actual cross section of mouse carotid artery under the microscope (~ 0.5 mm in diameter) showing the healthy artery wall in dark pink color and an open lumen.
B) Atherosclerosis plaques narrowing the lumen of an artery with an actual cross section of mouse carotid artery under the microscope (~ 0.5 mm in diameter) showing the plaque almost entirely occluding the lumen.
C) Rupture of advanced atherosclerosis lesion and formation of thrombus in-and outside the plaque and propagation of thrombus into the blood circulation.
D) Targeted microbubble attaching to biomarkers on diseases endothelial cells while circulating in a microvessels together with red blood cells (RBCs).

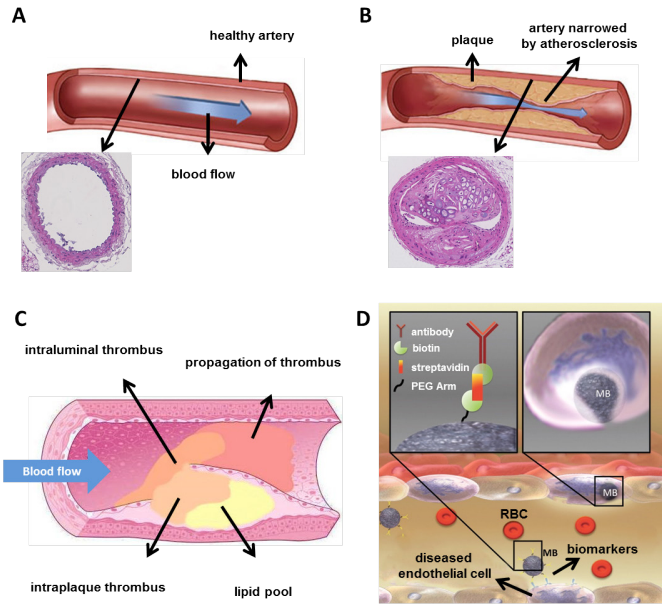

Figure. 5. High resolution images acquired by 4Pi microscopy showing the ligand distribution on DPPC microbubble (A) and DSPC microbubble (B). The color bar indicates the fluorescence intensity (see Ref. 8 for details).

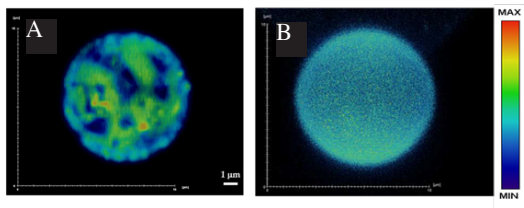

Outline of the thesis

Ultrasound molecular imaging is a multi-disciplinary endeavor which accommodates many fields of knowledge. Besides the everyday research and discoveries on new biomarkers for various diseases, manufacturing and functionalizing the tUCA, imaging and quantifying the tUCA with high enough sensitivity and specificity are the hotspots of current researches in the field. This thesis is aiming at improving the major phases in molecular imaging especially for micro-ultrasound and preclinical applications focused on atherosclerosis as the main clinical target. Current state-of-the-art for each of these divisions is extensively addressed in chapter 2.

In Micro-ultrasound molecular imaging applications where the excitation frequency is much higher than the resonance frequency of the MBs, an optimized nonlinear contrast imaging technique with high sensitivity and specificity is still a challenge. To overcome this challenge we have proposed to exploit the subharmonic (SH) response of the MBs. In chapters 3 and 4, using numerical simulations as well as acoustical investigations on a population and individual of MBs, we have optimized the excitation pulse parameters such as pulse envelope, pulse length and acoustic pressure for high frequency subharmonic imaging. Furthermore, in chapter 5, the widely used preclinical micro-ultrasound imaging platform (Visualsonics Vevo 2100) has been investigated to systematically compare the imaging parameters for optimization of imaging settings in various applications. In this chapter, first SH, nonlinear-fundamental (NF) and ultraharmonic (UH) imaging were compared *in vitro* for different image depths and UCA concentrations. Then, the best candidates from the *in vitro* study were tested *in vivo in* chicken embryo and mouse models.

Beside the imaging parameters, size distribution and manufacturing mechanism of the UCA have been shown to effect the SH response of the MBs [6-8]. This is perhaps due to distribution of lipid components and the ligands attached to the tMBs resulting in different microstructural materials on their shell. In our Lab Kooiman et al. [8] studied the lipid distribution of DSPC vs DPPC in the shells of the UCAs by adding the lipid dye DiD to the microbubbles before sonication and acquiring high-resolution images with 4Pi microscopy. The results clearly showed nonhomogeneous distribution of microstructure on the MB shell for DPPC (Figure 5A) versus homogeneous for DSPC (Figure 5B). Inspired by these result we performed a comparison study to investigate the nonlinear behavior especially the SH response of various homemade UCAs with widely used and commercially available MicroMarker contrast agent. The result of this study is presented in chapter 6.

Besides the improved detection and imaging of the UCA for high frequency ap-

plication, selective imaging of true bound tMBs from free flowing unbound ones is another challenge and a popular topic for research in the field of ultrasound molecular imaging [9-13]. Improving the quantification of tMBs is the focus of chapter 7 where a novel post-processing method is developed and tested *in vitro* and *in vivo*. This novel quantification method benefits from motion compensation and individual contrast spot detection, and is capable of distinguishing the b-MB from u-MB based on their displacement.

Quantification of angiogenesis in atherosclerosis and tumors is perhaps the application where ultrasound molecular imaging is used the most [14-24]. Atherosclerosis is the main target of micro-ultrasound molecular imaging in our research. Therefore the most commonly used small animal model, apolipoprotein E-deficient ($ApoE^{-/-}$) mice model, was chosen for *in vivo* validation of the methods we have developed. A number of pathophysiological mechanisms are thought to be involved in the progression of an atherosclerotic lesion into a vulnerable plaque. Among those, Intraplaque neovascularization of the vasa vasorum has gained interest as a preceding or concomitant factor in the development, progression, and instability of atherosclerotic plaques [25-27]. The intraplaque vasa vasorum are therefore increasingly investigated as a marker for the noninvasive identification of vulnerable plaques. It has been shown that along with angiogenic activities in the atherosclerosis plaques, $\alpha_v\beta_3$ integrins are expressed in the adventitial and intraplaque vasa vasorum [28-31]. Therefore, $\alpha_v\beta_3$ was chosen as an appropriate receptor for molecular imaging of plaque neovascularization in this research. Although, this molecular marker has been used for ultrasound molecular imaging of angiogenesis in tumors and hind limb ischemia [23,32], to the best of our knowledge, our study presented in chapter 8 is the first successful *in vivo* ultrasound molecular imaging of vasa vasorum neovessels with $\alpha_v\beta_3$ integrins in carotid plaques of a mouse model. We showed that, $\alpha_v\beta_3$-targeted UCA allows noninvasive assessment of the expression levels of $\alpha_v\beta_3$ on the vascular endothelium and may provide potential insights into early atherosclerotic plaque detection and treatment monitoring. During performing the experiments stated in chapter 8, symptoms suggesting plaque disruption in the right brachiocephalic artery of one of the animals were observed. Histological analysis of the affected carotid artery and brachiocephalic trunk confirmed presence of intraplaque haemorrhage in advanced atherosclerotic lesions in the brachiocephalic trunk, with plaque dissections, pointing towards plaque rupture as the cause of the observed event. Although features suggestive of plaque rupture in $ApoE^{-/-}$ mice have been reported [33-38], whether plaque disruption actually occurs in mice has been a matter of debate in the past decade [39-45]. For the first time, we observed

possible spontaneous plaque disruption in the right brachiocephalic artery of an ApoE$^{-/-}$ mouse real-time with contrast enhanced ultrasonography. These results are briefly reported in chapter 9.

Then, in chapter 9 a unique UCA consist of polymer-shell microbubble with potential use for local delivery of therapeutic gases is characterized using the Brandaris high-speed camera and an acoustical setup. This chapter describes the very unique fracturing mechanism of air-filled MBs, encapsulated by a cross-linked polyvinyl alcohol (PVA) shell[46] investigated by the ultra-high-speed Brandaris-128 camera, and an acoustic set-up. Both the qualitative (optical visualization) and quantitative (acoustical interrogation) assessment of PVA-MBs at high insonation pressures revealed that the fracturing mechanism of PVA-MBs was unique and different from the previously reported fracturing behavior of polymer-shelled MBs. We named this fracturing mechanism “pumping-out”, and this behavior could have potential use for the local delivery of therapeutic gases, such as nitric oxide. Local therapeutic gas delivery is of great clinical interest and the subject of extensive research [47].

Finally, chapter 10 summarizes the accomplishments and conclusions of our research and suggests the possible improvements in the field of ultrasound molecular imaging.

Targeted ultrasound contrast agents for ultrasound molecular imaging and therapy

02

Abstract

Ultrasound contrast agents (UCAs) are used routinely in the clinic to enhance contrast in ultrasonography. More recently, UCAs have been functionalized by conjugating ligands to their surface to target specific biomarkers of a disease or a disease process. These targeted UCAs (tUCAs) are used for a wide range of pre-clinical applications including diagnosis, monitoring, and therapy. In this review, recent achievements with tUCA in the field of molecular imaging, evaluation of therapy, drug delivery, and therapeutic applications are discussed. We present the different coating materials and aspects that have to be considered when manufacturing tUCAs. Next to tUCA design and the choice of ligands for specific biomarkers, additional techniques are discussed that are applied to improve binding of the tUCAs to their target and to quantify the strength of this bond. As imaging techniques rely on the specific behavior of tUCAs in an ultrasound field, it is crucial to understand the characteristics of both free and adhered tUCAs. To image and quantify the adhered tUCAs, the state-of-the-art techniques used for ultrasound molecular imaging and quantification are presented. This review concludes with the potential of tUCAs for drug delivery and therapeutic applications.

Based on a manuscript by **V. Daeichin***, T. van Rooija*, I. Skachkov, N. de Jong, and K. Kooiman, in International Journal of Hyperthermia in 2014 (* contributed equally).

Introduction

Ultrasound contrast agents (UCAs) consist of gas bubbles that are typically stabilized by an albumin, lipid or polymer shell. For over three decades, UCA have been clinically used to enhance ultrasound (US) imaging in different fields, such as cardiology and radiology [48,49]. Targeted UCAs (tUCAs) differ from clinically approved UCAs by the decoration of their shell with targeting ligands [50]. Due to their typical size (~1-10 μm) UCAs are confined to the blood pool only [51,52]. This makes tUCAs ideal agents to adhere to intravascular biomarkers expressed on endothelial cells, to target for instance cancer and cardiovascular disease, as covered in this review. Because of the large compressibility of the gas core of the microbubbles (MBs), they create nonlinear backscatter and reflection in an US field, allowing for differentiation between the highly echogenic agent and surrounding tissues and fluids [53,54]. Recently, smaller tUCAs have been synthesized which allow them to extravasate out of leaky vasculature offering opportunities for new applications [55,56].
This review focuses on tUCAs for ultrasound molecular imaging (UMI) and therapy. Manufacturing and functionalizing tUCAs will be covered, including targeting novel biomarkers. The binding and acoustic properties of bound tUCAs will be evaluated, as these properties are important for both UMI and therapy. The current state-of-the-art clinical and preclinical molecular imaging techniques and quantification methods are discussed. tUCA-mediated drug and gene delivery is a relatively new field as the first proof of concept was reported in 2011 [57]. The progress since then will be presented.

Targeting and binding of tUCAs

To compose tUCAs several aspects have to be accounted for. A choice for the coating has to be made, the biomarkers that are upregulated in the disease of interest have to be identified, and a suitable targeting ligand has to be found. This targeting ligand has to be firmly attached to the contrast agent and the binding properties of the tUCA have to be evaluated.

Coating materials

The commercially available UCAs have different coating materials to reduce the surface tension and gas diffusion out of the UCAs, thereby increasing their lifetime. These are: albumin (Albunex, Cardiosphere, Optison), galactose (Echovist, Levovist), lipids (Definity, Imagent, Levovist, Lumason, MicroMarker, Sonazoid, SonoVue, Targestar), or polymers (Acusphere, Sonovist) [58,59]. The main advantage of lipid-coated bubbles is that different mixtures can be easily formulated and modified [59]. Very recently, super-resolution fluorescence microscopy revealed that the main lipid in the coating coating (1,2-distearoyl-sn-glycero-3-phosphocholine, DSPC or 1,2-dipalmitoyl-sn-glycero-3-phosphocholine, DPPC) influences the ligand distribution on the shell [60] and it was also shown that the difference in ligand distribution also changes the acoustical properties [61]. This offers opportunities for designing UCAs with very specific and known properties. Most lipid-coated UCAs have a brush of polyethylene glycol (PEG) incorporated in their shell to prevent close contact between neighboring bubbles to inhibit their fusion and to shield them from the immune system [59]. But although this is generally accepted as a method to increase UCA lifetime, the necessity of incorporating PEG for tUCAs has been questioned [62]. This study indicated that small peptides either conjugated to the lipid directly or via a PEG-spacer (~10 monomers), might hinder access of the ligand to the target receptors when short PEG brushes (molecular weight of 350 kDa; i.e. 8 monomers) are part of the coating. Even when the MBs were prepared without a PEG brush in their coating, the introduction of a PEG spacer between the ligand and the lipid seemed to reduce binding. Their hypothesis is that the flexibility of the spacer possibly enabled the peptide to loop back onto the bubble surface. According to Marsh et al. [63] this is indeed what happens: due to their choice of incorporating relatively short PEG chains in the coating, the PEG chains will be in the mushroom regime and therefore assume a random configuration. If they would have used similar concentrations of PEG with longer chains, such as PEG(2000) containing [45] monomers, these chains would be in the brush state: a more stretched and less random configuration [63]. The random configuration of the PEG chain in the study of Myrset [62] could thus shield the ligand, whilst a brush configuration may have been advantageous.

Polymer tUCAs have a stiffer and thicker coating than lipid-coated bubbles, and the main acoustic difference is their echogenicity: usually a polymer bubble is destructed and the free gas bubble is detected, whereas a lipid-coated bubble can be used for non-destructive imaging [53]. Combinations of different shell materials have also been reported; Ottoboni et al. [64] used microcapsules with a cross-linked albumin outer layer and a poly-(DL-lactide) inner layer. The advantage of the two different layers is the possibility to tweak the acoustic performance via the inner polymer layer in terms of their stiffness and thickness, and

to change the biological activity via the protein outer layer.
In vivo, the adsorption of serum proteins on the shell (opsonization) is a major challenge in the design of UCA, as it might inhibit binding of the tUCA to its target. Lipid-coated MBs based on phosphatidylcholine (PC)—especially pure DSPC—have lower serum protein adsorption, higher stability in serum, and lower uptake by the reticuloendothelial system (RES) than negatively charged phospholipids, such as phosphatidylserine (PS) [62]. Another problem caused by opsonization is its triggering capacity for phagocytosis. As targeting ligands typically present nucleophilic groups (e.g., hydroxyl or amino) this could trigger complement C3/C3b activation to promote phagocytosis and decrease the tUCA circulation time. This can be partly overcome by using longer PEG chains that are in the brush state [62] to shield the ligands for complement activation ("overbrushing") thus reduce immunogenicity [65]. Unnikrishnan and Klibanov [59] on the other hand, state that complement activation aids MB adherence in the microvasculature. Although PEGylation of UCAs might decrease the circulation time, it does reduce immunogenicity and thus seems to be desirable.

Attaching ligands

The ligand that makes the tUCA functional is typically a peptide, protein, polymer, antibody, nanobody or aptamer [58,66-68] (Figure 1A). A reactive moiety suitable for conjugation with the ligand of interest needs to be attached to the tUCA shell, of which biotin (noncovalent), or covalent coupling via a carboxylate group, thiol, or maleimide are most common [59,69] (Figure 1A3). Covalent coupling does not require foreign proteins such as streptavidin, so the chances of immune response in a clinical setting are low [70]. A carboxyl group incorporated in the tUCA shell can be activated with carbodiimide, forming an active ester that reacts with the protein amino group, forming an amide bond. However, proteins possess multiple lysine residues, so coupling via amide bonds is random and may therefore interfere with ligand-receptor interaction. As an alternative, a maleimide on the shell is coupled to a thiol group on the ligand (or vice versa), forming a thioether. The advantage of maleimide-thiol coupling is oriented coupling: a ligand protein possessing a single thiol then has a single point attachment to the bubble shell. This retains the affinity of the ligand to its target [59]. A new class of ligands are camelid-derived single-domain antibody-fragments (~15 kDa) called nanobodies, that do not induce an immune response in humans [67].

Biomarkers and targeting strategies

tUCAs can be decorated with ligands against various diseases. As typical UCAs are confined to the vascular tree [52], the most commonly targeted biological processes are angiogenesis, inflammation, and thrombosis. With the introduction of smaller tUCAs that can extravasate, apoptosis can also be targeted [71].

Angiogenesis

Generally, tumors can be targeted by means of biomarkers for angiogenesis: $\alpha_v\beta_3$ integrin, vascular endothelial growth factor (VEGF), vascular endothelial growth factor receptor 2 (VEGFR2), endoglin (CD105) [58,66,72,73], or a combination hereof [22]. Cyclic RGD is a clinically translatable ligand that was confirmed to adhere to endothelial cells expressing $\alpha_v\beta_3$. In addition, the bubbles conjugated to cRGD had sufficient residence time to attach to the integrin and were specific for $\alpha_v\beta_3$-expressing cells [74]. Another strategy to target $\alpha_v\beta_3$ used the clinically approved contrast agent Sonazoid. The PS incorporated in the UCA coating was conjugated to lactaderin. This is analogous to the process of phagocytosis: apoptotic cells externalize PS allowing lactaderin to bind to PS to promote binding to the integrins on the surface of phagocytic cells [75]. Since adherence of the MBs functionalized with lactadherin to human umbilical vein endothelial cells (HUVEC) under flow was higher than for bare MBs, this complex has potential to be translated to the clinic for targeting angiogenesis.

For VEGFR2 targeting the lipid-coated BR55 bubble (Bracco Diagnostics) is most promising for translation to the clinic for which a heterodimer peptide is directly conjugated to the PEGylated lipid [72]. Recently, a phase 0 clinical trial with this agent for prostate cancer was successfully conducted [76].

Inflammation

Inflammation plays a role in several diseases, such as atherosclerosis, and transient ischemia [15-18]. Specific inflammation markers that have been used for tUCAs are intracellular adhesion molecule 1 (ICAM-1), vascular cell adhesion molecule 1 (VCAM-1), E-selectin, and P-selectin [64,66,77,78]. MBs targeted to VCAM-1 can be used to discriminate the severity of inflammatory burden in mice with various degrees of atherosclerosis [15]. This suggests that assessment of early inflammation in plaques is feasible. However, the same study showed that MB attachment to endothelial cells exposed to high wall shear stresses was very low (*in vitro*). This did improve with short interruptions of the high shear rate, as is the case with a pulsatile blood flow. Since the adhesion molecules ICAM-1 and VCAM-1 mediate the firmer adhesion of the leukocytes to the endothelium, and E-selectin and P-selectin promote the initial attachment and rolling of leukocytes [66], targeting both selectin and adhesion molecules can potentially improve initial binding and increase the binding strength.

Thrombosis

Targeting of thrombi is mainly focused on the glycoprotein IIb-IIIa (GPIIb-IIIa or CD41/CD61) expressed by activated platelets in the thrombus [55,58,66,79]. This glycoprotein mediates platelet-aggregation and is the most abundant receptor on the platelet surface [79]. Using Targestar-SA conjugated with anti-GPIIb/IIIa single-

chain antibodies, these bubbles bound specifically to activated platelets *in vitro*. This may allow for real-time *in vivo* molecular imaging of acute arterial thrombosis and monitoring of pharmacological thrombolysis. Next to antibodies, it has been shown that cRGD can also be used to target GPIIb-IIIa. Although this ligand is generally known as a marker for angiogenesis, cRGD was shown to be specific for GPIIb-IIIa (also known as integrin $\alpha_{iib}\beta_3$) as well [80]. cRGD was conjugated to the MBs via thiol-maleimide coupling and binding to GPIIb-IIIa was evaluated *in vitro* in the presence of plasma and under wall shear stresses up to 8 dynes/cm^2 [55]—a value representative for the human aorta averaged over the heart cycle [81]. Several studies have demonstrated that cRGD exhibits an ~30× higher binding efficiency than linear RGD, and indeed significantly more cRGD bubbles adhered up to the highest shear rate *in vitro* and in the larger arteries of mice [55].

Nakatsuka et al. [68] recently introduced a new concept using MBs that are only acoustically active at thrombin levels associated with clot formation. The targeting moiety of these bubbles was a thrombin aptamer crosslinking strand (TACS). Crosslinking limits the nonlinear signal generation of the MB due to the immobilization of the lipids in the shell. Upon decrosslinking the polymer-DNA strands completely displace from the TACS, allowing the MB to oscillate freely, enhancing their nonlinear response. The MBs consisted of DSPC, DPPA (1,2-dipalmitoyl-sn-glycero-3-phosphate), and 1,2-distearoyl-sn-glycero-3-phosphoethanolamine-poly(acrylic acid)-TACS (DSPE-PAA-TACS). When the bubbles are in contact with thrombin in the thrombus, this protein binds to the aptamer, which results in decrosslinking. The *in vitro* onset of decrosslinking was about 20 nM thrombin. Since *in vivo* clot formation starts with a concentration of ~25 nM thrombin this offers opportunities to detect small clots at an early stage [68]. This has been shown *in vivo* using similar MBs, but with different amounts of DSPE-PEG(5000) added to the mixture [82]. Small amounts of PEG were found to improve stability, while higher concentrations did not contribute significantly to stability. Indeed, it was also shown that these aptamer MBs enhanced US signal in the vicinity of clots.

Novel targeting strategies

The last few years molecular imaging using MBs has emerged and multiple novel targets have been proposed and investigated. Prostate cancer is difficult to diagnose noninvasively, and common practice is routine clinical testing in the laboratory to determine the level of prostate-specific antigen in the blood. However, this test lacks sensitivity and specificity [83]. The prostate-specific membrane antigen (PSMA) has higher expression levels in prostate cancer epithelial tissue than in normal prostate tissue and benign prostatic hyperplasia [84], and is therefore very promising for UMI and staging of prostate cancer as shown *in vitro*

[85]. Next to prostate cancer, other types of cancers have been successfully targeted *in vivo* using tUCA: 1) tumor vessels of angiosarcoma that were targeted via secreted frizzled related protein 2 (SFRP2) using DSPC:PEG(2000)-PE bubbles [86]; 2) ovarian cancer tumor vasculature that expresses CD276 with Target-Ready MicroMarker conjugated to anti-CD276 87; and 3) the neovasculature of pancreatic ductal adenocarcinoma targeted to thymocyte differentiation antigen 1 (Thy1 or CD90) using anti-Thy1 MBs [88]. The latter two are specific endothelial markers for human cancer types, which are a challenge to investigate in a preclinical setting. The group of Willmann [87,88] therefore developed a mouse model that expresses human vascular biomarkers by transfecting mouse endothelial cells with the human biomarker of interest and implanting these together with the tumor cells of interest.

In a preclinical setting Targestar-B was targeted to epidermal growth factor receptor (EGFR) and CD147 expressed in head and neck squamous cell carcinoma, where using the dual targeting was reported as most promising [89]. Although E-selectin is not a novel target, its upregulation due to inflammation can also be used to monitor tumor progression and metastasis. E-selectin can therefore be used as a new targeting strategy for early screening for tumors with metastatic potential [73]. Next to novel targeting strategies for tumors, ischemia-reperfusion after myocardial infarction was targeted to matrix metalloproteinase-2 (MMP-2) using polymer-shelled microcapsules. Apoptosis is another recently studied target, typically targeted to PS. Annexin V is known to specifically bind to PS [90] and was used for apoptosis imaging in breast cancer cells using nanobubbles [71].

Techniques to enhance binding

Binding of tUCAs to target biomarkers under *in vivo* conditions is a key factor for successful application of molecular imaging for diagnosis and therapy (Figure 1A). Methods to enhance binding of tMBs generally depend on adjustments in the coating of the tMBs and/or applying acoustic radiation force to push the tMBs to the target cells. Deflating the tMBs to increase the shell surface area [78], conjugating two [91] or three [92] different ligands to the coating, or optimizing the length of the ligand linker [93] are among those studies optimizing the tMBs for an enhanced binding effect. Also, the probability of successful binding may be increased by homogenizing the ligand distribution on the MB shell [60], but needs further investigation. In addition, larger tMBs have a higher binding force because of their larger binding area. Nevertheless, the shear forces induced by the blood flow experienced by larger tMBs are higher than those experienced by smaller tMBs: this increases the risk of detachment of larger tMBs from their targets. In a numerical study, the optimal tMB size for enhanced binding (assuming they keep their spherical shape) is suggested to be in the range of 2–4 µm in diameter [94]. In a very recent study, super-resolution microscopy was used to

compare tMBs based on DSPC or DPPC in terms of ligand distribution, binding area, and their shape upon binding (Figure 1B) [60]. This study shows that DSPC tMBs keep their spherical shapes after binding (Figure 1B1) and have significantly smaller binding areas than DPPC tMBs, which had a dome-shape after binding (Figure 1B2). Magnetic MBs have also been developed to enhance the targeting in UMI and therapy [95-97]. Magnetic targeting uses an externally applied magnetic field (typically a permanent magnet) to control the location of magnetically responsive MBs. Various magnetic MB preparations and applications have been published by Stride et al. in 2009 and 2012 [96,98]. For instance, the gas core of the MB can be surrounded by a ferrofluid and stabilized by an outer coating of L-α-PC. Such a magnetic MB could increase the dwell time of tMBs in a target volume, whilst specificity could be provided by biochemical targeting [98].
In addition to the tMB shell modifications, acoustic radiation force can be used to push the MBs against the vessel wall to further improve the targeting rate of the MBs [99-102]. This technique was also successfully used to improve the delivery of stem cells to the vessel wall which can be used for the repair of damaged tissue (Figure 1C) by developing echogenic complexes by conjugating tMBs to stem cells (StemBells) [103].

Measuring binding force

To evaluate the efficacy and strength of tUCAs, a measurement system capable of assessing the strength of various binding configurations is necessary. Several *in vitro* methods have been proposed. Kim et al. [104] used a micromanipulation technique to adhere a single tMB to an individual glass bead using two separate pipets (Figure 1D). The pressure applied by the bead pipet was incrementally increased until the MB detached from the bead. Using this method, the binding force was measured as a function of composition and structure of the lipid shell and the receptor-ligand pair in a controlled *in vitro* environment. For instance, the detachment force for the biotin-PEG-avidin system was measured to be in the order of 100 nN assuming the contact area of the MBs and the coated surface to be around 10 μm^2. In another study, atomic force microscopy (AFM) was used for assessing the adhesive interactions of tMBs with their target cells *in vitro* [105]. They used in-house developed lipid-shelled tMBs conjugated to the CD31 antibody using biotin-avidin bridging for adhesion to Sk-Hep1 hepatic endothelial cells and measured single distributions of the binding forces with a median of [93] pN. Controlled shear flow has also shown potential for monitoring the binding force of MBs targeted to P-selectin *in vitro* [106]. In this experiment attachment and detachment of tMBs to P-selectin immobilized on a culture dish was investigated in a parallel-plate flow chamber by increasing shear stress at intervals of 30 seconds. The accumulation rate first increased with shear stress, reached a maximum at ~0.6 dyn/cm^2 and then decreased. Half-maximal de-

tachment was reached at 34 dyn/cm^2. These results suggest that accumulation and retention of tMBs are possible under physiologic flow conditions [81]. Another approach for measuring binding force is the effect of secondary Bjerknes forces on tMBs, which was studied using a high-speed camera [107,108]. The secondary Bjerknes force is an averaged net force that neighboring MBs experience due to their oscillations in an ultrasound field. The direction of the force depends on the phase difference between the MB oscillations and the oscillating pressure gradient [109]. Kokhuis et al. [107] observed that bound tMBs deform in the direction of their neighboring MB when they were subjected to secondary Bjerknes forces. If low-intensity ultrasound is applied, the deformation induces an elastic restoring force, causing the MBs to recoil back to their equilibrium position. For higher acoustic pressures, the secondary Bjerknes force can break the bond between the tMB and the surface. Using this technique, the binding force between a single biotinylated MB and an avidin-coated surface was measured to be between 0.9 and 2 nN. In addition, the optical observation of the event suggests that lipid anchors are pulled out of the MBs shell, rather than destruction of the strong bond between biotin and avidin [107].

Characterization of tUCA

Non-targeted MBs for contrast-enhanced imaging, such as SonoVue and Definity, have been thoroughly characterized in terms of their acoustic behavior in an US field [110-113]. These studies mainly focused on bulk measurements, as regular contrast-enhanced US imaging is also performed in vessels containing high concentrations of microbubbles. However, for imaging of tMBs where only very few adhered MBs may be in the imaging field, the response of only a single MB or a cluster of MBs has to be detected. The response of a single MB in an US field is therefore of high interest to aid enhancement of the backscattered signal to improve imaging. A first step is to determine the MB properties after attaching a targeting ligand to it. The next step is the characterization of tMBs adhered to their molecular targets, and comparing this to the response of non-adhered tMBs to find parameters to distinguish them from each other.

Functionalized lipid-coated MBs

Only a few studies used functionalized MBs to determine the effect of functionalization on the MB properties; in particular their elasticity using either atomic force microscopy (AFM) or high-speed optical imaging. Using AFM, an elasticity

was found that was almost 30× higher for streptavidin-functionalized bubbles than for bare lipid-coated bubbles (710±41 vs 25±1.4 mN/m; DPPC:PE-biotin, 90:10 mol%) [114]. Recently, the same group performed AFM studies on bubbles with a C3F8 core and a lipid-coating of DPPC:DSPE-PEG(2000)-biotin or DPPC:DOPE-biotin (1,2-dioleoyl-sn-glycero-3-phosphoethanolamine-biotin) in a 90:10 ratio [115]. Both types were functionalized with streptavidin and bubbles with diameters between 3 and 4 μm were deformed up to 20% of their original size, whereas non-functionalized bubbles were deformed up to 50%. Here, streptavidin functionalization increased the elasticity to 26.9±1.4 mN/m for the PEGylated bubbles, but PEGylation itself was also found to increase the elasticity (17.7±0.7 vs 10.7±0.5 mN/m). However, the increase in elasticity between PEGylated and non-PEGylated MBs might actually be a consequence of the different lipids that were used for both bubble types: DSPE or DOPE as it has recently been shown that the main lipid of non-targeted biotinylated MBs changes the distribution of the lipids in the shell and its shell properties [60,61]. The authors do not explain the large difference in stiffness values between both studies [114,115]. Indeed, there does not seem to be a straightforward explanation. The preparation method is identical, but although the biotinylated lipids are different this cannot explain such a large difference. The major difference between both studies is the PEGylation [115], but this was found to increase the stiffness, and contradicts with their results.

To study the influence of functionalization on several MB properties, we functionalized identical biotinylated MBs—with either DSPC or DPPC as the main coating lipid [60]—with streptavidin via avidin-biotin bridging [116]. These unbound bubbles were investigated at frequencies between 1 and 4 MHz at a pressure of 50 kPa and their vibrational response was recorded by optical ultrahigh-speed imaging [61,117]. For DSPC and DPPC-based bubbles the acoustic stability increased after functionalization, although their shrinkage remained significant (Table I). The resonance frequencies of functionalized and non-functionalized DSPC MBs were similar, whereas those of DPPC MBs were higher for the functionalized ones. The number of MBs responsive at the subharmonic (SH) frequency was slightly lower for functionalized DSPC bubbles than for non-functionalized DSPC bubbles. For DPPC there was no change after functionalization. At the second harmonic frequency the functionalized and non-functionalized DSPC bubbles behaved similar, whereas after functionalization hardly any DPPC bubbles responded. The viscoelastic shell properties of both functionalized and non-functionalized MBs were estimated [61,117] using the Marmottant model [118]. The shell elasticity for DSPC slightly increased after functionalization, whereas for DPPC the elasticity increased almost fourfold. The shell damping and viscosity, on the other hand, did not change after functionalization.

Table I. Characteristics of streptavidin-functionalized and non-functionalized DSPC and DPPC bubbles

Type	Streptavidin-functionalized	Number of bubbles	Stability (%)*	Bubbles responding at the sub-harmonic frequency (%)	Bubbles responding at the second harmonic frequency (%)	Elasticity (N/m)	Viscosity ($\times 10^{-8}$ kg/s)*
DSPC	No #	15	95.9 (3.5)	27	67	0.17±0.06	1.2 (0.9)
	Yes	12	99.1 (2.8)	17	75	0.23±0.06	1.0 (0.5)
DPPC	No #	14	90.3 (8.2)	67	17	0.06±0.08	1.0 (0.3)
	Yes	6	94.4 (4.3)	71	79	0.21±0.08	1.8 (0.6)

* Median (IQR)

Data adapted from van Rooij et al. (14).

A critical side note regarding the elasticity estimated for the functionalized DPPC MBs is the narrow size distribution that did not cover the same range as the DSPC bubbles (DPPC: 4.8-6.2 μm; DSPC: 3.1-7.3 μm). However, our results clearly show an increase of the resonance frequency and thus of the elasticity, which corresponds with the results obtained using AFM [114,115]. The increase in elasticity after functionalization is believed to be due to the presence of crystallization of streptavidin around the lipid shell forming a stiffer external layer [115] as also observed on streptavidin-functionalized giant unilamellar phospholipid vesicles [119,120]. This is also consistent with the increased stability: a stiffer and thicker shell better prevents gas escape [121]. The above mentioned studies all found differences between streptavidin-functionalized MBs and non-functionalized MBs. In contrast, Overvelde et al. [122] concluded that the frequency of maximum response and the maximum amplitude of oscillation of functionalized bubbles (BG-6438, Bracco Imaging S.p.A., Milan, Italy) and non-functionalized bubbles (BG-6437, Bracco) did not seem to change. Although the main lipid component of BG-6438 and BG-6437 is not known, bubbles produced by Bracco are generally coated with DSPC as their main lipid [123-125], and indeed, this corresponds with our own data on DSPC-coated bubbles of which the resonance frequency did not change after functionalization (Table I).

Although streptavidin-biotin binding is a useful tool to gain insights into the effects of coupling of relatively large and heavy ligands to MBs *in vitro*, it can never be used clinically due to strong immune responses [70]. Therefore, alternatives for *in vivo* targeting have to be considered, such as peptides, polymers, or antibodies, as discussed in the Targeting and binding section. Peptides consist of a few amino acids (~100-200 Da) [126] and the RGD-peptide used typically for targeting has a molecular mass of ~380 Da. Since functionalizing bubbles with a small, low molecular mass ligand such as biotin (~250 Da) has hardly any effect on the MB response, it is expected that functionalization of MBs with a peptide has also minimal effect. Polymers are regularly used in MB designs to increase circulation times and to function as a stealth mechanism, mostly in the form of a PEG-lipid [127]. Abou-Saleh et al. [115] only mentioned a slight increase in elasticity upon PEGylation, but it is not known whether addition of a polymer changes other properties. Streptavidin-functionalization, on the other hand, has a significant effect on MB response. Since antibodies (~150 kDa) are more than 2× heavier than streptavidin (~60 kDa) an even larger effect, especially on the elasticity and resonance frequency, is expected. In addition, coupling an antibody covalently to a lipid could also induce cross-linking of the lipids as there are usually several reactive groups on an antibody.

Discriminating free from adhered MBs

The next step after functionalization of MBs is studying their behavior when they have bound to their molecular target. Moreover, the differences in acoustical signals between free and adhered bubbles are the key feature to facilitate discrimination.

Some of the non-functionalized biotinylated bubble types described in the previous section [60,61,128] were used to target an avidin-coated cellulose capillary using acoustic radiation force to promote binding [129]. Optical imaging was used to confirm bubble adhesion and high-speed optical imaging was used to visualize the oscillations [130]. The adherent MBs oscillated symmetrically in the plane parallel to the wall (similar to a free-floating MB) and asymmetrically in the plane normal to the wall. The side of the MB near the boundary expanded and contracted to a lesser extent than the side away from the boundary. The normalized radial expansion was larger for adherent bubbles in both imaging planes. When the transmission pressure was increased from 240 to 450 kPa, the center of the microbubble began to collapse toward the fixed boundary, producing a jet. At even higher pressures (650 kPa) fragmentation was observed in the plane parallel to the boundary, where the remaining fragments expanded and contracted, and were displaced along the wall away from the ultrasound source [129]. This can be advantageous for drug delivery applications when the drug is incorporated in or

attached to the shell of the MB. The response at the fundamental frequency was larger for adherent bubbles than for free bubbles [130], the responses at the SH frequency were similar, and the second harmonic component also increased [129]. At increasing pressures the signals at the third and fourth harmonic frequency were also higher for adhered MBs. One of the underlying causes of the higher fundamental (and maybe also harmonic) signals of adherent bubbles could be due to the small diameter of the bubbles (<< acoustical wavelength) and the nearly uniform spatial distribution of free bubbles, resulting in incoherent echo summation and a small backscattered intensity from each sample volume. Alternatively, a layer of tUCA adherent to the inside of a vessel wall reflects US coherently, resulting in a large reflection of the fundamental component. Secondly, the adherent bubbles formed aggregates, which increase the coupling between adjacent bubbles and thus their effective scattering cross section [130].

In addition to adhered and free floating microbubbles, Overvelde et al. [122] studied bubbles close to an OptiCell wall, using ultrahigh-speed imaging. For non-functionalized bubbles close to the wall the amplitudes at the frequency of maximum response were lower than for free-floating non-functionalized MBs. However, the OptiCell wall was not blocked for unspecific binding, hence these bubbles probably also adhered to the wall and cannot be considered as non-adherent. The observation that still holds is the 50% lower frequency of maximum response for adherent functionalized MBs than for functionalized and non-functionalized MBs in the unbounded fluid (150 μm away from the wall). The lower frequency of maximum response for bubbles bound to the OptiCell wall might be due to an increase in damping due to the coupling of the bubble and the wall.

Besides optical interrogation of bubbles, acoustical measurements have been used to characterize tMBs. Prior to the acoustical measurements, the biotinylated bubbles were sized by optical microscopy and subsequently injected in a capillary with or without streptavidin-coating [131]. Scattering of non-biotinylated bubbles and biotinylated bubbles at the fundamental frequency (2 MHz) was similar, whether or not the capillary was coated. The second harmonic resonance radius of an adherent MB was higher than that of a non-adherent targeted bubble, i.e. the second harmonic resonance frequency was higher. The reason that a difference between biotinylated and non-biotinylated bubbles was not found might be just a size or mass effect of the functionalization ligand. Not only is biotin (~250 Da) much smaller than streptavidin (~60 kDa), but one streptavidin molecule can bind up to four biotin molecules [127] that could form a protein layer around the shell, as suggested by others [115,120]. The effect of biotinylation on the resonance frequency might therefore be only minimal.

The most recent study that compared free with bound MBs focused on the SH

response frequencies at 11 and 25 MHz [132]. The rationale behind applying higher frequencies is imaging in a preclinical setting, but also in a clinical setting for the assessment of atherosclerosis in the carotid or for superficial tumors these high frequencies are needed. This study used the commercially available Target-ready MicroMarker (lipid-coated and streptavidin functionalized) which had stronger SH activity for larger bubbles when insonified at 11 MHz, i.e. the SH resonance frequency decreased upon binding. At 25 MHz the difference was smaller between free and bound MBs, but the amplitude of the adhered bubbles was 20% higher. In general, the pressure thresholds for SHs were lower at 11 MHz than at 25 MHz. Bound bubbles disrupted at lower pressure thresholds than unbound, especially at 11 MHz. At this frequency mainly compression-only behavior was observed for both bound and unbound MBs, whereas at 25 MHz the oscillations were expansion-dominated. Although differences in SH resonance were present, no shift in the fundamental resonance frequency was observed. This study also aimed to find a strategy to enhance the SH signal for imaging. Optimal pulse-inversion techniques require the same phase (0 radian phase shift) of the responses induced by both transmit pulses. Consequently, due to complete constructive interference (much like an opposite phase of π radian is desirable between fundamental echoes to ensure complete destructive interference) this would yield the maximal SH amplitude. At 11 MHz the SH emissions were consistently half a wavelength (π/2 radian) out of phase and at 25 MHz it varied more, but a similar trend was observed. This suggests that with the incorporation of a phase-shifting strategy; SH signal amplitudes from pulse-inversion techniques can be increased to 60% to enhance imaging.

Interestingly, the before mentioned studies show an opposite effect on the resonance frequency upon binding of the MBs. For streptavidin-functionalized MBs in an OptiCell insonified at pressures between 2 and 4 MHz, the resonance frequency decreased [122], while for biotinylated MBs in a streptavidin-coated capillary insonified at 2 and 3.5 MHz the resonance frequency increased [131]. At higher frequencies streptavidin-coated bubbles at 11 MHz showed an increase in resonance frequency, while it showed a decrease at 25 MHz [132]. A potential explanation for the observed opposing trends may be frequency-dependent boundary effects, for example caused by frequency-dependent boundary stiffness [132]. Nevertheless, these contradictions show that much is still unknown concerning the effects of binding on the bubble response. As this is the key factor for acoustical differentiation between bound and unbound MBs, single MB studies are needed for reliable determination of the bubble properties. Especially *in vivo* studies could aid the understanding of MB behavior in a clinically-translatable environment.

Other types of targeted tUCA

Next to the lipid-coated MBs described above, the characteristics of other types of tUCAs such as polymer and nanobubbles have been studied. Schmidt et al. [133] used poly(l-lactic acid) (PLA) capsules that bound to a neutravidin-adsorbed polystyrene surface (similar to an OptiCell wall). In this study the microcapsules adhered to the surface under flow conditions with wall shear stresses between 0.2 dyn/cm^2 and 1.5 dyn/cm^2. The capsules first slowed down before binding and were easier to detach at higher shear stresses and higher acoustic pressures. At the highest pressure of 291 kPa an appreciable fraction of the capsules also ruptured and released their gas content.

Recently, polyvinylalcohol (PVA) capsules gained specific interest due to their chemical versatility that enables functionalization with different ligands, for instance hyaluronic acid for the targeting of tumor cells and tissues [134]. The properties of the air-filled PVA capsules were compared to other polymer-coated capsules and commercially available bubbles with lipid and protein coatings [135]. At very high pressures up to 2.344 MPa (mechanical index (MI) = 1.58) the shell's shear modulus was estimated to be 3.7 MPa. Assuming a shell thickness of 0.5 µm [135] this corresponds to an elasticity parameter of 5.6 N/m: an order of magnitude higher than for lipid-coated bubbles [112,113,117]. The *in vitro* capsule concentration necessary to obtain the same signal was similar to Albunex, 5 to 10-fold lower than for SonoVue and Definity and even 35-fold lower than for Optison. Using the same concentrations for SonoVue and PVA bubbles the second and higher harmonic signals for PVA were up to 10 dB higher.

Sub-micron sized nanobubbles (~200 nm) may potentially extravasate by passing the capillary barrier to reach cells at the tumor cell target site [55]. This property makes them promising for targeted molecular imaging and drug delivery in tumors. Due to the higher permeability of tumor vasculature—enhanced permeability and retention (EPR) effect—nanobubbles are more likely to accumulate in tumors, known as passive targeting. The stability of the lipid-Pluronic nanobubbles was higher than that of Definity (*in vitro*). In mice, the lipid-Pluronic nanobubbles were imaged using contrast harmonic imaging at 8 MHz and their contrast in the tumor was higher than for Definity. This was ascribed to the possible extravasation of the nanobubbles, which retains them in the tumor and thus increased the signal.

Ultrasound molecular imaging

UMI that uses tUCAs is a multidisciplinary technology applicable for both diagnosis, monitoring of lesion formation, and therapy evaluation.

Contrast-specific imaging techniques

MBs generate higher harmonics, SH and ultraharmonic of the excitation frequency [136-141]. Upon excitation by multi-frequency bursts, MBs can also act as nonlinear mixers of the excitation frequencies and produce cross-products [142-144]. Conventional nonlinear imaging techniques, at lower frequencies (< 15 MHz), focus mainly on detection of higher harmonics [145-149]. The need for high resolution UMI in small animal applications has pushed the frequencies used in preclinical imaging to above 15 MHz [150]. At these frequencies similar nonlinear techniques have been implemented [151-155]. However, performance of these imaging methods is degraded because the excitation frequency is much higher than the resonance frequency of the MBs, attenuation is higher, and far-wall artifacts [156-160]. Therefore, improved imaging methods have been extensively studied, such as improved harmonic imaging methods [161-163], chirp coded excitation alone [164,165] or combined with pulse inversion [166]. Among the nonlinear components of the MB response the SH signal has drawn much attention lately, due to its MB specificity and artifact-free characteristics. Moreover, SH response of the MB has shown its potential for selectively imaging bound tMBs [167,168]. The SH signal is strongly dependent on the applied acoustic pressures, the ambient pressure variations [137,169-173], and the envelope of the excitation signal [174-178]. The SH signal is also less attenuated than the ultraharmonic and higher harmonics, and therefore a more suitable choice for high frequency applications. Next to the different strategies to improve the sensitivity of MB detection, adjusting the MBs is another approach to gain sensitivity. It has been shown that UMI of sorted 3 μm MBs results in an approximately 20 times higher video intensity than for unsorted populations [179]. This size lies within the optimal tMB size distribution for enhanced binding, as shown numerically [94]. This can significantly maximize the sensitivity to small numbers of MBs for UMI.

Selective imaging of true bound tMBs from free flowing unbound ones is another challenge that is extensively studied [9-13]. The most common approach for imaging and quantification of tMBs is to wait for a few minutes (2 [180] to 20 minutes [181]) so most of the circulating MBs have been taken up by the lungs and liver (i.e. RES system), or have been dissolved. This time also allows the tMBs to accumulate at the site of their targets. Then low power nondestructive pulses are applied

to image the tMBs, followed by a high power disruptive pulse (flash) to eliminate the MBs within the imaging plane which is again followed by low power pulses to image the residual circulating MBs (Figure 2A). The intensity difference before and after the flash corresponds to the amount of bound tMBs and is a measure for the biomarker concentration [182-185], as shown in Figure 2A. In such methods the quantification of bound tMBs strongly depends on the injected dose, imaging system gain, and local perfusion [9]. In addition, the influence of inhaled gasses in the anesthetic protocols influences the MBs longevity [186-189]. These studies confirmed longer circulation times of in-house lipid-shell decafluorobutane-filled UCAs and commercially available UCAs such as Definity® and Albunex® when animals breathe medical air instead of pure oxygen as the carrier gas for the isoflurane anesthetic. This is perhaps due to a reduced ventilation/perfusion mismatch and classical diffusion between the blood gasses and the gas inside the MBs (e. g. perfluorobutane), in which nitrogen plays a role by increasing the volume of the MBs and diluting other gas species in the MBs gas core [189].
The presence of tissue motion can compromise quantification, as well as high concentrations of freely recirculating MBs after the waiting period. Several methods for selectively imaging the bound tMBs in real time have been proposed: utilizing an image-push-image sequence [9]; transmission at a low frequency and reception at a high frequency [10]; using the SH response of the MBs and interframe filtering [11]; and using singular value spectra properties [12]. However, none of the proposed methods have yet been applied *in vivo*. Only Pysz et al. developed a quantification method based on dwell time MB signal measurements, which was tested *in vivo* in well vascularized tumors in mice [190]. However, in this *in vivo* model where attachment of tMBs is significant, the classical way of quantification also performs well. Thus, the performance of the method developed by Pysz et al. in applications with very few tMBs in the presence of circulating MBs remains unclear. Daeichin et al. have developed an off-line quantification method for the detection of biomarker concentrations *in vivo* in cases with a high number of bound MBs, as well as only very few bound MBs [191]. This method benefits from motion compensation and individual contrast spot detection, and is capable of distinguishing bound MBs from unbound MBs based on their displacement. Such a quantification method can be applied in studies performed with different imaging settings because it is less sensitive to imaging parameters.

In vivo molecular imaging

As discussed previously, the diagnostic focus of UMI is mainly on inflammation, thrombosis and angiogenesis. Assessment of angiogenesis is perhaps the application where UMI is used the most [14-24]. For evaluating tumor growth noninvasively, successful *in vivo* quantification of the expression levels of the angioge-

netic biomarkers $\alpha_v\beta_3$ integrin, endoglin, and VEGFR2, which vary during tumor growth in subcutaneous cancer xenografts, have been reported [24]. Recently, an UMI study using MBs targeted to $\alpha_v\beta_3$ in an ovarian cancer model in hens [192], suggested that the detection of ovarian tumor–associated angiogenic microvessels improved when using UMI. For assessing the efficacy of cell-based therapies, UMI has been used to image a genetically engineered cell-surface marker on endothelial progenitor cells to track the fate of these progenitor cells after their delivery into vascular engraftment *in vivo* within Matrigel plugs [193]. Next to the basic research that is performed using UMI, numerous studies are putting a step forward by investigating the possibilities of clinically translatable targeted MBs. In humans, the first phase 0 clinical trial for prostate cancer UMI was presented recently using BR55, a VEGFR2-tUCA [76]. Although it was only a safety study it was reported that 12 out of 14 lesions (proven by histology) could be detected with UMI. Bachawal et al. [194] used BR55 in transgenic mice with breast cancer and ductal carcinoma. UMI allowed for highly accurate detection of both breast cancer and ductal carcinoma in situ and this can be a promising clinical approach for early breast cancer detection. In addition, BR55 has shown its potential for early detection of liver dysplasia in transgenic mice [195].

UMI has also been used to noninvasively assess the effects of anti-inflammatory treatment on endothelial inflammation in early atherosclerosis in genetically modified mice [196,197]. UMI has also proven its ability to detect biomarkers of early response to chemotherapy in several cancer types by MBs targeted to single biomarker expressions (VEGFR2, $\alpha_v\beta_3$, endoglin, Annexin V, or VEGF-VEGFR complex) [71,198-201] and MBs targeted to two or more of these biomarker expressions [180]. Impressively, studies have shown that UMI using $\alpha_v\beta_3$-tMBs is a consistent method that can classify a tumor as a responder or a non-responder as early as two days after treatment [202,203]. To establish the link to clinical oncology Flisikowska et al. [204] have suggested the use of larger animal cancer models with more similarities to humans, such as genetically modified pigs. They proposed programs to generate gene-targeted pigs with mutations in tumor suppressor genes and proto-oncogenes that replicate key lesions responsible for a variety of human cancers. Whilst tumor models in large animals are challenging, cardiovascular disease can more easily be modeled. A study on miniswines suffering from atherosclerosis showed that an improved endothelial permeability through ultrasound-activated nitric oxide loaded echogenic immunoliposomes, can facilitate the delivery of anti-ICAM-1 conjugated echogenic immunoliposomes to inflammatory components in the arterial wall. This approach therefore has the potential to improve UMI of atheroma [205]. Next to pigs, the expression of P-selectin and VCAM-1 expression in the carotid of nonhuman primates has also been recently assessed with UMI. This study showed that endothelial cell adhesion molecule expression in large arteries could be an early event that coincides with

diet-induced obesity and insulin resistance in nonhuman primates [206]. In another recent study on nonhuman primates with myocardial ischemia, UMI showed to be both safe and effective for imaging recent myocardial ischemia. Lipid-coated MBs were functionalized with dimeric recombinant human P-selectin glycoprotein ligand-1, a recombinant ligand appropriate for humans were used [207]. The study suggests that UMI can be useful for detecting recent ischemia in patients with chest pain, even in the absence of necrosis [207].

Three dimensional UMI

It is challenging to image the same plane repeatedly in 2D UMI serial studies and small misalignments can already introduce a substantial error. tMBs are attached to their targets and are therefore stationary in UMI applications where tissue motion is absent. This thus opens up opportunities for three dimensional (3D) UMI using 2D probes, by mechanically moving the ultrasound probe over the target of interest. This is illustrated in Figure 2 where 3D UMI is performed with VEGFR2 Target-ready MicroMarker (VisualSonics Inc.) on subcutaneous human hepatocellular carcinoma tumor in a mouse.

Feasibility of 3D UMI has also been proven by other groups. Streeter at al. [208] performed 3D UMI of tumors expressing $\alpha_v\beta_3$ integrin by mechanically stepping the transducer across the tumor in 800 μm increments. In another study, it was shown that multiple injections of tMBs did not block sufficient binding sites to bias molecular imaging data in serial studies [209], which is an important finding. Using the clinically promising BR55 agent, 3D UMI was shown to be very well suited in depicting the angiogenic activity in very small breast lesions, suggesting its potential for detecting and characterizing these lesions in a very early stages [210]. Combining the effort to selectively image bound tMBs and 3D UMI, Hu et al. [211] used a broadband single pulse imaging sequence (transmitting at low frequencies and receiving at high frequencies) that is faster than the multi-pulse methods. Then, this method was combined with interframe filtering to selectively image targeted MBs without waiting for clearance of unbound MBs, thereby reducing acquisition time from 10 to 2 minutes. Their results suggest a feasible method for 3D UMI that is faster than current multi-pulse strategies.

Enhanced drug delivery

In combination with ultrasound, UCAs are known to enhance drug delivery. Despite the fact that the mechanism behind this enhancement is not well known, vibrating MBs can stimulate drug uptake through cell membrane pore formation, a process also known as sonoporation, opening of intercellular junctions, or endocytosis [53,212]. Whilst UCA-mediated drug delivery has been studied since 1997 [213], tUCA-mediated drug delivery is relatively new. In 2011, Kooiman et al. were the first to show that CD31-tUCAs could sonoporate primary endothelial cells *in vitro* [57]. Cell membrane permeability (Figure 3B) was already induced at acoustic pressures as low as 80-200 kPa (1 MHz, 6x10 cycles burst), indicated by uptake of the co-administered model drug propidium iodide (PI). Since then, several other studies reported tUCAs for drug delivery by either co-administrating the drug with the tUCAs or loading the drug in/on the tUCAs. Another co-administration *in vitro* study using PI showed that sonoporation of cancer cells by $\alpha_v\beta_6$-tUCAs was higher with chirp pulses from 3-7 MHz than with chirp pulses between 1.3 and 3.1 MHz or single frequency insonification at 2.2 or 5 MHz (110 kPa, 10 µs burst, pulse repetition frequency (PRF) 1 kHz, 2 min treatment) [214]. This can be explained by the fact that chirp pulses cover a broader range of resonance frequencies, as MBs with various sizes have different resonance frequencies; chirp pulses are therefore more efficient than single frequency pulses. In the chicken embryo model (*in vivo*), a single sine-wave burst (1 MHz, 1000 cycles at 150 or 200 kPa) was sufficient for vascular PI uptake using $\alpha_v\beta_3$-tUCA as shown in Figure 3C.

tUCAs can also be loaded with genetic drugs (plasmid DNA, siRNA, mRNA) or drugs for local gene/drug delivery. Philips et al. [215] used VCAM-1-tUCAs loaded with plasmid DNA to transfect smooth muscle cells with the model gene green fluorescent protein (GFP) *in vitro* at 1 MHz (200-300 kPa, PRF 100 Hz, ~5 sec per cell) and at 1.5 MHz (200 kPa, PRF 8 kHz, ~5 sec per cell). In another study ovarian cancer cells were transfected with wild-type p53 tumor suppressor gene using Luteinizing Hormone-Releasing Hormone analog (LHRHa)-tUCA to induce apoptosis (1 MHz, 0.5 W/cm^2, 30 s treatment) [216]. Two studies [217,218] showed that tUCAs loaded with luciferase plasmid can transfect vasculature *in vivo*. Xie et al. [219] used P-selectin tUCAs in a hindlimb ischemia skeletal muscle model (see Figure 3E; 1.6 MHz, 0.6-1.8 MPa, Power Doppler, pulsing interval 5 s, PRF 2.5 kHz for 10 min), whereas Tlaxca et al. [218] used mucosal addressin cell adhesion molecule-1 or VCAM-1-tUCA in a model for Crohn's disease (1 MHz, 5 W/cm^2, 25% duty cycle for 5 min).

Two types of drugs loaded in tUCAs have been reported for cancer treatment.

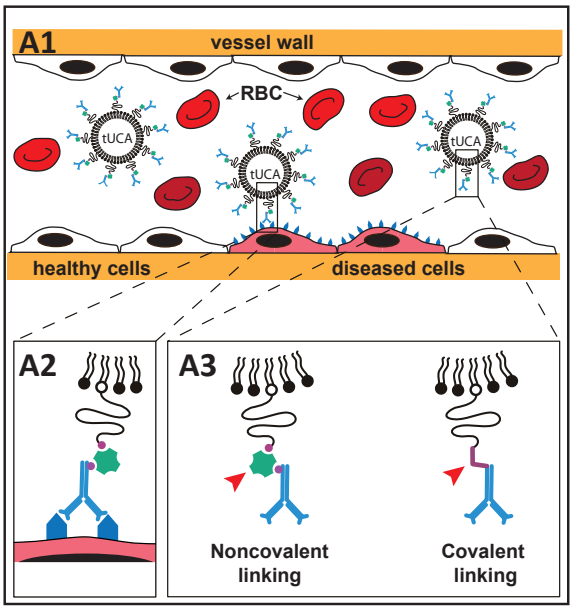

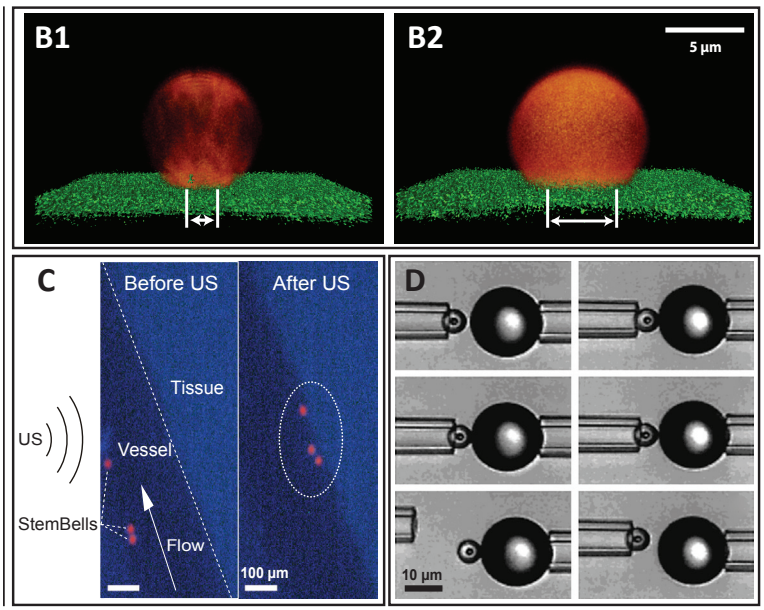

Figure 1
Targeting and binding of tUCAs.
A) tUCAs targeted to their specific biomarker via an antibody (the antibody is used as an example and can be replaced by other ligands, as mentioned in the text).
A1) Shows both free and adhered tUCAs in a blood vessel (RBC = red blood cell).
A2) Shows a detailed representation of a ligand that is coupled to the lipid-shell via biotin-streptavidin bridging, where the ligand adheres to the biomarker. The red arrows in
A3) point to an example of a noncovalent linker (i.e. biotin-streptavidin bridging) and a covalent linker.
B) A lipid-coated MB with a shell based on DSPC (B1) or DPPC (B2), where the DSPC-based MB has a smaller binding area (indicated by white arrow) and a more spherical shape than the DPPC-based MB (adapted from Kooiman et al. [13]).
C) StemBells before the application of US (left panel) are pushed towards the vessel wall due to acoustic radiation force (right panel) (adapted from Kokhuis et al [61]).
D) A MB attached to a glass bead via two micropipettes. The force needed to separate them is used to measure the binding force (adapted from Kim et al. [50]) 85x38mm (300 x 300 DPI)

Figure 2
Ultrasound Molecular Imaging.
A) Timeline of the imaging protocol and schematic representation of a typical time intensity curve in the region of interest (e.g. tumor).
B) B-mode (gray) overlaid with nonlinear contrast mode (green) US imaging in 3D to detect the $\alpha_v\beta_3$ expression via $\alpha_v\beta_3$-tMBs (MicroMarker) adhered to the SVEC cells, which were cultured in an OptiCell. The band in the middle of the Figure in which there is no green signal present, shows the destruction of the tMBs with the flash burst.
C-E): 3D micro-UMI using VEGFR-2 Target-ready MicroMarker on an subcutaneous human hepatocellular carcinoma tumor which was developed by injection of Huh7 cells in male nude NMRI mice.
C) 3D B-mode US render of the tumor.
D) 3D render of contrast images 10 minutes after bound tMBs within the entire volume of the tumor.
E) 3D render of contrast images 10 minutes after injecting the control MBs. Lack of signals within the tumor indicates no attachment of control MBs to the VEGFR-2 receptors.
For B-E, imaging was performed with a Vevo 2100 US imaging system and MS250 probe at 18 MHz. The probe was moved with increments of 32 µm using a step motor (VisualSonics Inc.). 149x93mm (300 x 300 DPI).

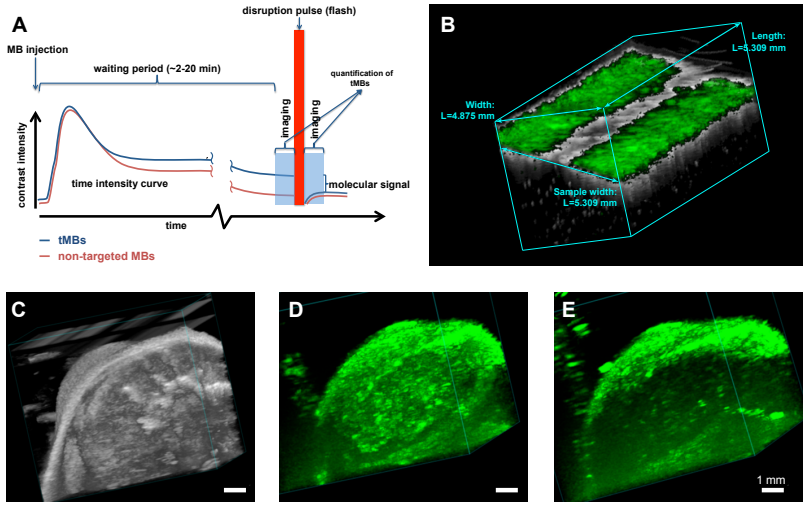

Figure 3
US and targeted microbubble mediated drug delivery.
A) Schematic of co-administration of the drug together with tUCAs.
B) Propidium iodide (PI) uptake in endothelial cells in vitro induced by vibrating CD31-tUCAs; dashed lines indicate cell borders. Left panel: bright field before US; middle panel: fluorescence before US; right panel: fluorescence after US showing PI uptake (adapted from Kooiman et al. [10]).
C) PI uptake in endothelial cells *in vivo* induced by vibrating $\alpha_v\beta_3$- tUCAs. Left panel: bright field before US showing a cluster of six tUCAs; middle panel: fluorescence before US showing the DiI-labeled tUCAs; right panel: fluorescence after US showing PI uptake.
D) Delivery of the drug when it is attached to or incorporated in the tUCA shell.
E) P-selectin-tUCAs are 5 times more efficient than non-targeted UCAs for gene delivery *in vivo* in a hindlimb ischemia skeletal muscle model. Validation of Luciferase Reporter Plasmid transfection in rats using bioluminescence (left two panels) and imunohistochemistry (right four panels; arrows point to plasmid transfection in endothelial and perivascular cells; adapted from Xie et al.[186]). 112x76mm (300 x 300 DPI)

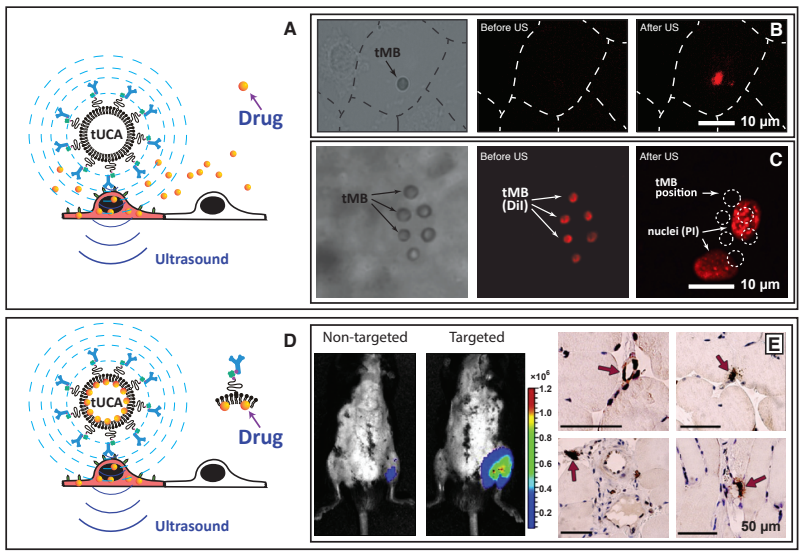

Paclitaxel loaded into tUCAs induced tumor cell apoptosis *in vitro* in ovarian cancer cells (LHRHa-tUCAs, 0.3 MHz, 0.5 W/cm^2, 30 sec treatment) [220] and breast cancer cells (LyP-1-tUCA, 1 MHz, 4 W/cm^2, 50% duty cycle, 2 min. treatment) [221] as well as *in vivo* (LHRHa-tUCAs, 0.3 MHz, 1 W/cm^2, 50% duty cycle, 3 min treatment) [222]. *In vivo*, the tUCAs were administered intraperitoneally allowing the tUCAs to adhere to the ovarian cancer cells. The other anti-cancer drug loaded into VEGFR2-tUCAs was BCNU (1,3-bis(2-chloroethyl)-1- nitrosourea) for the treatment of glioma brain tumors *in vitro* (1 MHz, 0.5 MPa, 10,000 cycles, PRF 5 Hz for 1 min treatment at 2 sites) and *in vivo* (1 MHz, 0.7 MPa, 10 ms burst, 5% duty cycle, PRF 5 Hz, 1 min treatment at 2 sites), where *in vivo* the tUCAs were also used to open the blood brain barrier [223].

tUCA versus non-tUCA for enhanced drug delivery

Strikingly, when tUCAs for drug delivery are directly compared with their non-targeted UCA counterparts, tUCAs are more efficient both *in vitro* [215, 216, 220, 221,224] (up to 7.7-fold higher [221]) and *in vivo* [218, 219, 222, 223] (up to 5-fold higher [219]), irrelevant whether the drug was co-administered with the tUCAs or whether the drug was loaded on/in the tUCAs. Although the reasons for this higher efficiency have not yet been investigated, several could be possible. Possibly the main reason could be that tUCAs vibrate against the cells directly as they are bound to the cells, which may result in a more efficient transfer of acoustic energy, especially because sonoporation was only reported in cells adjacent to vibrating microbubbles for non-tUCAs [225,226]. The acoustic behavior of the tUCAs itself could also explain this difference, as *in vitro* studies have shown that tUCAs are acoustically more stable, vibrate with a larger amplitude at the fundamental frequency, fragment in the plane parallel to the boundary and have a different resonance frequency (see characterization of tUCA section). Microbubble clustering could also be a phenomenon contributing to the higher efficiency of tUCAs, as a clus-

ter of bubbles is known to behave as one large bubble, which is also associated with a shift in their resonance frequency [227]. This is substantiated by the chicken embryo study in which clusters of 10 to16 tMBs had a 16-fold higher sonoporation efficacy than single tMBs [60].

A disadvantage of using tUCAs for drug delivery was reported by Hu et al. [228] who showed that insonified $\alpha_v\beta_3$-tUCAs temporarily decreased blood flow within the insonified area after application of a 5 MHz, 2 or 4 MPa color-Doppler destruction pulse (6-cycle pulse length, PRF 124 Hz, 900 ms duration). Although such high frequency and pressure pulses are not typically used for drug delivery, temporarily reducing the blood flow could be advantageous to keep the delivered drug in the treated area. The reduced blood flow could also reduce tumor size by itself as has been reported for non-tUCA.

With tUCAs now also being used for drug delivery, the terms ultrasound-mediated targeted drug delivery or ultrasound and microbubble targeted drug delivery (UMTD) have become confusing. UMTD is used for drug delivery using non-targeted UCA where “targeted” refers to the local application of the ultrasound itself. We therefore suggest banning the UMTD term and use ultrasound and microbubble mediated drug delivery (UMMD) for non-targeted UCAs and ultrasound and targeted microbubble mediated drug delivery (UtMMD) for tUCAs instead.

HIFU

tUCAs can also be used as theranostic agent without the addition of a drug or gene. High intensity focused ultrasound (HIFU) techniques utilize high-energy focused ultrasound to locally increase the temperature at the focal point for tumors ablation. UCAs, as synergists, have become a research topic to improve the efficiency of HIFU treatment [229,230]. In this field, a folate-tUCA (phase transition nanoemulsion) has shown great potential to enhance HIFU ablation of ovarian cancer *in vivo* [231].

Outlook and conclusions

Recent studies on larger human-like animals such as pigs and nonhuman primates, as well as the first phase 0 clinical trial for prostate cancer with the VEGFR2 tUCA BR55 show the capability of clinical UMI in the near future. Recent insights in shell coating properties of tUCAs, new strategies for targeting, and the development of nanoscale tUCAs will open up a new range of opportunities and will broaden the spectrum of diseases that can be targeted.

Intrinsic properties of the tUCAs, such as deformability due to low elasticity could be used as an advantage to improve binding. This underlines the necessity of single tMB investigation to further understand their properties. Upon binding, opposite effects on the resonance frequency are reported, which also reflects a change in harmonic frequencies. The increase in their SH amplitude upon binding could potentially be utilized for selective imaging of adhered tMBs, which could speed up the UMI and increase its specificity. Obviously, 3D imaging is desired for UMI applications, either by mechanically moving a two dimensional probe or using a volumetric 3D probe.

By using tUCAs as local drug delivery systems, intracellular drug uptake can be enhanced several fold in comparison to non-tUCAs. tUCAs able to carry and deliver a high payload are needed, as is the elucidation of the mechanism by which tUCA stimulate drug uptake. A novel therapeutic use of tUCAs for cancer treatment could be the functionalization with kinase inhibitors. These molecules have a high affinity for cancer cell receptors and are already approved or in clinical trials as anticancer drugs, such as gefitinib (EGFR), sunitinib (FLT-1), Bevacizumab (VEGF) [232]. Bound kinase inhibitor-tUCAs could therefore facilitate both UMI and act as inhibitor activators for apoptosis. With BR55 now undergoing regulatory approval for clinical use, this will hopefully pave the way for other tUCA with other targets as well. However, for every new tUCA or drug-loaded tUCA regulatory approval will be needed before clinical use. In conclusion, adding to the wide applications of UMI for diagnosis, the therapeutic benefits of this technology also play a major role in its popularity. Detection of diseased cells using tUCAs combined with local drug delivery, sonoporation, and HIFU are good examples of the applications and the potential of UMI for therapy.

Effect of self-demodulation on the subharmonic response of contrast agent microbubbles

03

Abstract

Subharmonic (SH) emission from the ultrasound contrast agent (UCA) is of interest since it is produced only by the UCA and not by tissue, opposite to harmonic imaging modes where both tissue and microbubble show harmonics. In this work the use of the self-demodulation (S-D) signal as a mean of microbubble excitation at the SH frequency to enhance the SH emission of UCA is studied. The S-D wave is a low-frequency signal produced by weakly nonlinear propagation of an ultrasound wave. It is proportional to the second time derivative of the squared envelope of the transmitted signal. A diluted population of BR14 UCA (Bracco Research SA, Geneva, Switzerland) was insonified by a 10 MHz transducer focused at 76 mm firing bursts with different envelopes, durations and peak pressure amplitudes. The center frequency of the S-D signal changes from low frequencies (around 0.5 MHz) towards the transmitted frequency (10 MHz) by modifying the envelope function from Gaussian to rectangular. For 6 and 20 transmitted cycles, the SH response is enhanced up to 25 dB and 22 dB, respectively, when using a rectangular envelope instead of a Guassian one. The experimental results are confirmed by numerical simulation. The effects of the excitation duration and pressure amplitude are also studied. This study shows that a suitable design of the envelope of the transmit excitation to generate a S-D signal at the SH frequency can enhance the SH emission of UCA and the SH imaging is feasible at high frequencies with shorter transmit burst (6-cycle) and low acoustic pressure (~100 KPa).

Based on a manuscript by **V. Daeichin**, T. Faez, G. Renaud, J. G Bosch, A. F. W. van der Steen, and N. de. Jong, in the journal of Physics in Medicine and Biology in 2012.

Introduction

Ultrasound contrast agents (UCA) are micron size gas bubbles encapsulated by a lipid, protein, albumin or polymer shell. They enhance the contrast of blood pool for ultrasound imaging. When exposed to ultrasound, the microbubbles behave as a nonlinear mechanical resonators whereas tissue scattering is linear. The result of such a nonlinear behavior is the leakage of energy to harmonic multiples of the transmit frequency (f_0). In order to extract the nonlinear signal, different techniques such as harmonic imaging [233] and pulse inversion [147] were developed.

In general, nonlinear imaging approaches are thought to perform best when the bubbles are insonified at or near their resonance frequencies [234]. The resonance frequencies of conventional UCA bubbles range generally between 1 MHz and 8 MHz [112,235-237], which are therefore well-suited for the majority of diagnostic ultrasound applications. There is, however, increasing interest in employing transmit frequencies of 10 MHz and beyond for applications requiring a higher spatial resolution such as carotid (10 MHz), intravascular coronary vasa vasorum imaging and small animal imaging (15 to 50 MHz) [139,151,236,238]. Under these circumstances the performance of nonlinear imaging techniques is degraded because the driving frequency is higher than the resonance frequency [151]. In addition second harmonic imaging techniques are hampered because of the increase in the amplitude of harmonics produced by tissue as a result of nonlinear propagation of ultrasound.

Gas filled microbubbles can also act as nonlinear mixers producing frequency cross-products in dual frequency insonation [144, 171, 239, 240]. Recently, several techniques utilizing radial modulation of the microbubbles have been reported [241-244]. In these techniques, microbubbles are excited simultaneously with two ultrasound waves, a low-frequency manipulation wave to modulate the microbubble size, and a high-frequency imaging pulse for high-resolution detection of the changes in the acoustic cross section of UCA induced by the manipulated wave. Such periodic changes in the acoustic cross section of microbubbles modulate the amplitude and the phase of the backscattered imaging signal. Also a dual-frequency difference excitation technique was developed to induce an efficient low-frequency nonlinear scattering from microbubbles using high-frequency ultrasound [144, 234, 245, 246]. The dual-frequency excitation involves the simultaneous transmission of two high-frequency sinusoids to produce a component at the difference frequency. When the difference frequency is equal to the mean resonance frequency of the UCA, the difference frequency component scattered by

the UCA is maximal [247].

The emission of energy at subharmonic (SH) ($0.5f_0$) and ultraharmonic ($1.5f_0$, $2.5f_0$, etc) frequencies by UCA was proposed to be exploited as a new imaging modality [235, 248-250]. No SH signal is generated during propagation in tissue and no SH scattering is produced by tissue. The SH signal has a greater penetration distance since its attenuation is lower than that at the fundamental frequency, offering a potentially powerful diagnostic tool for clinical examinations [138, 248, 251-256].

Unlike the second and higher harmonic amplitudes that increase monotonically with the amplitude of the incident wave (for moderate acoustic pressures) [109,146], the SH response has a threshold behavior [137,248]. This threshold exhibits two minima: when the frequency of the excitation signal is close to the resonance frequency of the microbubble and close to twice the resonance frequency which is usually a lower minima than the first one [257]. The SH signal is strongly dependent on the applied acoustic pressure, the hydrostatic pressure variations [171-173,244,258], the envelope of the excitation signal [175-178] and equilibrium state of the microbubble [259].

Zheng et al. [175] presented an application of multi-frequency excitation, where rectangular and triangular waveforms with four harmonics were used to excite the UCA through numerical modeling via a modified Rayleigh-Plesset equation. They showed that the rectangular envelope is effective in improving the nonlinear signal scattered by microbubbles, with effective scattering cross-section area significantly higher (up to 35 times) than the widely-used Gaussian envelope. Biagi et al. [176] examined ultrasound bursts with three different envelopes in order to evaluate the SH response of the contrast agent. They found a decrease up to 30 dB and 21 dB in the SH response for a pulse with a Gaussian envelope and a composite pulse (two-tone burst), respectively, compared with a sinusoidal burst having a rectangular envelope. Their experimental results confirmed that the envelope of the transmitted signal strongly affects the SH emission. They hypothesized that the smoothness of the beginning of an excitation with Gaussian envelope can inhibit the generation of SH from the contrast agents. In another study, Masotti et al [177] reported that the SH behavior of UCA is not only pressure and concentration dependent but also a phase dependent phenomenon. Changing the phase between the transmitted signals of different frequencies modifies the envelope of the excitation burst. It has been shown that the phase between the two high frequency transmit pulses in the dual-frequency excitation method, therefore the shape of the excitation burst, plays an important role in maximizing the amplitude response of the microbubbles at the SH frequency [177,260]. Zhang et al [178] also compared an excitation technique, made of dual-frequency, with the conventional single frequency sinusoidal technique to enhance the SH emission

from UCA. They showed numerically and experimentally that a dual-frequency signal (2 and 4 MHz) is able to improve the amplitude of the SH component up to 13 dB over the single frequency sinusoidal excitation technique. In another study Zhang et al [173] showed theoretically and experimentally that using chirp excitation techniques with a center frequency of 5 MHz, a frequency range of 1 MHz and a pulse length of 40 μs can enhance the amplitude of the SH emission of the UCA by 15-22 dB compared with a sine burst having a Gaussian envelope.
Needles et al [151] studied different conventional nonlinear contrast imaging methods such as pulse inversion, amplitude modulation and combination of these two together with SH imaging technique both *in vitro* and *in vivo*. They wanted to optimize a strategy for real time nonlinear contrast imaging with good performance in canceling the signal from the tissue, using a commercial high frequency ultrasound system (18-24 MHz) with an array based transducer. Using pulse inversion with SH imaging and excitation bursts with rectangular envelopes showed 15 dB enhancement in contrast to tissue ratio compared with the fundamental imaging.
In this paper, we investigate the effect of the self-demodulation (S-D) signal on the SH response of phospholipid-coated microbubbles excited at 10 MHz. Our hypothesis is that the enhancement of the SH signal using an excitation wave with a rectangular envelope can be explained by the S-D stimulation effect on the SH response of the UCA. This may be the origin of experimental findings reported in literatures [151,176]. We show that understanding the effect of the S-D signal on the UCA behavior can help to optimize the envelope of the excitation signal for SH imaging especially at high frequencies.

Theory and numerical simulations

In order to investigate the influence of the S-D signal and the driving frequency on the SH response of the UCA, we analytically extracted the frequency components of the S-D signal for waves with different envelopes. Then we linked the Khokhlov, Zabolotskaya, and Kuznetsov (KZK) model as implemented by Vos et al [234] to a model describing the dynamics of lipid-coated microbubbles [261]. The calculated pressure wave from the KZK model is used as an excitation wave in the Marmottant model in order to compute the radial response of a microbubble with a diameter of 2 μm. Figure 1 indicates the flow chart of the simulation steps and the input and output acoustic signals in the time and frequency domains for each simulation model.

Theoretical derivation of the frequency content of the self-demodulation signal

In a weakly nonlinear regime the propagation of an ultrasound pulse gives rise to a low-frequency signal due to the S-D phenomenon. The S-D pressure wave, $p_{sd}(t)$, is related to the envelope of the transmitted signal, E(t), as follows [262 263,264]:

$$p_{sd}(t) \propto \frac{\partial^2 E^2(t)}{\partial t^2} \qquad (1)$$

The frequency content of the S-D signal of different envelopes is calculated analytically. Let us assume that the envelope function of the transmit burst is:

$$E(t) = e^{-(\frac{2t}{T})^{2M}} \qquad (2)$$

where T is the duration of the signal and the integer M determines the rise and decay time of the envelope. For M equal to 1 this function represents a Gaussian envelope which can be approximated by a cosine term and a constant [265].
Assuming these simplifications one can rewrite the envelope function (Eqn. 2) as the following :

$$\begin{aligned} E(t) = e^{-(\frac{2t}{T})^{2M}} &\approx (A + B\cdot\cos(\omega_e t))^M \\ &= \sum_{k=0}^{M} \binom{M}{k} A^{M-k}\cdot B^k \cdot \cos^k(\omega_e t) \\ &= \sum_{n=1}^{M} A_n + B_n \cdot \cos(n\omega_e t) \quad , \quad -\frac{T}{2} \le t \le \frac{T}{2} \end{aligned} \qquad (3)$$

Where $\omega_e = 2\pi/2T$ is the center frequency of the envelope for M=1, A_n and B_n are the constants.
Eqn. 3 demonstrates the leakage of energy into higher harmonics of ω_e for higher integer values of M. For example for M=3, the envelope contains the second and the third harmonics of ω_e. This means that for a rectangular envelope, more harmonics of ω_e are present.
Combining Eqn. 3 and Eqn. 1 we obtain the frequency component of the S-D signal for an arbitrary value of M:

Where A'_n and B'_n are constants. Eqn. 4 presents a series of the envelope center frequency and its harmonics. It can be seen that for higher M values, more harmonics of the envelope center frequency are involved in the frequency content of the S-D pressure signal.

Effect of the transmit signal envelope on the self-demodulation signal

We used the equation derived by KZK [266] to calculate the nonlinear propagation of a collimated ultrasound beam. The KZK model considers diffraction, absorption, and nonlinear propagation in the medium. It has been shown that such a model can accurately simulate the S-D of a sine burst [263, 264, 267-269]. We adopted this model as implemented by Vos et al [234] for our simulations. As an excitation source, a transducer focused at 76 mm with a diameter of 10 mm was used.

Figure 2 depicts the results of the KZK simulations to estimate the nonlinear propagation of a 10 MHz ultrasound pulse, for three different envelopes (M=1; 3; 15 and T=2 μs). The transmitted acoustic pressure at focus was set to 50 kPa. For M=1 (Gaussian envelope), the S-D signal is concentrated at low frequencies around ω_e and $2\omega_e$ (Eqn. 4) which appears as a peak around 0.75 MHz in the frequency domain (Figure 2c, M=1). For M=3 (Figure 2c, M=3) a more distributed S-D signal with center frequency around 1 MHz is obtained. Increasing M to higher values (e.g. M=15) results in the leakage of energy to higher harmonics of ω_e until when no distinct peak can be seen for the S-D signal in the frequency domain due to the distribution of the energy from ω_e up to the 30th harmonic of ω_e (Figure 2c, M=15).

Comparing the frequency content of the propagated waves with the three different envelopes (Figure 2c) indicates that the transmitted pulse with a rectangular envelope has the highest S-D energy around the SH frequency (5 MHz). It can be seen in Figure 2c that the amplitude of the S-D signal is around 50 dB below the fundamental frequency for M=1 and M=3. For M=15 the S-D signal is a broad band low frequency signal which overlaps with the side lobes of the fundamental frequency peak (10 MHz).

Effect of the self-demodulation signal on the subharmonic emission of a microbubble

According to the model of Marmottant et al [261], a sharp change in the shell stiffness, occurring when the coating buckles, can enhance the SH response. The initial surface tension was shown to be a key parameter in the generation of low amplitude SH emission by lipid coated microbubbles [170,259]. We conducted a parametric study by varying the initial surface tension from 0 to 0.07 N/m (the surface tension of water) and investigated the amplitude of the SH oscillation of a single microbubble in response to three different excitation bursts as shown in Figure 3. The shell elasticity (χ) and the shell viscosity (κ_s) were set to 2.5 N/m and 10-9 kg/s, values for BR14 UCA (Bracco Research SA, Geneva, Switzerland) used for *in vitro* experiments [170,259]. The diameter of the microbubble was set to 2 μm which is also the mean diameter of BR14 UCA [270].

The amplitude of the SH signal is strongly dependent on the initial surface ten-

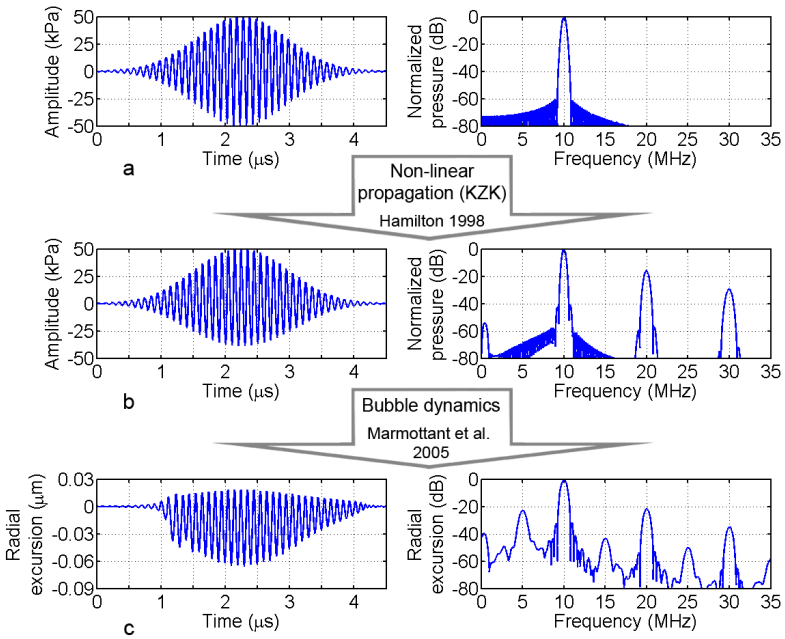

Figure 1
Flow chart of the simulation steps showing the pressure wave (for M=1) and its spectra at:
a) the surface of the transducer (input of the KZK model).
b) the focus of the transducer (76 mm) (KZK output).
c) Radial excursion of a 2 μm bubble with initial surface tension of 0.014 N/m (output of Marmottant model).

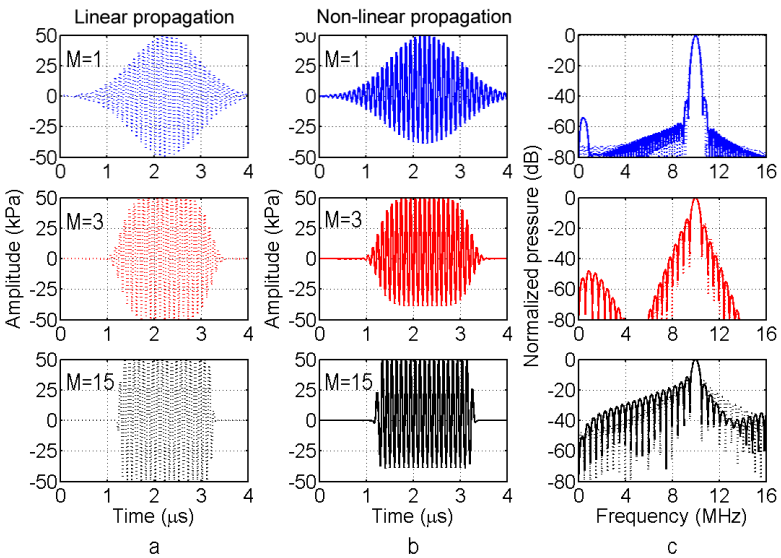

Figure 2
Numerical computations based on KZK model showing the propagation of a 10 MHz burst with three different envelopes (M=1, 3 and 15) in a nonlinear medium;
a) after linear propagation,
b) after non-linear propagation, and
c) their corresponding frequency spectra.

Figure 3
Simulation results showing the amplitude of the SH radial response of a single microbubble (2 μm diameter) as a function of the initial surface tension to a burst with three different envelops after nonlinear propagation (at the focus): M=1 dashed-dotted curve, M=3 dashed curve and M=15 solid curve. The horizontal line indicates the noise level in the simulations.

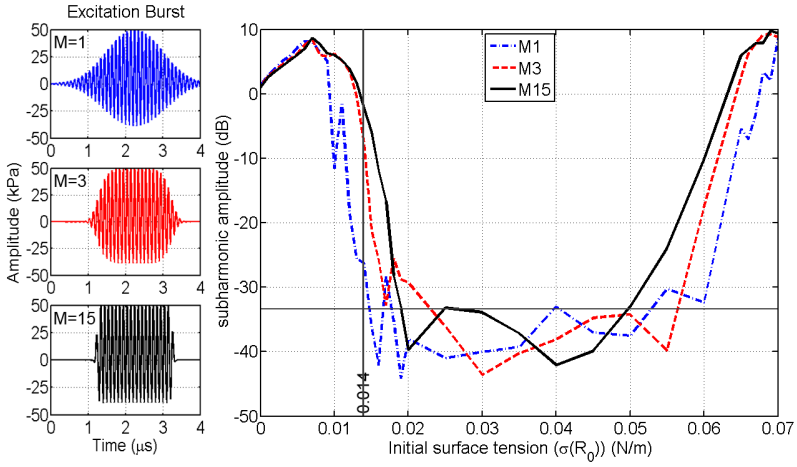

Figure 4
Radial excursion of a 2 μm diameter microbubble excited by a 20-cycle burst with three different envelopes after nonlinear propagation (at the focus): M=1 (dashed-dotted curve), M=3 (dashed curve) and M=15 (solid curve) and their corresponding amplitude spectra for an initial surface tension of 0.014 N/m.

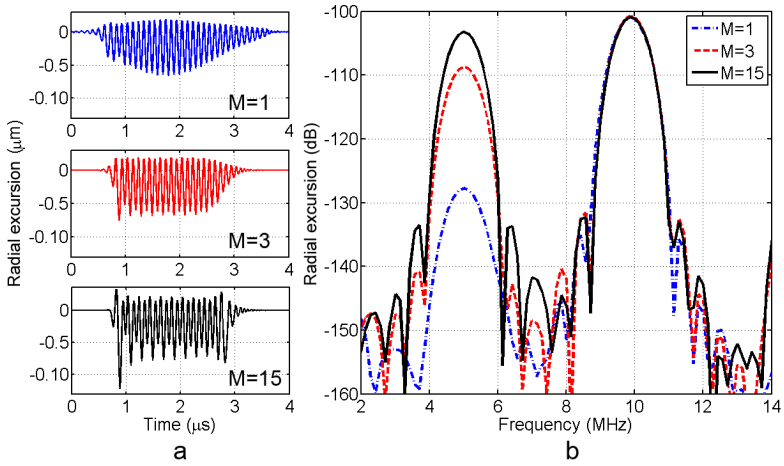

sion $\sigma(R_0)$ of the microbubble. Figure 3 shows the SH amplitude of a 2 μm bubble as a function of its initial surface tension in the Marmottant model. The SH oscillations are observed only when the bubble is around either the buckling or the rupturing regimes. However the margins for these regimes are wider for the excitation bursts with higher M values. By increasing the value of M, the amplitude of the SH vibration is enhanced for an initial surface tension between 0.01 and 0.02 N/m and between 0.05 and 0.065 N/m. As an example, the radial excursions of such a 2 μm diameter microbubble in response to the three excitation bursts in time and frequency domains are shown in Figure 4 for the initial surface tension of 0.014 N/m indicated by a vertical line in Figure 3.

Figure 3 shows that the stimulation effect of the S-D signal on the SH response of the microbubble is significant when the initial state of the microbubble is just outside the buckling regime ($0.01<\sigma(R_0)<0.02$ N/m) or close to the rupturing regime ($0.05<\sigma(R_0)<0.07$ N/m).

The energy of the S-D signal is located at the beginning and the end of the transmitted burst [263]. Therefore in order to remove that part of the signal which corresponds to the linear response to the S-D signal, three periods at 10 MHz from the beginning and the end of the radial excursion signal were discarded. Then a Hanning time window was applied to the rest of the signal to smoothen the spectra. Since the energy of the excitation bursts is the same, fundamental peaks appear to be at the same level. However the SH response of such a bubble is enhanced up to 23 dB by increasing the M in the envelope function of the excitation burst.

Experiments

Materials and methods

The schematic view of the setup is depicted in Figure 5. A 10 mm diameter thin shell cylindrical tube made of Polypropylene film backing coated with a water based acrylic adhesive (tesa® 4024 PV 2) having a total thickness of 52 μm was mounted in the center of a triangular water tank at the focus of two transducers used for transmitting and receiving the ultrasound signals. The tube was filled with distilled, saturated water (Isoton II, Beckman Coulter, The Netherlands). BR14 microbubbles were reconstituted to manufacturer's specifications and diluted 10,000 times then poured in the tube and mixed gently using a magnetic stirrer in order to have a homogeneous suspension. The microbubbles consist of a phospholipid monolayer shell with a perfluoropropane gas core. A broad-band transducer with centre frequency of 10 MHz and 76 mm focal length, (Panametrics V311; 3-13 MHz) was used for transmit. The transducers were calibrated

using a 0.2 mm PVDF probe hydrophone in a separate experiment (Precision Acoustics Ltd., Dorchester, UK). The echoes from the microbubbles were received at half the transmitting frequency (5 MHz) by another focused transducer with the same focal length (Precision Acoustics PA076; 1-9 MHz). Acoustic pressure amplitudes of 50, 100 and 150 kPa were applied. The transmitted signals were calculated in MATLAB using Eqn.2 and generated by an arbitrary wave generator (8026, Tabor Electronics Ltd., Tel Hanan, Israel) and amplified with a 60 dB pulse amplifier (150A100B; Amplifier Research, Limerick, Ireland). The scattered pressure waves were received, amplified by 60 dB and digitized by a 12-bit digitizer with a sampling frequency of 500 MHz.

10 MHz bursts of 2, 6, 10 and 20 cycles were transmitted. The envelope of the transmit burst was varied from the Gaussian to the rectangular shape by changing the value of M to 1, 3 and 15 (Eqn. 2). Averaging over 50 pulses in the frequency domain with a pulse repetition frequency of 1 kHz was applied, and this sequence was repeated for each of the transmitted signals with different envelopes. The amplitude spectrum of the received pressure signals (Figure 6a) have been calculated after discarding three cycles at 10 MHz from the beginning and the end of the received scattered signals for the 20-cycle burst and applying a Hanning window. The beginning and the end of the received scattered signal was taken away to remove the direct effect of the 5 MHz component of the S-D signal linearly scattered by UCA which could be mistaken as enhancement of the SH response.

Experimental results

Effect of the self-demodulation signal on the subharmonic emission of microbubbles

Figure 6 shows the signals scattered by the microbubbles in response to a 20-cycle 10 MHz burst with three envelopes changing from a Gaussian shape (M=1) to a more rectangular shape (M=15). The energy of the SH response produced by the UCA increases from -55 dB to -33 dB for M=1 to M=15, thus a 22 dB enhancement is observed. The acoustic pressure amplitude at the focus of the transducer was set to 50 kPa. This is the pressure that the microbubbles experience. Clear SH peaks for all the three different excitation bursts in Figure 6 show that 50 kPa pressure amplitude is already above the SH threshold level of the BR14 UCAs.

Effect of the excitation duration on the subharmonic emission of microbubbles

Short signals are more favored for imaging purposes since they provide a higher spatial resolution. However, with such signals, it is difficult to separate the SH component from the fundamental component in the frequency domain. To investigate the effect of the excitation burst duration on the SH emission of the UCAs,

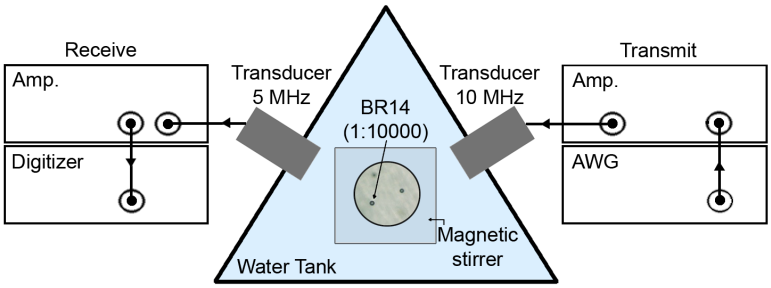

Figure 5
Schematic view of the experimental setup

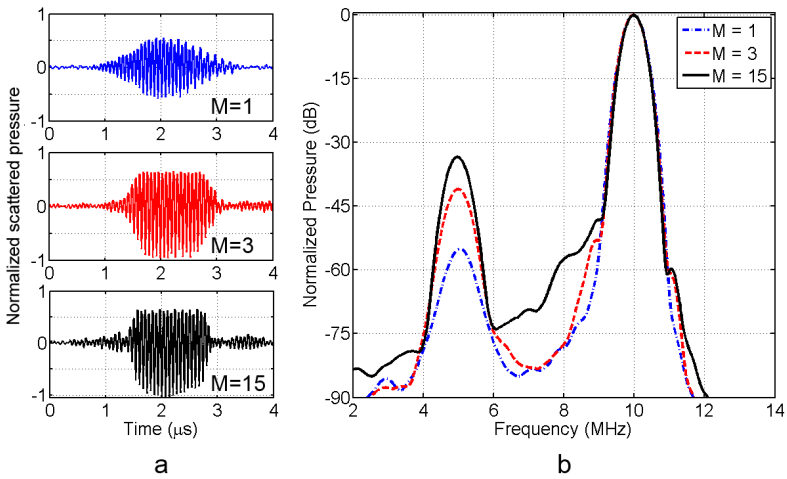

Figure 6
a) Pressure signal scattered by the microbubbles excited by a 10 MHz, 50 kPa peak pressure burst with three different envelopes in time domain.
b) The amplitude spectrum of the scattered signal from the microbubbles (average of 30 acquisitions in the frequency domain).

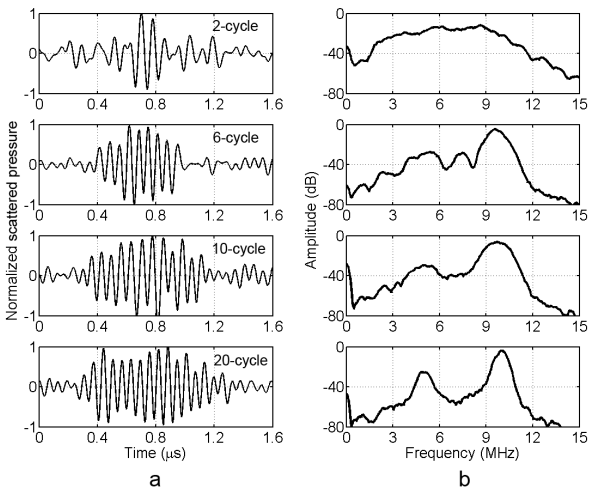

Figure 7
a) Pressure signals scattered by the microbubbles excited by a 10 MHz burst with 2, 6, 10 and 20 cycles in time domain.
b) Corresponding amplitude spectra (average of 30 acquisitions in frequency domain). All the pulses were modulated with a rectangular envelope (M=15) and the applied acoustic pressure peak amplitude is 50 kPa.

Figure 8
a) Pressure signal scattered by the microbubbles excited by a 6-cycle, 10 MHz, 50 kPa peak pressure burst with three different envelopes in time domain.
b) The amplitude spectrum of the signal scattered from the microbubbles (average of 50 acquisitions in frequency domain).

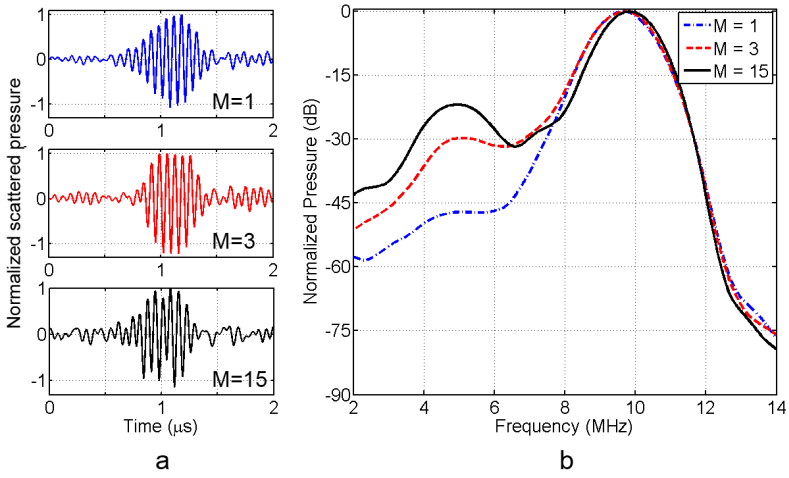

Figure 9
Amplitude spectra of the signals scattered from the microbubbles excited by a 6-cycle pulse with different envelopes at three acoustic pressure amplitudes of a) 50 kPa, b) 100 kPa and c) 150 kPa.

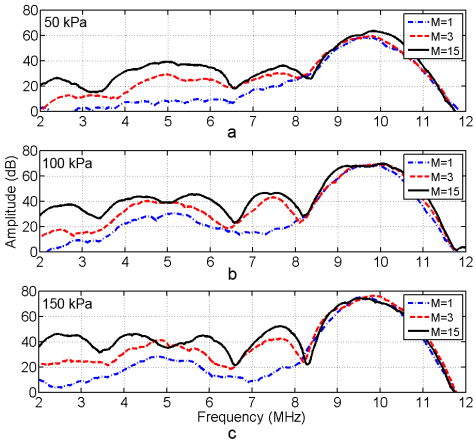

Figure 10
a) Excitation bursts with and without the S-D signal in time domain,
b) Corresponding amplitude spectra of the excitation bursts,
c) Radial response of the microbubbles in time domain,
d) Corresponding amplitude spectra of the microbubble radial response.
All the pulses were modulated with a rectangular envelope (M=15) and the applied acoustic pressure peak amplitude is 30 kPa. The microbubble has a diameter of 2 μm and the initial surface tension ($\sigma(R_0)$) of 0.014 N/m.

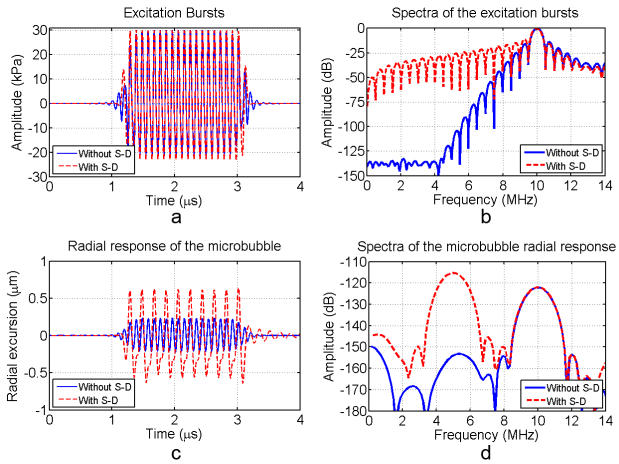

four bursts with the same rectangular envelope (M=15) and acoustic pressure peak amplitude of 50 kPa but different number of cycles (2, 6, 10 and 20) were applied. Figure 7 shows examples of time signals scattered by the UCA for each transmitted burst and their amplitude spectra averaged over 30 sequences in frequency domain.
The excitation with only 2 cycles results in a very broad-band scattered signal with no distinguishable peak around the SH frequency. Increasing the transmit burst durations to 6, 10 and 20 cycles results in the equal 22 dB ratio of the SH amplitude to fundamental amplitude. The advantage of using a longer pulse as can be seen in Figure 7 is that a better separation of the SH and fundamental peaks is obtained. Independently from the duration of the transmitted burst, the enhancement of the SH response due to the envelope of the burst is still valid for a short burst of 6 cycles (Figure 8). Similar to a 20-cycle burst (Figure 6) the energy of the SH response produced by the microbubbles increases up to 25 dB when changing the value of M from M=1 to M=15, for a 6-cycle burst.

Effect of acoustic pressure on the subharmonic emission of microbubbles
To see how the SH response of the microbubbles is influenced by the incident pressure amplitude, a 6-cycle burst was transmitted with three different acoustic pressures of 50 kPa, 100 kPa and 150 kPa (peak negative). Figure 9 shows the amplitude spectra of the scattered signals from the microbubbles averaged 30 times in the frequency domain.
For a 50 kPa transmitted pressure, the increase in the SH amplitude for M=15 compared with M equal to 1 and 3 is about 31 dB and 10 dB, respectively (Figure 9a). Increasing the transmit pressure to 100 kPa decreases the enhancement of the SH response with M=15 to 0 dB and 9 dB compared with M=3 and M=1, respectively (Figure 9b). Rising the transmit pressure even higher to 150 kPa results in even less enhancement of the SH response due to a rectangular envelope (M=15), -4 dB and 7 dB compared with M=3 and M=1, respectively (Figureure 9c). The other interesting point in this Figure is the appearance of different low frequency components which are enhanced for a burst with a rectangular envelope. These peaks become more dominant when the transmit pressure is increased.

Discussion

Effect of the self-demodulation signal on the subharmonic emission of microbubbles

The frequency content of S-D signal for different burst envelopes was derived according to the KZK equation (Eqn. 4 & Figure 2). For a 2 μs burst with a Gaussian envelope (M=1), the frequency content of the S-D signal is limited to the very low frequency and it appears as a clear peak around 0.75 MHz (Figure 2c, M=1). This peak becomes broader by increasing M to 3 (Figure 2c). Finally such a clear peak in the frequency domain disappears for an ultrasound burst with a rectangular envelope (Figure 2c, M=15). The S-D signal for a rectangular envelope contains a large number of harmonics of the center frequency of the envelope (up to 30th harmonic for M=15). Although the S-D signal is not concentrated at a specific low frequency for a burst with a rectangular envelope, it has higher energy at half the transmit frequency ($\omega_0/2$) than for a Gaussian envelope. Our results including numerical simulations and *in vitro* experiments suggest that such a broad-band frequency content of the S-D signal acts as a stimulator which triggers enhanced SH responses of microbubbles.

Simulation results (Figure 3) show that far from the buckling regime ($0.02<\sigma(R_0)<0.05$ N/m), the microbubble exhibits no SH oscillation and the S-D signal is not strong enough to "push" the bubble into that regime in the range of acoustic pressure investigated in this study (50-150 kPa). Also, when the bubble is already placed in the buckled state ($\sigma(R_0)=0$) the S-D signal does not enhance the SH emission since it is already in its maximum level. However for intermediate state, the S-D signal in the burst with rectangular envelope has enough energy to "push" the bubble towards the buckling regime and increase the SH response of the microbubble. The same reasoning applies for the bubbles close to their rupturing state. The enhancement of the SH energy at $\sigma(R_0)=0.014$ N/m is depicted in Figure 4. As can be seen the SH response of a microbubble, thanks to the S-D signal, increases up to 23 dB by changing the burst envelope from Gaussian (M=1) to rectangular (M=15).

A microbubble with a diameter of 2 μm was chosen for the numerical simulation since it is reported as the mean diameter of BR14 UCA [270]. The SH resonance frequency of such a microbubble is around 5 MHz [170]. Therefore the 10 MHz excitation bursts have a center frequency of twice the resonance frequency of the microbubble which is known to give the minimum threshold of SH emission from the UCA [257]. Exciting the microbubbles at twice their resonance frequencies results in the maximum amplitude of SH signal. In such a condition the enhancement of the SH response of UCA due to the S-D signal is more visible. Deviating from this excitation frequency decreases the amplitude of the SH response and

consequently the effect of the S-D will be less detectable. Such a limitation in using the SH signal is less of a concern for *in vivo* applications because in the UCA solution usually there are enough microbubbles with desired radius for the applied frequency. However choosing the appropriate frequency for the excitation burst or manipulating the size distribution of the UCAs can be beneficial when doing SH imaging.

To validate experimentally the stimulating effect of the S-D signal on the SH emission predicted by numerical simulations, scattering measurements were performed on a population of microbubbles. Experimental results (Figure 6) showed that the SH amplitude scattered by the UCA increases monotonically up to 22 dB by changing the burst envelope from Gaussian (M=1) to rectangular (M=15). These results are in excellent agreement with the simulations (23 dB SH enhancement) (Figure 4). At this stage a quantitative comparison between the absolute SH amplitude in the simulation and experiment is not possible since the initial surface tension $\sigma(R_0)$ as well as the size distribution of the microbubbles in the experiment is a priori not known.

The enhancement of the SH emission because of the envelope of the pulse was also reported before [175-178]. However, none provided a physical explanation for this observation. We believe that the stimulation effect of a burst having a rectangular envelope is due to its S-D signal as shown in Figure 2. The enhancement in the SH response of the UCA caused by the low frequency S-D signal is supported by numerical simulation and experiments performed in this study.

To see the effect of the S-D signal on the SH emission for excitation bursts with similar rectangular envelopes, new sets of simulations were conducted at a peak negative pressure of 30 kPa and shown in Figure10. The S-D signal was filtered out using an 8^{th} order Butterworth high pass filter with cutoff frequency of 9 MHz (Figure 10a and 10b). The radial response of a 2 μm microbubble with initial surface tension of 0.014 (N/m) was calculated using the Marmottant model (Figure 10c and 10d). It can be seen from the radial excursion of the microbubble in Figure 10c that with the S-D signal the frequency becomes half (blue curve) of the one without S-D signal (red curve). The broadband low frequency S-D signal at the beginning of the excitation burst effectively stimulates the resonance of the microbubble and pushes it to the buckling regime. We believe such an effect results in much higher amplitude oscillation at SH frequency even in response to the rest of the excitation signals which are identical in both bursts. The spectra of the radial response of the microbubble to these two excitation bursts shows 38 dB enhancement of the SH response for the burst having the S-D signal compared with the one without the S-D signal (Figure 10d).

Effect of the excitation duration on the subharmonic emission of microbubbles

The effect of the burst duration on the SH response of the UCA for a rectangular envelope (M=15) is demonstrated in Figure 7. Rectangular envelope was chosen because it gives the maximum enhancement in the SH emission (Figure 6). It was reported before by Faez et al [170] that the ratio between the SH amplitude and the fundamental amplitude is independent from the excitation duration above three cycles. The same result was obtained in this study (Figure 7), indicating the enhancement of SH emission due to the S-D signal is still evident for a shorter transmitting pulse consisting of 6 cycles (Figure 8).

Effect of acoustic pressure on the subharmonic emission of microbubbles

The effect of acoustic pressure on the SH enhancement stimulated by the S-D signal was also investigated in a separate experiment (Figure 9). Three acoustic pressures of 50, 100 and 150 kPa were applied with a 6-cycle burst and three different envelopes. A 6-cycle burst was chosen since it provides a good compromise between the axial resolution and SH peak separation in the frequency domain. Three different states have been observed for amplitude of the SH response of UCAs by increasing the incident pressure [271]: First stage is the initial occurrence stage where the incident pressure surpass the threshold level needed for SH oscillation. Growth stage is the next one where the SH amplitude increases with increasing the incident pressure. The third state is the saturation state where increasing the pressure of the excitation burst does not change the SH amplitude. It can be seen in Figure 9 that when the excitation burst has a Gaussian envelope (M=1) and a peak pressure of 50 kPa, no SH signal is observed from the UCAs. However increasing the incident pressure to 100 kPa results in 22 dB increase in the SH signal above the noise level. Further increase in incident pressure to 150 kPa does not change the amplitude of the SH response. This suggests that the saturation state has been already reached by 100 kPa incident pressure. For M=3, 50 kPa peak pressure has already passed the threshold level for SH emission from the UCAs. Increasing the incident pressure to 100 kPa results in 10 dB increase in the SH amplitude showing the growth state as well as reaching the saturation level since further increase in the incident pressure to 150 kPa does not change the amplitude of the SH response of the microbubbles. However, for a burst with rectangular envelope (M=15) there is no growth state and the maximum SH amplitude is reached by 50 kPa incident pressure. Instead appearance of peaks in different frequencies is observed. We believe this is due to the broad-band low frequency S-D signal in the excitation burst with rectangular envelope triggering different bubbles with different sizes and therefore different resonance frequencies.

Practical implications for subharmonic imaging

The stimulation effect of the S-D signal on the SH response of the UCA can be even more effective if combined with the conventional contrast imaging techniques such as pulse inversion. Excitation bursts with rectangular envelopes were used by Needles et al [151] for SH imaging together with pulse inversion resulting in 15 dB enhancement in contrast to tissue ratio compared with fundamental imaging. Such an increase in the SH response of the microbubbles using waves with rectangular envelopes together with pulse inversion techniques can be explained by the stimulation effect of the S-D signal on the SH emission.

Since the SH response of the UCAs is strongly dependent on their initial surface tension ($\sigma(R_0)$), SH imaging can be difficult for detecting a single bubble with an initial surface tension far from buckling or rupturing regime. However using an excitation burst with a rectangular envelope increases the range of the $\sigma(R_0)$ in which the SH emission takes place.

Although the enhancement of the SH response because of the S-D signal is significant, and high enough for SH imaging the amplitude of the enhanced SH signal is still 33 dB below the fundamental amplitude in our experiment (Figure 7). This amplitude can be increased to improve the signal to noise ratio by adjusting the size distribution of the UCAs. Our simulation result in Figure 4 shows that if the excitation fundamental frequency is twice the resonance frequency of the microbubbles, the amplitude of the SH signal can be as high as the fundamental amplitude.

The S-D signal is developed during the nonlinear propagation of the acoustic wave in the medium, therefore it is scattered by UCA and also by tissue. However, for a low acoustic pressure (50 kPa) since the amplitude of the S-D signal is very low (around 0.2 kPa) the direct scattering of this signal by the tissue does not affect the contrast to tissue ratio. On the other hand, the enhancement of the SH response of UCAs due to the S-D signal is considerably high (around 20 dB). Therefore optimizing the shape of the transmit signal in a way to have the maximum energy of the S-D signal at the SH frequency, will always be beneficial in increasing signal scattered at the SH frequency and

Conclusion

The low frequency self-demodulation acoustic signal resulting from nonlinear propagation of the ultrasound wave, stimulates the subharmonic response of ultrasound contrast agents. The microbubbles are pushed towards the buckling or rupturing regimes by the self-demodulation signal resulting in enhanced subharmonic emission.

Effect of excitation envelope on volumetric subharmonic vibrations of single contrast agent microbubbles using an acoustical camera

04

Abstract

Recently we have shown that a suitable design of the excitation envelope to generate a self-demodulation signal at the subharmonic (SH) frequency can enhance the SH emission of microbubble (MB) contrast agents at 10 MHz. In this study we investigated effects of the excitation envelope on volumetric SH response of individual MB excited in the frequency range of 5-8 MHz with an acoustical set up (acoustical camera) measuring relative volume variations of single MB. Using the acoustical camera, we retrieved the radial response of single BR14 MB (Bracco) to 2 μs pressure waves (25 kPa to 200 kPa peak to peak) with Gaussian and rectangular envelopes. Each single MB is excited by a sequence of 10 signals with Gaussian and rectangular envelopes and with frequencies of 5, 6, 7 and 8 MHz. The 5 MHz pair is exactly repeated at the end of the sequence to check the MB for possible deflation or disruption. The total length of the excitation waves sequence was 30 μs ensuring that the same single MB was excited with all excitation bursts. The vibration responses of the single MB to the 10 excitations are received through the nonlinear coupling with a 50 μs 30 MHz probing wave. Amplitudes of relative radial SH vibration of single MB excited with rectangular envelope bursts were in average 2 times larger than when excited with Gaussian envelope bursts. This study suggests that excitation with rectangular envelope enhances the volumetric radial SH response of a single MB compared with excitation with Gaussian envelope at low acoustic pressures (<200 kPa peak to peak). Such an enhanced SH response can be then used for imaging the UCA.

Based on a manuscript by **V. Daeichin**, G. Renaud, J.G. Bosch, A.F.W. van der Steen, and N. de Jong., in Ultrasonic Symposium (IUS, IEEE), in 2013.

Introduction

Ultrasound contrast agents (UCA) are micron size gas bubbles encapsulated by a lipid, protein, albumin or polymer shell. High compressibility of their gas core and their size make them ideal agents for enhancing the contrast of blood pool for ultrasound imaging. When exposed to ultrasound, the microbubbles (MBs) behave as nonlinear mechanical resonators whereas tissue scattering is linear. One result of such nonlinear behavior is the subharmonic (SH) response (half the transmit frequency). The emission of energy at SH was proposed to be exploited as a new imaging modality [235,249]. No SH scattering is produced by tissue. The SH signal has a greater penetration distance since its attenuation is lower than that at the fundamental frequency, offering a potentially powerful diagnostic tool for clinical examinations [255,256].

The SH signal is strongly dependent on the applied acoustic pressure, the hydrostatic pressure variations [244], the envelope of the excitation signal [176-178] and equilibrium state of the microbubble [259].

Previously, we have reported *in vitro* and with numerical simulations that a suitable design of the excitation envelope to generate a broadband low frequency self-demodulation (S-D) signal can enhance the SH emission of UCA more than 20 dB at 10 MHz transmit frequency [174]. The S-D wave is a low-frequency signal produced by nonlinear propagation in the medium. In the present work we have minimized the effect of such a nonlinear propagation of the excitation wave by reducing the propagation length. This way, we have investigated the effect of the excitation envelope itself rather than the effect of the S-D signal on the volumetric SH response of the individual BR14 contrast agent (Bracco Research SA, Geneva, Switzerland).

Methods

Acoustical camera

The principle of the acoustical camera is to retrieve the radial response of single microbubbles to a pressure wave by means of a low-amplitude probing wave. If the frequency of the probing wave is sufficiently higher than the resonance frequency of the MB, the relative amplitude modulation in the signal scattered in response to the probing wave is quasi-equal to the radial strain induced by the pressure wave [272]. A reference probe signal before and after the transmission of

the pressure wave is used to calculate the radial strain (relative change in bubble radius) and assess the compression-expansion asymmetry in microbubble oscillations.

Numerical simulation

Using the model of Marmottant et al [261], the radial oscillation of a single MB in response to 8 MHz 2μs long excitations with Gaussian and rectangular envelope were calculated. The shell elasticity (χ) and the shell viscosity (κ_s) were set to 2.5 N/m and 10-9 kg/s, values for BR14 UCA used for *in vitro* experiments [259]. The initial surface tension of the MB was set to 0.02 N/m and the diameter to 3.5 μm to investigate the effect of the excitation envelope on MB excited far from its resonance frequency.

Experimental set-up

Using the acoustical camera an experimental set-up was developed to insonify single BR14 microbubbles simultaneously with two focused ultrasound beams to transmit the probing wave (30MHz sine burst, 100 kPa peak pressure amplitude, 50 μs duration) and a sequence of 10 bursts with frequencies of 5, 6, 7, 8 and again a 5 MHz at the end of the sequence each with a Gaussian and rectangular envelope. The 5 MHz pair was exactly repeated at the end of the sequence to monitor the changes in the MB properties (deflation or possible disruption of the MB). Each transmit burst in the sequence was 2 μs long and there was 1 μs of silence between each burst in the excitation. A wideband ultrasound transducer (1–9 MHz, 23 mm diameter, Precision Acoustics, Ltd., Dorchester, Dorset, UK) transmitted the excitation wave and a 30MHz center-frequency transducer (6 mm diameter, Olympus NDT, Inc. (Panametrics), Waltham, MA, USA) transmitted the probing wave.

The acoustic pressure of both transmitted signals was measured in separate experiments with a needle hydrophone (Precision Acoustics, Ltd., Dorchester, Dorset, UK). The impulse response of the low frequency transducer was measured with the hydrophone and used to apply inverse filtering to the excitation signals to avoid overshooting and ring downs due to the sharp edges of the rectangular envelope.

A second 30 MHz frequency transducer (6 mm diameter) collects the signal scattered by bubbles in response to the probing wave. The focal distance is 24 mm for the low frequency transducer and 19 mm for the two 30 MHz transducers. Their focal volumes overlap (Figure 1).

A highly diluted (1:500,000) suspension of BR14 contrast agent was prepared in the 300 mL water tank of our setup, resulting in 1 MB per mm^3 on average. A

magnetic stirrer ensured a regular motion of microbubbles. The one-way -6 dB lateral beam width of the 30 MHz transducers was 0.4 mm in transmission and reception, so the actual volume being interrogated (volume of the intersection of the two 30-MHz focal zones) was about 0.064 mm^3. Assuming that the number of MBs present in the interrogated volume had a Poisson distribution, the probability that there were two or more of them in the interrogated volume was about 0.03. This gives the probability of 0.97 for if only one or no MB was present, asserting that we assayed individual MBs. The lateral beam width of the 1–9 MHz transducer was nearly an order of magnitude larger than that of the 30 MHz transducer. As a result the acoustic pressure created by the excitation sequence was considered uniform within the focal volume of the 30 MHz transducer. Single MBs passing through the acoustic focal volume at 30 MHz were considered quasistatic within the duration of the probing wave (50 μs). The rotation speed of the magnetic stirrer was adjusted so that the amplitude of the signal scattered at 30 MHz remained constant during the 50 μs of the probing wave. This was achieved when the velocity of an individual microbubble was of the order of 0.1 m/s. The excitation sequence was transmitted twice with 20 μs delay in between. The first series were fired such that the signal scattered in response to the probing wave consisted of three parts: 10 μs before the transmission of the first sequence used as a reference, 30 μs during which the bubble was responding to the first excitation sequence, 10 μs after the end of the excitation used as a post-reference (Figure 2). Then the excitation sequence was transmitted for the second time in the absence of the probing signal.

The response of the MBs to this second excitation sequence was used as reference to minimize the effect of direct scattering of higher harmonic response of the MB to the excitation sequence which can be picked up by the 30 MHz received transducer. The measured signals scattered by MBs were first cut to separate the response of the MB to the excitation sequence in the absence of the probing signal. Then each segment was band-pass filtered (4-15 MHz) and adjusted for the best matching between the two signals using cross correlation. When the time shift for the best matching was defined, it was applied to the two unfiltered segments. Then the segments were subtracted from each other. The resulting signal was then band-pass filtered around the probing frequency (in the frequency range 17–43 MHz). Then the modulus of the analytic signal provided the envelope of the probe signal from which the relative amplitude modulation was calculated. The absolute amplitude of the probing signal recorded before and after the action of the excitations was the reference used to compute the relative amplitude modulation. The radial strain was approximately equal to the relative amplitude modulation in the probing signal [272].

Results

Numerical simulation

Figure 3 shows the results of the numerical simulation using the Marmottant model in which a single MB was excited with the sequences explained earlier.
To compensate for the total energy of the signal with Gaussian envelope compared with rectangular envelope, an extra excitation with Gaussian envelope and double the amplitude was tested. Figure 2 shows that the amplitude of the SH response of such a simulated MB is significantly higher when excited with a rectangular envelope burst than with Gaussian envelope bursts with both amplitudes. The response of the MB in the time domain shows an early development of SH oscillation when excited by the rectangular envelope burst whereas for the Gaussian envelope excitation with double amplitude, the SH oscillation is more visible later in time and after the excitation has reached its maximum amplitude. And no SH is observed for the Gaussian envelope excitation at 100 kPa

Experimental results

Figure 4 demonstrates an example of a received signal (Figure 4a), retrieved radial oscillation of a single BR14 MB in response to 5 pairs of excitations with a frequency range of 5 to 8 MHz (Figure 4b) and their corresponding Fourier transforms (Figure 4c). Before computing the FFT, a Tukey window was applied on each retrieved radial response with 0.2 as the ratio of cosine-tapered section length to the entire window length. Figure 4 shows that for such a particular MB, there is no SH response for 5 and 8 MHz excitations with Gaussian envelope and there are only low amplitude SH responses for 6 and 7 MHz excitation. However the SH response is visible for all the frequencies when the rectangular envelope excitation is applied. Also the response of the MB in time domain shows the early buildup of the SH behavior for excitations with rectangular envelope, similar to the results of numerical simulations.
Response of 50, 97 and 397 MBs to the excitation sequence at pressures of 25, 100 and 200 kPa peak to peak were recorded and analyzed. Figure 5 shows the scatter plots of amplitude of SH response to the rectangular envelope excitation along the y axis versus the Gaussian envelope excitations along the x axis for these three transmitted pressures.
The vertical and horizontal gray lines in Figure 5 indicate the noise levels for SH amplitude in response to rectangular and Gaussian envelope excitations respectively. The identity lines are also plotted in this Figure. All the scatter plots for dif-

ferent transmit pressures show higher amplitude of SH response for rectangular envelope excitations. It can also be seen from this Figure that the amplitude of the SH response of many MBs excited with Gaussian envelope is below noise level while they show SH behaviors to the rectangular excitations. The ratio of SH amplitude in response to rectangular envelope over Gaussian envelope excitations (only including MBs showing SH response above the noise level for both excitations) and the percentage of number of captured MBs showing SH behavior at three pressures are quantified in Figure 6a and b. The Although the number of bubbles showing SH behavior in response to both the rectangular and Gaussian envelope is highly dependent on the transmit pressure (Figure 6b), the mean ratio of SH amplitude for these two excitations is about the same and around 2 times higher for excitation with rectangular envelope (Figure 6a). Similar ratio is seen in the number of MBs with SH response at each transmit pressure as well. Because the energy of a burst with rectangular envelope is higher than a burst with the same length but Gaussian envelope an extra set of experiments were performed in which all the bursts with Gaussian envelope had amplitudes two times higher than those with rectangular envelope. Results are shown in Figure 7.

Similar to the previous results the amplitude of the volumetric SH response of most of the individual MBs were higher when excited with rectangular envelope bursts compared to Gaussian envelope burst with double amplitude. This results confirms that the main cause of the observed enhancement in the SH behavior of the MB is not due to higher energy of the burst with rectangular envelope but the shape of such an envelope.

Discussion

Numerical simulations using the Marmottant model showed that the rectangular envelope excitation makes the MB oscillate at its SH frequency earlier and higher than the Gaussian excitation envelope even with double amplitude (Figure 3). Such a behavior in individual MBs was experimentally confirmed using an acoustical camera (Figure 4). The effect of the rectangular envelope on enhancing the SH response of the MB is very similar to the effect of the S-D signal of such an envelope that we have previously reported. Although the S-D signal is proportional to the second time derivative of the squared envelope [263] the fre-

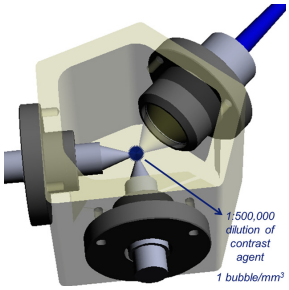

Figure 1
Schematic of the acoustical camera used for investigating the volumetric subharmonic response of individual microbubbles in response to excitations with rectangular and Gaussian envelopes.

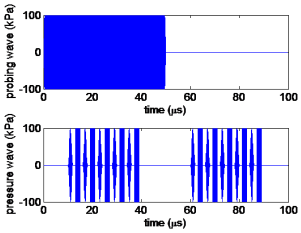

Figure 2
Pulse sequence transmitted with the acoustical camera. Top: 30 MHz probing wave. Bottom: signal sequence of sine bursts of different frequencies and envelopes repeated twice.

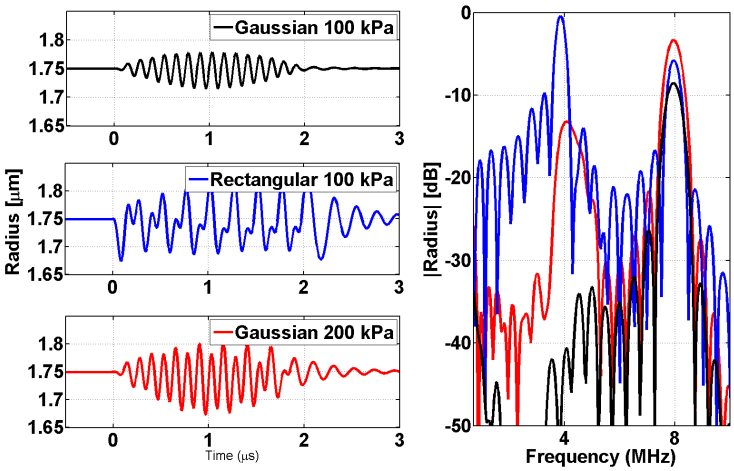

Figure 3
Numerical simulation using the Marmottant model showing the response of a single microbubble to 2 μs long excitations with rectangular and Gaussian envelopes (shell elasticity (χ) = 2.5 N/m, shell viscosity (κ_s) were set to = 10-9 kg/s, initial surface tension = 0.02 N/m and diameter = 3.5 μm).

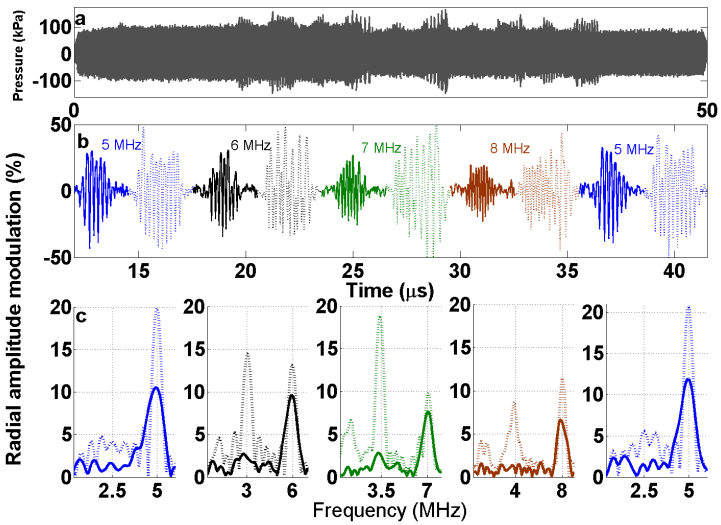

Figure 4
An example of
a) received scattered signal from a single BR14 microbubble in response to an excitation sequence with 100 kPa peak pressure,
b) retrieved radial oscillation and,
c) their corresponding Fourier transforms.

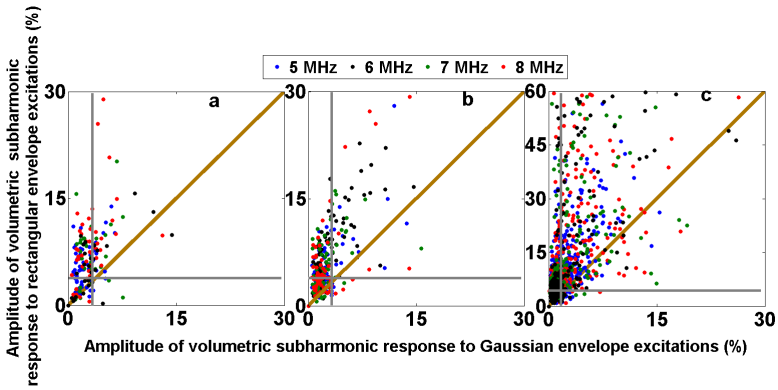

Figure 5
Amplitude of SH response to the rectangular envelope excitation versus the Gaussian envelope excitations at: a) 25 kPa, b) 100 kPa and c) 200 kPa peak to peak pressure. Gray lines are the noise level for each excitation envelope and the thick brown line is the identity line.

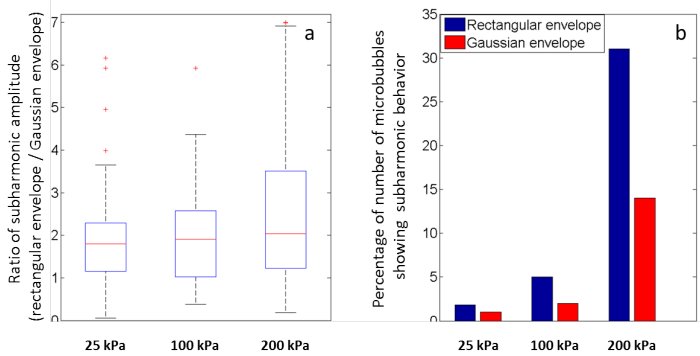

Figure 6
a) Ratio of SH amplitude in response to rectangular envelope over Gaussian envelope excitations,
b) percentage of number of captured MBs showing SH behavior for two excitation envelopes and three transmitted pressures.

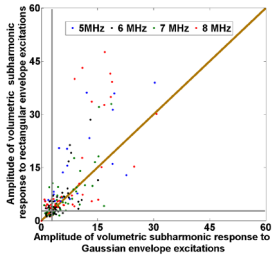

Figure 7
Amplitude of SH response to the rectangular envelope excitation (50 kPa peak to peak pressure) versus the Gaussian envelope excitations with double amplitude (100 kPA peak to peak pressure).

quency component of a rectangular envelope itself, similar to its self-demodulated signal, is a broadband low frequency wave but with lower amplitude. Up to 20 dB enhancement of the SH response was observed in the previous study in which a population of BR14 MBs were excited with a 10 MHz burst with different envelopes. In this work the effect of the S-D signal was minimized by having a 3 times shorter focal distance (24 mm), however, still 6 dB enhancement of the SH response due to the excitation envelope was observed on average for more than 280 single MB. This suggest that a rectangular envelope has similar effect in enhancing the SH response of the MB as its self-demodulated signal, but lower in amplitude.

Our results suggest that for contrast imaging techniques, focusing on exploiting the SH component of the MB response can strongly benefit from rectangular envelope excitations. One issue of such excitations is the strong side-lobes of the fundamental peak due to the envelope characteristics which may well appear around the SH frequency and reduce the contrast to tissue ratio. However, applying simple pulse sequence techniques which remove the fundamental frequency from the backscattered signals (such as pulse inversion) can easily overcome such a problem.

Subharmonic nonlinear fundamental and ultraharmonic imaging of microbubble contrast at high frequencies

05

Abstract

Ultrasound contrast agent (UCA) is increasingly applied in high-frequency ultrasound imaging. However, conventional contrast detection methods perform poorly at high frequencies. We performed systematic *in vitro* comparisons of subharmonic (SH), nonlinear-fundamental (NF) and ultraharmonic (UH) imaging for different depths and UCA concentrations (VisualSonics Vevo 2100 system, MS250 probe, MicroMarker UCA). Four, six and ten cycles bursts at three power levels were investigated with following pulse sequences: B-mode, amplitude-modulation (AM), pulse-inversion (PI) and combined pulse-inversion/amplitude-modulation (PIAM). Contrast-to-tissue ratio (CTR) and contrast-to-artifact ratio (CAR) were calculated. At 8 mm depth, SH-PI imaging performed the best (CTR: 26 dB, CAR: 18 dB) and at 16 mm depth, NF-AM imaging was the best contrast imaging method (CTR: 10 dB). UH imaging did not result in acceptable CTR and CAR. The best candidates from the *in vitro* study were tested *in vivo* in chicken embryo and mouse models and the results were in a good agreement with the *in vitro* results.

Based on a manuscript by **V. Daeichin**, J.G. Bosch, A. Needles, F. S. Foster, A.F.W. van der Steen, and N. de Jong, in the journal of Ultrasound in Medicnice and Biology (in press).

Introduction

The need for high resolution ultrasound imaging have increased the diagnostic use of high frequency ultrasound (HFU, > 15 MHz) [150,151,273-276]. Beside numerous applications of HFU for small animal imaging [150], it is widely used in clinical diagnosis such as intravascular, dermatological and ophtalmological applications [277]. Within HFU, the use of ultrasound contrast agent (UCA) is also growing [150,151]. Although UCA has been used and studied extensively at frequencies below 15 MHz [278], the behavior of the UCA microbubbles is not fully understood above 15 MHz [150].

Stronger scattering behavior of the UCA is the key factor for linear contrast detection techniques [273]. However, these methods cannot provide sufficient contrast in images for many applications such as detection of small capillaries in tissue perfusion or in the presence of tissue motion. Therefore, UCA-specific nonlinear contrast imaging techniques are essential at high frequencies (>15 MHz). Conventional nonlinear imaging techniques, at lower frequencies, focus mainly on detection of higher harmonics [145-149]. Similar techniques have been implemented at higher frequencies [151-155,279]. However, the performance of these methods is degraded in HFU imaging because the driving frequency is much higher than the resonance frequency of the UCA. In addition to this, the propagation of the transmitted acoustic wave in tissue is more nonlinear at higher frequencies [280]. Therefore, techniques exploiting higher harmonics are hampered because of the increase in the amplitude of harmonics produced by tissue [255]. These limitations motivate the exploitation of the nonlinear components of the UCA response at lower frequencies: the nonlinear fundamental (NF), subharmonic (SH) and ultraharmonic (UH) frequencies.

Contrast imaging focusing on the NF component of the UCA works best if the excitation frequency is close to the resonance frequency of the microbubbles. To get strong enough NF signal from the currently used UCA at frequencies above 15 MHz, high transmit pressures are required, which may disrupt the microbubbles. Another challenge of NF imaging is the so-called nonlinear propagation artifact or far-wall artifact [156-160] produced by nonlinear propagation of the excitation wave through UCA which is backscattered by the tissue behind it, resulting in a false response at the site of the linearly scattering tissue.

The emission of energy by UCA at half the excitation frequency f_0, the SH response [137], was proposed to be exploited as a new imaging modality [171]. No SH signal is generated during propagation in tissue and no SH scattering is produced by tissue. The backscattered SH signal is attenuated less in tissue than

the signals at the fundamental and higher harmonic frequencies, offering a potentially powerful diagnostic tool for clinical examinations [249]. Nevertheless, the required excitation bursts for SH imaging should also be considered. The SH signal is strongly dependent on the applied acoustic pressures, the ambient pressure variations [137,169] and the envelope of the excitation signal [174,281]. Previously, we have reported that the self-demodulation (S-D) signal can enhance the SH response of phospholipid-coated microbubbles by up to 20 dB at 10 MHz [174]. The S-D signal is a low-frequency signal component produced by weakly nonlinear propagation of an ultrasound wave. It is proportional to the second time derivative of the squared envelope of the transmitted signal [174,262-264]. Rectangular envelopes were shown to produce strong SH stimulation in UCA.

The UH response (at 3/2 f_0) constitutes another UCA-specific signal which is not generated by tissue [282]. UH contrast imaging can be performed with a low-bandwidth probe (40% bandwidth) while SH or higher harmonics imaging require at least 70% bandwidth [282]. Also the lateral resolution in UH imaging is higher than that in SH and NF imaging [255]. The drawbacks are the relatively weak level of the UH signal from the UCA and higher attenuation of UH signals because of the frequency dependent attenuation.

In the current study, we systematically compare in an *in vitro* setup the value of the three different frequency components: SH, NF and UH. We use excitation bursts with rectangular envelope together with conventional nonlinear contrast detection methods; pulse inversion (PI) [147], amplitude modulation (AM) [283] and a combination of PI and AM (PIAM) Haider [284]. The comparison is based on measurements of the ratio of the detected UCA signal to the residual tissue signal (this is termed the contrast-to-tissue ratio or CTR) and the ratio of the detected UCA signal to the far-wall artifact signal (this is termed the contrast-to-artifact ratio or CAR). Target depth, pulse duration, UCA concentration and transmit pressure are systematically varied to find the optimal nonlinear imaging approaches for HFU applications in different conditions. Finally, those combinations with the highest CTR and CAR *in vitro* were chosen for an *in vivo* verification in mouse and chicken embryo models.

The results shown in this manuscript are the primary findings of our comprehensive systematic *in vitro* analysis (108 measurements and 648 analyses in total). The rest of the results and details of the *in vivo* experiments are presented in the online supplement (available online at http://www.umbjournal.org). We will refer to this supplementary material as “supp.” throughout the manuscript. All the referred CTR and CAR values in this manuscript are highlighted and numbered as (1) to (6) in tables 2 to 10 in the supplementary document.

Methods

A high frequency ultrasound scanner with linear array transducer (Vevo 2100 with MS250 probe, VisualSonics Inc., Toronto, ON, Canada) was operated at three frequencies (15 MHz, 22 MHz and 30 MHz). We insonified the UCA at a transmit frequency f_0 and we examined the frequency responses at around $1/2f_0$ for SH imaging, f_0 for NF imaging and $3/2f_0$ for UH imaging. The MS250 probe has a center frequency of 22.5 MHz and a -6dB two-way frequency bandwidth of 70% (15-30 MHz) [151]. In order to benefit from the transducer sensitivity both in transmission and reception, the selection of the transmit frequencies was done as follows: 15 MHz for UH imaging, resulting in a received UH component at 22.5 MHz; 22 MHz for NF imaging; and 30 MHz for SH imaging, with a received SH component at 15 MHz. Please note that in this study the terms SH and UH are defined with respect to the frequency of the transmitted ultrasound signal, not with respect to the resonance frequency of the UCA microbubbles.

In vitro measurements

A tissue mimicking phantom (TMP) was prepared according to the recipe of Teirlinck [285]. Two wall-less cylindrical cavities (5 mm in diameter) were created in two depths (center of the cylinders at 8 mm and 16 mm) by removing metallic rods from the TMP after the material solidified. The MicroMarker contrast agent (VisualSonics Inc., Toronto, ON, Canada) was reconstituted according to the manufacturer's instructions, resulting in a concentration of approximately $2{\cdot}10^9$ bubbles/mL, with a mean bubble diameter of 1.2 μm [151]. UCA suspensions in saline with three dilutions (1:500, 1:1,000 and 1:10,000) were prepared. The microbubble solutions were gently stirred with a magnetic stirrer to ensure a homogeneous distribution of the UCA, and then poured into the two cavities in the phantom while scanning. The ultrasound probe was mounted on the phantom in such a way that the center of the cylinder containing the UCA at a depth of 8 mm was at the focus of the transducer. We noticed there was no more than 2 dB change in the relative CTR at 16 mm depth when the focal depth was changed from 8 to 16 mm. Therefore, the focal point was kept at 8 mm depth throughout all experiments. Bursts with rectangular envelopes were transmitted with the following pulse sequences: AM, PI, PIAM and Bmode. The received echoes for each of the 108 combinations of pulse length (3), pressure (3), concentration of microbubbles (3), and pulse sequence (4), were recorded as IQ data. RF data were reconstructed from the IQ data of 10 consecutive frames (with a rate of 18 frames per second) and were analyzed off-line using MATLAB (Ver. R2012b, The MathWorks, Natick, MA, USA). The RF data were digitally band-pass filtered

around SH, UH and fundamental frequencies, with 5th order Butterworth filters designed in MATLAB. The -6 dB frequency cutoffs of the filters were set to: 14-16 MHz for SH imaging, 21.5-23.5 MHz for UH imaging and 21-23 MHz for NF imaging. Five identical rectangular regions of interest in the TMP and UCA (black boxes in Figure 1) were selected. From the band-pass filtered RF signals of the recorded 10 frames in the Fourier domain, mean echo powers and standard deviations were calculated for each region of interest and used to determine the CTR and the CAR according to equations 1, 2 and 3:

$$\text{CTR at 8 mm depth} = P_1/P_2 \quad (1)$$
$$\text{CTR at 16 mm depth} = P_5/P_4 \quad (2)$$
$$\text{CAR} = P_1/P_3 \quad (3)$$

where P_i is the mean echo power in the region i ϵ {1…5}. Figure 1 depicts the *in vitro* setup.

In vivo measurements

The best candidate combinations for nonlinear contrast imaging with the highest CTR and CAR *in vitro* were applied in an *in vivo* validation in three chicken embryos and in a kidney of a healthy adult mouse. Chicken embryo is an example of a superficial and weakly attenuating target whereas the mouse kidney represents a deeper target with higher attenuation (see supp. for details of preparation of these models).

Only SH and NF imaging are tested *in vivo*, since UH showed very low sensitivity. Real-time SH and 3D SH imaging were conducted with the PI sequence (see supp. for details of imaging method). This pulse sequence showed the maximum CTR *in vitro* at 8 mm depth (low attenuation), and therefore seemed a suitable method for contrast imaging in the chicken embryo model. The combination of NF imaging and AM sequence performed the best *in vitro* at 16 mm depth (high attenuation); therefore this was selected for contrast imaging in the mouse kidney model.

Results

In vitro

Figure 2 shows an example of SH, NF and UH phantom images as acquired with the four different pulse sequences (AM, PI, PIAM and Bmode) for the most representative combination of parameters. Figure 3 shows the CTRs and CARs for 8 mm and 16 mm depths for 10 cycle burst at 10 % transmit power, 1:1000 concentration of Micromarker. The dynamic range for all images was 50 dB and

they were all normalized to a single reference value (maximum gray scale value of the entire image set).

Subharmonic imaging

At 8mm depth, SH imaging performed much better than NF and UH. The SH images had the highest CTRs for 8 mm depth (blue bars in the first column of Figure 3). Among the SH images, the highest CTR (20 dB) was achieved with the PI sequence (Figure 3). The CTR for SH-PI-8mm generally increased by increasing the burst length at 4% and 10% transmit powers with the maximum increase of 12 dB (supp. table 5, (1) & (4)). Increasing the transmit power from 4% to 10% also generally increased the CTR for SH-PI-8mm. Such enhancement in the CTR due to the transmit power was maximum 7 dB (supp. table 8, (3) & (4)). However, further increase in the transmit power to 50% significantly decreased the CTR values (with a maximum drop of 18 dB (supp. table 5, (4) & (6))).

At 16 mm depth, CTR values for SH imaging were significantly lower for all the combinations. At 4% and 10% transmit power the CTR values were below 2dB for all the SH images. Increasing the transmit power to 50%, the CTR stayed below 2 dB for the SH images with the PI sequence.

Nonlinear fundamental imaging

At 16mm depth, NF was the best modality. The CTR of the NF images at 16 mm depth reached 10 dB with the AM and PIAM sequence and medium transmit power (4% and 10%) (supp. table 9, (3) & (4)). The CTR decreased up to 9 dB in the NF images at higher depth (16 mm) but this drop in the CTR was considerably less than that in the SH images. However, at 8 mm depth, the highest CTR in the NF images was 8 dB lower than the highest CTR achieved in the SH images. The CTR in the NF-AM-16mm images improved up to 5 dB by increasing the pulse length to 10 cycles (supp. table 9, (1) & (3)). Increasing the transmit power in such configuration did not improve the CTR more than 3 dB (supp. table 9, (2) & (3)).

Ultraharmonic imaging

UH imaging performed inferior to NF or SH in any combination in our experiments. At 8 mm depth, the highest CTR was 16 dB for UH images with PI sequence at 50% transmit power (supp. table 8, (5)). The CTR in UH images changed only marginally when the transmit power was increased from 4% to 10%. However, the CTR increased up to 9 dB when transmit power was further increased to 50% (supp. table 5, (2) & (3)). No relevant CTR (<4dB) was observed for the UH images at 16 mm depth even at the highest transmit power (50%).

Artifact suppression

SH imaging suppressed the far-wall artifact the most. The SH images in Figure 3

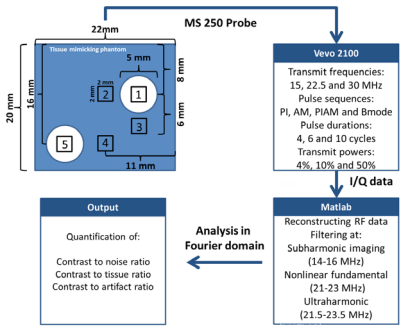

Figure 1
Experimental setup for the *in vitro* characterization. Acoustic echoes were received with the MS250 array transducer and the I/Q sampled signals were exported from the Vevo 2100 and processed off-line in MATLAB. Five regions of interest (black rectangular boxes) were selected in the ultrasound contrast agent and the tissue mimicking material for quantifying the contrast-to-tissue and contrast-to-artifact ratios.

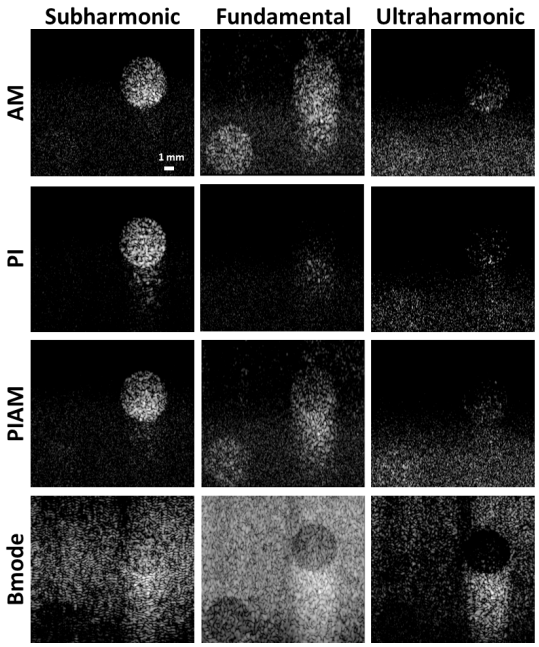

Figure 2
Example of the *in vitro* images for three nonlinear components (subharmonic, nonlinear fundamental and ultraharmonic) and four pulse sequences (amplitude modulation, pulse inversion, combination of pulse inversion and amplitude modulation and Bmode) (1:1000 MicroMarker, 10% power, 10 cycles).

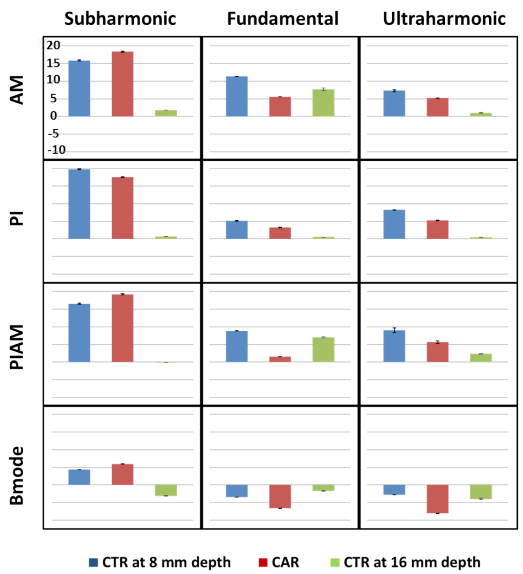

Figure 3
Contrast-to-tissue ratio at 8 and 16 mm depth and contrast-to-artifact ratio for three nonlinear components (subharmonic, nonlinear fundamental and ultraharmonic), and four pulse sequences (amplitude modulation, pulse inversion, combination of pulse inversion and amplitude modulation and Bmode). Error bars indicate the standard deviation. Transmit pressure was 10%, pulse duration was 10 cycles, and MicroMarker dilution was 1:1000.

Figure 4
Bmode and real-time SH images of a 6-day chicken embryo.
a and b: B-mode and subharmonic images before injecting ultrasound contrast agent,
c and d: B-mode and subharmonic images after injecting ultrasound contrast agent and applying a maximum intensity projection on 480 frames. (5µl MicroMarker, 10% power, 6 cycles).

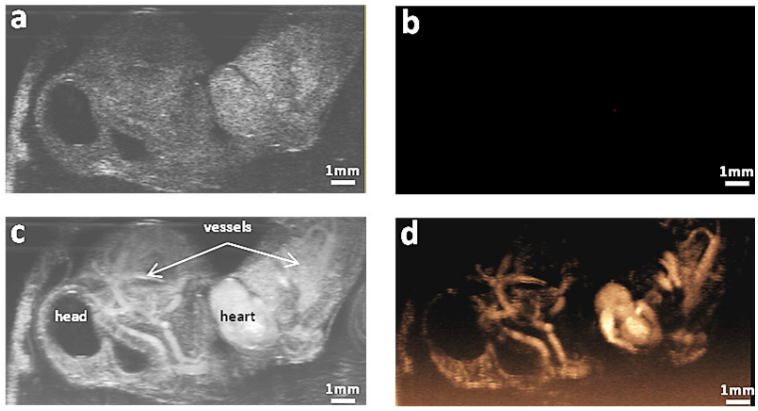

Figure 5
3D real time subharmonic image of heart and vasculature of an 8-day chicken embryo after MicroMarker ultrasound contrast agent administration taken by Vevo 2100 and MS250 probe using temporal filters and stepper motor. (5µl MicroMarker, 6-cycle, 30 MHz, rectangular envelope, ~300 kPa, rendered in Vevo 2100 3D Mode).

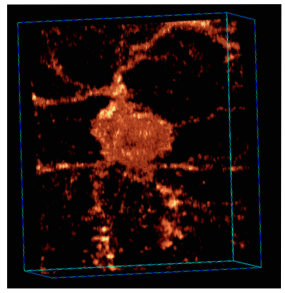

Figure 6
a: Optical image of a 10-day chicken embryo.
b: 3D subharmonic image of another 10-day chicken embryo after MicroMarker ultrasound contrast agent administration (5µl MicroMarker, 6-cycle, 40 MHz, rectangular envelope, ~300 kPa, rendered in Vevo 2100 3D Mode).

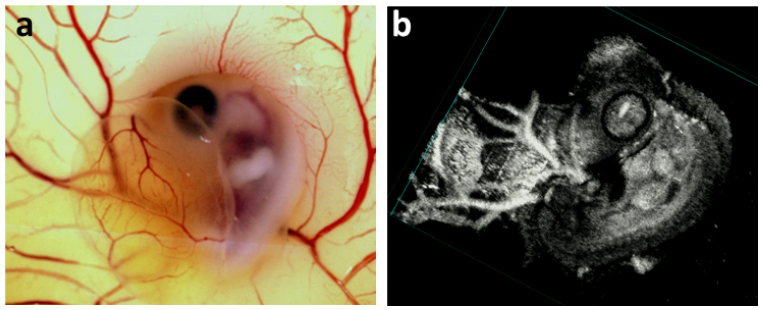

Figure 7
Bmode, subharmonic and nonlinear fundamental images of a mouse kidney.
a, b and c: B-mode, subharmonic and nonlinear fundamental images before injecting ultrasound contrast agent,
d, e and f: B-mode, subharmonic and nonlinear fundamental images after injecting ultrasound contrast agent (100µl MicroMarker, 10% power, 6 cycles).

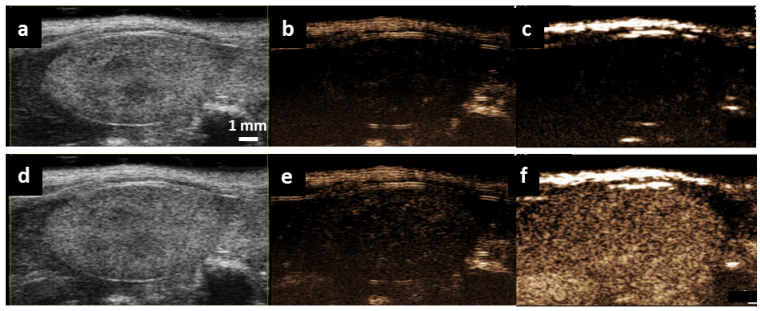

had up to 11 dB and 8 dB higher CAR values than the NF and UH images. The variation patterns of the CAR values with transmit power and excitation length followed the same trends as the CTR values (supp. table 4, 7 and 10). The CAR increased up to 9 dB for the SH-PI-8mm images when the concentration of the UCA was increased from 1:10,000 to 1:1,000 (supp. table 4, (1) and 7, (1)). No improvement in the CAR was observed when the concentration was further increased to 1:500 for this configuration.

In vivo

According to our *in vitro* results, SH-PI images had the highest CTR and CAR at 8 mm depth (low attenuation) and NF-AM images performed better at 16 mm depth (high attenuation). Based on these results a series of *in vivo* experiments on chicken embryo (low attenuation) and mouse models (high attenuation) were conducted.

Chicken embryo model – low attenuation

Figure 4 demonstrates real-time SH-PI *in vivo* imaging of a 6-day chicken embryo. Figure 4a and 4b show single frames in Bmode and SH-mode before injecting the UCA and panels 4c and 4d illustrate maximum intensity projection of 480 frames after injecting the UCA. In the Bmode image, signals from the tissues around the vessels and heart hinder a clear visualization of the UCA in the blood pool (Figure 4c), therefore reducing the sensitivity and specificity of quantitative and qualitative analysis. In the SH image the signals from the tissue are suppressed and only the UCA is visualized (Figure 4d). The trajectory of smaller vessels (about 100 μm in diameter) and the three chamber heart as well as perfused surrounding tissue are clearly visible in the SH image after injecting UCA.

3D subharmonic imaging

Figure 5 shows a 3D SH image of the heart and vasculature of an 8-day chicken embryo after MicroMarker UCA administration using the system's temporal filters. In the SH image, signals from the surrounding tissue have been canceled and only the microbubbles in the heart and vasculature around the heart are visualized.

As was suggested by Needles et al. [151], at even higher frequencies (> 24 MHz) SH imaging is preferred. In our study, an *in vivo* experiment was conducted in a 10-day chicken embryo using a higher frequency probe (MS 550s) with transmit frequency of 40 MHz. The temporal filters of the system were used for real-time SH imaging by filtering the received echoes in the Bmode configuration. 3D images were acquired after injection of 5 μL of MicroMarker (Figure 6b). The enhancement of the three chamber heart and the sub-millimeter vessels coming out of the heart can be appreciated.

Mouse model – high attenuation

Figure 7 shows a kidney of a mouse before and after injecting the UCA for conventional Bmode imaging, SH-PI imaging and NF-AM imaging. In the Bmode image the microbubble signals were lost in the tissue signals in the kidney (Figure 7d). The SH image before injecting the UCA (7b) had a good tissue cancellation within the kidney but the UCA is enhanced only minimally in the post-injection image (Figure 7e). The NF images have good tissue cancellation (Figure 7c) except for the top part of the image containing strong backscatter signals from the skin of the animal. The perfused kidney after injecting the UCA is very well visualized with NF-AM image (Figure 7f).

Discussion

In vitro

Comparing the CTR measurements at 8 mm depth and 16 mm depth in Figure 3 separately, revealed that the best candidate for nonlinear contrast imaging at low attenuation is SH-PI imaging and at high attenuation NF-AM imaging is the best. Figure 3 shows quantitative measures derived from the contrast images in Figure 2. In the following sections each image modality is discussed in detail and the effect of several imaging parameters is considered. The effect of UCA concentration and excitation pulse length on the discussed imaging modalities are discussed in the supplementary document.

Subharmonic imaging

This imaging mode provides the highest CTR and CAR at 8 mm depth (Figure 2 and 3). These factors reached their maximum with the PI sequence, long excitation (10 cycles) and low transmit power (4%). One reason for this strong SH response of the UCA even with 30 MHz excitation frequency could be the stimulation effect of the S-D signal at low transmit power. We have previously shown that a burst with rectangular envelope generates an S-D signal which enhances the SH response of the UCA [174]. Although the transmit frequency for SH images in this work (30 MHz) is higher than in the previous work (10 MHz), the S-D signal is still present and the stimulation effect is apparently effective in enhancement of the SH response of the UCA. It has been shown that the S-D signal is related to the second time derivative of the squared envelope of the excitation burst [262] [263]. Therefore, both excitation bursts in the PI sequence have an in-phase S-D signal, although the excitations at the fundamental frequency are in anti-phase. Such in-phase S-D signals in the two transmit bursts can in turn trigger an in-

phase SH response in the UCA. Consequently the SH response of the UCA in the received echoes is enhanced when summation is applied in the PI sequence. Also, the PI sequence removes the linear fundamental components in the received echo signals. The spectral leakage of the linear fundamental components into SH frequencies is one of the main causes of image degradation in SH imaging which can be prevented by applying the PI sequence [286]. Improved CTR of SH-PI imaging has also been reported by Needles et al. [151] at frequencies above 15 MHz. Furthermore, the narrow-band excitation (10 cycles) improves the isolation of the SH component in the frequency domain. These effects can contribute to the improved CTR and CAR with the PI sequence and long excitations.

At 16 mm depth, the CTR decreased significantly (18 dB, Figure 3) for the SH images. This is mainly due to the severe attenuation of the excitation bursts that propagate through the medium (supp. Figures 1, 2 and 3). Transmit signals for SH images were at 30 MHz, whereas transmit frequencies for NF and UH images were 22 MHz and 15 MHz. Attenuation of the acoustic wave in the tissue mimicking material is about 1dB per MHz per cm of propagation [287]. Therefore the amplitude of the excitation burst at 30 MHz used for SH imaging is 2.5 times (8 dB) more attenuated than the bursts used for NF imaging (22 MHz). This highly attenuated burst may not be capable of stimulating the SH response of the UCA at 16 mm depth, especially since the SH response of the UCA has a threshold behavior with regard to the excitation amplitude [137, 248]. Helfield et al. [6] reported the pressure threshold for SH generation to be 119 kPa at 25 MHz for majority of MicroMarker in a native population, and Sprague et al. [167] observed thresholds of 110 kPa at 30 MHz for bound, targeted MicroMarker.

SH-PI imaging was also demonstrated by Goertz et al. [288] with a 30 MHz intravascular ultrasound transducer, resulting in a CTR range of 10-15 dB. Their results are in very good agreement with what we observed *in vitro*, noticing that the image depth in their study was 1 to 6 mm (low depth). They also reported that at high frequencies the CTR decreases dramatically, as imaging depth and transmit pressure are increased. We argued that the reason for the decrease in CTR for SH imaging at higher depth is the severe attenuation of the excitation signal. Increasing the transmit power with the current system does not improve the CTR of the SH images at 16 mm depth because the amplitude of the low frequency ring-down and the S-D signals (around 15 MHz) increase significantly at higher transmit powers while the amplitude of the pressure wave at the fundamental frequency (30 MHz) stays low (around 100 kPa) (supp. Figure 3). The S-D and ring-down signals in the excitation burst have a component at around the SH frequency (15 MHz) which is backscattered by the tissue and degrades the CTR at high transmit powers for SH imaging. This undesired effect of the S-D and ring-down signal is discussed in more detail in the supplementary materials. Increasing the transmit power from 4% to 10% in our experiment increased

the CTR for SH images at 8 mm depth, indicating the SH response to be in the growth regime at such transmit pressures [271]. However the improvement in the CTR did not continue when the power was raised to 50% because of the discussed effects of the high-amplitude S-D signal and the ring-down signal of the transducer.
One solution to overcome such a limitation is to benefit from coded excitations as suggested by Shekhar et al [289]. Also, optimization of the envelope of the excitation bursts for less spectral leakage of the S-D signal into the SH frequencies, or the use of a transducer with broader bandwidth can improve the SH imaging at high frequencies. Unfortunately with the imaging platform used in this study such optimizations were not possible.
The CAR values were 12 dB higher in the SH images than in the NF images in Figure 3. This is due to the fact that the SH signal is produced only by the UCA and tissue does not exhibit any SH responses. Therefore, the SH imaging is free from the artifact produced by the nonlinear propagation of the acoustic wave through the UCA [290].

Nonlinear fundamental imaging
Our result suggests that with the current hardware used in this study, NF imaging is the only possibility for contrast imaging at 16 mm depth (Figure 3). The *in vitro* results showed that the CTR decreased only 3 dB between 8 at 16 mm depth for the NF-AM images. NF imaging is less affected by attenuation especially since there is no threshold behavior for the NF response of the UCA with regard to the excitation pressure amplitude.
The NF components of the UCA response were best extracted with the AM sequence, resulting in the highest CTR and lowest artifact compared with other pulse sequences. Increasing the excitation burst length at 16 mm depth enhanced the CTR and CAR values in NF images However; 14 dB CTR with the shortest excitation (supp. Table 8, (1)) suggests that 4-cycle bursts are appropriate for NF imaging providing the highest axial resolution.
The lower CTR of NF images at 8 mm depth (e.g. 8 dB in Figure 3) is because of severe nonlinear propagation and distortion at such high frequencies and high transmit power, especially when multi-pulse excitations with different amplitudes such as in the AM sequence are performed. Further reduction of the transmit power to avoid such a problem would also suffer from electronic limitations of the transmitting and receiving hardware such as imbalance in transistor end stages and diode offsets.

Ultraharmonic imaging
Our *in vitro* results showed 12 dB lower CTR for UH imaging than for the SH imaging (Figure 3). However, increasing the transmit power to 50% increased

the CTR up to 8 dB for the UH imaging while the CTR decreased for the SH and NF images. One reason for such enhancement in the CTR is the disruption of the UCA at such a high transmitted pressure (0.8 MPa) and lower excitation frequency (15 MHz) (MI of 0.2). Moreover, the low frequency components of the S-D and the ring-down signals in the transmit wave are absent or very weak at the UH frequency. Therefore, increasing the pressure will improve the CTR by increasing the amplitude of the UH response of the UCA with minimal increase of the tissue signal at UH frequency. The good performance of the UH imaging at high transmit power is in agreement with the result found by Maresca et al. [282] where high amplitude excitations were used (0.88 MPa). However, the CTR of UH imaging at low transmit pressure is much lower than for SH imaging, making UH less suitable for nondestructive nonlinear contrast imaging. Further investigation is required to fully understand the UH behavior of the UCA at high frequencies.

In vivo

Chicken embryo model – low attenuation

Using the temporal filters in the Vevo 2100 ultrasound system we were able to perform real time side-by-side Bmode and SH imaging. We also realized 3D SH imaging by mechanically moving the MS250 2D probe. The Bmode images give us the opportunity to assess the anatomical structure while the functionality of the cardiovascular system can be assessed in the real time SH images. Overlaying of the SH images on the anatomical Bmode images in real time can also be beneficial for more precise monitoring during experiments. Advantages of side-by-side Bmode and SH imaging in real-time and 3D SH imaging have been reported previously at lower frequencies (transmit frequencies of 2.5 MHz and 5.8 MHz) [271,291,292]. However, to the best of our knowledge, no such *in vivo* studies have been reported at frequencies above 15 MHz. Needles et al. [151] performed SH imaging *in vitro* at high frequencies but no *in vivo* results were reported due to the inconsistency between their *in vitro* and *in vivo* experiments. We showed that in superficial *in vivo* targets such as chicken embryo model SH-PI imaging is feasible at transmit frequencies of 30 MHz and 40 MHz.

The good performance of high frequency SH imaging for superficial targets allows us to introduce chicken embryo as a useful model for studying cardiovascular parameters and diseases. Ultrasound imaging of such a model has been reported before [293-295] but with a very poor image resolution and sensitivity. Moreover, to our knowledge there is no study showing the possibility of doing real-time nonlinear contrast imaging at high frequencies in this model. We showed that sensitive SH imaging can be performed in this model at frequencies up to 40 MHz, providing the opportunity of assessing anatomical structure and physiological functions of cardiovascular system of chicken embryo model (Figures

4, 5 and 6).

Mouse model – high attenuation

In vivo contrast images of mouse kidney (Figure 7) as a target with higher attenuation than the chicken embryo model are in agreement with our *in vitro* results. SH-PI imaging had a poor CTR in the kidney and the NF-AM image showed an excellent performance as a real-time high frequency contrast imaging mode for such *in vivo* conditions. The targets in the mouse model are deeper than in the chicken embryo model, but also the skin of the mouse reflects a large amount of excitation acoustic signal (bright layer in Figure 7). Therefore, the excitation signal experienced by the UCA deeper in the imaged area is considerably attenuated. This large attenuation of the transmitted signal reduces the SH response of the UCA. This attenuation effect is less challenging for NF imaging, as is seen in the NF images (Figure 7f).

Calculating the perfusion parameters from time intensity curves (TIC) in the SH and NF images (see supplementary material for details) showed that the NF imaging is more sensitive in the estimation of the relative blood volume in the kidney compared with the SH imaging. The relative blood volume is estimated from the peak intensity in the TIC, which can be estimated with more sensitivity by NF. This is in agreement with our *in vitro* results where we showed that the SH response of the UCA at 16 mm depth is weaker than the NF response. The measurement of blood velocity however is only dependent on the speed at which the UCA enters the imaging plane and independent of the concentration (intensity in the contrast image) [296]. The velocity measurements from the slope of the normalized TIC showed the same results for NF and SH images. This suggests that although SH imaging is less sensitive than NF, it can still be used for deriving perfusion parameters at high-depth.

Limitations

Our results in this study are derived with a particular ultrasound system, transducer and UCA type. Although we expect that the results are applicable more generally, this has to be confirmed. This study was explorative in nature, and investigated a large set of parameter combinations and circumstances to locate promising combinations. We could not explore certain promising parameter combinations (e.g. lower power levels) because of the practical limitations of the hardware. The respective findings should be further investigated in more detail, with a smaller number of interesting parameters, over a wider range. Also, the statistical value of the found differences can be improved by large-scale repetitions of the most important experiments. Because of the huge number of parameter combinations investigated (648) we had to severely limit the number of repetitions per experiment. Additionally, it should be further investigated how these results can be translated for *in vivo* applications. Future work should focus

on optimizing the imaging parameters *in vivo*, and on advancements in the technology of imaging systems, transducers and the UCA to improve on the results obtained here. Extrapolating the findings of this study to even higher frequencies should be done with more caution. For frequencies > 80 MHz, the microbubble radius can no longer be assumed to be small compared to the wavelength of the excitation wave. Therefore, the formulations for a multitude of well-known parameters used in the acoustics of UCA can no longer be trusted.

Practical implementations

Our results illustrate that with the most frequently used HFU platform for small animal imaging (Vevo 2100, MS250 probe), improvements in high-frequency UCA detection are achievable with the SH-PI combination for superficial targets and the NF-AM combination for deeper targets. Examples of *in vivo* images in chicken embryo and mouse models confirm the promise for nonlinear contrast imaging at high frequencies.

Further optimization of the pulse sequences and transducer response for SH-PI at higher transmit power and better implementation of the AM sequence at low transmit power for NF imaging can significantly improve the sensitivity of SH-PI and NF-AM for HFU contrast imaging.

We showed that the suppression of the far-wall artifact with SH-PI imaging (CAR of 17 dB in Figure 3) is an important feature of this imaging modality. Although, to the best of our knowledge, the effect of this artifact for HFU contrast imaging has not been reported, our *in vitro* results confirm the existence of the artifact especially for the NF imaging at high frequencies.

Length of the excitation bursts is directly affecting the axial resolution in the ultrasound images. Although long narrow-band excitations have higher CTR for SH and NF imaging, our results showed that the 6-cycle bursts for SH imaging and 4-cycle burst for NF imaging are good compromises between high CTR values (up to 19 dB and 14 dB) and high axial resolution both *in vitro* (supp. table 8, (1) & (2)) and *in vivo* (Figures 4, 5, 6 and 7).

Conclusion

In our *in vitro* results subharmonic imaging performed the best in media with low attenuation. Nonlinear fundamental imaging is a more suitable approach for deeper and more attenuating media. The largest contrast–to-tissue and contrast-to-artifact ratios for the subharmonic images are achieved when pulse inversion is applied and for the nonlinear fundamental images when amplitude modulation is used. To benefit from the advantages of the subharmonic signal as an imaging modality for deeper targets, hardware improvements will be needed.

Optimization of ultrasound contrast agent for high frequency ultrasound molecular imaging using subharmonic oscillation

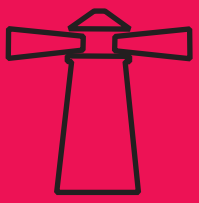

06

Abstract

Ultrasound molecular imaging visualizes disease biomarkers using targeted ultrasound contrast agents (tUCA). Different lipids result in UCA with different acoustic behavior. In this study, subharmonic (SH) response of MicroMarker UCA and four homemade UCA with different lipid coatings were compared *in vitro* with a high frequency ultrasound system (Vevo 2100 with MS250 probe). UCA with different size distribution were made with DSPC (UCA A and C) or DPPC (UCA B and D) as main lipid by sonication or Vialmix. We transmitted long bursts (20-cycle, 30 MHz, 10% power, MS250 probe) with pulse inversion sequence for optimized SH imaging. The effect of the UCA concentration on SH imaging was tested using two concentrations: 8.0×106 and 4.0×105 microbubbles per milliliter. For A, B and D type UCA, attenuation effect is dominant at high concentration. MicroMarker and C type UCA had the highest and most spatially homogeneous distribution of SH response throughout the entire UCA area at high concentration. SH amplitude of MicroMarker dropped about 11 dB when UCA concentration was reduced by a factor of 20. For this low concentration, SH amplitude of B type UCA was 10 dB higher than that for MicroMarker and was homogeneous throughout the UCA area. We showed that for 30 MHz transmit frequency, at low concentration of UCA, DPPC microbubbles have higher SH response than DSPC ones and at high concentration, smaller bubbles (MicroMarker and C) produced the most homogeneous SH responses. Our results suggest that for molecular imaging applications where UCA concentration is low, our B-type and MicroMarker UCA are suitable choices for SH imaging.

Based on a manuscript by **V. Daeichin**, K. Kooiman, I. Skachkov, J.G. Bosch, A.F.W. van der Steen, and N. de Jong, in Ultrasonic Symposium (IUS, IEEE), in 2014.

Introduction

Ultrasound molecular imaging featuring high sensitivity, availability, rapid execution of imaging protocols and relatively low cost [297] has shown its potential for imaging biological processes at the molecular level in both cardiology and radiology [150,298]. The key element in this technique is the use of ultrasound contrast agents (UCA) decorated with binding ligands such as antibodies or small peptides. These functionalized UCA, so called targeted microbubbles (tMBs), specifically bind to biomarkers expressed on the diseased endothelial cell membrane. Combined with dedicated ultrasound imaging sequences and the latest transducer technology, molecular ultrasound imaging allows quantitative assessment of molecular target expression with a high sensitivity [150].

MBs are effective ultrasound contrast agents with a rich resonance structure and inherently nonlinear behavior in response to a time varying pressure field. These nonlinear oscillators can generate higher and subharmonic oscillations. The nonlinear signals generated by the MBs are utilized in imaging techniques to separate the UCA from the surrounding tissue signals. Methods based on detection of higher harmonics are hindered by artifacts when the excitation frequency is high (> 15 MHz) [174]. Aside from the nonlinear propagation artifacts, higher harmonics undergo dramatic attenuation because of their high frequencies. Such a strong attenuation effect will limit the depth achieved in high frequency ultrasound imaging. High frequency ultrasound is required when higher resolution ultrasound images are needed (e.g. ophthalmology, intravascular coronary atherosclerosis and small animal imaging applications). On the other hand, subharmonic (SH) imaging is free from nonlinear propagation artifacts, is less attenuated and neither generated during propagation in tissue nor scattered by tissue. Moreover, methods have been proposed for selectively imaging bound tMBs from unbound ones for molecular applications based on the differences in the amplitude of their SH responses [167,168]. A SH signal can be achieved with minimum amplitude excitation if the driving frequency is twice the resonance frequency of the MB [167]. Such resonance behavior is inversely related to the diameter of the MB [167]. Therefore, manufacturing UCAs with smaller bubbles sizes can improve the sensitivity of SH imaging at high frequencies. Beside the size of the MBs, their shell properties and distribution of their microstructural lipid materials play a role in their SH behavior [6-8]. The coating of commercially available MBs mainly consists of either 1,2-distearoyl-sn-glycero-3-phosphocholine (DSPC) or 1,2-dipalmitoyl-sn-glycero-3-phosphocholine (DPPC). Using super-resolution microscopy, Kooiman et al. [8] recently reported that the lipid microstructure and

ligand distribution on the DPPC MBs are more homogeneous than those of the DSPC MBs. Such inhomogeneity in the shell microstructure seems to affect the nonlinear behavior of MBs such as their SH responses upon ultrasound sonication [6,7].

Using the most commonly used high frequency ultrasound imaging platform (Vevo 2100, VisualSonics Inc. Toronto, ON, Canada), previously we have optimized the imaging parameters for SH imaging at 30 MHz transmit frequency. In this study, similar settings were applied to compare the SH response of the widely used MicroMarker UCA (VisualSonics Inc.) and four homemade UCA with homogeneous and inhomogeneous distribution of lipid coatings and various size distributions in an *in vitro* setup.

Methods

Microbubble contrast agents preparation

UCA with a C_4F_{10} gas core were made with DSPC (P6517; Sigma-Aldrich, Zwijndrecht, the Netherlands) (MBs A and C) or DPPC (850355; Avanti Polar Lipids, Alabaster, AL, USA) (MBs B and D) as main lipid by sonication for 2 minutes as previously described [8,128] (MBs A and B) or Vialmix (MBs C and D). The coating of MBs A and B was composed of: 59.4 mol% of the main lipid; 35.7 mol% polyoxyethylene-40-stearate (PEG-40 stearate) (P3440; Sigma-Aldrich); 4.1 mol% 1,2-distearoyl-sn-glycero-3-phosphoethanolamine-N-carboxy(polyethylene glycol)-2000 (DSPE-PEG(2000)) (880125; Avanti Polar Lipids); and 0.8 mol% 1,2-distearoyl-sn-glycero-3-phosphoethanolamine-N-[biotinyl(polyethylene glycol)-2000] (DSPE-PEG(2000)-biotin) (880129; Avanti Polar Lipids). The coating of MBs C and D was composed of: 92.4 mol% of the main lipid; 6.4 mol% DSPE-PEG(2000); and 1.2 mol% DSPE-PEG(2000)-bioton.

Size distributions of the UCA were measured with a Coulter Counter (Multisizer 3, Beckman Coulter, Mijdrecht, The Netherlands). Measurements were repeated three times for each UCA and mean was calculated. MicroMarker UCA was prepared from the target-ready kit (VisualSonics Inc.) according to the manufacturer's recipe. These microbubbles consist of a phospholipid shell encapsulating a C_4F_{10}/N_2 gas core. They were obtained after reconstituting a lyophilisate cake with 1 mL of 0.9% sodium chloride saline, resulting in a concentration of approximately 2×109 MBs/mL, with a mean MB diameter of 0.8 μm.

A 10 mm diameter thin shell cylindrical tube made of polypropylene film backing coated with a water based acrylic adhesive (tesa® 4024 PV 2) having a total thickness of 52 μm was mounted in a water tank with its center at the focus of the imaging probe. The tube was filled with 15 ml satured PBS UCA dilutions

were pipetted in the tube and mixed gently using a magnetic stirrer in order to have a homogeneous suspension. The effect of the UCA concentration on SH imaging was tested using two concentrations: 8.0×106 and 4.0×105 MBs/mL, hereafter referred to as high and low concentration respectively. For each new UCA or dilution, the tube was washed with distilled, saturated water and placed in the same location in the water tank.

Imaging and quantification method

A high frequency pre-clinical ultrasound scanner was operated at 30 MHz, with a 256-element linear array transducer (Vevo 2100 with MS250 probe, VisualSonics Inc.). The used MS250 probe has a center frequency of 22.5 MHz and a -6dB two-way bandwidth of 70% (15-30 MHz) [151]. In order to benefit from the transducer's sensitivity both in transmission and reception, we selected a transmit frequency at the upper limit of the -6 dB bandwidth of the probe (30 MHz). Therefore, the received SH signal would be at the lowest limit of -6 dB bandwidth of the transducer (15 MHz).

The MS250 probe was run at 10% transmit power in the contrast mode (pulse inversion [151]) and wide beam-width setting was chosen in order to have a low uniform transmit pressure over depth in tissue (~400 kPa). For better separation of the SH component in the frequency domain, pulses with length of 20 cycles were transmitted. All measurements were made within 10 minutes of preparing the MB suspensions in the tube. The selection of the above SH imaging parameters such as transmit frequency and power, pulse sequence and length were based on the previous study in which these parameters were optimized for SH imaging [174].

RF signals were reconstructed from I/Q samples and appropriate post-processing of the RF signals was applied off-line, using MATLAB (2012b, The MathWorks, Natick, MA, USA). Three regions of interest (ROI) were selected within the UCA area: ROI 1 was placed before focus (15 mm); ROI 2 at focus (18 mm); and ROI 3 after focus (21 mm). 200 RF lines were averaged in the frequency domain for analysis of UCA responses at fundamental (30 MHz) and SH (15 MHz) frequencies within each ROI.

Guided by the FFT spectra, RF data were digitally band-pass filtered around SH frequencies, with a Butterworth filter of order 5 designed in MATLAB. We set the -6 dB frequency cutoff for the SH component to be in the range 13 MHz to 17 MHz. A schematic of our experimental setup is depicted in Figure 1.

Using the ultrasound simulation software Field II [299] the beam profile of the MS250 probe focused at 18 mm depth was simulated in axial direction with the following parameters: center frequency of 22.5 MHz, transmit F-number of 4, kerf of 10 μm, pitch of 90 μm, subdice of 10 μm, element length of 2.8 mm and PZT thickness of 75 μm. Figure 2 shows the result of the simulation. The locati-

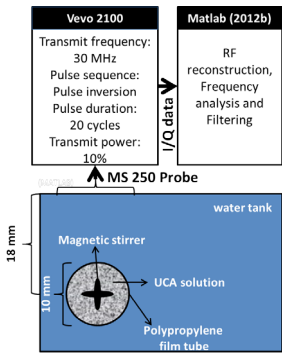

Figure 1
Experimental setup for the in vitro characterization of MicroMarker and four homemade ultrasound contrast agents. Acoustic echoes were received with the MS250 array transducer and the I/Q sampled signals were exported from the Vevo 2100 and processed off-line in MATLAB. Reconstructed RF signals were used for frequency analysis.

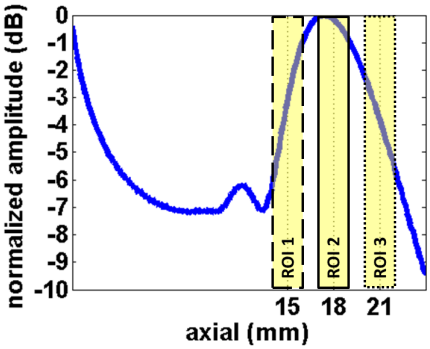

Figure 2
Axial pressure beam profile of MS250 probe with the ultrasound simulation software Field II. The locations of the three regions of interest (ROIs) within the microbubbles area in respect to the beam profile are highlighted.

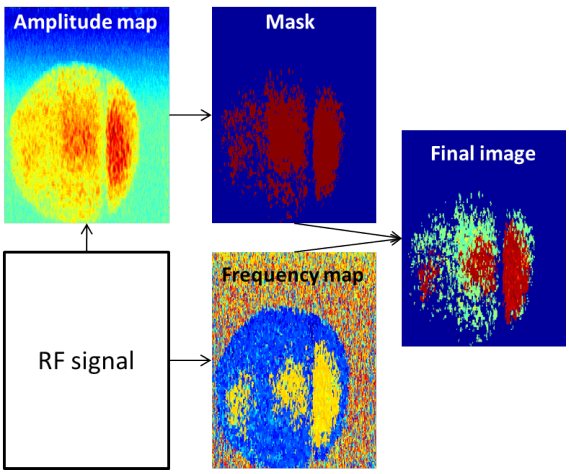

Figure 3
Different steps of our frequency based filter applied on the recorded RF signals.

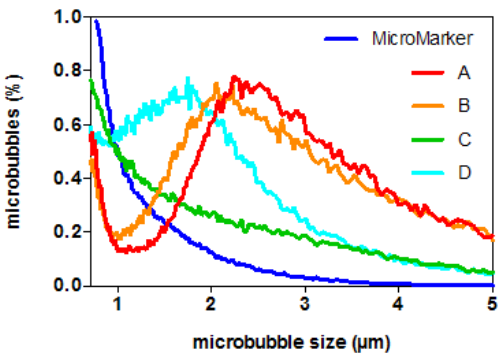

Figure 4
Size distribution of MicroMarker, A, B, C, and D UCA measured by Coulter Counter.

Figure 5
Subharmonic images of MicroMarker UCA and homemade A, B, C and D type UCA at high (8.0×106 microbubbles/mL) and low (4.0×105 microbubbles/mL) concentrations (top panel) and the corresponding spectra of each region of interest at three depths for each image (bottom panel).

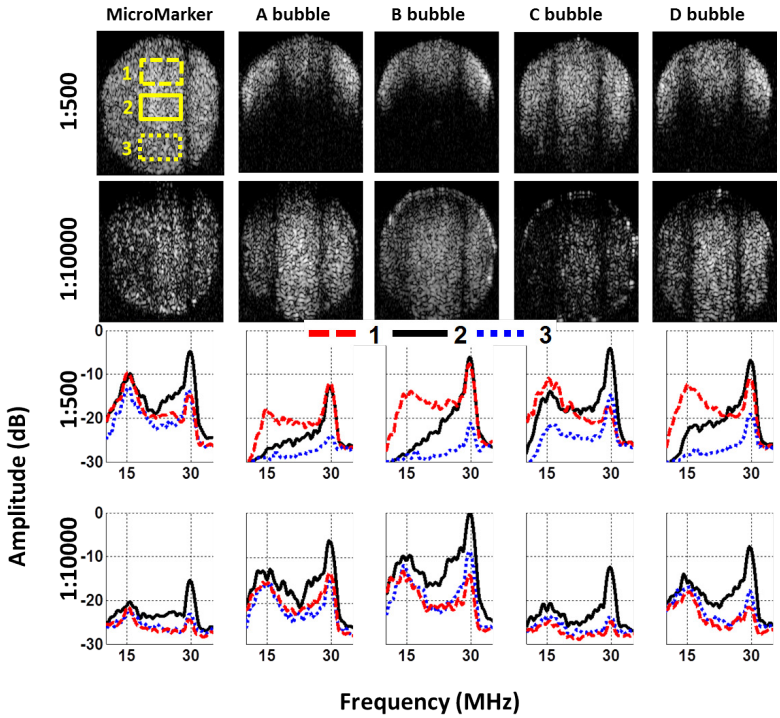

Figure 6
Frequency based filtered images of MicroMarker UCA and homemade A, B, C and D type UCA at high (8.0×10^6 microbubbles/mL) and low (4.0×10^5 microbubbles/mL) concentrations.

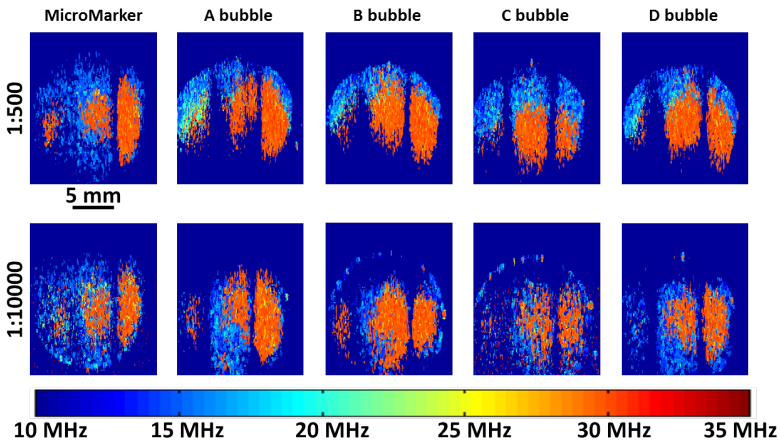

ons of the three ROIs with respect to the pressure distribution of the probe in the axial direction are highlighted on the simulated beam profile in Figure 2.
A dedicated frequency based filter was designed and implemented in order to detect the frequencies in which the microbubbles have their responses with maximum amplitude. Briefly, the design of the filter is as follows: first the back-scattered RF signals were partitioned applying a sliding window with a size of the length of the excitations bursts (~ 1mm for a 20-cycle burst at 30 MHz) and 70 percent overlapping between segments. Then the FFT spectra for each segment were computed. In the next step, two maps were created: one showing the maximum amplitude of the spectra of each partition, and another one showing frequencies for which the amplitude of the spectra was maximal. Then, the amplitude map was used to create a mask based on 70th percentile of the maximum amplitudes. This mask was applied on the frequency map to acquire the final frequency based images. Figure 3 shows the output of each of the mentioned steps and the final output image.

Results

Figure 4 shows the size distribution of all the five UCA used in this study measured by Coulter Counter. The MicroMarker UCA had the lowest mean diameters of 0.8 μm. The UCA made by the VialMix had a slightly higher mean diameter (C: 1.14 μm, and D: 1.47 μm). UCA made by sonication were the largest ones (A: 1.95 μm, B: 1.95 μm). Different main lipid component did not result in clear changes in the size distribution.
Images of the UCAs at high (dilution of 1:500) and low (1:10000) concentrations, filtered around their SH frequency (15 MHz), and the corresponding spectra for the three ROIs are presented in Figure 5. At high concentration, attenuation effect is dominant for A, B and D type UCAs, resulting in shadows deeper in the SH images. Such attenuation effect is also reflected in the corresponding spectra of these UCAs where the amplitude of the spectra at the SH frequency drops considerably for the deeper ROIs (number 2 and 3). MicroMarker and smaller size C-type UCA had the highest and most homogeneous SH response throughout the entire UCA area at high concentration. At low concentration of the UCA, the attenuation effect was less pronounced. The SH amplitude of MicroMarker dropped about 11 dB when UCA concentration was reduced by a factor of 20. Furthermore, SH amplitude of B type UCA at such low concentration was 10 dB higher than that for MicroMarker and was homogeneous throughout UCA area. In all the corresponding spectra of the UCA signals in both high and low concentration, the amplitude of the signal at the fundamental frequency (30 MHz)

was maximum at the focus of the transducer, where the acoustic energy is at its maximum (ROI number 2).
The output of our frequency analysis based on amplitude masking is presented in Figure 6. The dark blue background in the images is the result of masking. The hot color in the center of the tube, where the focus of the transducer is, indicates that the majority of MBs exhibited a strong response around the fundamental frequency (30 MHz). Conversely, away from the focal point the SH response is the dominant signal from the MBs. The shadowing effect due to the attenuation of the excitation burst through the UCA is also visible for the A, B and D type MBs at high concentration.

Discussion

To increase the sensitivity of high frequency ultrasound molecular imaging the optimization of imaging techniques and MBs design is required. Previously we have optimized the imaging parameters for high frequency SH imaging with Vevo 2100 and MS250 probe. Utilizing such parameters the role of MB design was investigated in this work.
Larger MBs (A, B and D) showed strong attenuating properties at high concentrations. The attenuation effect was more pronounced for the SH component than the responses at the fundamental frequency. This is perhaps due to the threshold behavior of SH oscillations [174]. The MBs at the lower part of the focal point may not have been excited with high enough pressure to undergo SH oscillation. However, when the concentration was decreased 20 times, the SH response of these larger MBs became stronger and more homogenous throughout the sample. The simulation of the MS250 beam profile showed that the excitation pressure at the ROI at the focus can be up to 2 times higher than that in the ROI 1 and 3. All of the MBs showed stronger fundamental than SH responses at the focus of the probe. However, this was otherwise outside the focal zone suggesting that moderate excitation pressure can be beneficial for SH imaging especially for molecular imaging applications where attenuation of the excitation wave through the MBs is not an issue since the concentration is very low.
Comparing the A and B bubbles with similar size distribution but different main lipid component showed that the DPPC B-type MBs are more nonlinear at both the fundamental and SH frequencies. At low concentration, the amplitude of the B-type MBs response at the fundamental and SH frequency was 6 and 3 dB higher than for the DSPC A-type MBs. Such behavior has also been reported by Van Rooij et al. [7] utilizing microbubble spectroscopy in the range of 1-4 MHz. MicroMarker UCA had the smallest size distribution in our study. Our results

suggest that MicroMarker is the most consistent of the UCA tested. The small size distribution of these MBs seems to play an important role in their nonlinear behavior particularly their SH response at high frequency excitation. The majority of the MBs have a diameter below 1.5 μm, corresponding to a resonance frequency around and higher than 15 MHz 300. It is conventionally thought that SH generation is achieved most readily (i.e., at lowest pressure threshold) when bubbles are excited at twice their resonant frequency [257]. This means that for the majority of the MicroMarker MBs, the 30 MHz excitation used in this study is around twice their resonance frequency. Such high amplitude SH response of MicroMarker UCA has also been reported by Helfield et al. [6], although that study was done on individual MBs in an acoustical setup.

In an *in vitro* setup, mimicking a practical imaging condition, we showed that both the microstructural lipid component of MBs as well as their size distribution have a considerable impact on their nonlinear behavior in particular their SH responses. We showed that for 30 MHz transmit frequency, at low concentration of UCA, DPPC bubbles have higher SH responses than DSPC ones and at high concentration, smaller bubbles (MicroMarker and C) produce the most homogeneous SH responses. The advantage of using homemade UCA is that the composition of the coating is known. For MBs A and B, we previously observed differences in lipid distribution [8]. The lipid DPPC has a lower elastic compressibility modulus than DSPC [301,302], which may be related to SH behavior as our DPPC MBs showed more SH than did our DSPC MBs. Unfortunately, the coating composition of MicroMarker MBs is unknown, so we do not know how our homemade MBs resemble MicroMarker in composition.

Conclusion

Our results suggest that for molecular imaging applications where UCA concentration is low, our DPPC microbubbles produced by sonication (B-type) and MicroMarker UCA are suitable choices for SH imaging

Quantification of bound microbubbles in ultrasound molecular imaging

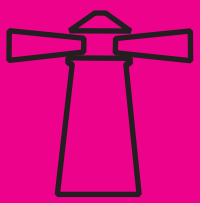

07

Abstract

Molecular markers associated with diseases can be visualized and quantified noninvasively with targeted ultrasound contrast agent (tUCA) consisting of microbubbles (MBs) that can bind to specific molecular targets. Techniques used for quantifying tUCA assume that all unbound MBs are taken out of the blood pool few minutes after injection and only MBs bound to the molecular markers remain. However, differences in physiology, diseases, and experimental conditions can increase longevity of unbound MBs. In such conditions, unbound MBs will falsely be quantified as bound MBs. We have developed a novel technique to distinguish and classify bound from unbound MB. In the post-processing steps, first tissue motion was compensated using block matching (BM) techniques. To preserve only stationary contrast signals, a minimum intensity projection (MinIP) or 20th percentile intensity projection (PerIP) was applied. The MinIP or PerIP after-flash was subtracted from MinIP or PerIP before-flash. This way, tissue artifacts in contrast images were suppressed. In the next step, bound MB candidates were detected. Finally detected objects were tracked to classify the candidates as unbound or bound MBs based on their displacement. This technique was validated *in vitro* followed by two *in vivo* experiments in mice. Tumors (n=2) and salivary glands of hypercholesterolemic mice (n=8) were imaged using a Vevo 2100 scanner. Boluses of 100 μL of MicroMarker tUCA targeted to angiogenesis markers and untargeted control UCA were injected separately. Our results show considerable reduction in misclassification of unbound MBs as bound ones. Using our method, the ratio of bound MBs in salivary gland for images with targeted UCA vs. control UCA was improved up to two times compared to unprocessed images.

Based on a manuscript by **V. Daeichin**, Z. Akkus, I. Skachkov, K. Kooiman, A. Needles, J. Sluimer, M.J.A.P. Daemen, A. F.W. van der Steen Fellow, N. de Jong, and J.G. Bosch., in IEEE Trans Ultrason Ferroelectr Freq Control, in press.

Introduction

Molecular imaging with ultrasound using targeted ultrasound contrast agents (tUCA) is a valuable tool that is being used increasingly for noninvasive quantification of angiogenesis [150]. Angiogenesis is known to be an essential marker of tumor growth and metastasis [303]. Various biomarkers associated with angiogenesis can be detected and quantified with different techniques such as positron emission tomography [304], magnetic resonance imaging [305], computed tomography [306], optical imaging [307], and ultrasonography using tUCA [308]. Molecular imaging using tUCA is a compelling imaging technique, as it allows real-time monitoring of anatomy and functionality and it is inexpensive and portable [308]. This technique has been applied to characterize atherosclerosis [309], thrombosis [310], neovasculature [182,310], lymph nodes [311], as well as inflammation [312,313]. Also, ultrasound molecular imaging has been proven to be highly sensitive to the identification of molecular structures or expression when using tUCA; thus, it provides helpful insights into genesis, progression and prevention of diseases [201,250,314-316].
The most widely utilized methods for contrast ultrasound molecular imaging encompass injection of tUCA followed by a waiting time (up to 10 minutes) to allow binding to targets and clearance of unbound microbubbles (u-MBs) from the blood. Consecutively, a combination of ultrasound imaging sequences and a high power burst (flash) are applied, where the flash is used to destroy all MBs in the imaging plane. The intensity difference before and after the flash corresponds to the amount of bound MBs (b-MBs) which is a measure for molecular signals (we call it “classical approach” in this manuscript) [182-185]. In such methods the quantification of b-MBs is strongly dependent on the injected tUCA dose, imaging system gain, local perfusion [9] and the physiology and the state of the animal. However in many conditions such as presence of tissue motion, high concentration of freely recirculating u-MBs after the waiting period, limited number of recorded frames, low frame rates and small region of interest (ROI), such classical methods will not result in reliable quantification of b-MBs. Moreover, as these techniques are strongly dependent on imaging system settings, comparison between different studies performed with different imaging settings are not yet possible.
We have developed a new quantification method which benefits from motion compensation and individual contrast spot detection, and is capable of distinguishing the b-MB from u-MB based on their displacement. Our quantification method can be applied in studies performed with different imaging settings because it is less sensitive to imaging parameters. Moreover, it is more robust to tissue motion artifacts.

A high frequency pre-clinical ultrasound scanner was operated at 18 MHz, with a 256-element linear array transducer (Vevo 2100 with MS250 probe, VisualSonics Inc., Toronto, ON, Canada). The used MS250 probe has a center frequency of 22.5 MHz and a -6dB two-way bandwidth of 70% (15-30 MHz) [151]. The transducer operated at 10% transmit power (~400 kPa at the focus of the probe, MI of 0.1) in the contrast mode and wide beam-width setting was chosen in order to have a low, uniform transmit pressure over depth. Side-by-side Bmode and nonlinear contrast mode images were acquired with a frame rate of 30 to 40 frames per second. Nonlinear fundamental imaging with amplitude modulation [151] was used for the contrast images. Lossless DICOM (Digital Imaging and Communications in Medicine) images were exported to MATLAB for further processing.

Imaging protocol

Figure 1a schematically shows a time sequence for molecular imaging in mice. After injecting the tUCA a waiting time of about 10 minutes is required for u-MBs to be taken out of the blood circulation by lungs and liver. Also this waiting period gives more time for the tMBs to find the binding sites, thus increasing the number of tMBs attached to the desired biomarker. After the 10 minutes waiting period, a series of about 300 frames (~10 seconds) was acquired with high power bursts in the middle to disrupt all MBs in the imaging plane. A schematic representation of a typical time intensity curve in the ROI is shown in Figure 1b for two separate UCA injections (tUCA in blue and non-targeted (control) UCA in red). Shortly after injecting the UCA, the intensity of contrast in the ROI increases rapidly, reaching a maximum and followed by a slow decay of intensity for both tUCA and control UCA (c-UCA). However, because of the binding of the tMBs to the targeted biomarkers in the ROI, the level of intensity, 10 minutes after the injection, will be higher for tUCA than for c-UCA. Ideally, 10 minutes after injecting c-UCA, image intensity in the ROI should fall back to the baseline level (similar to the level before injection) and there should be no difference in image intensity before and after the flash pulse. On the other hand, there will be a difference in the intensity levels for tUCA before and after the flash due to the b-MBs, which is a measure of the molecular signals in the ROI. Unfortunately, such an ideal situation will not always happen and even 10 minutes after injection there will be recirculating u-MBs for both tUCA and c-UCA injections. Therefore the actual difference in the intensity of the pre- and post-flash frames depends on the amount of both b-MBs and u-MBs the ROI. The increase in the intensity after the flash is also showing the presence of recirculating u-MBs.

Quantification method

Subsets of the images captured 10 minutes after injecting the UCA were used for quantification of the b-MB in the ROI. The flowchart in Figure 2 shows the steps of our quantification method.

Correction for tissue motion in the imaging plane was the first step of our technique. Akkus et al. [317] have developed an algorithm for tracking tissue motion for local contrast quantification using multidimensional dynamic programming (MDP) [318] combined with apodized block matching (BM). This technique was adapted for the features of our DICOM images such as pixel size and intensity range and applied to the acquired images. The motion pattern of tissue in the ROI was extracted from B-mode images and applied to the contrast images to correct the motion of the ROI. In BM, a 60x40 (lateral x axial) pixels (2.4x1.6 mm) fixed template derived from the chosen B-mode image was scanned over a 60x20 (lateral x axial) pixels (2.4x0.8 mm) search field. Then normalized correlation coefficients (NCC) for each 2D displacement in each frame were used to construct a 3D block of cost values. MDP was used to find the optimal 2D tissue displacement path over time (the connective path in the time direction that had the highest sum of NCC values).

The noise levels in each data set were obtained by drawing a ROI in the background of a contrast frame immediately after the flash pulse and calculating the mean intensity value (μ) and standard deviation (σ) in the ROI. Then all image intensities below a noise threshold level of $\mu+4\times\sigma$ were set to zero. In the next step, the motion-compensated contrast mode frames were separated into two groups: pre-flash and post-flash groups. To show the effect of the number of frames on our quantification method, two subsets of images were chosen: a subset of 20 frames as the short sequence (10 frames each from pre- and post-flash groups); and a subset of 100 frames as the long sequence (50 frames each from pre- and post-flash groups). Next, a minimum intensity projection was applied on all the frames of each pre- and post-flash group resulting in a single MinIP image for each of these groups. The MinIP technique will collect per pixel the minimum intensity throughout all frames. This way the signal of non-stationary contrast spots will be minimized, since for each pixel the intensity will be low at some time point. Then each of the single pre- and post-flash MinIP images were smoothened using a 2D Gaussian filter of 3x3 pixels with sigma=1 to remove background noise (e.g. electronic noise). Objects smaller than the characteristic bubble size are removed with this filter. Because the MinIP step is a very radical step for removing the moving contrast spots, which might also erroneously remove b-MBs, an alternative intensity projection step based on the 20th percentile

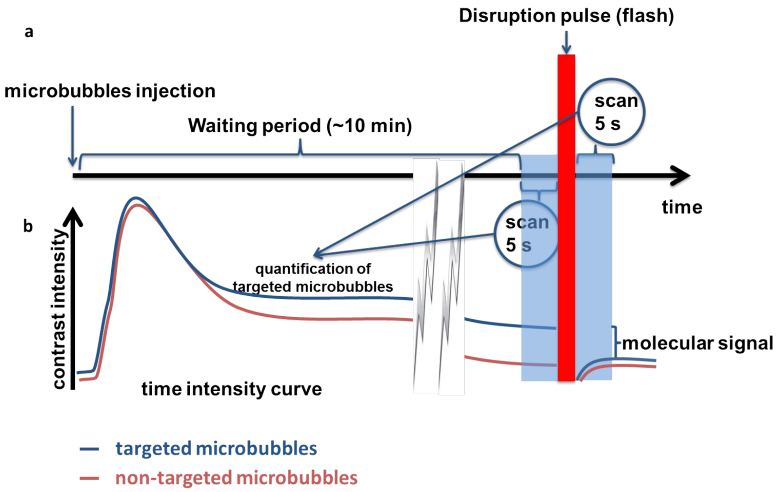

Figure 1
a) Timeline of the imaging protocol. b) Schematic representation of a typical time intensity curve in the region of interest (e.g. salivary gland) corresponding to the timeline (intensity level for targeted microbubbles is slightly shifted from non-targeted (control) microbubbles for better illustration).

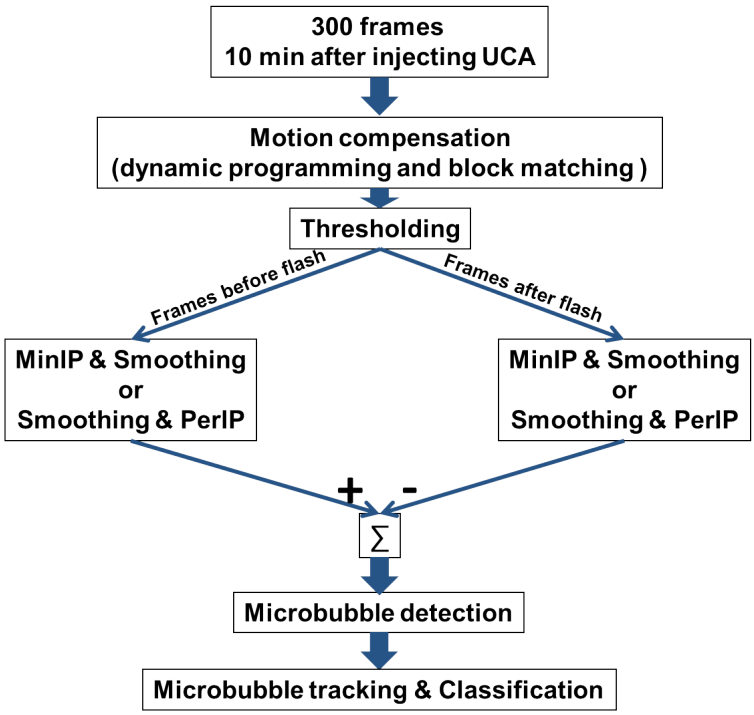

Figure 2
Flowchart showing the steps of our technique for the quantification and classification of bound targeted microbubbles.

Figure 3
In vitro validation experiment:
a) Bmode image.
b) MinIP of pre-flash Bmode frames (10 frames).
c) MinIP of post-flash Bmode frames (10 frames).
d) their subtracted image.

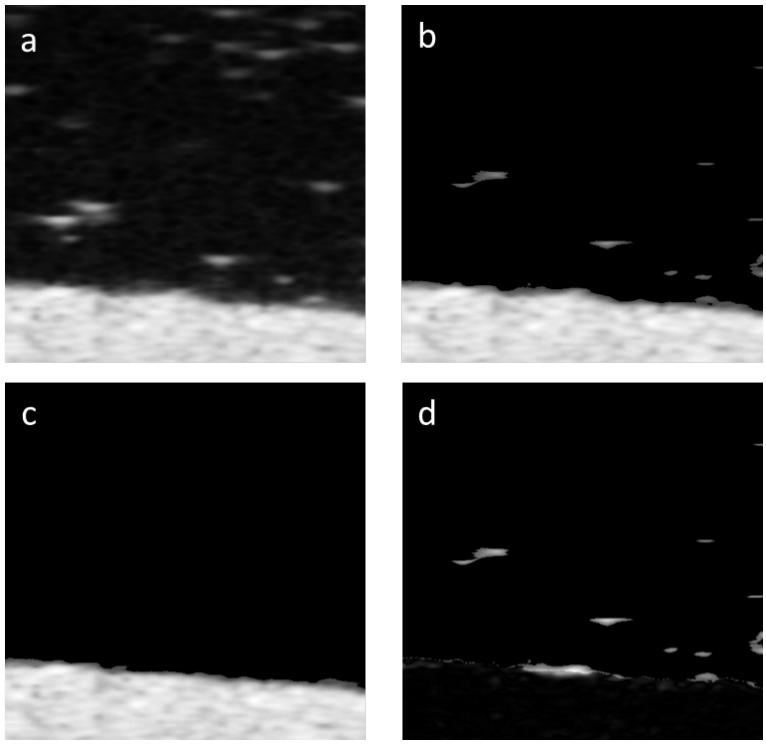

Figure 4
Subtracted images after applying MinIP on a) the short sequence c) the long sequence and after PerIP on b) the short sequence and d) the long sequence. In Figure 4a and 4b, detected microbubbles are overlaid as red dots and pointed out with white arrows and stationary microbubbles as yellow circles. Extra detected microbubbles in Figure 4b are numbered.

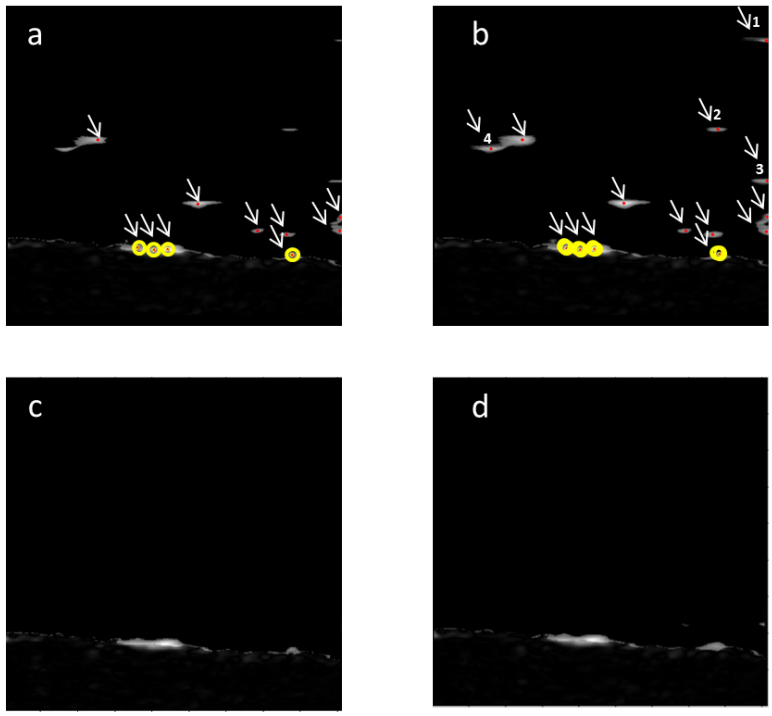

of the intensity distribution per pixel over time (PerIP) was also applied instead of MinIP. The PerIP is more forgiving towards short intensity variations or out-of-plane motion effects. The frames were smoothened using the same 2D Gaussian filter before applying the PerIP. The resulting post-flash MinIP or PerIP images were subtracted from the pre-flash counterpart to reduce stationary artifacts and remaining tissue signal.
In the subtracted MinIP or PerIP images, individual contrast spots were detected using artificial bubble templates [319]. The templates mimic size and intensity pattern of contrast spots. Several radii (3, 5, and 7 pixels) of artificial bubbles were used for detection of different sizes of contrast spots. Each artificial template was scanned over the chosen ROI and normalized cross correlation coefficients were calculated. In the resulting correlation coefficient matrix, the maximal correlation was located. After that, the correlation values in a 10x10 pixel-neighborhood around this location were set to zero. This was iteratively performed until the maximal correlation value was below 0.6, which is the threshold for a contrast spot to be considered as a bubble.
Ideally, after the above processing steps, what should remain is the signal from the bound, stationary MBs that were destroyed by the flash. However, because of the low frame rate, the limited number of frames and also the high concentration of recirculating MBs, in some cases there will still be some u-MBs in the resulting image. Therefore further processing is required to classify the true b-MB from such u-MB. This was done by tracking all the detected MBs in the subset of 10 frames (short sequence) or 50 frames (long sequence) in the pre-flash image set. The tracking algorithm was based on MDP combined with BM as is described in [317,319]. All the detected MBs with displacement less than 3 pixels (~ 60 μm) were classified as stationary or b-MBs and the rest were discarded as u-MB.
In the classical approach, pre- and post-flash frames were averaged and subtracted from each other. Then the total intensity in the subtracted image was calculated for a ROI and normalized to the area of the ROI. The results of the classical approach were compared with the results of our quantification method *in vivo*, using the same ROI in the subtracted MinIP and PerIP images.

In vitro experiment

An *in vitro* experiment was conducted to validate the ability of the MinIP and PerIP in reducing the u-MBs and also the classification step based on the single contrast spot detection and tracking. A thin layer (5 mm) of tissue mimicking material (TMM) was prepared according to the recipe of Teirlinck et al. [285]. Target-ready UCA were prepared from MicroMarker kit (VisualSonics Inc. Toronto, Canada) according the manufacturer's recipe. The TMM was placed at the bottom of a water tank filled with degassed water and a low concentration of Micro-

Marker was injected above the top of the material. The imaging probe (MS250) was mounted 17 mm above the phantom and the focal zone was set at the top of the phantom. Then side-by-side B-mode and contrast mode images of MBs being pushed towards the phantom due to the radiation force were acquired. The imaging settings and acquisition protocol were similar to those used *in vivo*.

In vivo experiment

UCA were prepared as described for the *in vitro* experiment. MBs were targeted with biotinylated scVEGF (SibTech, Brookfield, CT, USA) or with biotinylated antibodies against $\alpha_v\beta_3$-integrin (BD Biosciences, San Jose, CA, USA) for making tUCA. Inactive forms of biotinylated scVEGF (SibTech) and biotinylated IgG(κ) (BD Biosciences) were used for making the c-UCA.

First, well-vascularized subcutaneous Huh7 tumors with numerous targeting sites were imaged in which classical method shows good differences for targeted and control injections. Our method was compared to the classical method and validated in this model. Secondly, salivary glands as a model with weaker molecular signals were analyzed as a test of our method.

For the first experiment at Erasmus Medical Center, male NMRI nu/nu mice of 8 weeks old (n=2) were purchased from Charles River Laboratories (Margate, UK) and fed ad libitum. Animals were kept under 2% isoflurane anesthesia and $5*10^6$ Huh7 cells, a human hepatocellular carcinoma cell line, were injected in total volume of 100 µL in the right hind limb. When the tumor size reached 8 mm animals were anesthetized with 2% isoflurane and placed on the Vevo Rail System heating stage (VisualSonics Inc. Toronto, Canada) and ultrasound imaging was performed. First, a bolus of 100 µL of control MicroMarker UCA was injected and 20 minutes after the first injection a bolus of 100 µL of tUCA was injected via a tail vein catheter, with a flush of 0.9% saline after both injections. The injections were done using a programmable syringe pump (11 Pico Plus Elite, Harvard Apparatus, Kent, UK) with a rate of 600 µL per minute.

The second experiment was conducted at Maastricht University on hypercholesterolemic male ApoE knockout mice (n=8) on a C57/Bl6 background from an in-house breeding colony (originally from Iffa Credo, Lyon, France) and fed chow till the age of 50 weeks. Mice were anesthetized with ketamine (0.1 g/kg) and xylazine (0.02 g/kg) by subcutaneous injection and peri-operative ibuprofen (s.c). Animals were intubated and artificially ventilated using room air at the rate of 160 strokes per minute. The left jugular vein was exposed, and a heat-stretched polyethylene-25 cannula was inserted (1.5 cm) and subcutaneously guided to the neck of the mouse. Here the catheter was fixed, extended, filled with heparinized saline (10 U/ml), and plugged. The rest of the experimental procedure was similar to the previous animals except that the UCA injections were done via the jugular vein cannula and the order of the injections was randomized in these animals. The right salivary gland was chosen as a target for this study, as

it contains abundant neovascularization which expresses biomarkers to which our tUCA could bind.
All animal work was approved by the regulatory authorities of Erasmus Medical Center and Maastricht University and performed in compliance with the Dutch government regulations.

Results

In vitro experiments

Figure 3a shows a single frame of a B-mode recording of a layer of TMM (bright layer in the bottom of the image) and MBs floating above, in degassed water (bright spots floating in the dark background) . Because of the radiation force of the ultrasound, MBs were pushed towards the bottom, against the TMM layer. The MBs which were at the TMM layer from the beginning were not moving during the recorded frames, and therefore could be considered as stationary MBs. The MinIP images of the pre- and post- flash frames and their subtracted image for the short sequence (20 frames) are also shown in Figure 3b to 3d. In Figure 3d the stationary tissue signal was suppressed since it was present in both pre- and post-flash frames while the signals from the MBs were preserved in the subtraction step since they were destroyed by the flash and were not present in the post-flash frames.
MinIp and PerIP images were applied on short and long sequences and the results are depicted in Figure 4. Some floating MBs were still preserved in both the MinIP and PerIP images when the short sequences were used (Figure 4a and 4b) with a few more MBs in the PerIP image. However when the long sequences were used all the floating MBs were suppressed in both the MinIP and PerIP images and only those stationary MBs just above the TMM layer were preserved (Figure 4c and 4d).
The MB detection and tracking steps were applied on images of Figure 4a and 4b. All the detected MBs in the images were overlaid as red dots and pointed out with white arrows in Figure 4a and 4b. All such detected contrast spots were tracked over all pre-flash frames in the short sequence (10 frames) and those with total motion less than 3 pixels were classified as stationary MBs and overlaid as yellow circles on these Figures.
Four extra MBs were detected in the PerIP image (numbered from 1 to 4 in Figure 4b) compared with the MinIP image. However, after tracking all the MBs

and accepting only those which were moving less than 3 pixels (yellow circles in Figure 4a and 4b), the same four stationary MBs were detected in both images.

In vivo experiments

The motion compensation step is crucial *in vivo* especially when fast moving targets such as plaques in carotid artery walls are imaged. Figure 5 shows the result of our motion tracking for a point on the upper wall of the right common carotid of a mouse in radial (Figure 5a) and longitudinal (Figure 5b) directions.

Our motion compensation method provides motion detection with a smallest step of 0.1 pixel. In general, it is more difficult to follow the longitudinal motion of the vessel as the speckle pattern of the wall tissue is very similar along the longitudinal direction. The error seen in Figure 5b which looks like a quantization error is possibly caused by a shadow artifact in the image, hindering the tracking beyond a certain point.

Figure 6 shows the result of our experiment on two tumors in B-mode (Figure 6a and 6d) and contrast mode 10 minutes after injecting tUCA (Figure 6b and 6e) and c-UCA (Figure 6c and 6f). In both tumors an enhanced intensity can be seen for the tUCA (Figure 6b and 6e) compared to the c-UCA (Figure 6c and 6f). Our quantification method and the classical approach were performed on the dataset of these two tumors and the results are presented in Figure 7. In both cases there are many b-MBs in the tumor for the targeted group and the difference between the targeted and control group is visible with the most commonly used classical approach. This confirms that our new method also gives good results in a situation with a high concentration of MBs and is similar to the classical method. The intensities obtained from the subtracted PerIP were less sensitive to the number of frames used in the analysis. The intensity in the subtracted MinIP image for the long sequence was about three times lower than for the short sequence. After tracking and classifying the detected MBs in both the subtracted MinIP and PerIP images the number of detected b-MBs are shown in Figure 7b and 7d. These results were in very good agreement with what we visually saw in these tumors and also with the results of the classical method.

For the second *in vivo* experiment on salivary glands, 7 mice out of 8 showed successful targeting. The intensities within the salivary glands for these 7 mice were quantified using the classical method for the tUCA and c-UCA injections. Also the numbers of detected b-MBs using our method were calculated for these two injections for the short sequences. The ratio of intensities and the ratio of number of b-MBs in the targeted group over the control group for these 7 mice are presented as boxplots in Figure 9. The boxplots in Figure 9 show that with the classical quantification approach shows there is not a big difference between the targeted and control injections. In contrast, our technique, which detects the

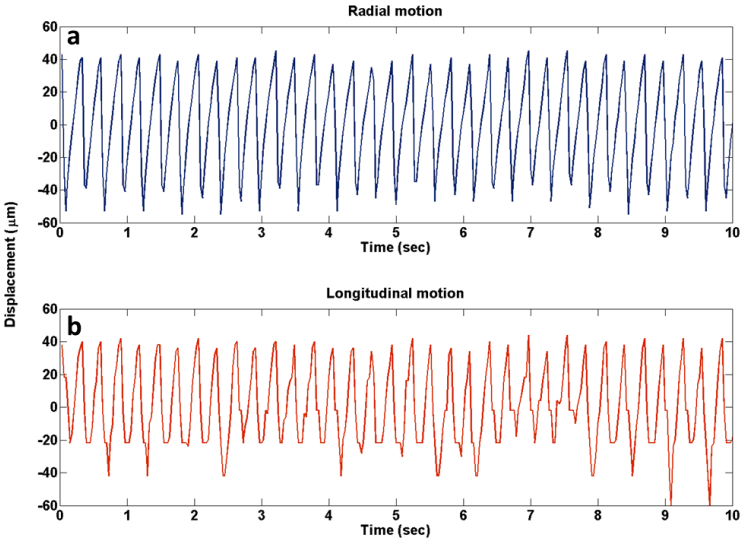

Figure 5
Displacement of upper wall of right common carotid in radial (a) and longitudinal (b) directions in a mouse using automated motion tracking.

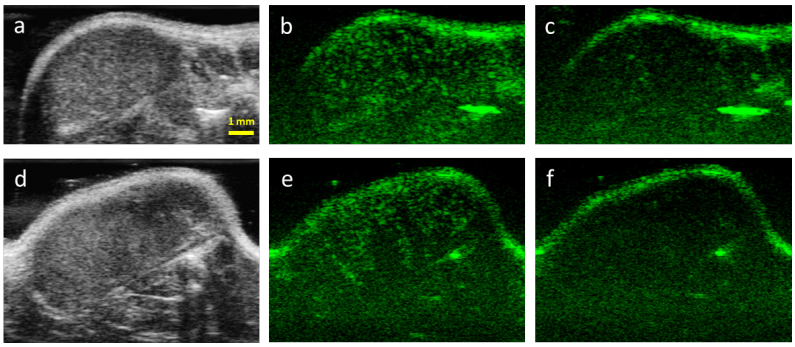

Figure 6
B-mode (a and d) and contrast mode (b-f) ultrasound single frame images of two subcutaneous Huh7 liver tumors in two different mice (a, b and c: tumor 1, d, e and f: tumor 2). b and e: contrast mode images 10 minutes after injecting the targeted microbubbles. c and f: contrast mode image 10 minutes after injecting the control microbubbles.

Figure 7
Comparison of bound microbubbles quantifications on two tumors (a and b: tumor 1, c and d tumor 2). Differences of pre- and post-flash image intensities in two tumors according to the classical subtraction method compared with differences of image intensities after applying minimum intensity projection (MinIP) and alternative intensity projection based on 20th percentile of the intensity distribution per pixel over time (PerIP) (a and c) and number of detected bound microbubbles after performing our method on short and long sequences (b and d).

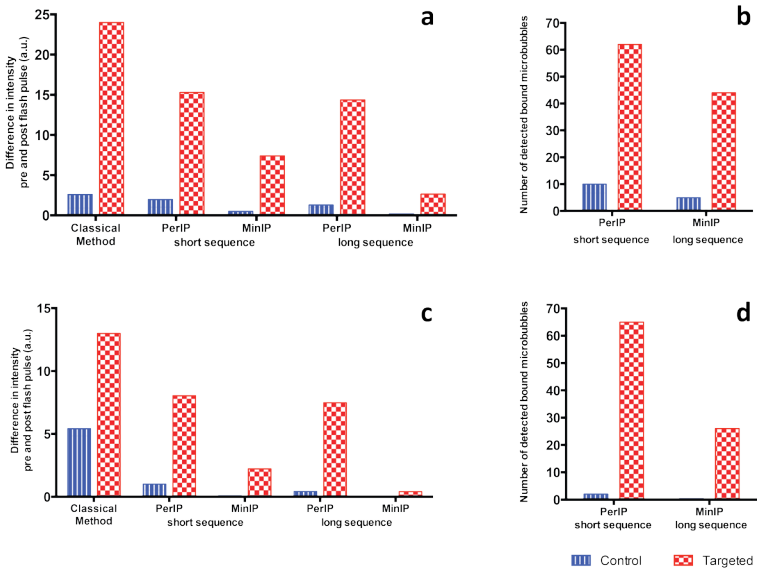

Figure 8
B-mode (a) and contrast mode (b-d) ultrasound images of right salivary gland and right carotid including the bifurcation of an ApoE -/-, 50 weeks old mouse. b: the contrast mode before injecting the UCA, c, d: single frame unprocessed images 10 minutes after injecting targeted (c) and control (d) microbubbles and their corresponding processed images for salivary gland by MinIP (e,g) and PerIP (f,h). All the bright spots in the e-h images are contrast signals.

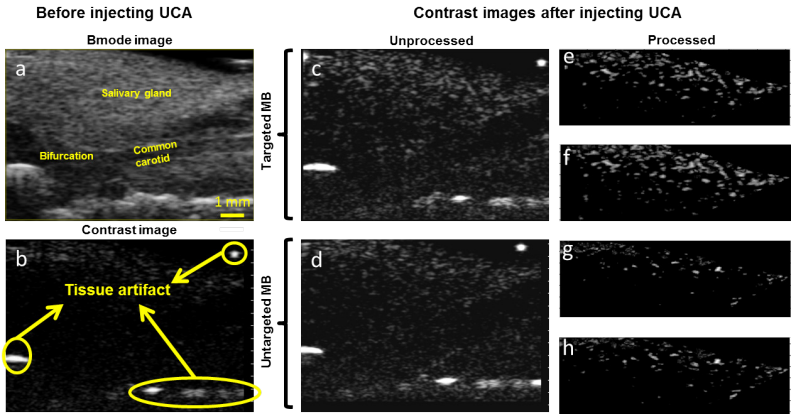

Figure 9 Ratio of image intensities and ratio of number of detected bound microbubbles in targeted UCA injection vs. control injection in the salivary gland of 7 mice.

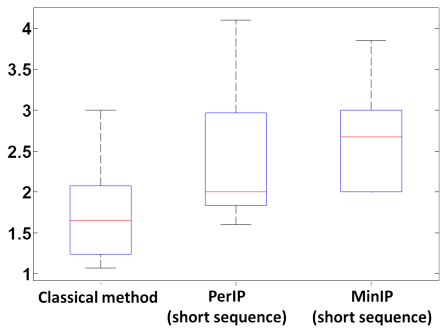

number of b-MBs, clearly enhances the difference between these two injections. Also, a higher mean ratio in these 7 animals was observed when the MinIP is used compared with when PerIP is used.

Discussion

We have developed a method which detects single contrast spots and classifies them into bound and unbound MBs based on their displacement in the recorded frames. The processing steps such as motion compensation and MinIP or PerIP assure that artifacts due to the motion of the ROI are minimized and only the stationary contrast spots are enhanced. In an *in vitro* setup we showed that applying the MinIP or PerIP is sufficient to discard the u-MBs in the image if the recorded sequences are long enough (50 frames for each pre- and post-flash group). However, due to the limited number of recorded frames, limited frame rate, motion artifacts, complex *in vivo* conditions and variations in the concentration of remaining u-MBs in animals, the MB detection, tracking and classification steps will be beneficial *in vivo* (Figures 6 to 9). Additionally, quantification of the molecular signals as number of b-MBs instead of image intensities is less dependent of imaging settings and therefore more valuable for comparison and longitudinal studies.

The PerIP step was tested as an alternative to MinIP, since in the MinIP contrast spots will be disqualified even if they disappear in a single frame of the sequence, e.g. due to out-of-plane motion. 20^{th} percentile was chosen to deal with heartbeat-related motion, where we have about 10 frames per heartbeat. 20^{th} percentile assures that the contrast spots, which might disappear in one or two frames per cardiac cycle, will be still preserved after the PerIP step. Although with PerIP instead of MinIP more u-MBs may be preserved in case of low number of frames or slow moving MBs (MBs labeled with 1 to 4 in Figure 4b), the MB detection and tracking steps are able to distinguish them from truly stationary MBs.

Although our quantification method successfully detected and tracked the MBs *in vitro*, it needed to be validated in a more complex *in vivo* condition. Therefore, the *in vivo* experiments on the murine tumor model were conducted (n=2) (Figure 6). In this model, the results of our method showed very good agreement with visual evaluation of the images and the classical approach (Figure 7). Intensities in the subtracted MinIP and PerIP images for short and long sequences showed significant differences for the targeted and control injections in these subjects. As expected, PerIP was less sensitive to the length of the analyzed sequences. However, when MinIP was applied, in the longer sequence more contrast spots were missed in the images due to out-of-plane motion. Therefore, for our quan-

tification method with the MinIP step short sequences are more suitable. And in the case of long sequences the PerIP step performed better than the MinIP step. Although gated acquisition (e.g. ECG) can be applied in applications with more severe out-of-plane motion, it can introduce errors in tracking contrast spots due to lower frame rate. These *in vivo* experiments showed that our quantification method is specific to the b-MBs in a complex *in vivo* environment.

The right salivary glands of 8 mice were scanned in the second *in vivo* experiment to test our method. Being right above the pulsating carotid, this target moves more than the tumor model. Quantification of the b-MBs with the classical approach in such a model is more difficult than the tumor model because of: larger motion artifacts, less binding of the tMBs and more recirculating leftover MBs 10 minutes after injection. However, using our quantification method, sensitivity of the molecular imaging with tMBs was improved for such a target (Figures 8 and 9). The ratio of the intensity and number of detected b-MBs in targeted injections vs. the control injections were presented in Figure 9 for 7 out of 8 scanned animals. One animal was discarded from the analysis because b-MBs were higher in the control injection than in the targeted injection (perhaps due to some leftover tUCA in the injection tubes from the first injection). The result of our quantification method in this *in vivo* model for both the MinIP and PerIP approaches show higher ratios of targeted over control injection than the classical approach. Applying the MB detection and tracking steps on the subtracted MinIP images showed the highest average ratio for the targeted injection vs. the control injection although the absolute number of b-MBs was the highest when PerIP was applied. This is due to the fact that there are more b-MBs missed by the MinIP step than by the PerIP. Therefore the number of detected bound MBs in the control injection will also be lower when MinIP is applied. Since the number of b-MBs in the control injection is often very few, a small change can increase such a ratio of detected MBs. This implies that the PerIP approach might be a better option for general applications.

There have been some studies proposing methods for selectively imaging the b-MBs in real time: utilizing an image-push-image sequence [9]; transmission at a low frequency and reception at a high frequency [10]; using subharmonic response of the MBs and interframe filtering [11]; using singular value spectra properties [12]. However, none of the proposed methods in mentioned publications have been applied in a complex *in vivo* condition. Only Pysz et al. on developed a quantification method based on dwell time MB signal measurements which was tested *in vivo* in well vascularized tumors in mice [190]. In such *in vivo* model where attachment of tMBs is significant, the classical way of quantification also performs well. Thus, the performance of the method developed by Pysz et al. in applications with very few tMBs in presence of circulating MBs remains unclear. Our quantification method on the other hand has shown reliable detection of

molecular signals *in vivo* in cases with many as well as very few b-MBs, although it is an offline image processing method. Moreover counting the b-MBs instead of reporting a sum of image intensities in the ROI, implies that the result does not need to be adjusted for imaging parameters such as gain, dynamic range, attenuation, etc. This gives the opportunity of comparing studies done with different ultrasound systems. Motion compensation, contrast detection and tracking steps of our method have been validated previously [317,319]. However, the falsely detected and missed b-MBs in more complex *in vivo* conditions needs to be quantified more accurately than visual validation.

Our quantification methods have been validated for high frequency ultrasound. Although high frequency ultrasound has its limitation in clinical application due to the limited penetration depth, we believe our technique can also be applied on images acquired at lower frequencies since individual MBs can be imaged at frequencies as low as 7 MHz [128]. Another concern for the application of tUCA in human is the waiting time for freely floating MBs. The major factor to consider is therefore the half-life of MBs in the bloodstream. Definity and SonoVue, both commercially available contrast agents for human use, have a half-life of ~ 6 minutes [321,322] which is similar to that in mice (~ 7 minutes [323]). If targeted microbubbles based on these contrast agents have a similar half-life, a waiting time of 10 minutes would be sufficient.

Conclusion

A dedicated targeted ultrasound contrast agent quantification method has been eveloped to reliably detect individual contrast spots and classify them into bound and unbound microbubbles *in vitro* and *in vivo*. Because of the pre-processing steps such as motion compensation, minimum intensity projection and 20th percentile intensity projection, this technique should be more reliable and robust in different experimental conditions.

Quantification of endothelial $\alpha_v\beta_3$ expression with high frequency ultrasound and targeted microbubbles

08

Abstract

Angiogenesis is a critical feature of plaque development in atherosclerosis and might play a key role in both the initiation and later rupture of plaques. The precursory molecular or cellular events that initiate plaque growth and that ultimately contribute to plaque instability, however, cannot be detected directly with any current diagnostic modality. This study is designed to investigate the feasibility for molecular imaging of endothelial $\alpha_v\beta_3$ expression *in vitro* and *in vivo* using the $\alpha_v\beta_3$-targeted ultrasound contrast agents (UCA). In the *in vitro* study, $\alpha_v\beta_3$ expression were confirmed by Western blotting in murine SVEC cells and tracked by using the targeted UCA and further imaged under ultrasound imaging system at 18 MHz transmit frequency. In the *in vivo* study, expression of endothelial $\alpha_v\beta_3$ integrins in murine carotid artery vessels and salivary gland were quantified using targeted UCA and high-frequency ultrasound in 7 animals. Our results showed that endothelial $\alpha_v\beta_3$ expression was significantly higher in the carotid wall artery containing atherosclerosis lesions compared with parts without any lesions. We also showed that the salivary gland can be used as an internal positive control for successful binding of targeted UCA to $\alpha_v\beta_3$ integrin. In conclusion, $\alpha_v\beta_3$-targeted UCA allows noninvasive assessment of the expression levels of $\alpha_v\beta_3$ on the vascular endothelium and may provide potential insights into early atherosclerotic plaque detection and treatment monitoring.

Based on a manuscript by **V. Daeichin**, I. Skachkov, K. Kooiman, J. C. Sluimer, A. Janssen, B. Janssen, J.G. Bosch, N. de Jong, M.J.A.P. Daemen, A. F.W. van der Steen., in preparation.

Introduction

Ultrasound molecular imaging featuring high sensitivity, availability, rapid execution of imaging protocols and the relatively low cost [297] has shown its promising potentials for imaging biological processes at the molecular level. The key element in this technique compared with regular diagnostic ultrasound imaging is the ultrasound contrast agents (UCA) decorated with binding ligands such as antibodies or small peptides. These functionalized UCA, so called targeted microbubbles (tMB), recognize receptor proteins involved in various disease processes. Combined with dedicated ultrasound imaging sequences and the latest transducer technology, ultrasound molecular imaging allows quantitative assessment of molecular target expression with a high sensitivity. The mentioned features of this technique open new applications including arteriosclerosis [309], thrombosis [324], neovasculature [182,310] lymph nodes [311], inflammations [312,313], as well as providing helpful insights into genesis, progress and prevention of diseases [201,250,314,315,325].

Atherosclerosis is characterized by accumulation of lipids, inflammatory cells, and connective tissue within the arterial wall. A number of pathophysiological mechanisms are thought to be involved in the progression of an atherosclerotic lesion into a vulnerable plaque [326]. Intraplaque neovascularization and vasa vasorum have gained interest as a preceding or associated factor in the development, progression, and instability of atherosclerotic plaques [25-27]. The presence of intraplaque vasa vasorum has been identified as an independent predictor of intraplaque hemorrhage and plaque rupture [327,328]. The intraplaque vasa vasorum are therefore increasingly investigated as a marker for the noninvasive identification of vulnerable plaques. It has been shown that along with angiogenic activities in the atherosclerosis plaques, $\alpha_v\beta_3$ integrins are expressed in the adventitial and intraplaque vasa vasorum [28-31]. Therefore, $\alpha_v\beta_3$ is an appropriate receptor for targeted ultrasound imaging where adhesion of tMBs to endothelial cells provides the signal enhancement. This molecular marker has been used for ultrasound molecular imaging of angiogenesis in tumors and hind limb ischemia [23,310]. Although, mural $\alpha_v\beta_3$ integrin expression has been quantified ex-vivo using near-infrared optical imaging in mice [329] and *in vivo* with magnetic resonance imaging in rabbits [330] and positron emission tomography in mice [331], to the best of our knowledge, no successful *in vivo* ultrasound molecular imaging of plaque vasa vasorum with such an intgring has been reported.

Here, we provide *in vitro* and *in vivo* proof-of-concept for molecular imaging of $\alpha_v\beta_3$ in carotid artery lesions and expanded vasa vasorum neovessels in in ani-

mal models of atherosclerosis in apolipoprotein E-deficient (ApoE$^{-/-}$) mice. We hypothesized that molecular imaging of $\alpha_v\beta_3$ integrin with tMB could be used to quantify the vasa vasorum neovessels in atherosclerosis plaques. To test our hypothesis, attachment of $\alpha_v\beta_3$ targeted MicroMarker UCA to endothelial SVEC cells was evaluated *in vitro*. Attachment of the tMBs *in vivo* and signal enhancement of the carotid plaques were assessed in ApoE$^{-/-}$ mice.

Methods

A high frequency pre-clinical ultrasound scanner, with a 256-element linear array transducer (Vevo 2100 with MS250 probe, VisualSonics Inc., Toronto, ON, Canada) was operated at 18 MHz. The transducer was operated at 10% transmit power and wide beam-width setting was chosen in order to have a low, uniform transmit pressure over depth (~400 kPa, MI of 0.1). Side-by-side Bmode and nonlinear contrast mode (amplitude modulation[151]) images were acquired with a frame rate of 20 frames per second. UCA were prepared from Target-Ready Vevo MicroMarker UCA (VisualSonics Inc. Toronto, Canada) according the manufacturer's instruction. MBs were targeted with biotinylated antibodies against $\alpha_v\beta_3$ integrin (BD Biosciences, San Jose, CA, USA) for making tMB. Inactive form of biotinylated IgG(κ) (BD Biosciences) were used for making control microbubbles (cMB).

In vitro

The murine SV40 virus modified endothelial cells (SVEC) were purchase from ATCC (LGC Standards, Wesel, Germany) and cultured in Dulbecco's Modified Eagle Medium/Ham's F-12 (Gibco, Life Technologies Europe, Bleiswijk, the Netherlands) with 1% penicillin-streptomycin solution (1% v/v penicillin-streptomycin solution containing 5000 units penicillin (Gibco) and 5 mg streptomycin (Gibco) per mL) and 10% of heat-inactivated fetal calf serum (Gibco) in a humidified atmosphere of 5% CO_2 at 37°C. The cells were cultured in the acoustically transparent OptiCell (NUNC, Wiesbaden, Germany) chambers until confluence before passage number 5. To determine $\alpha_v\beta_3$ expression the fluorescent staining was done. The cells were fixated in 4% formaldehyde for 5 min and blocked in 5% BSA in PBS solution for 1 h. After the fixation the 1×1 cm pieces of the OptiCell membrane containing cells were cut out. Then the specimens were incubated with rat anti-mouse antibody against $\alpha_v\beta_3$ integrin (BD Biosciences) for 1.5 h and after being thoroughly washed were incubated with goat anti-rat antibody conjugated with AlexaFluor $\alpha_v\beta_3$ (Invitrogen, Groningen, the Netherlands) for 1h. All procedures were done at room temperature. After incubation the specimens

were washed with PBS and embedded in Mowiol (Sigma-Aldrich, Zwijndrecht, the Netherlands), with Hoechst 33342 (Invitrogen; 5 µg/ml) to stain the cell nuclei. The fluorescent microscopy was done with Olympus microscope equipped with AxioCam MRc camera (Carl Zeiss B.V., Sliedrecht, the Netherlands), and 40× water-immersed objective (LUMPlanFI, NA 0.8, Olympus).
To access the adhesion of microbubbles to SVEC cells the cells were cultured as previously described 30 µl of tMB or cMB, made as stated above, were added to the cells. Then the OptiCell was turned upside down to let microbubbles adhere to the cells by flotation. Then the chamber was incubated at 37°C for 5 min. After incubation the OptiCell was again turned upside down and incubated for 5 min at 37°C to let all MB which are not adhered to the cells to float to the top membrane of the OptiCell chamber. The bright field microscopy was done with the Olympus microscope equipped with the heating stage. For each specimen 20 random fields of view were acquired for both MB adhered to cells on the bottom and free MB on the top of the OptiCell. The ratio of the adhered UCA to the total adhered plus free floating UCA was calculated and presented as percentage of attached MBs.
For ultrasound imaging of MB adhered to SVEC cells, the cells were incubated with MB as described above, and then the upper membrane of the OptiCell was cut out. Cells were washed with 37°C fresh warm media and placed in the tank filled with PBS, where the temperature was maintained at 37°C. Then, the MS250 probe was positioned on top of the OptiCell in the axial direction of the ultrasound beam. To prevent the overwhelming specular reflection from the OptiCell to washout the scattering signal from the sample under examination received by the US transducer, the OptiCell were placed tilted at 20 degrees angle with respect to the bottom of the water tank, thus, specular reflected US signals from the OptiCell could not reach the US transducer [325]. In addition to the 2D images, 3D Bmode and nonlinear contrast mode images were acquired by mounting the probe on a linear stepper motor (VisualSonics Inc., Toronto, ON, Canada). The probe was translated over ~4.9 mm, while acquiring frames every 0.032 mm. The series of images were then rendered in 3D using the Vevo 2100 3D Mode software (VisualSonics Inc., Toronto, ON, Canada).

In vivo

Hypercholesterolemic male ApoE knockout mice (n=7) on a C57/Bl6 background from an in-house breeding colony (originally from Iffa Credo, Lyon, France) and fed chow till the age of 50 weeks. Mice were anesthetized with ketamine (0.1 g/kg) and xylazine (0.02 g/kg) by subcutaneous injection and pre-operative ibuprofen (s.c). Animals were intubated and artificially ventilated using room air at the rate of 160 strokes per minute. The left jugular vein was exposed, and a heat-stretched polyethylene-25 cannula was inserted (1.5 cm) and subcutaneously

guided to the neck of the mice. Here the catheters were fixed, extended, filled with heparinized saline (10 U/ml), and plugged. Animals were placed on the Vevo Rail System heating stage (VisualSonics Inc. Toronto, Canada) and ultrasound imaging was performed. For each animal cMBs and tMBs (100 µL each) were injected with 20 minutes time in between each injection using a programmable syringe pump (11 Pico Plus Elite, Harvard Apparatus, Kent, UK) with a rate of 600 µL per minute. The focus of the transducer was set at 7 mm where the upper wall of the common carotid laid. In the field of view the right common carotid artery and its bifurcation was visible. In the imaging field, on the top of the right carotid the right salivary gland was located. Bmode gain was 20 dB and contrast gain was 30 dB. DICOM (Digital Imaging and Communications in Medicine) images were exported to MATLAB (Ver. R2012b, The MathWorks, Natick, MA, USA) for further off-line processing.

After injecting the UCA a waiting time of about 10 minutes is required for MBs to be taken out of the blood circulation by lungs and liver. Also this waiting period gives more time for the tMBs to find the binding sites, thus increasing the number of tMBs attached to the $\alpha_v\beta_3$ integrin. After the 10 minutes waiting period, a series of about 300 frames (~10 seconds) was acquired with high-intensity ultrasound bursts (flash) in the middle to disrupt the MBs in the imaging plane. Shortly after injecting the UCA, the intensity of contrast in the ROI increases rapidly, reaching a maximum and followed by a slow decay of intensity for both tMBs and cMBs. However, because of the binding of the tMBs to the $\alpha_v\beta_3$ integrin, the level of intensity, 10 minutes after the injection, will be higher for tMBs than for cMBs. Ideally, 10 minutes after injecting cMB, image intensity in the region of interest (ROI) should fall back to the baseline level (similar to the level before injection) and there should be no difference in image intensity before and after the flash pulse. On the other hand, there will be a difference in the intensity levels for tMB before and after the flash due to the destruction of bound tMBs, which is a measure of the molecular signals in the ROI. Unfortunately, such an ideal situation will not always happen and even 10 minutes after injection there will be recirculating unbound UCA for both tMBs and cMBs injections. Therefore the actual difference in the intensity of the pre- and post-flash frames depends on the amount of both bound and unbound UCA in the ROI. The increase in the intensity after the flash is also an indication of the presence of recirculating UCA.

Molecular signal quantification method

Subsets of the images (100 frames) captured 10 minutes after injecting the UCA

were used for quantification of the bound MBs in the ROI around the carotid plaques, healthy part of the carotid artery and in the salivary glands. The captured frames with a flash in the middle to destroy the MBs in the imaging plane were separated into two groups: pre-flash and post-flash groups (50 frames each from pre- and post-flash groups). The noise levels in each data set were obtained by drawing a ROI in the background of a contrast frame immediately after the flash pulse and calculating the mean intensity value (μ) and standard deviation (σ) in the ROI. Then all image intensities below a noise threshold level of $\mu+4\times\sigma$ were set to zero. Next, averaging was applied on all the frames of each pre- and post-flash group resulting in a single mean image for each of these groups. The averaging will emphasize the signal of stationary contrast spots. Then each of the single pre- and post-flash mean images were smoothened using a 2D Gaussian filter of 3x3 pixels with sigma=1 to remove objects smaller than the characteristic bubble size. The resulting post-flash mean images were subtracted from the pre-flash counterpart to reduce signals of non-stationary contrast spots, stationary artifacts and remaining tissue signal. In the subtracted mean images, mean intensity within each ROI were calculated and presented as molecular signals.

Immunohistochemistry

At sacrifice blood was drawn from the right ventricular apexes. Subsequently the mice were gently perfusion fixed via the left cardiac ventricles with sodium nitroprusside (0.1mg/ml; Sigma-Aldrich, Seelze, Germany), followed by 1% paraformaldehyde (PFA). The right carotid arteries and salivary glands were excised, fixed in 1% PFA for 24 hours, and paraffin-embedded. The right carotid arteries and salivary glands were serially sectioned (4 μm), and stained at 20 μm intervals with Hematoxylin and Eosin (HE, Sigma-Aldrich) for microscopical examinations. Serial sections were stained with the rat anti-mouse MAC3, a macrophage marker to show the deposition of macrophages in the lesions. Blood vessels were stained with CD31 primary antibody

Statistical evaluation

Statistical analysis for integrin expression and attachment number of MBs with cells was performed using unpaired t-test. *In vivo*, quantified molecular signal based on video intensity of contrast-enhanced sonograms of processed images in 7 animals was analyzed using paired t-test and presented as mean ± standard error of mean ($p < 0.01$ were considered to show significant).

Results

In vitro

To examine binding affinity of UCA, $\alpha_v\beta_3$-tMBs or cMBs were incubated with SVEC cells. Results showed there was significantly higher (3.7 times, $p < 0.0001$) attachment of the tMBs (Figure 1b) to the cells than the cMBs (Figure 1a). Immunofluorescent staining of $\alpha_v\beta_3$-integrin expression in SVEC cell (Figure 1F) reveals that the ligand is constantly expressed on the cell surface especially in cell-cell border regions. This also proofs that the $\alpha_v\beta_3$-tMBs which has been used in this study are able to adhere to the cells.

To examine whether tMBs adhered to $\alpha_v\beta_3$ integrin can be detected with high frequency nonlinear contrast imaging, SVEC cells were incubated with the tMBs and imaged by ultrasound imaging system in 3D (Figure 2). Figure 2a shows the imaging setup schematically. In Figure 2b contrast-mode image was overlaid in green on the grayscale Bmode image. First a 2D image was acquired and the microbubbles in such 2D imaging plane were destroyed using a flash burst. Then the probe was moved over a range of ~4.9 mm to acquire the frames for the 3D image. Figure 2b demonstrated that the ultrasonic signals of SVEC cells bound with tMBs were significantly enhanced. The band in the middle of the Figure 2b in which there is no green signals presented, shows the destruction of the tMBs with the flash burst.

In vivo

To further examine the application of the $\alpha_v\beta_3$-tMBs to the effect of imaging the expression of $\alpha_v\beta_3$ integrin *in vivo*, the atherosclerosis lesions at the bifurcation of carotid artery, part of the wall of common carotid artery containing no lesions and salivary gland of the $ApoE^{-/-}$ mice were examined. Figure 3a shows a microscopic photo of an $ApoE^{-/-}$ mouse indicating the anatomical structure and presence of atherosclerosis lesions in the aortic arch, brachiocephalic trunk and carotid bifurcations. Examples of cross-sectional histopathological sections showing the morphology of the carotid artery and the atherosclerosis lesions are presented in Figure 3b and 3c. Big and advanced atherosclerosis lesions

at and around the carotid bifurcation are visible in Figure 3b and absence of the atherosclerosis lesions in the common carotid artery can be noticed in Figure 3c. Representative Bmode, contrast mode images and analyzed ROI for the plaque area, Representative Bmode, contrast mode images and analyzed ROI for the plaque area, salivary gland and no-plaque ROI in the common carotid are presented in Figure 4. Similar to *in vitro* results, there was evident enhancement in the ultrasound signal from the tMBs retained in the vessel walls and salivary glands after applying our quantification steps (Figure 4c and 4e). Only a weak molecular signal was detected in the case of cMBs injections (Figure 4d and 4f). Enhancement of the ultrasound signal in the no-plaque ROI was significantly lower than the plaque ROI (Figure 4g and 4h).

Quantitative analysis of the sonograms in the plaques ROI showed that the difference between the molecular signals using tMBs (4.25±0.84) vs. cMBs (1.08±0.39) was significant (Figure 5). These difference for the salivary gland (6.61±1.23 for tMB and 2.63±0.60 for cMB) was also significant (Figure 5). However there was no statistically significant difference for tMB and cMB in the no-plaque ROI (1.16±0.24 for tMB and 0.41±0.07 cMB) (Figure 5). Also the mollecular signal in the plaque ROI (4.25±0.84) was significantly higher than that for the no-plaque ROI (1.16±0.24) for the tMBs whereas this difference, as expected, was not significant for the cMBs (1.08±0.39 vs. 0.41±0.07).

To validate the results of ultrasonography, the carotid artery and salivary gland of mice were harvested and subsequently analyzed for expression of blood vessels and macrophages by CD31and MAC3 staining. Results showed large levels of macrophages in the endothelium of carotid artery plaques and salivary gland microvessels.

Discussion

Ultrasound molecular imaging with tMBs has some advantages in preclinical applications over other imaging modalities including: its readily availability, being easy to use and it has the fast response-time to provide real-time imaging. Also, ultrasound imaging uses UCAs that remain exclusively intravascular, minimizing nonspecific signals from extravasated contrast material. Our *in vitro* and *in vivo* results showed successful binding of tMBs to $\alpha_v\beta_3$ integrin as well as successful detecting of tMBs corresponding to the intensity of $\alpha_v\beta_3$ integrin expression

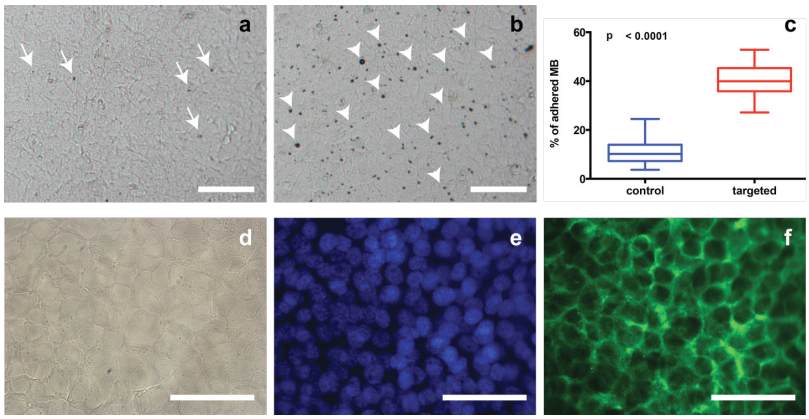

Figure 1
$\alpha_v\beta_3$-integrin expression in SVEC cells. Bright field images of cMB (a) and tMB (b). cMB are marked by arrows and tMB by arrow heads. The % of tMB and cMB adhered to SVEC (c). Immunofluorescent staining of $\alpha_v\beta_3$-integrin expressed in SVECs (f). Corresponding bright field image (d) and cell nuclei staining (e). Bar 50 µm.

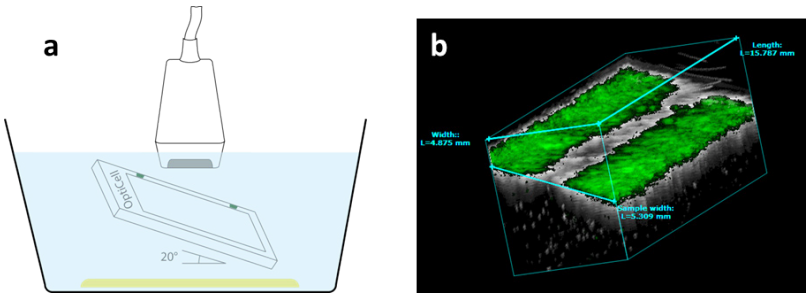

Figure 2
Ultrasound molecular imaging of $\alpha_v\beta_3$-tMBs expression in vitro. a) schematic diagram of in vitro ultrasound molecular imaging $\alpha_v\beta_3$-tMBs expression in vitro. b) Bmode (gray) overlaid with nonlinear contrast mode (green) ultrasound imaging in 3D to detect the $\alpha_v\beta_3$ expression via $\alpha_v\beta_3$-tMBs adhered to the SVECcells, which were cultivated in an OptiCell. Imaging was performed with Vevo 2100 ultrasound imaging system and MS250 probe at 18 MHz.

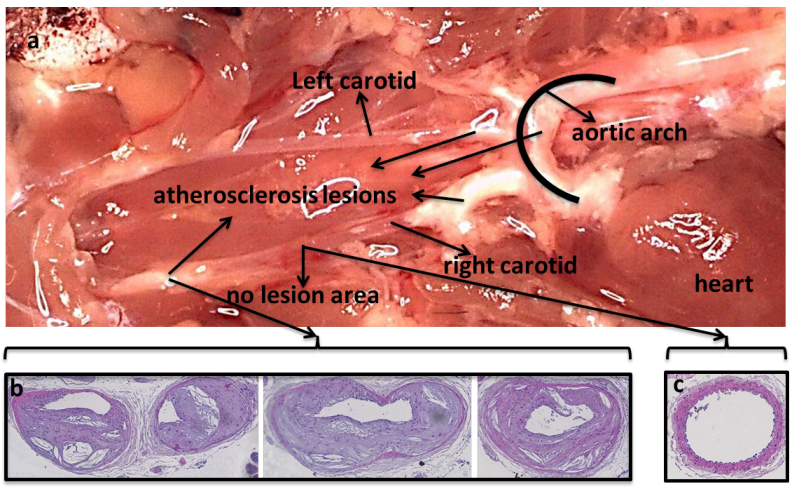

Figure 3
Microscopic photo and cross-sectional histopathological sections of a ApoE$^{-/-}$ mouse:
a) Anatomical structure of the right carotid and presence of atherosclerosis lesions in the aortic arch, brachiocephalic trunk and carotid bifurcations and the absence of lesions in the common carotid,
b) HE stain of the three corresponding slices just before, at and just after the carotid bifurcation where there advanced atherosclerosis lesions are visible,
c) HE stain of a corresponding slice in the middle of the common carotid where there is no atherosclerosis lesion.

Figure 4
Molecular sonogram of carotid artery vessels and salivary gland.
a) Bmode image of the right carotid and right salivary gland with region of interest in the salivary gland, around the plaque at the carotid bifurcation and around the common carotid artery where there is no plaque present.
b) Nonlinear contrast mode image (maximum intensity projection over 100 frames) of the right carotid and salivary gland after injecting the UCA.
c) Detected bound UCA in the plaque region of interest for the tMBs injection.
d) Detected bound UCA in the plaque region of interest for the cMBs injection.
e) Detected bound UCA in the salivary gland region of interest for the tMBs injection. f
) Detected bound UCA in the salivary gland region of interest for the cMBs injection.
g) Detected bound UCA in the region of interest around the common carotid artery wall where there is no plaque present for the tMBs injection.
h) Detected bound UCA in the region of interest around the common carotid artery wall where there is no plaque present for the cMBs injection.

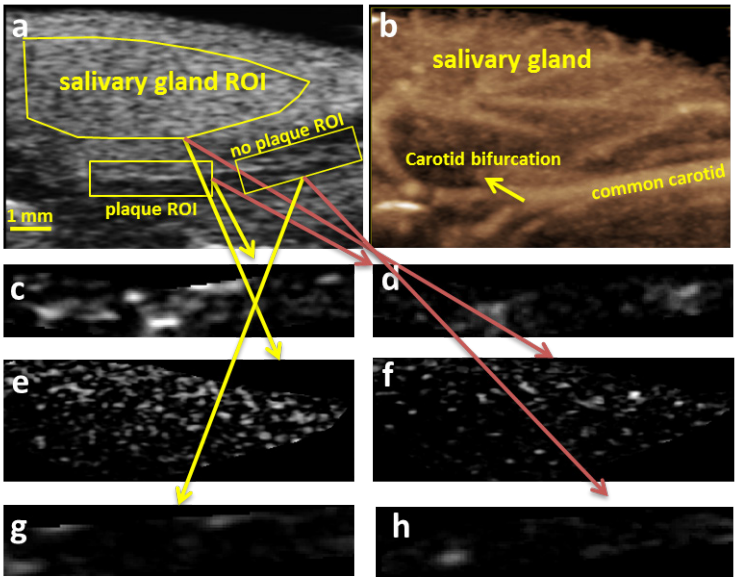

Figure 5
Quantified molecular signals in the plaque ROI, salivary gland and no-plaque ROI for cMB and tMB.

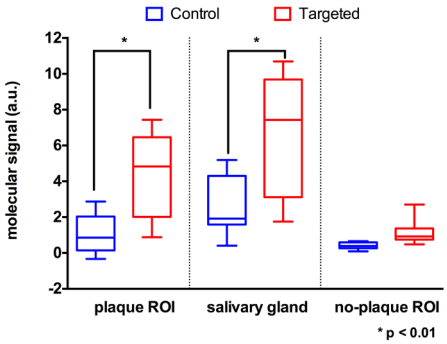

Figure 5
Expression of microvessels (CD31 staining) and macrophages (MAC3 staining) in atherosclerosis plaque of right carotid artery (a and d) and right salivary gland (b and e) the insets are demonstrated in c and f.

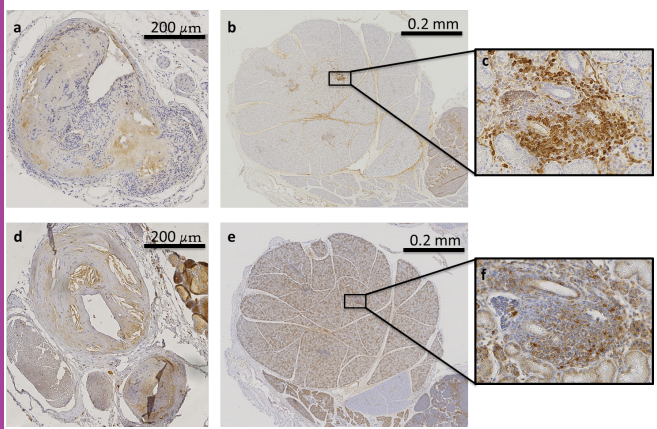

on the endothelial cells. The expression of $\alpha_v\beta_3$ was confirmed by immunocytochemistry for the *in vitro* study. *In vivo*, the expression of $\alpha_v\beta_3$ was confirmed indirectly using CD31 and MAC3 staining which together show the density of macrophages in the microvessels. It is known that macrophages play an important role in the pathogenesis of atherosclerosis and strongly correlate with plaque vulnerability[332,333]. The expression of $\alpha_v\beta_3$ integrin on activated macrophages which are recruited into the arterial wall has been confirmed earlier [334]. Our results are especially valuable since imaging can provide an alternative strategy for evaluating plaque neovascularization in terms of spatial extent and amount of endothelial $\alpha_v\beta_3$ integrin in a noninvasive or minimal-invasive manner. In fact, numerous investigators have adopted approaches in which molecular imaging has been attained through the use of tMBs and many proteins related to atherosclerosis such as CD81 [335], ICAM-1 [336], VCAM-1 [337], P-selectin [116], von Willebrand factor [338] and integrin [310], have been imaged with tMBs. Also imaging the $\alpha_v\beta_3$ expression has been used in few studies with near-infrared optical imaging [329], magnetic resonance imaging [330] and positron emission tomography [331]. However, to the best of our knowledge, this is the first study reporting successful *in vivo* ultrasound molecular imaging of plaque neovascularization using MBs targeted to $\alpha_v\beta_3$ integrin in mice model of atherosclerosis.

In our study, the carotid artery vessels were particularly selected as target to examine. Reasons mainly result from the following facts. First, it's believed that the most reproducible site for studies of lesions in mice is the carotid artery, which is a better model for human atherosclerosis [339] and the carotid and subclavian arteries are often the first involved vessels in atherosclerosis [340]. Second, the carotid artery vessels are readily accessible and detected under ultrasound imaging systems. Third, the salivary gland which is in the field of view on top of the carotid is a suitable internal positive control for binding of tMBs. Finally, the middle part of the common carotid which is free from lesions is an ideal intra-animal negative control.

It was observed that there are still $\alpha_v\beta_3$-tMBs attached to the middle part of the common carotid artery where there is no atherosclerosis lesion present. The reason is that $\alpha_v\beta_3$ integrin is also expressed in neointimal vascular smooth muscle cells [29]. However the intensity of $\alpha_v\beta_3$ expression in the healthy part of the common carotid artery was significantly lower than that in the plaque ROI. As expected, there was no statistically significant difference between the molecular signal in the plaque and no-plaque ROIs for the cMBs as well as for tMBs versus cMBs in the part of the vessel where no plaque was presented.

Salivary gland is a large and very well vascularized organ which is located above the right carotid in our imaging field of view. Since the density of vasculatures

(both healthy and diseased) is very high in the gland the expression $\alpha_v\beta_3$ integrin is also high in this organ. Therefore, it's an ideal target to have as an internal positive control for successful binding of tMBs to their targets. Our immunocytochemistry analysis of the salivary glands also confirmed the presence of macrophages in the microvessels as an indirect confirmation of $\alpha_v\beta_3$ expressions. This result was with a good agreement with our ultrasound molecular imaging findings.

Our quantification method assures that the signal from only bound MBs are enhanced and considered as molecular signals. The processing steps such as averaging pre- and post-flash frames and subtracting the result frames from each other assure that tissue artifacts are minimized and only the stationary contrast spots are enhanced. We have previously shown both in an *in vitro* and *in vivo* comparison study that amplitude-modulation pulse sequence to extract the nonlinear response of the UCA at the fundamental frequency is a suitable nonlinear contrast mode for imaging targets such as mouse carotid artery with the imaging platform used in this study [341].

There are several limitations of this study. First, for the preparation of targeted UCA, biotin binds to avidin in a non-covalent and very stable manner by which biotinylated antibodies or peptides can then be linked to the UCA. However, this strategy is not translatable since avidin is immunogenic in humans from the clinical perspective. Second, it cannot be assumed that the models we used to test the feasibility of $\alpha_v\beta_3$-tMBs are identical to disease-related $\alpha_v\beta_3$ expression. In the clinical setting, more complex factors such as disease-related inducers, individual differences and intricate signal pathway are often involved into the regulation of $\alpha_v\beta_3$ expression. Although there is still a long way to translate this technique from the animal model to the clinical situation, it is eventually desirable to couple the level of video-intensity signal from the tMBs to the stage of the disease and to the risk assessment of atherosclerosis. Also, precise spatial correlation between ultrasonography and immunohistology is not always possible due to the difficulty of spatially matching the ultrasound plane with histologic sections and the fact 2-dimensional ultrasonography is formed from signals received over a beam elevation of almost a millimeter. Accuracy of $\alpha_v\beta_3$ quantification using the tMBs may be limited by some degree of nonspecific binding due to the wide and overlapping expression of $\alpha_v\beta_3$ by the vascular endothelium. In addition, more complex factors, such as acoustic radiation force, UCA concentration, blood flow velocity and targeted UCA affinity are involved and need to be further investigated.

Conclusion

This study demonstrated the successful preparation of the $\alpha_v\beta_3$-tMB and the potential of target specific UCA to detect the increased expression of $\alpha_v\beta_3$ integrin *in vitro* and *in vivo*. Our initial experience in molecular ultrasonography using the $\alpha_v\beta_3$-tMB has shown that it may enable *in vitro* and *in vivo* molecular imaging of $\alpha_v\beta_3$ expression on vascular endothelium. This imaging modality may provide reference values of relative expression of $\alpha_v\beta_3$ and information likely to be very useful to address the detection, prognosis, vulnerable potential of atherosclerosis or susceptibility to anti-atherosclerosis drugs.

Live observation of atherosclerotic plaque disruption in apolipoprotein E-deficient mouse

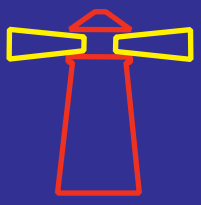

09

Abstract

Actual occurrence of spontaneous plaque rupture in mice has been a matter of debate. Hereby we report on an *in vivo* observation of the actual event of possible plaque disruption in a living ApoE$^{-/-}$ mouse. During live contrast enhanced ultrasonography of a 50-week old ApoE$^{-/-}$ male mouse, symptoms suggesting plaque disruption in the right brachiocephalic artery were observed. Histological analysis confirmed the presence of advanced atherosclerotic lesions with dissections and intraplaque hemorrhage in the affected brachiocephalic trunk, pointing towards plaque rupture as the cause of the observed event. However, we did not detect a luminal thrombus or cap rupture, which are the key criteria for plaque rupture in human atherosclerosis. This study reports the real-time occurrence of a possible plaque rupture in a living ApoE$^{-/-}$ mouse.

Based on a manuscript by **V. Daeichin**, J. C. Sluimer, K. Van der Heiden, I. Skachkov, K. Kooiman, A. Janssen, B. Janssen, J.G. Bosch, N. de Jong, M.J.A.P. Daemen, and A. F.W. van der Steen., submitted.

Introduction

Atherosclerosis is a lipid- and inflammation-driven disease of the arteries that leads to development of plaques. Plaque disruption, either by rupture of the fibrous cap or dissection of the plaque from the tunica media [342,343], is the main cause of cardiovascular events, such as stroke and myocardial infarction [344,345]. While human plaque histopathology provides valuable data on plaque disruption [344,346,347], there is an urgent need for representative animal models in which prospective examination of the events leading up to plaque disruption, the disruption itself, and the effect of plaque stabilizing therapies can be studied. The most abundantly used animal model to study atherosclerosis is the mouse. However, whether plaque disruption actually occurs in mice has been a matter of debate in the past decade [39-45]. Features suggestive of plaque rupture in apolipoprotein E-deficient ($ApoE^{-/-}$) mice with spontaneously developed unstable atherosclerosis in the brachiocephalic artery have been reported [33-38]. However, these were criticized by Schwartz et al.[39], who suggested that the reported findings may actually be sectioning artifacts, intra-plaque hemorrhage, or a completely different form of lesion disruption not seen in human plaques. Furthermore, the interpretation of "buried caps" as indirect evidence for previous plaque ruptures is still under debate. Acknowledging that plaques in mice by nature differ from those in humans [348], unequivocal proof of spontaneous plaque disruption in mice is currently non-existing. We observed symptoms suggesting spontaneous plaque disruption in the right brachiocephalic artery of a 50-week old male $ApoE^{-/-}$ mouse. This animal was part of a study which aimed at quantification of carotid atherosclerotic neovascularization with targeted microbubbles and ultrasound. To the best of our knowledge, this is the first *in vivo* observation of the actual event of possible spontaneous plaque disruption in a living mouse.

Methods

Animal Handling

A hypercholesterolemic male ApoE$^{-/-}$ mouse (33 g) derived from a C57/Bl6 background from an in-house breeding colony (originally from Iffa Credo, Lyon, France) was fed chow until the age of 50 weeks. The animal was anesthetized with ketamine (0.1 g/kg) and xylazine (0.02 g/kg) by subcutaneous injection and ibuprofen (s.c.) was given as additional analgesic. The mouse was intubated and artificially ventilated using room air at the rate of 160 strokes per minute. The left jugular vein was exposed, and a heat-stretched polyethylene-25 cannula was inserted (1.5 cm) and subcutaneously guided to the neck of the mouse. Here the catheter was fixed, extended, filled with heparinized saline (10 U/ml), and plugged. The animal was placed on the Vevo Rail System heating stage (VisualSonics Inc. Toronto, Canada) and ultrasound imaging was performed. A series of injections were done using a programmable syringe pump (11 Pico Plus Elite, Harvard Apparatus, Kent, UK) at a rate of 600 µL per minute. The interval between ultrasound contrast agent (UCA) injections (100 µL per injection) was 20 minutes to prevent sudden increase in the blood pressure due to volume overload. All animal work was approved by the regulatory authorities of Maastricht University and performed in compliance with the Dutch government guidelines.

Ultrasound imaging

UCA was prepared from Target-Ready Vevo MicroMarker contrast agent (VisualSonics Inc. Toronto, Canada) according to the manufacturer's instruction. Microbubbles were targeted with biotinylated antibodies against $\alpha_v\beta_3$-integrin (cat. no. 551380, BD Biosciences, San Jose, CA, USA) for making targeted UCA. Inactive form of biotinylated IgG(κ) (cat. no. 553923, BD Biosciences) were used for making control UCA. In order to check the specific binding of the targeted UCA to the $\alpha_v\beta_3$-integrin receptors in the animals, pure antibodies (200 µl with concentration of 0.5 mg/mL, cat. no. 550024, BD Biosciences) were injected to block the receptors after injecting the first targeted UCA. Then, another injection of the targeted UCA was performed. A high frequency pre-clinical ultrasound scanner, with a 256-element linear array transducer (Vevo 2100 with MS250 probe, VisualSonics Inc., Toronto, ON, Canada) was operated at 18 MHz. The system was operated at 10% transmit power in the contrast mode with wide beam-width, resulting in low and uniform transmit pressure over imaging depth (~400 kPa, MI of ~0.09). Side-by-side B-mode and nonlinear contrast mode (Nonlinear Fundamental [151]) images were acquired with a frame rate of 20 frames

per second. The field of view was 11 mm deep and 17 mm wide. The focus of the transducer was set at 7 mm where the upper wall of the common carotid was located. In the field of view, part of the aortic arch, the right brachiocephalic trunk, the right common carotid artery and its bifurcation were visible. In the imaging field, on the top of the right carotid the right salivary gland was located. B-mode gain was 20 dB and contrast gain was 30 dB. DICOM (Digital Imaging and Communications in Medicine) images were exported to MATLAB (Ver. R2012b, The MathWorks, Natick, MA, USA) for further off-line processing.

Tissue collection and histology

At sacrifice blood was drawn from the right ventricular apex. Subsequently the mouse was gently perfusion fixed via the left cardiac ventricle with sodium nitroprusside (0.1mg/ml; Sigma-Aldrich, Seelze, Germany), followed by 1% paraformaldehyde (PFA). The right carotid artery including the brachiocephalic artery was excised, fixed in 1% PFA for 24 hours, and paraffin-embedded. The right carotid artery was serially sectioned (4 µm), and stained at 20µm intervals with Hematoxylin and Eosin (HE, Sigma-Aldrich) [349] for microscopical examination by an experienced cardiovascular pathologist (M.D.). Serial sections were stained with the Martius Scarlet Blue (MSB) method to detect fibrin/fibrinogen as bright red, and Perl's Prussian Blue for Ferric Iron [349].

Results

Figure 1a shows the anatomical structure of the animal in the ultrasound B-mode image. No physiological abnormalities were observed in the animal during the injections of the first control and the first targeted UCA (Figures 1b and 1e, supplementary video 1). During injection of $\alpha_v\beta_3$-integrin antibody, 42 minutes after first injection, a sudden cessation of flow through the common carotid artery was observed. Flow cessation coincided with a decrease in common carotid pulsation followed by vessel constriction (Figure 1f, supplementary video 2). Flow cessation in the common carotid continued for approximately 30 minutes. At this time, another injection with targeted UCA was performed. During the first 5 seconds after arrival of the microbubbles in the aortic arch, hardly any micro-

bubbles passed through the occluded area in the brachiocephalic trunk (Figure 1c, supplementary video 3). Then, microbubbles slowly started to pass through and reached the common carotid in the next 10 seconds. Strikingly, flow through the salivary gland was not restored (Figure 1d, supplementary video 3).

Histological analysis revealed plaque disruption in three advanced atherosclerosis lesions (Figure 2) associated with intraplaque hemorrhage and fibrin (Figure C, F, I, L and O). Plaques with iron deposits (Perl's staining in Figure 2 B, E, H, K and N), indicative of remnants of old hemorrhage, and with fibrin deposits (MSB staining in Figure 2 C, F, I, L and O), were present in the brachiocephalic trunk (Figure 2 A-I) and at the bifurcation of the brachiocephalic artery into the right subclavian artery (Figure 2 M-O) and the right common carotid artery (Figure 2 J-L). Dissection of the plaque from the tunica media was observed at the bifurcation in both lesions. The presence of fibrin at the point where the plaque is still connected to the tunic media suggests this dissection occurred *in vivo* and was not an artifact due to histological processing.

Discussion

In a contrast enhanced ultrasonography study aimed to quantify carotid atherosclerotic neovascularization with microbubble targeted to $\alpha_v\beta_3$-integrin in an ApoE$^{-/-}$ mouse, we observed a live sudden flow cessation which coincided with a decrease in common carotid pulsation and vessel constriction. Subsequently, we investigated the possible cause for this phenomenon by histological analysis of the affected carotid artery and brachiocephalic trunk. The presence of advanced atherosclerotic lesions in the brachiocephalic trunk, with dissections, points towards a possible plaque rupture as the cause of the observed arterial occlusion. To the best of our knowledge, this is the first study to report a live case of possible plaque rupture in ApoE$^{-/-}$ mice. We observed dissection and intraplaque hemorrhage, which is a common feature of complex lesions preceding acute ischemic events and is considered a characteristic of plaque rupture in mouse models of atherosclerosis [38,350]. However, we did not detect a luminal thrombus or cap rupture, which are key criteria for plaque rupture in human atherosclerosis.

The classical definition of plaque rupture in humans is considered cap disruption of a fibroatheroma with a luminal thrombus communicating with the underlying necrotic core [344]. This definition was extended to animal models [346]. Nevertheless, not all the criteria of plaque rupture in humans are translatable into animals [351,352]. A luminal thrombus communicating with a ruptured fibrous cap is very uncommon in ApoE$^{-/-}$ mice, possibly due to a much higher rate of thrombolysis due to low levels of plasma plasminogen activator inhibitor-1 and thrombin-activated fibrinolysis inhibitor in mice compared to humans [34-36]. Yet we did detect fibrin/fibrinogen at the base of the plaques.

Besides the possibility that flow was restored because the thrombus resolved, another possibility for the temporary occlusion is embolization of either plaque material or a thrombus. Our observation that flow was not restored in the salivary gland could point to an obstruction distal to the internal common carotid artery and supports the latter hypothesis.

At the same time, we cannot ignore the possible impact our handling of the animal had on the plaques. Firstly, the animal was exposed to multiple injections, which could have introduced hypervolemia or air-bubbles. However, we consider this unlikely as the site of injection was the left jugular vein and at the time of the event only 200 µl was injected at a slow injection rate. Secondly, we need to consider possible damage generated by UCA in combination with high frequency ultrasound. It has been reported that targeted UCA and high intensity ultrasound can have destructive effects on microvessels in rat spinotrapezius muscle [353] and can produce regions of reduced blood flow within tumor microvasculature in mice [228], but none of such effects were shown to occur in larger vessels like the carotid artery. Moreover, at the time of the event no high intensity ultrasound was applied. Thirdly, the animal was subjected to physical handling, namely slight straightening of the neck and coupling an ultrasound transducer via gel to the neck. This could induce some pressure on the artery although we never observed deformation of the artery during imaging. Also, simultaneous ECG readings excluded a potential cardiac cause for the flow cessation. Finally, the occurrence of the event during injection of antibody is more likely to be a coincidence since no plaque disruption induced by injection of antibody hasbeen reported.

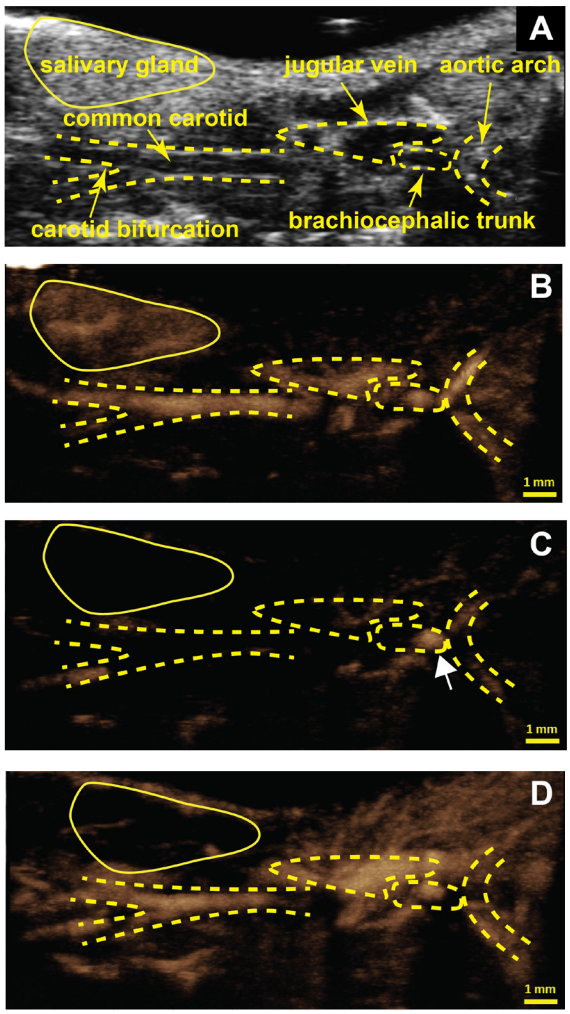

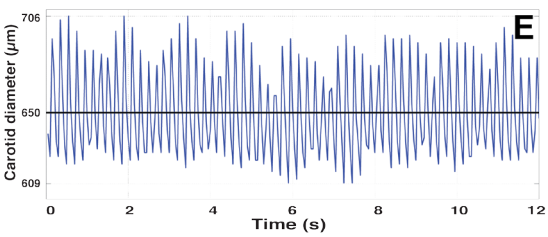

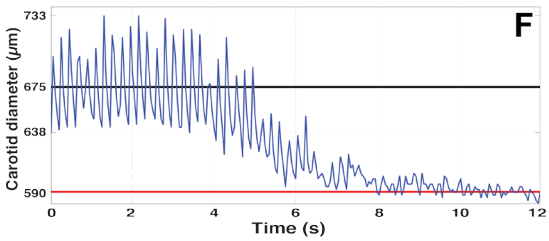

Figure 1
Dynamics of plaque disruption , imaged with contrast enhanced ultrasound
A) B-mode image of part of aortic arch, beginning of brachiocephalic trunk, common carotid, carotid bifurcation (dashed lines) and right salivary gland (solid lines) of the ApoE$^{-/-}$ mouse.
B) Maximum Intensity Projection (MIP) over 100 frames (5 seconds) after arrival of UCA in the aortic arch (first UCA injection) showing the trajectory of the aortic arch, carotid artery, and the perfused salivary gland.
C) MIP over 100 frames (5 seconds) after arrival of UCA in the aortic arch (third UCA injection) showing the accumulation of UCA in beginning of brachiocephalic trunk (white arrow) and significant reduction of the blood flow in the carotid artery and no perfusion of the UCA in the salivary gland.
D) Longer MIP of the sequence in c (15 seconds) showing the return of the UCA in the common carotid but still no perfusion of the UCA in the salivary gland.
E) Normal pulsation of the common carotid walls (subtraction of upper and lower walls displacement) before plaque disruption.
F) Pulsation of the common carotid walls during plaque disruption showing the decrease in common carotid pulsation followed by vessel constriction.

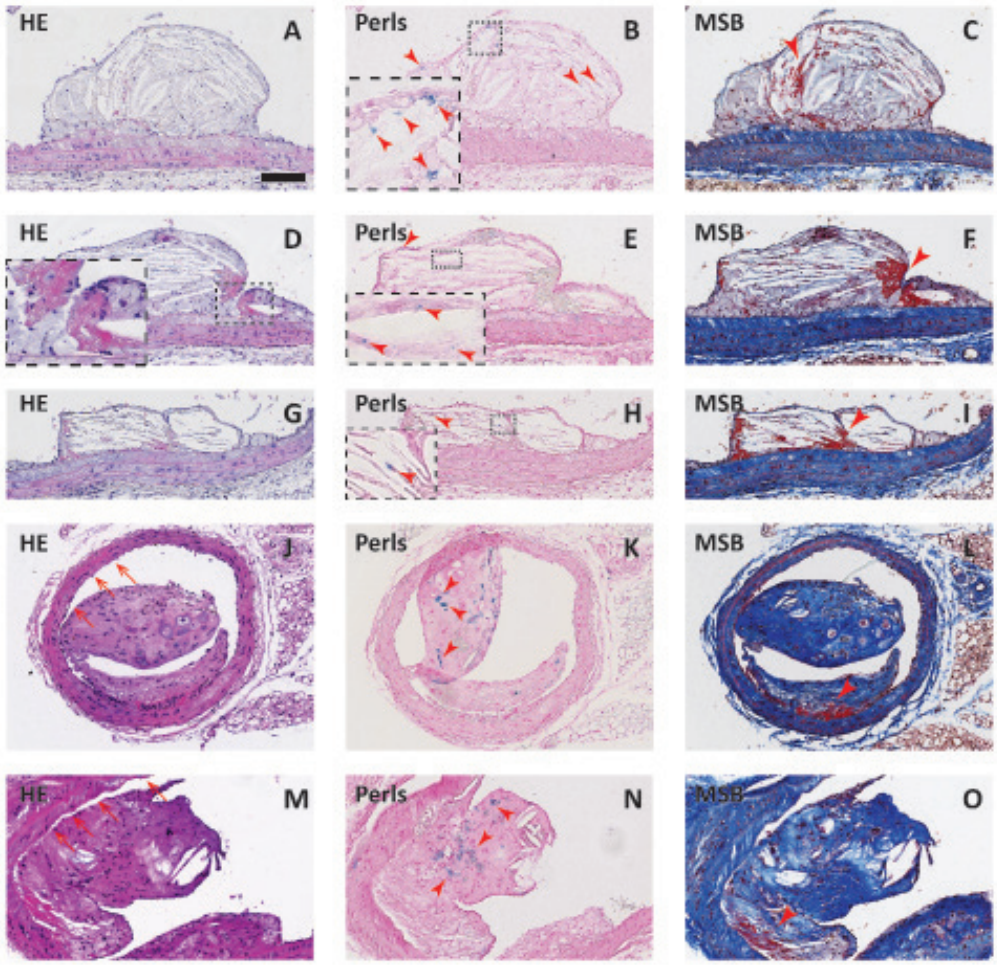

Figure 2
Plaque disruption in brachiocephalic trunk. (A, D, G, J, M: HE staining; B, E, H, K, N: Perl's Ferric Iron staining; C, F, I, L, O: MSB staining). Histological analysis of the brachiocephalic trunk revealed a plaque in the brachiocephalic artery with iron (blue staining in Perl's indicated by arrowheads in B, E and H) as a remnant of an earlier intraplaque bleeding and fibrin/fibrinogen deposition (red color in MSB staining; arrowheads in C, F and I). At the bifurcation of the brachiocephalic artery into the right subclavian artery (M-O) and the right common carotid artery (J-L), plaques with remnants of an earlier intaplaque bleeding (Perl's Ferric Iron staining; arrowhead in K and N) and fibrin/fibrinogen deposits (red in MSB staining; arrowheads in L and O) were present. At both locations dissection of the plaque from the tunica media (indicated by arrows in J and M) was observed, which is more likely to have occurred *in vivo* rather than due to histological processing, as fibrin/fibrinogen is present at the site, where the plaque is still attached to the vessel wall (arrowheads in L and O). Magnification: 800x, scale bar: 100 µm.

Conclusion

For the first time, possible spontaneous plaque disruption in the right brachiocephalic artery of an ApoE$^{-/-}$ mouse was observed real-time with contrast enhanced ultrasonography. Although no thrombus was found in the carotid artery, plaque dissection from the media and presence of intraplaque hemorrhage in the advanced atherosclerotic lesions, provide the supporting histological evidence for plaque disruption as the possible cause of temporary arterial occlusion.

Unique ♦pumping-out♦ fracturing mechanism of a polymer-shelled contrast agent: an acoustic characterization and optical visualization

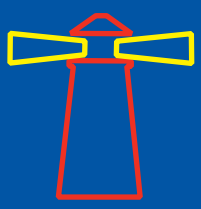

10

Abstract

This work describes the fracturing mechanism of air-filled microbubbles, MBs, encapsulated by a cross-linked poly(vinyl alcohol), PVA, shell. The radial oscillation and fracturing events following the ultrasound exposure were visualized with an ultra-high-speed Brandaris-128 camera, and backscattered time domain signals were acquired with the acoustic set-up specific for harmonic detection. No evidence of gas emerging from defects in the shell with the arrival of the first insonation burst was found. In optical recordings, more than one shell defect was noted, and the gas core was drained without any sign of air extrusion when several consecutive bursts of 1 MPa amplitude were applied. In acoustic tests, the backscattered peak-to-peak voltage gradually reached its maximum and exponentially decreased when the PVA-based MB suspension was exposed to approximately 20 consecutive bursts arriving at pulse repetition frequencies of 100 and 500 Hz. Keeping in mind that the PVA shell is porous and possibly contains large air pockets between the cross-linked PVA chains, the above mentioned acoustic behavior might be attributed to pumping gas from these pockets in combination with gas release from the core through shell defects. We named this fracturing mechanism “pumping-out”, and this behavior could have potential use for the local delivery of therapeutic gases, such as nitric oxide.

Based on a manuscript by S. V. V. N. Kothapalli, **V. Daeichin**, F. Mastik, L. Åke Brodin, B. Janerot-Sjoberg, G. Paradossi, N. de Jong, and D. Grishenkov., submitted to IEEE Trans Ultrason Ferroelectr Freq Control, in 2014.

Introduction

Ultrasound contrast agents (UCAs) are a suspension of injectable micro-sized gas bubbles (MBs) stabilized by proteins, lipids or polymers. UCAs are routinely used to increase the ultrasound backscattered power from blood cells, thereby improving the diagnostic sensitivity of ultrasound imaging [354-357]. The shell of gas-filled UCAs, if excited with a high enough acoustic pressure (typically >1 MPa), can be disrupted. The gas that escapes from the core of disrupted UCAs can form shell-free gas bubbles, which can interact with ultrasound bursts and create transient, high amplitude and broadband echoes [356,357]. The transient disruption phenomenon is utilized in harmonic triggered imaging to find myocardial abnormalities [358] and in intermittent perfusion imaging to quantify tissue blood flow [359]. In the specific case of polymer-shelled MBs, the polymer shell is intact after the MB disruption, which is further utilized pre-clinically in ultrasound-triggered drug delivery applications [360,361]. In addition, assessment of the rupture pressure threshold can be utilized in the evolution of potential bio-effects [362].

Until now, passive and active cavitation detection, assessment of acoustic attenuation spectra, and direct optical visualization of MB oscillations have been employed to identify the rupture pressure threshold of UCAs [363]. In particular, in the case of passive cavitation detection, a receiver was used to detect the acoustic response from MBs excited by another emitter [364]. In the case of active cavitation detection, a receiver (maintaining a low-pressure pulse amplitude) was utilized to investigate the possible cavitation effects from MBs that were fired by series of high power ultrasound pulses from another source [365]. In the opto-acoustic method, an ultra-high-speed camera captures single MB oscillation dynamics simultaneously upon insonation having a frequency between 1 to 10 MHz [366]. Direct visualization is the first and preferable application to interpret and understand the physical phenomena involved in single MB oscillatory behavior upon insonation, but it is currently still subject to limited availability.

The high-speed optical recordings of the UCAs destruction mechanism revealed that different UCAs have different fracturing mechanisms, in which the shell composition plays a vital role. For example, lipid-shelled MBs at peak negative pressures (P^-_{pk}) above 300 kPa initially expanded more than five times their original radii, followed by instantaneous shell fragmentation and the appearance of several smaller uncoated gas bubbles [367]. On the other hand, the gas content of polymer-shelled MBs escaped through small shell defects, i.e. cracks, at incidental pressures above 1 MPa. The shell remained almost intact, thereby resembling a punctured and flattened tire [360]. The release of gas from the core

gave rise to new daughter shell-free gas bubbles that lasted a few milliseconds and disappeared due to dissolution [360,366]. The similar shedding behavior where the bubble mass was drained out gradually was also observed in lipid-shelled MBs when they were exposed to a series of insonation pulses having P^{-}_{pk} below the rupture pressure threshold [368]. This sequential dissociation of lipid molecules is proposed to be useful in theranostics, i.e. the combined delivery of attached drug molecules and monitoring of the therapeutic effect, at low acoustic pressures in a particular area of interest [369]. All above-mentioned facts illustrate the particular importance and clinical relevance of not only identifying the UCAs rupture pressure threshold but also understanding their fracture mechanisms.

Herein, the assessment of the fracture mechanism of a novel polymer-shelled MB, developed by Paradossi et al. [370], is of interest. These MBs have a gas core encapsulated by a thick, cross-linked telechelic poly(vinyl alcohol), PVA, shell [46]. Initially, these PVA-MBs were proposed to be a stable ultrasound contrast agent in the blood circulation [46,370,371]. They have exhibited a longer shelf-life and offer a large number of reservoir sites to adhere extensive amounts of drug moieties or nanoparticles to due to their robust shell [372,373]. However, the thick shell dampens the radial oscillation of these MBs making them potentially less echogenic. Nevertheless, their measured echogenicity was surprisingly higher than expected when considering the shell thickness of the PVA-based MBs [371]. In 2007, Pecorari et al. demonstrated that it was possible to fracture PVA-MBs with a 2 MPa ultrasound burst [374]. It was proposed that the fracturing events of MBs can be identified using cross-correlation methods, when the cross-correlation coefficient is below 95% between the consecutive backscattered signals from the MB suspension. Moreover, the authors assessed the release of the gas content when the PVA-MB suspension was excited with a single high-power burst followed by monitoring with low power ultrasound pulses. Using the cross-correlation method Grishenkov et al. [375] rigorously conducted experiments to identify the rupture pressure threshold for three types of PVA-MBs (MB-pH5-RT, MB-pH5-cool, and MB-pH2-cool) prepared at different pHs (2 and 5) and temperatures (room temperature (RT) and 4°C (cool)). Experiments were carried out at varied driving frequency, number of cycles in the pulse, temperature, and exposure time. The cross-correlation analysis estimated the rupture pressure threshold of PVA-MBs to be above 1 MPa with an excitation frequency of 2.2 MHz and a pulse length of 10 cycles [375]. Such a pressure value corresponds to a mechanical index (MI) of approximately 0.67, which is well below the medically approved upper limit of 1.9. Previous studies have utilized backscattered acoustic signals to report not only on the oscillatory and mechanical properties but also on the acoustic cavitation of PVA-MBs. The current study, for the first time, demonstrates the direct optical visualization of the radial oscillation of PVA-MBs during high-speed imaging. Visualization of such dynamics, especially the frac-

ture mechanisms of a PVA shell can be explicitly beneficial for the optimization of the acoustic parameters in contrast-guided therapeutic applications.
In this study, the fracturing behavior of the MB-pH5-RT is explored both qualitatively (where a single MB behavior at a high insonation pressure of approximately 1 MPa is captured by the Brandaris-128 camera [376]) and quantitatively (where the amplitudes of a received backscattered time domain signal from the MB suspension are estimated at three different pressure values 0.75, 0.9, and 1 MPa). Both qualitative (optical recordings) and quantitative (acoustical investigation) data are deliberately interrogated and compared with currently reported UCA fracturing mechanisms.

Methods

Microbubbles

PVA-MBs were produced in our lab according to the protocol described by Cavalieri et al. [46]. The PVA (Sigma-Aldrich, Chemie Gmbh, Germany) powder was diluted in water and oxidized with sodium (meta)periodate, where the polymer chain was tailored to single moieties. This solution was then subjected to high shear stirring using an Ultra-Turrax® (Ika, Germany). Thus, the polymer-shelled gas-filled MBs were formed at the water/air interface from the cross-linking telechelic PVA hydrogel. The floating gas-filled MBs were separated from the polymer debris in a series of washing steps. The concentration and diameter of PVA-MBs were assessed with an optical light microscope (Olympus IX71, Japan) and were found to be approximately 5×10^8 MBs/ml and 3.8±0.8 μm, respectively. The thickness of the cross-linked PVA shell, as estimated with an atomic force microscope (Nanowizard I, JPK Instruments AG, Germany) [377], was determined to be approximately 300 nm.

Opto-acoustic set-up

The characteristic radial oscillation of a MB during the interaction with the ultrasound was visualized using an ultra-high-speed Brandaris-128 camera [376]. The schematic representation of the opto-acoustic setup is illustrated in Figure 1. The microscope with a 40x water-immersed objective (NA= 0.7) was focused at the PVA-MBs inside an OptiCellTM chamber (NUNC, Thermo Fisher Scientific, Wiesbaden, Germany). The total magnification of the system was further increased to 80x using an additional 2x magnification lens inside the microscope. The initial concentration of the PVA-MB suspension was diluted in Isoton® II (Beckman Coulter, The Netherlands) approximately 1000 times (1:1000 ratio) and introduced with a syringe into the OptiCellTM chamber. An optical

light guide (SCHOTT AG, Mainz, Germany) combined with a Xenon flash lamp (A-260 Vision Light Tech, Uden, the Netherlands) was fixed at the bottom of the water tank. A broadband focused ultrasound transducer (PA275, 1-9 MHz, Precision Acoustics, Dorchester, UK) was mounted at the side of the bottom of the water tank. The transducer was driven by a programmable arbitrary waveform generator (8026, Tabor Electronics Ltd., Tel Hanan, Israel) that provided signals for further amplification by a power amplifier (150A100B Amplifier Research, Limerick, Ireland). A 12-cycle transmitted burst was apodized by the Gaussian-shaped window function. The apodization tapered the first and last cycles in the excitation burst. The MBs were insonified at a P^{-}_{pk} of approximately 1 MPa. The frequencies of excitations varied between 2 and 4 MHz in intervals of 0.2 MHz (16 insonations in total) with a pulse repetition frequency (PRF) of 10 Hz. The transducer was calibrated in a separate experiment with a 0.075-mm needle hydrophone (Precision Acoustic Ltd., Dorchester, UK). For each PVA-MB, a series of 17 clips of 128 frames was captured by the Brandaris-128 camera at a rate of 15 million frames per second. The first clip in each series was acquired without the application of the ultrasound to estimate the initial radius of the MBs. The following 16 clips revealed the dynamics of the MBs in response to ultrasound excitations at 1 MPa and frequencies ranging from 2 to 4 MHz. In total, in these experiments, the radial oscillations of 11 PVA-MBs were recorded and analyzed in Matlab.

Acoustic characterization

We also investigated the fracture events of the PVA-MBs using the pure acoustic set-up previously described by Pecorari et al. [374]. Briefly, the bulk suspension of PVA-MBs was excited by a 2.2 MHz focused ultrasound transducer (Krautkramer, Gamma Series, Lewistown, PA, USA; -6 dB bandwidths: 1.8-3.4 MHz). Backscattered signals from the PVA-MBs were assessed with a 5 MHz focused transducer (Panametrics V309, Waltham, MA, USA; -6 dB: 3.3-6.7 MHz). This set-up has previously been employed to assess both higher harmonic responses and rupture pressure thresholds of PVA-MBs [374,375]. A schematic illustration of the set-up is presented in Figure 2. The two transducers (the emitter and receiver) were mounted approximately 5 cm away from, and perpendicular to, the custom designed cylindrical tissue phantom. This cylindrical phantom (4 cm high, 2 cm wide, and with a 0.5 cm wall thickness) was made of a pure agar solution. The attenuation loss of the acoustic wave propagating through the agar wall of the phantom is estimated to be below 1.0 dB at 2.2 MHz [378] and is disregarded in further calculations. A high-power burst pulser/receiver (SNAP Mark IV; Ritec Inc., Warwick, RI, USA) was employed to excite the emitter transducer. The backscattered acoustic signals from the MB suspension were retrieved by another pulser/receiver (Panametrics, Inc., PR 5072, Waltham, MA, USA), were

amplified to 40 dB and were further transferred to a PC-based oscilloscope (CompuScope 14200, Gage Applied Technologies, Lockport, IL, USA). The time delays between the emitter and receiver pulses were adjusted by a delay/pulse generator (BNC 565, Berkeley Nucleonics corp., San Rafael, CA, USA). The digitized time domain signals from the MBs were stored in a PC for further analysis. The excitation pulse consisted of a 10 cycle burst apodized by a rectangle window function. The PRF was varied between 100 and 500 Hz, and the P^{-}_{pk} of the excitation pulse was set to 3 different levels: 0.75, 0.91 and 1 MPa. The PVA-MB suspension was diluted 1000 times in deionized and degassed water (approximately 5×10^{5} MBs/ml) and then introduced by a syringe into the cylindrical tissue phantom. After every test run, the MB suspension was removed, replaced with a fresh MB suspension and gently stirred to attain homogeneity.

Results

Optical Visualization

The high-speed optical visualization of a PVA-MB insonified by the first high-power acoustic burst of 2 MHz frequency is presented in Figure 3. Here we demonstrate 48 frames (frames 26 to 73) out of the 128 frames taken to display the radial excursions of the PVA-MBs upon a high insonation pressure. The MB diameter at rest, as measured in the 26th frame, is equal to 4.14 μm. When exposed to ultrasound, the shell buckled and compressed (frames 27-32) and later the bubble recovered and expanded, as illustrated in frame 33. In frames 46-48, the PVA-MB exhibits more compression-like behavior than expansion behavior. We estimated the maximum expansion and compression diameters of the MB before it ruptured. At maximum expansion, the MB diameter measured approximately 4.83 μm (0.6 μm above the initial diameter at rest) and at maximum compression, the diameter was approximately 2.3 μm (1.9 μm below the initial diameter). The first crack in the PVA shell was observed in frame 50, noted by an arrow. There is evidence of cracking in the PVA shell, but gas leakage through the shell was not observed. The later frames demonstrate that the MB held back the gas and recovered its spherical shape upon insonation. In the consecutive acoustic cycle, the MB experienced more compression, while, in the recovery phase (frame 60), two tailpieces attached to the MB (possibly cracks) were observed. The indentation sources increased with the insonation cycles (as noted in frame 70). The diameter of MB also decreased with the insonation cycles. There was a clear indication of several indentation sources in the shell; however, there was no visual sign of rapid gas release from the fragmented shell (compare clip C3_20130918_174417_023 @17.43MHz_align with the clips reported in pre-

vious studies of phospholipid and polymer MBs [360,366]).
The shape of the cracked MB obviously became asymmetric as a result of the uneven distribution of crosslinks in the polymer shell. Interestingly, the fractured shell managed to maintain the portion of gas and the MB as a whole remains acoustically active upon consecutive insonation pulses. The optical visualization of the broken MB oscillations at 2.2 MHz, 2.4 MHz, 2.6 MHz, and 3.0 MHz frequencies is presented in a video clip ("C3_20130918_174417_024@17.43MHz_align") and the image frame sequence from the video is provided in Figure 4. It can be noted that the gas was squeezed out slowly through several pores in the shell as the MB interacted with the compression acoustic cycles. The volume fraction of the gas in the PVA-MB decreased when it was exposed to several consecutive bursts of high insonation pressure. The gas was squeezed out completely from the MB after five insonation bursts while the PVA shell remained almost intact with the shape of a deflated football (last row in Figure 4).

Acoustic assessment

The average peak-to-peak ($A_{pk\text{-}pk}$) voltage of the scattered signals from the PVA-MBs in a bulk suspension versus time are presented in Figure 5a and 5b. These signals were obtained by insonifying the suspension with a 2.2 MHz focused transducer at a PRF equal to 100 and 500 Hz, respectively. The three lines in each plot correspond to the PVA-MB responses to excitation at a P^{-}_{pk} of 0.75 MPa, 0.9 MPa, or 1 MPa, respectively. It can be noted that the $A_{pk\text{-}pk}$ voltage of the scattered signal increased as the incidental acoustic pressure and PRF rises.
Individual inspection of each curve illustrated in Figure 5 revealed several characteristic regions. First, at a low acoustic pressure, typically below 0.3 MPa, a low $A_{pk\text{-}pk}$ voltage response was acquired. As the PVA-MBs were exposed to high power bursts (arrows in Figure 5a and 5b), the $A_{pk\text{-}pk}$ voltage of the scattered signals increased steadily with consecutive insonation pulses, until certain maximum voltage (1.5 and 2.5 volts for 100 and 500 Hz, respectively). This was followed by an exponential decrease to a plateau at approximately 0.2 volts. Although the maximum value of the scattered amplitude was observed at different time points for the same PRF value, the exponential decay started from approximately the same time point (0.18 s for PRF=100 Hz and 0.06 s for PRF=500 Hz) for all three P^{-}_{pk} values. The trends of the $A_{pk\text{-}pk}$ voltage curves reveal that several closely spaced in time consecutive destructive insonation pulses are required to efficiently rupture the PVA-MBs and to obtain the maximal acoustic enhancement from the MB suspension.
By using a quantitative analysis of the $A_{pk\text{-}pk}$ voltage decay curves shown in Figure 5a and 5b, the gas dissolution time can be calculated. The MB gas dissolution curves were fitted with an exponential decay function of time using the curve fitting toolbox (cftool) in Matlab, and a mathematical interpretation is given

by Equation 1,

$$y = A \times e^{-kt} + C \qquad (1)$$

where, A is the maximum peak-to-peak amplitude, k is the decay rate constant and C is the magnitude of the offset. The estimated coefficients are given in Table I. The maximum A increased with an increase in the P^{-}_{pk} and PRF. The k for all three curves was similar with small fluctuations around the average 26.7 s^{-1} and 38.7 s^{-1} for the PRF equal to 100 Hz and 500 Hz, respectively. The offset values, C, were below 0.2 in all measurements.

Table 1. Coefficients defining the peak-to-peak amplitude of the scattered signal from the PVA-MBs

PRF	P^{-}_{pk}	A (Volts)	k (s^{-1})	C (Volts)
100	0.75	0.7	26.1	0.1
	0.90	1.5	26.2	0.2
	1.00	1.5	27.9	0.2
100	0.75	1.5	40.3	0.2
	0.90	2.4	39.9	0.2
	1.00	2.5	43.4	0.2

Analogues among the optical and acoustical observations

The characteristic regions identified by the acoustic tests and noted in the scattered signal were further labelled as A, B, C, and D and the corresponding optical visualization for each category is illustrated in Figure 6. The power spectra for each region are presented in Figure 7. In region A, the PVA-MBs were excited with 0.3 MPa, and minor radial oscillations were observed and a lower $A_{pk\text{-}pk}$ voltage was obtained (Figure 6a). The corresponding power spectrum has only a fundamental frequency response (Figure 7a), representing a linear response of the MB. In region B, with the arrival of the first high amplitude insonation burst, the $A_{pk\text{-}pk}$ voltage increased gradually but did not reach its absolute maximum. A gradual and rather rapid increase of the $A_{pk\text{-}pk}$ voltage up to a certain maximum value was observed following several consecutive high-energy bursts. In region C, the $A_{pk\text{-}pk}$ voltage was exponentially decreased due to gas escape from the MB. In the optical experiments, it was demonstrated that the PVA-MB was not disrupted into several fragments with the first insonation burst, but rather violent oscillations were noted and the shell cracked locally with some portion of encapsulated gas leaking out. The consecutive high-energy bursts caused new cracks to appear and new portions of gas to escape. During the violent oscillati-

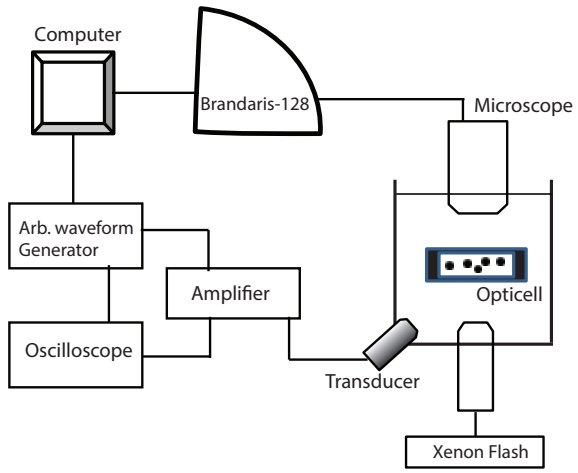

Figure 1
Schematic illustration of the opto-acoustic experimental setup including the ultra-high-speed optical Brandaris-128 camera.

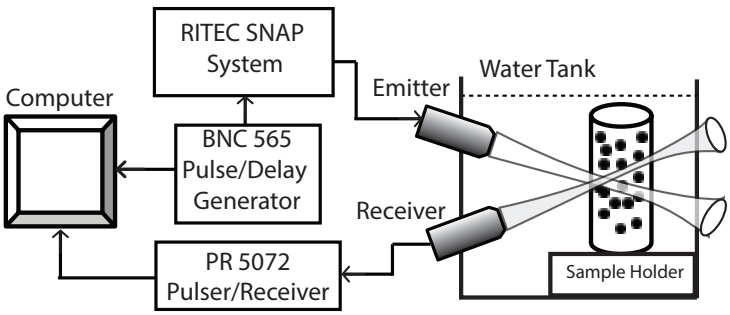

Figure 2
Schematic illustration of the acoustic set-up

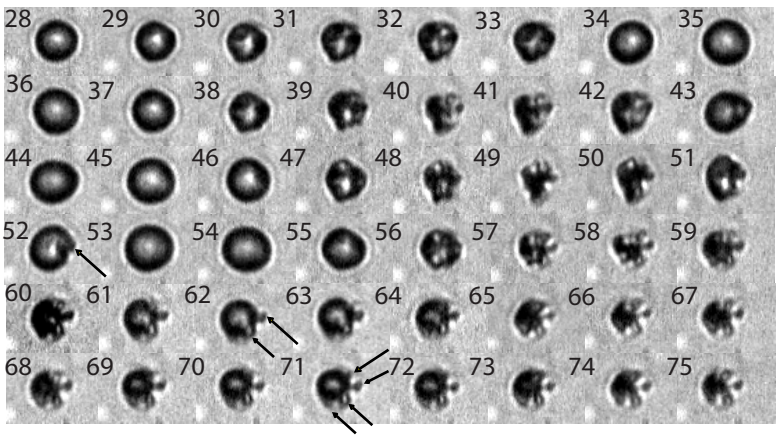

Figure 3
Sequence of 50 image frames of a 4.2 µm PVA-MB driven by 10 cycles of an ultrasound burst at a 2 MHz frequency with a P-pk=1 Mpa.

Figure 4
Sequence of 7 image frames of a broken PVA-MB at insonation frequencies of 2.2, 2.4, 2.6, 2.8, and 3.0 MHz.

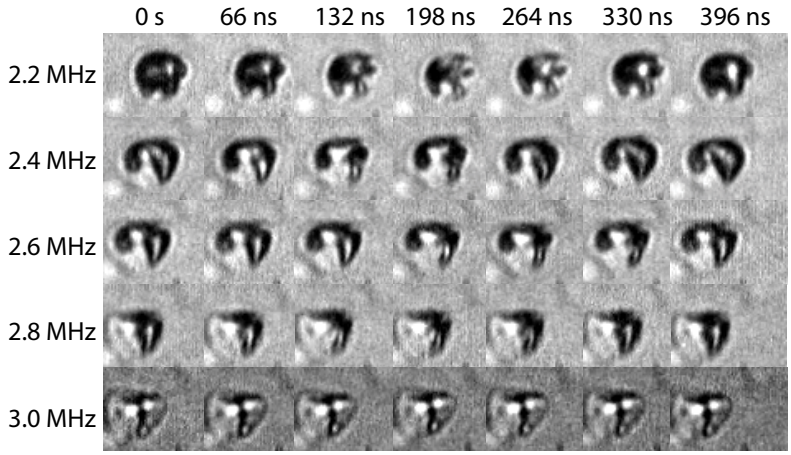

Figure 5
Average peak-to-peak amplitude of the scattered signal upon insonation by an incident pulse with a P-pk of 0.75 MPa, 0.9 MPa, or 1.0 MPa at a PRF equal to 100 Hz (a) or 500 Hz (b).

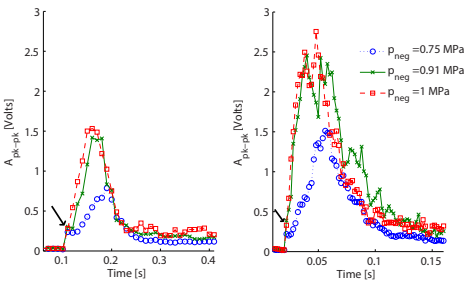

Figure 6
The average peak-to-peak amplitude of the scattered signal upon insonation by an incident pulse with P-pk of 1 MPa at PRF equal to 100 Hz. 4 characteristic regions A,B,C, and D are highlighted.

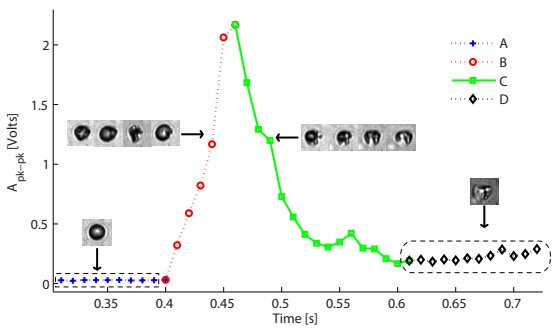

Figure 7
Average power spectra of the backscattered signals at corresponding regions (A, B, C, and D) illustrated in Figure 6.

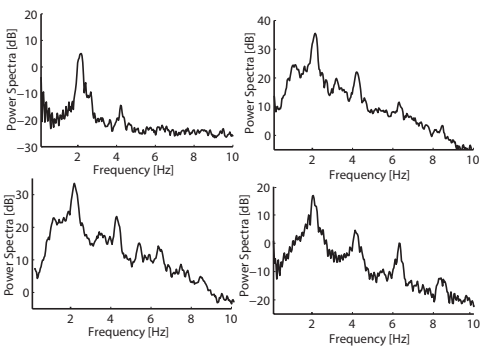

ons, the shell exhibited buckling modes. In Figure 7b and 7c, such behavior was characterized by the presence of an acoustic emission that constituted second-, ultra- and sub-harmonics, which is typical for non-linear stable cavitation [363]. In region D, the shell was intact after gas had escaped, which was also observed in other types of polymer-shelled MBs [360,361,380,381]. In this regime, the $A_{pk\text{-}pk}$ voltage reached a plateau, which represented the scattered signals from the intact gasless shell. The optical experiments confirmed this finding with the absence of radial oscillations of the broken PVA-MB. The high harmonics observed in the corresponding power spectrum (Figure 7d) are mostly due to non-linear propagation of the excitation pulse [357].

Discussion

Both the qualitative (optical visualization) and quantitative (acoustic scattered signal interrogation) assessment of PVA-MBs at high insonation pressures revealed that the fracturing mechanism of PVA-MBs was unique and different from the previously reported fracturing behavior of polymer-shelled MBs. The optical experiments performed on the hard-shelled MBs such as albumin-shelled MBs, e.g., QuantisonTM (Upperton Limited, Nottingham, UK), bi-layered shelled MBs (where the outermost layer is albumin and the inner layer is a biodegradable polymer), e.g., PB127 (POINT Biomedical Corporation, San Carlos, CA), polymer-shelled MBs, BG1135 (Bracco Diagnostics, Inc.), and polymer-shelled MBs, based on PFO-PLLA microcapsules, demonstrated that the gas escapes through the shell defects and that the escaped gas formed a new free gas bubble that lasted for approximately 40 ms [360,361,366,380,381]. The opto-acoustical experiments on PVA-MBs presented in this paper revealed buckling modes of oscillation at high, i.e., P^{-}_{pk} = 1 MPa, amplitude excitations. This is a novel feature of PVA-MBs that was not reported previously, which also does not follow the traditional governing theory described by the Marmottant model [382,383].

Both experimental approaches indicate that the PVA-MBs were not destroyed with the arrival of the first ultrasonic burst of high power. Several consecutive, closely spaced in time, and high power bursts are required to rupture these MBs or, in other words, to release the gas from the PVA shell. For every compression acoustic cycle, only a small fraction of gas squeezes out through the cracks. The broken PVA-MB with several tailpieces was still acoustically active, and the acoustical response to the high power bursts increased continuously to its maxi-

mum, which was followed by an exponential decrease after 10 to 30 insonation bursts. Moreover, there was no evidence of release of significant amounts of gas through the PVA shell defects in the optical experiments, demonstrating that the gas escapes slowly through the thick shell. Tzvetkov et al. reported that the shell of PVA-MBs is anisotropic and contains not only polymers but rather a combination of cross-linked PVA chains mixed with water and air [384]. In addition, a substantial gradient density was depicted with a more compact structure closer to the core and less dense structures towards the outer surface. The gas escaping not directly from the core but from/through the PVA shell itself is similar to the lipid shedding behavior. Here, the diameter of the lipid-shelled MB decreased with the number of insonation pulses and the shrunk MB subsequently returned to a stable spherical state [368]. The gas shedding from the PVA shell, which we refer to as "pumping-out" behavior, that was observed during several insonation pulses might be the reason for the gradual increase in the acoustic scattered signal (region B Figure 6). In the power spectrum, as shown in Figure 7b, such behavior is characterized by the presence of second-, ultra- and sub-harmonics, which shows a typical view of non-linear stable cavitation [355]. To the best of author's knowledge, such "pumping-out" behavior is unique and not reported elsewhere. This "pumping out" behavior could be primarily due to the air molecules that are trapped between the cross-linked PVA chains that constitute the MB shell. In all previous studies on the destruction/replenishment method for tissue perfusion quantification, a sharp increase in the video intensity followed by a decrease in amplitude due to gas dissolution was found [385]. Thus, there was no "pumping-out" behavior, and region B, evaluated previously [359,386], was simply a step function for thin-shelled phospholipid MBs or thick-shelled polymer MBs. The air pockets in the cross-linked PVA chains could be utilized for loading therapeutic gases, such as nitric oxide (NO). The loaded therapeutic gases could be efficiently and selectively delivered to the area of interest using the above described "pumping-out" behavior. Local therapeutic gas delivery is of great clinical interest and the subject of extensive research [47]. Thus, the NO loading possibilities of PVA-MBs and their delivery capabilities with the "pumping-out" mechanism should be tested. In addition, single PVA-MBs could be detected using special signatures, i.e., sub- and ultra- harmonics generated from different modes of PVA-MB oscillation. Moreover, the PVA shell offers the possibility to attach larger target amounts of ligands. Thus, local, targeted and tissue-specific drug delivery is possible [46,134,372]. This new type of ultrasound contrast agent possesses a multi-supportive robust shell that can successfully be utilized for local ultrasound triggered therapeutic gas as well as drug/gene delivery applications.

Conclusion

The unique “pumping-out” of gas through the PVA-MBs shell was observed with a Brandaris-128 camera and was confirmed acoustically. The “pumping-out” mechanism can be further utilized to deliver therapeutic gases, such as nitric oxide (NO), or anesthetic gases, such as nitrogen dioxide (NO_2). Additionally, upon high power insonation, the PVA-MBs experienced violent oscillations in which the MB exhibits buckling. The buckling modes of oscillation generate the sub- and ultra-harmonics, which can be further utilized in the development of novel contrast specific visualization algorithms.

Discussion

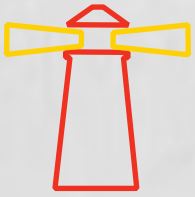

Contribution of this research

Ultrasound molecular imaging (UMI) with which biomarkers associated with diseases are imaged and quantified, have significantly contributed to understanding of pathological processes in cancer and cardiovascular diseases, especially atherosclerosis and neovascularization. In this research we focused on angiogenesis biomarkers, $\alpha_v\beta_3$ integrin, to quantify atherosclerosis plaque neovascularization using targeted microbubbles (tMBs) in apolipoprotein E-deficient ($ApoE^{-/-}$) mouse model. After a very general introduction in the first chapter, the state-of-the-art for UMI and therapy was extensively reviewed in the second chapter.

As it was discussed, the need for ultrasound images with higher resolution and the technological development in the manufacturing of ultrasound arrays have pushed the frequencies to above 15 MHz. Established contrast-specific imaging methods however, showed a disappointing sensitivity and specificity when applied to micro- ultrasound imaging. This posed the challenge we had to solve in the first place before going further with micro-UMI. As one possible solution, the use of the self-demodulation (S-D) signal was proposed as a means to enhance the subharmonic (SH) response of the MBs. This was initiated by the work of Vos et al. in 2011 [234], in which the S-D signal was used to excite the MBs. That approach was not a suitable method for our applications because a very high transmitted pressure is required to generate an S-D signal with enough amplitude. However, whether the S-D signal could be a push in generating the SH response of the MBs was still an open question. In the third and the fourth chapters, we extensively discussed how the envelope of an excitation signal generates S-D signals with different frequency content and how this can be applied for enhanced SH imaging of the ultrasound contrast agent (UCA). We showed that among the most commonly used excitation envelopes in the UMI (Gaussian, rectangular and an intermediate envelope), a rectangular envelope excitation can significantly enhance the SH response of the UCA compared to a Gaussian envelope excitation. We hypothesized that the reason for the observed enhancement was the broadband S-D signal with most of its energy at half the transmitted (subharmonic) frequency. However, care should be taken when exploiting this feature of a rectangular envelope, since an increase in the amplitude of the excitation can rapidly increase the low frequency S-D signal. A strong S-D signal in turn results in strong artifacts at the SH frequency, therefore degrading the contrast to tissue ratio (CTR) in SH images, as described in the fifth chapter.

In chapter five, using the most frequently used micro-ultrasound system in pre-

clinical applications (Vevo 2100, VisualSonics Inc.) we systematically compared the SH imaging with nonlinear fundamental (NF) and ultraharmonic (UH) imaging. SH imaging with rectangular envelope excitation performed very well with high sensitivity and specificity in media with low attenuation such as in a chicken embryo model. However, NF imaging was a more suitable approach for deeper and more attenuating media such as a mouse model. The largest CTR and contrast-to-artifact ratios for the SH images were achieved when pulse inversion was applied and for the NF images when amplitude modulation was used.

With these optimized imaging parameters for SH imaging of UCA at high frequencies, in the sixth chapter, SH response of MicroMarker UCA and four homemade UCAs with DSPC or DPPC as main lipid and different size distributions were compared *in vitro*. This was inspired by recent studies which have shown that the size distribution, manufacturing mechanism and microstructure on the lipid shell can influence the MBs SH response [6-8]. Our results showed that DPPC MBs have higher SH response than DSPC ones. At high concentration of the UCA, smaller MBs such as MicroMarker and our 'C' type UCAs produce the most homogeneous SH responses and are less affected by attenuation. Acknowledging the fact that the concentration of the UCA for UMI applications is very low, our findings suggested that our 'B' type MBs (main lipid DPPC, mean diameter of 1.95 μm) and the commercially available MicroMarker UCA are suitable choices for micro-ultrasound SH imaging.

Our research challenge in the seventh chapter was to develop an accurate and reliable method to quantify the bound tMBs in an *in vivo* environment. We presented a new quantification method which benefits from motion compensation and individual contrast spot detection, and is capable of distinguishing the bound MBs from unbound MBs based on their displacement. Our quantification method can be applied in studies performed with different imaging settings because it is less sensitive to imaging parameters. Moreover, it is more robust to tissue motion artifacts. Another advantage of our technique is that it can be applied without changing the imaging protocols which are widely used for ultrasound molecular imaging, since it is a post-processing method that utilizes the commonly used imaging sequences.

After improving the various steps involved in UMI, in the eighth chapter, we provided *in vitro* and *in vivo* proof-of-concept for UMI of $\alpha_v\beta_3$ integrin in carotid artery lesions and expanded vasa vasorum neovessels in animal models of atherosclerosis ($ApoE^{-/-}$ mice). We also showed that the salivary gland can be used

as an internal positive control for successful binding of tMBs to $\alpha_v\beta_3$ integrin. We showed that UMI with tMBs allows noninvasive assessment of the expression levels of $\alpha_v\beta_3$ on the vascular endothelium and may provide insights into early atherosclerotic plaque detection and treatment monitoring. Moreover, during the *in vivo* study, symptoms suggesting plaque disruption in the right brachiocephalic artery were observed in one of the animals. Histological analysis of the affected carotid artery and brachiocephalic trunk confirmed presence of intraplaque haemorrhage in advanced atherosclerotic lesions in the brachiocephalic trunk, with dissections and even cap rupture, pointing towards plaque rupture as the cause of the observed event. Although features suggestive of plaque rupture in $ApoE^{-/-}$ mice have been reported [33-38], whether plaque disruption actually occurs in mice has been a matter of debate in the past decade [39-45]. For the first time, we observed possible spontaneous plaque disruption in the right brachiocephalic artery of an $ApoE^{-/-}$ mouse in real-time with contrast enhanced ultrasonography. This observation is briefly documented in the ninth chapter.
In the tenth chapter, a new PVA MB was investigated using the high-speed Brandaris camera and an acoustical setup. the Its unique fracturing mechanism and pumping-out of gas through the shell was investigated optically and acoustically. Local delivery of therapeutic gas is great clinical interest and the subject of new researches [205]. Using the new PVA-shell microbubbles capable of encapsulating gas in between their crosslink, we hypothesized that the observed fracturing mechanism can be further utilized to deliver therapeutic gases such as nitric oxide (NO) or anesthetic gases such as nitrogen dioxide (NO_2).

Summary and outlook

In the last decade, micro-ultrasound molecular imaging has demonstrated its potentials for preclinical applications. Translation of the technology into the clinic is expected in the coming decade for early diagnostics of cancer and atherosclerosis and even for therapy when combined with drug delivery, sonoporation and high intensity focused ultrasound (HIFU). Moreover with recent improvements in the field of nanotechnology and nano-droplets, the application of UMI can stretch beyond vascular targets [387-395].
In this thesis we have investigated the major necessary steps for micro-ultrasound molecular imaging. Benefiting from acoustical and optical investigation methods on single MBs and populations of MBs, we have developed detection methods for imaging the UCA at high frequencies; we compared and optimi-

zed different lipid coated MBs for nonlinear contrast imaging; imaging protocols have been optimized for *in vivo* UMI preclinical applications. Furthermore, methods have been tested and proven in animal models of atherosclerosis and cancer. A plaque rupture event in an ApoE$^{-/-}$ mouse was captured live. Moreover, a unique PVA-shell UCA was investigated with the potential of local delivery of therapeutic gases.

Although numerous improvements in the field of UMI have been achieved, there is of course still plenty of room for further research and development. Some of these topics are: discovery of new molecular biosensors as well as more specific biomarkers associated with particular pathological process; enhancing the functionalization of MBs and targeting abilities; developing sensitive ultrasound imaging platforms dedicated to tMB imaging; and ideally real-time selective imaging of bound MBs in 3D. Moreover, the nonspecific binding of the tMBs which decreases the sensitivity and specificity of UMI methods needs more in-depth research.

In addition to mouse models, animal models that are naturally immunodeficient, such as the CAM (chicken chorioallantoic membrane) assay, are already used as translational models for cancer research. Its translucency and aese of use have made the CAM model a very suitable cancer model for optical tumor imaging methods. This includes real-time visualization and quantization of human cancer processes, such as tumor growth, neovascularization and dissemination, as well as validating novel anticancer drugs [396-400]. Contrast enhanced ultrasound imaging of the CAM model has been reported before for studying cardiovascular parameters and diseases [293-295] but with a very poor image resolution and sensitivity. However, as we showed in the sixth chapter of this thesis, sensitivity and specificity of contrast imaging in this model can be dramatically enhanced with real-time high frequency SH imaging. This can potentially introduce micro-UMI as a new imaging modality for monitoring tumor progression and effect of therapy in the CAM model.

One of the recent discoveries which might open up new potentials for UMI are gas vesicles produced by micro-organisms, such as bacteria and archaea. These gas-filled protein-shelled compartments have typical widths of 45–250 nm and lengths of 100–600 nm that exclude water and are permeable to gas [401,402]. Shapiro et al. [403] have very recently shown the potential applications of these gas vesicles as stable UCA *in vitro* and *in vivo*. Strikingly, the physical properties of these nano-structure gas vesicles are genetically encoded, enabling multiple modes of imaging.

UMI could also benefit from an improved imaging platform for SH imaging. Such an imaging platform needs to be equipped with broadband (> 70%) arrays and

optimized in transmit burst envelope, frequency, and amplitude. Furthermore, dedicated pulse sequences should be investigated to improve the SH imaging. Moreover SH imaging could potentially be used for real-time selective imaging of bound MBs, according to recent studies suggesting that bound MBs produce stronger SH signal than unbound ones [167,168].

Three dimensional (3D) UMI is also becoming more important, especially in serial studies in which imaging the same plane repeatedly in 2D is very challenging (if not impossible). As was discussed extensively in the second chapter, 3D UMI can be achieved by mechanically moving a 2D ultrasound probe in a controlled manner in applications where the target is not moving fast. However, with technological improvement in the field of 3D ultrasound transducers and imaging techniques, real-time 3D UMI of fast moving targets such as the heart would be possible also.

Also, perhaps combining imaging modalities in which endogenous as well as multimodal exogenous contrast agent are used can be beneficial. One of the possible applications for such multimodality molecular imaging is combining UMI with photoacoustic imaging. Photoacoustic imaging has shown its potentials for molecular imaging with both endogenous and exogenous contrast agent in various applications including atherosclerosis and cancer [404-413]. In photoacoustic imaging tissue chromophores are excited with a short laser pulse leading to thermoelastic expansion of the tissue. The result of such a process is a wideband ultrasonic wave which can be picked up by an ultrasound transducer. Nanodroplets are examples of exogenous dual-contrast agents that utilize vaporization for photoacoustic signal enhancement. They are consists of liquid perfluorocarbon nanodroplets with encapsulated nanoparticles. Upon pulsed laser irradiation and/or high intensity ultrasound pulses, liquid perfluorocarbon undergoes a liquid-to-gas phase transition generating very strong photoacoustic signals and the gaseous phase acts as UCAs [414,415].

Bibliography

1. Kusnetzky, L.L., et al., American College of Cardiology, 2008. 51(17): p. 1704-1706.
2. Dolan, M.S., et al., American College of Cardiology, 2009. 53(1): p. 32-38.
3. Abdelmoneim, S.S., et al., JACC: Cardiovascular Imaging, 2009. 2(9): p. 1048-1056.
4. Shaikh, S. M. C. K., et al., Ultrasound in Medicine, 2012. 31(11): p. 1863-1864.
5. Gabriel, R.S., et al., The American Journal of Cardiology, 2008. 102(9): p. 1269-72.
6. Helfield, B.L., et al., Ultrasound Medicine & Biology, 2012. 38(5): p. 846-63.
7. van Rooij, T., et al., Ultrasonics Symposium (IUS), IEEE International, 2013. 310(313): p. 21-25.
8. Kooiman, K., et al., European Journal of Lipid Science and Technology, 2014: p. 1217–1227.
9. Zhao, S., et al., Physics in Medicine & Biology, 2007. 52(8): p. 2055-72.
10. Hu, X., et al., Ultrasonics, Ferroelectrics, and Frequency Control, IEEE Transactions on, 2010. 57(2): p. 305-16.
11. Needles, A., et al., Ultrasound in Medicine & Biology, 2009. 35(9): p. 1564-73.
12. Mauldin, F.W., et al., Physics in Medicine and Biology, 2012. 57(16): p. 5275-93.
13. Pysz, M.A., et al., Clinical radiology, 2010. 65(7): p. 500-16.
14. Liu, H., et al., Journal of clinical ultrasound, 2011. 39(2): p. 83-90.
15. Kaufmann, B.A., et al., Circulation, 2007. 116(3): p. 276-284.
16. Kaufmann, B.A., et al., European heart journal, 2007. 28(16): p. 2011-7.
17. Kim, H., et al., Investigative Radiology, 2010. 45(10): p. 685-91.
18. Kaufmann, B.A., et al., Arteriosclerosis, Thrombosis, and Vascular Biology, 2010. 30(1): p. 54-9.
19. Hamilton, A., et al., Circulation, 2002. 105(23): p. 2772-8.
20. Deshpande, N., et al., Clinical radiology, 2010. 65(7): p. 567-81.
21. Korpanty, G., et al., Clinical cancer research, 2007. 13(1): p. 323-30.
22. Willmann, J.K., et al., Radiology, 2008. 248(3): p. 936-944.
23. Ellegala, D.B., Circulation, 2003. 108(3): p. 336-341.
24. Deshpande, N., et al., Radiology, 2011. 258(3): p. 804-811.
25. Barger, A.C., et al., The New England Journal of Medicine, 1984. 310(3): p. 175-7.
26. Moreno, P.R., et al., Circulation, 2006. 113(18): p. 2245-52.
27. Langheinrich, A.C., et al., Journal of Thrombosis and Haemostasis, 2007. 97(6): p. 873-9.
28. Hynes, R.O., Cell, 1987. 48(4): p. 549-54.
29. Hoshiga, M., et al., Circulation Research, 1995. 77(6): p. 1129-35.
30. Brooks, P.C., et al., Science, 1994. 264(5158): p. 569-71.
31. Haubner, R., European Journal of Nuclear Medicine and Molecular Imaging, 2006. 1: p. 54-63.
32. Leong-Poi, H., et al., Circulation, 2005. 111(24): p. 3248-54.
33. Rosenfeld, M.E., et al., Arteriosclerosis, Thrombosis, and Vascular Biology, 2000. 20(12): p. 2587-92.
34. Johnson, J.L. and Jackson, C.L., Atherosclerosis, 2001. 154(2): p. 399-406.
35. Calara, F., et al., The Journal of Pathology, 2001. 195(2): p. 257-63.
36. Zhou, J., et al., Arteriosclerosis, Thrombosis, and Vascular Biology, 2001. 21(9): p. 1470-6.

37. Jackson, C.L., et al., Arteriosclerosis, Thrombosis, and Vascular Biology, 2007. 27(4): p. 714-20.
38. Sasaki, T., et al., Arteriosclerosis, Thrombosis, and Vascular Biology, 2006. 26(6): p. 1304-9.
39. Schwartz, S.M., et al., Arteriosclerosis, Thrombosis, and Vascular Biology, 2007. 27(4): p. 705-713.
40. Jackson, C.L., Arteriosclerosis, Thrombosis, and Vascular Biology, 2007. 27(4): p. 973-977.
41. Hansson, G.K. and Heistad, D.D., Arteriosclerosis, Thrombosis, and Vascular Biology, 2007. 27(4): p. 697.
42. Bentzon, J.F. and Falk, E., Current Opinion in Lipidology, 2010. 21(5): p. 434-40.
43. Jawien, J., Current Pharmaceutical Biotechnology, 2012. 13(13): p. 2435-9.
44. Jin, S.X., et al., Arteriosclerosis, Thrombosis, and Vascular Biology, 2012. 32(10): p. 2372-9.
45. Falk, E., et al., Arteriosclerosis, Thrombosis, and Vascular Biology. 2007;27(4): p. 969-72.
46. Cavalieri, F., et al., Langmuir, 2005. 21(19): p. 8758-8764.
47. Kim, H., et al., International journal of nanomedicine, 2014. 9: p. 155.
48. Kaul, S., Circulation, 2008. 118(3): p. 291-308.
49. Alzaraa, A., et al., Hepatology Research, 2013. 43(8): p. 809-19.
50. Klibanov, A.L., Journal of Cardiovascular Translational Research, 2013. 6(5): p. 729-39.
51. Correas, J.M., et al., Acta radiologica. Supplement, 1997. 412: p. 101-12.
52. Greis, C., Clinical Hemorheology and Microcirculation, 2009. 43(1): p. 1-9.
53. Kooiman, K., et al., Advanced Drug Delivery Reviews, 2014. 72: p. 28-48.
54. Hernot, S. and Klibanov, A.L., Advanced Drug Delivery Reviews, 2008. 60(10): p. 1153-66.
55. Wu, H., et al., Ultrasound Medecince & Biology, 2013. 39(11): p. 2137-46.
56. Wang, L., et al., Prostate, 2013. 73(11): p. 1147-58.
57. Kooiman, K., et al., Journal of Controlled Release, 2011. 154(1): p. 35-41.
58. Alzaraa, A., et al., The American Journal of Surgery, 2012. 204(3): p. 355-66.
59. Unnikrishnan, S. and Klibanov A.L., American journal of roentgenology, 2012. 199(2): p. 292-9.
60. Kooiman, K., et al., European Journal of Lipid Science and Technology, 2014. 116(9): p. 1217–1227.
61. van Rooij, T., et al., Ultrasonics Symposium (IUS), IEEE International, 2013. 310(313): p. 21-25.
62. Myrset, A.H., et al., Ultrasound in Medicine & Biology, 2011. 37(1): p. 136-50.
63. Marsh, D., et al., Biochimica et Biophysica Acta, 2003. 1615(1-2): p. 33-59.
64. Ottoboni, S., et al., Contrast Media & Molecular Imaging, 2006. 1(6): p. 279-90.
65. Chen, C.C. and Borden, M.A., Biomaterials, 2011. 32(27): p. 6579-87.
66. Kiessling, F., et al., Advanced Drug Delivery Reviews, 2014. 72: p. 15-27.
67. Hernot, S., et al., Journal of controlled release, 2012. 158(2): p. 346-53.
68. Nakatsuka, M.A., et al., Advanced Materials, 2012. 24(45): p. 6010-6.
69. Wheatley, M.A., et al., Biomacromolecules, 2007. 8(2): p. 516-22.
70. Paganelli, G., et al., European Journal of Nuclear Medicine, 1992. 19(5): p. 322-9.
71. Wei, X., et al., Translational Oncology, 2014. 7(2): p. 284-91.
72. Pochon, S., et al., Investigative Radiology, 2010. 45(2): p. 89-95.
73. Fokong, S., et al., Investigative Radiology, 2013. 48(12): p. 843-50.
74. Jun, H.Y., et al., Academic Radiology, 2010. 17(1): p. 54-60.
75. Otani, K. and Yamahara, K., Molecular Imaging and Biology, 2013. 15(5): p. 534-41.
76. Wijkstra H, et al., The 17th European Symposium on Ultrasound imaging. 2012.
77. Wen, Q., et al., Journal of Nanoscience and Nanotechnology, 2014. 14(1): p. 190-209.

78. Rychak, J.J., et al., Journal of controlled release, 2006. 114(3): p. 288-99.
79. Wang, X., et al., Circulation, 2012. 125(25): p. 3117-26.
80. Schumann, P.A., et al., Investigative Radiology, 2002. 37(11): p. 587-93.
81. Cheng, C., et al., Atherosclerosis, 2007. 195(2): p. 225-35.
82. Nakatsuka, M.A., et al., Biomaterials, 2013. 34(37): p. 9559-65.
83. Thompson, I.M., et al., The New England Journal of Medicine, 2004. 350(22): p. 2239-46.
84. Perner, S., et al., Human Pathology, 2007. 38(5): p. 696-701.
85. Sanna, V., et al., Molecular Pharmacology, 2011. 8(3): p. 748-57.
86. Tsuruta, J.K., et al., PLOS ONE, 2014. 9(1): p. e86642.
87. Lutz, A.M., et al., Clinical cancer research, 2014. 20(5): p. 1313-22.
88. Foygel, K., et al., Gastroenterology, 2013. 145(4): p. 885-894 e3.
89. Knowles, J.A., et al., Archives of otolaryngology--head & neck surgery, 2012. 138(7): p. 662-8.
90. Koopman, G., et al., Blood, 1994. 84(5): p. 1415-20.
91. Ferrante, E.A., et al., Journal of Controlled Release, 2009. 140(2): p. 100-107.
92. Warram, J.M., et al., Journal of Ultrasound in Medicine, 2011. 30(7): p. 921-931.
93. Ham, A.S., et al., Langmuir, 2009. 25(17): p. 10038-10044.
94. Maul, T.M., et al., Biotechnology and bioengineering, 2010. 107(5): p. 854-64.
95. Kawan, S. and Hiroshi, W., Japanese Journal of Applied Physics, 2000. 39(5S): p. 3230.
96. Stride, E., et al., Ultrasound in Medicine & Biology, 2009. 35(5): p. 861-8.
97. Soetanto, K. and Watarai H., The 25th Annual International Conference of the IEEE, 2003. 2:p.1226-1229.
98. Owen, J., et al., International Journal of Hyperthermia, 2012. 28(4): p. 362-373.
99. Borden, M.A., et al., Molecular imaging, 2006. 5(3): p. 139-47.
100. Borden, M.A., et al., Molecular imaging, 2013. 12(0): p. 1-8.
101. Wang, S., et al., Physics in Medicine and Biology, 2014. 59(2): p. 465-484.
102. Frinking, P.J., et al., Ultrasound in Medicine & Biology, 2012. 38(8): p. 1460-9.
103. Kokhuis, T.J.A., et al., Biotechnology and bioengineering, 2014: p. 220-227.
104. Kim, D.H., et al., Langmuir, 2000. 16(6): p. 2808-2817.
105. Sboros, V., et al., Biointerfaces, 2010. 80(1): p. 12-17.
106. Takalkar, A.M., et al., Journal of controlled release, 2004. 96(3): p. 473-82.
107. Kokhuis, T.J.A., et al., Ultrasound in Medicine & Biology, 2013. 39(3): p. 490-506.
108. Garbin, V., et al., Applied Physics Letters, 2007. 90(11): p. 114103.
109. Leighton, T.G., The Acoustic Bubble1994, London, UK: Academic Press.
110. Chetty, K., et al., IEEE Trans Ultrason Ferroelectr Freq Control, 2008. 55(6): p. 1333-42.
111. Faez, T., et al., Ultrasound in Medicine & Biology, 2011. 37(2): p. 338-42.
112. Gorce, J.M., et al., Investigative Radiology, 2000. 35(11): p. 661-71.
113. Helfield, B.L. and Goertz D.E., Journal of the Acoustical Society of America, 2013. 133(2): p. 1158-68.
114. McKendry, J.E.G., et al,. Bubble Science, Engineering and Technology, 2010. 2(2).p. 48-54.
115. Abou-Saleh, R.H., et al., Langmuir, 2013. 29(12): p. 4096-103.
116. Lindner, J.R., et al., Circulation, 2001. 104(17): p. 2107-2112.
117. van der Meer, S.M., et al., Journal of the Acoustical Society of America, 2007. 121(1): p. 648-56.
118. Marmottant, P., et al., Journal of the Acoustical Society of America, 2005. 118(6): p. 3499-3505.

119. Dieluweit, S., et al., Langmuir, 2010. 26(13): p. 11041-9.
120. Darst, S.A., et al., Biophysical Journa, 1991. 59(2): p. 387-96.
121. Borden, M.A., et al., IEEE Trans Ultrason Ferroelectr Freq Control, 2005. 52(11): p. 1992-2002.
122. Overvelde, M., et al., Ultrasound in Medicine & Biology, 2011. 37(9): p. 1500-8.
123. Schneider, M., et al., Investigative Radiology, 1995. 30(8): p. 451-7.
124. Schneider, M., et al., Investigative Radiology, 1997. 32(7): p. 410-7.
125. Krause, W., Topics in Current Chemistry, 2002: P.222.
126. Life Technologies, Proteins and Amino Acids, Thermo Scientific Inc.: Waltham, MA, USA.
127. Klibanov, A.L., Medical & Biological Engineering & Computing, 2009. 47(8): p. 875-82.
128. Klibanov, A.L., et al., Investigative Radiology, 2004. 39(3): p. 187-95.
129. Zhao, S., et al., Applied Physics Letters, 2005. 87: p. 134103.
130. Zhao, S., et al., Journal of the Acoustical Society of America, 2006. 120(6): p. EL63-9.
131. Casey, J., et al., Ultrasound in Medicine & Biology, 2013. 39(5): p. 903-14.
132. Helfield, B.L., et al., Ultrasound in Medicine & Biology, 2013. 39(2): p. 345-59.
133. Schmidt, B.J., et al., Journal of controlled release, 2008. 131(1): p. 19-26.
134. Cerroni, B., et al., Biomacromolecules, 2011. 12(3): p. 593-601.
135. Grishenkov, D., et al., Ultrasonics, 2011. 51(1): p. 40-8.
136. de Jong, N., et al., Echocardiography, 2002. 19(3): p. 229 - 240.
137. Eller, A. and Flynn H.G., Journal of the Acoustical Society of America, 1969. 46(3 (part2)): p. 772 - 727.
138. Chomas, J., et al., IEEE Trans Ultrason Ferroelectr Freq Control, 2002. 49(7): p. 883-892.
139. Goertz, D.E., et al., Ultrasound in Medicine & Biology, 2007. 33(12): p. 1859-72.
140. Needles, A., et al., Ultrasound in Medicine & Biology, 2008. 34(7): p. 1139-51.
141. Wu, C.Y., et al., Ultrasound in Medicine & Biology, 2005. 31(9): p. 1199-210.
142. Deng, C.X., et al., Ultrasound in Medicine & Biology, 2000. 26(5): p. 819-31.
143. Shi, W.T. and Forsberg F., Ultrasound in Medicine & Biology, 2000. 26(1): p. 93 - 104.
144. Chen, S., et al., Ultrasonics, 2006. 44 Suppl 1: p. e123-6.
145. Burns, P.N., et al. Ultrasonics Symposium (IUS), IEEE International, 1994. 3: p. 1547-1550.
146. Pi Hsien, C., et al., Ultrasonics, Ferroelectrics, and Frequency Control, IEEE Transactions on, 1995. 42(6): p. 1020-1027.
147. Simpson, D.H. and Burns P.N., Ultrasonics Symposium (IUS), IEEE International, 1999. 46: p. 372-382.
148. de Jong, N., et al., Ultrasonics, 2000. 38(1–8): p. 87-92.
149. Deng, C.X. and Lizzi F.L., Ultrasound in Medicine & Biology, 2002. 28(3): p. 277-86.
150. Foster, F.S., et al., Interface Focus, 2011. 1(4): p. 576-601.
151. Needles, A., et al., Ultrasound in Medicine & Biology, 2010. 36(12): p. 2097-106.
152. Lyshchik, A., et al., Journal of Ultrasound in Medicine, 2007. 26(11): p. 1575-1586.
153. Rychak, J., et al., Molecular imaging, 2007. 6(5): p. 289-96.
154. Willmann, J.K., et al., Radiology, 2008. 246(2): p. 508-518.
155. Moran, C.M., et al., Ultrasound in Medicine & Biology, 2002. 28(6): p. 785-91.
156. ten Kate, G.L., et al., Ultrasound in Medicine & Biology, 2012. 38(4): p. 593-600.
157. Tang, M.-X., et al., Ultrasound in Medicine & Biology, 2010. 36(3): p. 459-466.
158. Renaud, G., et al., Ultrasonics Symposium (IUS), IEEE International, 2012. 1(4): p. 7-10.

159. Yu, H., et al., American journal of roentgenology, 2010. 194(3): p. 653-9.
160. Thapar, A., et al., Radiology, 2012. 262(2): p. 672-9.
161. Hansen, R., et al. The 10th European Symposium on Ultrasound Contrast Imaging, 2005.
162. Frijlink, M.E., et al., The Journal of the Acoustical Society of America, 2006. 120(3): p. 1723-31.
163. Jimenez-Fernandez, Ultrasonics, 2012. 52(6): p. 784-93.
164. Park, J., et al., Ultrasonics, 2013. 53(2): p. 369-376.
165. Shen, C.C. and Lin, C.H., IEEE Trans Ultrason Ferroelectr Freq Control, 2012. 59(11): p. 2420-30.
166. Park, J., et al., Annals of Biomedical Engineering, 2013. 41(1): p. 41-52.
167. Sprague, M.R., et al., Ultrasound in Medicine & Biology, 2010. 36(2): p. 313-24.
168. Helfield, B.L., et al., Ultrasound in Medicine & Biology, 2013. 39(2): p. 345-359.
169. Tjo/tta, J.N. and Tjo/tta, S., The Journal of the Acoustical Society of America, 1980. 68(1): p. 334-339.
170. Faez, T., et al., Ultrasound in Medicine & Biology, 2011. 37(6): p. 958-970.
171. Shankar, P.M., et al., Ultrasound in Medicine & Biology, 1998. 24(3): p. 395-399.
172. Forsberg, F., et al., IEEE Trans Ultrason Ferroelectr Freq Control. 200, 552(4):581-3.
173. Zhang, D., et al., Physics in Medicine and Biology, 2007. 52(18): p. 5531-44.
174. Daeichin, V., et al., Physics in Medicine and Biology, 2012. 57(12): p. 3675-91.
175. Zheng, H., et al., Ultrasound in Medicine & Biology, 2005. 31(1): p. 99-108.
176. Biagi, E., et al., IEEE Trans Ultrason Ferroelectr Freq Control. 2006, 53(11): p. 2174-82.
177. Masotti, L., et al., Acoustical Imaging, 2007, Springer Netherlands. p. 307-315.
178. Zhang, D., et al., Physics in Medicine and Biology, 2009. 54(13): p. 4257-72.
179. Streeter, J.E., et al., Molecular imaging, 2010. 9(2): p. 87-95.
180. Sorace, A.G., et al., Journal of Ultrasound in Medicine, 2012. 31(10): p. 1543-50.
181. Streeter, J.E., et al., Molecular Imaging, 2011. 10(6): p. 460-8.
182. Stieger, S.M., et al., Contrast Media & Molecular Imaging, 2008. 3(1): p. 9-18.
183. Piedra, M., et al., Cerebrovascular diseases, 2009. 2: p. 66-74.
184. Dayton, P.A. and Rychak, J.J., Front Biosci, 2007. 12: p. 5124-42.
185. Anderson, C.R., et al., Investigative Radiology, 2011. 46(4): p. 215-24.
186. Itani, M. and Mattrey, R.F., Molecular imaging and biology, 2012. 14(1): p. 40-6.
187. Wible, J.H., Jr., et al., Journal of the American Society of Echocardiography, 1996. 9(4): p. 442-51.
188. McDannold, N., et al., Ultrasound in Medicine & Biology, 2011. 37(8): p. 1259-70.
189. Mullin, L., et al., Contrast Media & Molecular Imaging, 2011. 6(3): p. 126-31.
190. Pysz, M.A., et al., Quantitative imaging in medicine and surgery, 2012. 2(2): p. 68-80.
191. Daeichin, V., et al. Ultrasonics Symposium (IUS), IEEE International, 2013. 1825(1828): p. 21-25.
192. Barua, A., et al., International Journal of Gynecological Cancer, 2014. 24(1): p. 19-28
193. Kuliszewski, M.A., et al., Cardiovascular research, 2009. 83(4): p. 653-62.
194. Bachawal, S.V., et al., Cancer Research, 2013. 73(6): p. 1689-98.
195. Grouls, C., et al., Radiology, 2013. 267(2): p. 487-95.
196. Khanicheh, E., et al., PLOS ONE, 2013. 8(3): p. e58761.
197. Khanicheh, E., et al., Arteriosclerosis, Thrombosis, and Vascular Biology, 2013. 33(9): p. 2187-92.
198. Pysz, M.A., et al., Radiology, 2010. 256(2): p. 519-27.
199. BaronToaldo, M., et al., the official publication of the Academy of Molecular Imaging, 2014.

200. Korpanty, G., et al., Clinical Cancer Research, 2007. 13(1): p. 323-30.
201. Palmowski, M., et al., Molecular Cancer Therapeutics, 2008. 7(1): p. 101-9.
202. Sirsi, S.R., et al., Ultrasound in Medicine & Biology, 2012. 38(6): p. 1019-29.
203. Streeter, J.E., et al., Technology in cancer research & treatment, 2013. 12(4): p. 311-21.
204. Flisikowska, T., et al., Transgenic Research, 2013. 22(4): p. 673-80.
205. Kim, H., et al., International Journal of Nanomedicine, 2014. 9: p. 155-65.
206. Chadderdon, S.M., et al., Circulation, 2014. 129(4): p. 471-8.
207. Davidson, B.P., et al., Journal of the American Society of Echocardiography, 2014. 27(7): p. 786-793.
208. Streeter, J.E., et al., Molecular imaging, 2011. 10(6): p. 460-8.
209. Streeter, J.E. and Dayton, P.A., Theranostics, 2013. 3(2): p. 93-8.
210. Bzyl, J., et al., European Radiology, 2013. 23(2): p. 468-75.
211. Hu, X., et al., American Journal of Nuclear Medicine and Molecular Imaging, 2013. 3(4): p. 336-49.
212. Lentacker, I., et al., Advanced Drug Delivery Reviews, 2014. 72: p. 49-64.
213. Bao, S., et al., Ultrasound in Medicine & Biology, 1997. 23(6): p. 953-9.
214. McLaughlan, J., et al., IEEE Trans Ultrason Ferroelectr Freq Control, 2013. 60(12): p. 2511-20.
215. Phillips, L.C., et al., IEEE Trans Ultrason Ferroelectr Freq Control, 2012. 59(7): p. 1596-1601.
216. Chang, S., et al., Ultrasonics Sonochemistry, 2013. 20(1): p. 171-9.
217. Xie, A., et al., JACC Cardiovascular Imaging, 2012. 5(12): p. 1253-1262.
218. Tlaxca, J.L., et al., Journal of Controlled Release, 2013. 165(3): p. 216-25.
219. Xie, A., et al., JACC Cardiovascular Imaging, 2012. 5(12): p. 1253-1262.
220. Liu, H., et al., Molecular Pharmaceutics, 2014. 11(1): p. 40-8.
221. Yan, F., et al., Ultrasound in Medicine & Biology, 2011. 37(5): p. 768-79.
222. Pu, C., et al., Molecular Pharmaceutics, 2014. 11(1): p. 49-58.
223. Fan, C.H., et al., Biomaterials, 2013. 34(8): p. 2142-55.
224. McLaughlan, J., et al., IEEE Trans Ultrason Ferroelectr Freq Control, 2013. 60(12): p. 2511-20.
225. Fan, Z., et al., Journal of Controlled Release, 2010. 142(1): p. 31-9.
226. van Wamel, A., et al., Journal of Controlled Release, 2006. 112(2): p. 149-55.
227. Kotopoulis, S. and Postema, M., Ultrasonics, 2010. 50(2): p. 260-268.
228. Hu, X., et al., Investigative Radiology, 2012. 47(7): p. 398-405.
229. Joo Ha, H. and Crum, L.A., Engineering in Medicine and Biology Society, 2009. EMBC 2009. Annual Internati onal Conference of the IEEE, 2009: p. 130-133
230. Xiaoping, L. and Leizhen, Z., International Journal of Hyperthermia, 2013. 29(7): p. 678-82.
231. Zhou, Y., et al., Advanced Materials, 2013. 25(30): p. 4123-30.
232. Rask-Andersen, M., et al., Trends in Pharmacological Sciences, 2014.
233. Burns, P.N., Clinical radiology, 1996. 1: p. 50-5.
234. Vos, H.J., et al., IEEE Trans Ultrason Ferroelectr Freq Control, 2011. 58(5): p. 924-34.
235. Shi, W.T., et al., Ultrasonics Symposium (IUS), IEEE International, 2002. 2: p. 8-11.
236. Feinstein, S.B., Heart and circulatory physiology, 2004. 287(2): p. H450-7.
237. Sarkar, K., et al., Journal of the Acoustical Society of America, 2005. 118(1): p. 539 - 550.
238. Goertz, D.E., et al., Investigative Radiology, 2006. 41(8): p. 631-8.
239. Newhouse, V.L. and Shankar, P.M., Journal of Acoustical Society of America, 1984. 75(5): p. 1473-1477.

240. Wu, C.Y. and Tsao J., The Journal of the Acoustical Society of America, 2003. 114(5): p. 2662-71.
241. Bouakaz, A., et al., Ultrasonics, Ferroelectrics, and Frequency Control, IEEE Transactions on, 2007. 54(11): p. 2283-2290.
242. Cherin, E., et al., Ultrasound in Medicine & Biology, 2008. 34(6): p. 949-62.
243. Masoy, S.E., et al., IEEE Trans Ultrason Ferroelectr Freq Control, 2008. 55(5): p. 1112-21.
244. Faez, T., et al., Physics in Medicine and Biology, 2011. 56(19): p. 6459.
245. Yeh, C.K., et al., IEEE Trans Ultrason Ferroelectr Freq Control, 2008. 55(10): p. 2164-76.
246. Yeh, C.K., et al., IEEE Trans Ultrason Ferroelectr Freq Control. 2009. 56(5): p. 1113-8.
247. Shen, C.C., et al., IEEE Trans Ultrason Ferroelectr Freq Control, 2007. 54(7): p. 1370-81.
248. Shankar, P.M., et al., The Journal of the Acoustical Society of America, 1999. 106(4 Pt 1): p. 2104-10.
249. Forsberg, F., et al., Ultrasonics, 2000. 38(1-8): p. 93-8.
250. Dayton, P.A. and Ferrara, K.W., Journal of Magnetic Resonance Imaging, 2002. 16(4): p. 362-77.
251. Lotsberg, O., et al., The Journal of the Acoustical Society of America, 1996. 99(3): p. 1366-1369.
252. Krishna, P.D., et al., Physics in Medicine and Biology, 1999. 44(3): p. 681-94.
253. Shi, W.T., et al., Ultrasonic Imaging, 1999. 21(2): p. 79-94.
254. Bhagavatheeshwaran, G., et al., Ultrasound in Medicine & Biology, 2004. 30(2): p. 199-203.
255. Goertz, D., et al., IEEE Trans Ultrason Ferroelectr Freq Control, 2005. 52(1): p. 65-79.
256. Forsberg, F., et al., Radiology, 2007. 244(3): p. 718-26.
257. Katiyar, A. and Sarkar, K., The Journal of the Acoustical Society of America, 2011. 130(5): p. 3137-3147.
258. Shi, W., et al., Ultrasound in Medicine & Biology, 1999. 25(2): p. 275-283.
259. Sijl, J., et al., The Journal of the Acoustical Society of America, 2010. 128: p. 3239.
260. Shen, C.C., et al., IEEE Trans. Ultrason. Ferroelectr. Freq. Control, 2011. 58(2): p. 379-388.
261. Marmottant, P., et al., Journal of the Acoustical Society of America, 2005. 118(6): p. 3499 - 3505.
262. Berktay, H.O., Journal of Sound and Vibration, 1965. 2(4): p. 435-461.
263. Averkiou, M.A., et al., The Journal of the Acoustical Society of America, 1993. 94(5): p. 2876-2883.
264. Vos, H.J., et al., The Journal of the Acoustical Society of America, 2010. 127(3): p. 1208-17.
265. Raab, D. and Green, E., Psychometrika, 1961. 26(4): p. 447-450.
266. Hamilton, M.F. and Blackstock, D.T., Nonlinear Acoustics1998: Academic Press.
267. Lee, Y.S. and Hamilton, M.F., The Journal of the Acoustical Society of America, 1995. 97(2): p. 906-917.
268. Averkiou, M.A. and Hamilton, M.F., The Journal of the Acoustical Society of America, 1997. 102(5 Pt 1): p. 2539-48.
269. Callé, S., et al., Ultrasonics, 2002. 40(1–8): p. 873-878.
270. Conversano, F.R.F., et al., Sensors & Transducers. IFSA Publishing S.L. , 2010. 9: p. 21-27.
271. Eisenbrey, J.R., et al., Ultrasonics, 2011. 51(8): p. 890 - 897.
272. Renaud, G., et al., Applied Physics Letters, 2012. 100(10): p. 101911.
273. Ritter, T.A., et al., Ultrasonics, Ferroelectrics, and Frequency Control, IEEE Transactions on, 2002. 49(2): p. 217-230.
274. Lukacs, M., et al., Ultrasonics, Ferroelectrics, and Frequency Control, IEEE Transactions on, 2006. 53(10): p. 1719-1729.
275. Brown, J.A., et al., IEEE Trans Ultrason Ferroelectr Freq Control, 2007. 54(9): p. 1888-94.
276. Foster, F., et al., Ultrasound in Medicine & Biology, 2009. 35(10): p. 1700-8.

277. Shung, K., et al., Conf Proc IEEE Eng Med Biol Soc, 2009. 5(10): p. 5333463.
278. Wilson, S.R. and Burns, P.N., Radiology, 2010. 257(1): p. 24-39.
279. Cachard, C., et al., Ultrasound in Medicine & Biology, 1997. 23(5): p. 705-17.
280. Blackstock, D.T., Fundamentals of physical acoustics, New York: New York : Wiley, 2000.
281. Cosgrove, D. and Lassau, N., Journal de Radiologie, 2009. 90(1 Pt 2): p. 156-64.
282. Maresca, D., et al., Ultrasound in Medicine & Biology, 2013. 39(4): p. 706-13.
283. Brock-Fisher, G.A., M.K.D. Poland, and P.G. Rafter, Means for increasing sensitivity in non-linear ultrasound imaging systems, Patents 1996.
284. Haider, B. and Chiao, R.Y., Ultrasonics Symposium (IUS), IEEE International, 1999. 2: p. 1527-1531.
285. Teirlinck, C.J.P.M., et al., Ultrasonics, 1998. 36(1–5): p. 653-660.
286. Harput, S., et al., IEEE Trans Ultrason Ferroelectr Freq Control, 2013. 60(12): p. 2532-44.
287. Sun, C., et al., Ultrasound in Medicine & Biology, 2012. 38(7): p. 1262-70.
288. Goertz, D.E., et al., Ultrasound in Medicine & Biology, 2006. 32(4): p. 491-502.
289. Shekhar, H. and Doyley, M.M., Medical Physics, 2012. 39(4): p. 2049-60.
290. Renaud, G., et al., Ultrasonics Symposium (IUS), IEEE International, 2011..
291. Eisenbrey, J.R., et al., Academic Radiology, 2012. 19(6): p. 732-9.
292. Sridharan, A., et al., Investigative Radiology, 2013. 48(9): p. 1-7.
293. Schellpfeffer, M.A., et al., Birth Defects Res A Clin Mol Teratol, 2005. 73(1): p. 39-49.
294. Schellpfeffer, M.A. and Kolesari, G.L., Ultrasound in Medicine & Biology, 2012. 38(3): p. 504-10.
295. Fechner, S., et al., Ultrasound Obstet Gynecol, 2008. 31(3): p. 277-83.
296. Arditi, M., et al., IEEE Trans Ultrason Ferroelectr Freq Control, 2006. 53(6): p. 1118-29.
297. Kaufmann, B.A. and Lindner, J.R., Current opinion in biotechnology, 2007. 18(1): p. 11-6.
298. Iagaru, A. and Gambhir, S.S., American journal of roentgenology, 2013. 201(2).
299. Jensen, J.A., 10th nordicbaltic conference on biomedical imaging,1996. 4: p. 351-353.
300. Huo, E., et al., The Journal of the Acoustical Society of America, 2010. 128(4): p. 2280-2280.
301. Dynarowicz-Latka, P. and Hac-Wydro, k., Colloids Surf B Biointerfaces, 2004. 37(1-2): p. 21-5.
302. Kurniawan, Y., et al., Langmuir, 2013. 29(34): p. 10817-10823.
303. Carmeliet, P. and Jain, R.K., Nature, 2000. 407(6801): p. 249-57.
304. Alauddin, M.M. and Gelovani, J.G., Current Topics in Medicinal Chemistry, 2010. 10(16): p. 1617-32.
305. Sipkins, D.A., et al., Nature Medicine, 1998. 4(5): p. 623-6.
306. Li, J., et al., Physics in Medicine and Biology, 2010. 55(15): p. 4389-97.
307. Shao, Q. and Xing, B., Chemical Society Reviews, 2010. 39(8): p. 2835-46.
308. Klibanov, A.L., Bioconjugate Chemistry, 2005. 16(1): p. 9-17.
309. Kaufmann, B.A., Cardiovascular research, 2009. 83(4): p. 617-25.
310. Leong-Poi, H., Circulation, 2002. 107(3): p. 455-460.
311. Hauff, P., et al., Radiology, 2004. 231(3): p. 667-73.
312. Lindner, J.R.,. Cardiovascular research, 2009.
313. ten Kate, G.L., et al., Journal of nuclear cardiology, 2010. 17(5): p. 897-912.
314. Lanza, G.M., et al., Circulation, 1996. 94(12): p. 3334-3340.
315. Lindner, J.R., Nature Reviews Drug Discovery, 2004. 3(6): p. 527-533.
316. Klibanov, A.L., et al., Contrast Media Mol Imaging, 2006. 1(6): p. 259-66.

317. Akkus, Z., et al. SPIE 8320, Medical Imaging 2012: Ultrasonic Imaging, Tomography, and Therapy, 2012: p. 83200C-83200C-12.
318. Uzumcu, M., et al., Investigative Radiology, 2006. 41(1): p. 52-62.
319. Hoogi, A., et al., Ultrasound in Medicine & Biology, 2012. 38(12): p. 2072-83.
320. Leunig, M., et al., Cancer Research, 1992. 52(23): p. 6553-60.
321. Schneider, M., Echocardiography, 1999. 16(7, Pt 2): p. 743-746.
322. Kitzman, D.W., et al., American Journal of Cardiology, 2000. 86(6): p. 669-74.
323. Wang, D.S., et al., Radiology, 2012. 264(3): p. 721-32.
324. Alonso, A., et al., Stroke, 2007. 38(5): p. 1508-14.
325. Klibanov, A.L., Investigative Radiology, 2006. 41(3): p. 354-62.
326. Naghavi, M., et al., Circulation, 2003. 108(15): p. 1772-8.
327. Purushothaman, K.R., et al., Journal of the American College of Cardiology, 2003. 41(6, Supplement 2): p. 352-353.
328. Moreno, P.R., et al., Circulation, 2004. 110(14): p. 2032-8.
329. Tedesco, M.M., et al., Arteriosclerosis, Thrombosis, and Vascular Biology, 2009: p. ATVBAHA.109.187757.
330. Winter, P.M., et al., Circulation, 2003. 108(18): p. 2270-2274.
331. Laitinen, I., et al., Circulation: Cardiovascular Imaging, 2009. 2(4): p. 331-338.
332. Redgrave, J.N., et al., Circulation, 2006. 113(19): p. 2320-8.
333. Boyle, J.J., Curr Vasc Pharmacol, 2005. 3(1): p. 63-8.
334. Antonov, A.S., et al., The American journal of pathology, 2004. 165(1): p. 247-258.
335. Yan, F., et al., Ultrasound in Medicine & Biology, 2012. 38(4): p. 670-80.
336. Demos, S.M., et al., Journal of the American College of Cardiology, 1999. 33(3): p. 867-75.
337. Hamilton, A.J., et al., Journal of the American College of Cardiology, 2004. 43(3): p. 453-460.
338. McCarthy, A.J. and Lindsay, J.A., BMC Microbiology, 2010. 10(173): p. 1471-2180.
339. Ni, M., et al., Am J Physiol Heart Circ Physiol, 2009: p. 01202.2008.
340. Rigatelli, G. and Zanchetta, M., The American Journal of Geriatric Cardiology, 2005. 14(4): p. 195-199.
341. Daeichin, V., et al. Ultrasonics Symposium (IUS), IEEE International, 2012: p.1110-1113.
342. Fitzgerald, P.J., et al., Circulation, 1992. 86(1): p. 64-70.
343. Falk, E., et al., European heart journal, 2013. 34(10): p. 719-28.
344. Virmani, R., et al., Arterioscler Thromb Vasc Biol, 2000. 20(5): p. 1262-75.
345. Stary, H.C., et al., Circulation, 1995. 92(5): p. 1355-74.
346. Glass, C.K. and Witztum, J.L., Cell, 2001. 104(4): p. 503-16.
347. Mahoney, W.M. and Schwartz, S.M., Journal of Clinical Investigation, 2005. 115(2): p. 221-4.
348. Bond, A.R. and Jackson, C.L., Journal of Biomedicine and Biotechnology, 2011. 379069(10): p. 7.
349. Suvarna, S.K., et al., Bancroft's theory and practice of histological techniques. 2013; Available from: http://www.clinicalkey.com/dura/browse/bookChapter/3-s2.0-C20090426369.
350. von der Thusen, J.H., et al., Circulation, 2002. 105(17): p. 2064-70.
351. Hansson, G.K., New England Journal of Medicine, 2005. 352(16): p. 1685-1695.
352. Ni, M., et al., Heart, 2009. 95(17): p. 1393-8.
353. Skyba, D.M., et al., Circulation, 1998. 98(4): p. 290-3.
354. Faez, T., et al., Ultrasonics, Ferroelectrics and Frequency Control, IEEE Transactions on, 2013. 60(1): p 7-20.

355. de Jong, N., et al., Medical & biological engineering & computing, 2009. 47(8): p. 861-873.
356. Burns, P.N. and Becher, H., Handbook of contrast echocardiography, 2000, Frankfurt: Springer Verlag.
357. Hoff, L., Acoustic characterization of contrast agents for medical ultrasound imaging 2001: Springer.
358. Senior, R., et al., American heart journal, 2000. 139(2): p. 245-251.
359. Wei, K., et al., Circulation, 1998. 97(5): p. 473-483.
360. Bloch, S.H., et al., Applied Physics Letters, 2004. 84(4): p. 631-633.
361. Kooiman, K., et al., Journal of Controlled Release, 2009. 133(2): p. 109-118.
362. Miller, D.L., et al., Journal of Ultrasound in Medicine, 2008. 27(4): p. 611-632.
363. Ammi, A.Y., et al., Ultrasonics, Ferroelectrics and Frequency Control, IEEE Transactions on, 2006. 53(1): p. 126-136.
364. Chomas, J.E., et al., IEEE Transactions on, 2001. 48(1): p. 232-248.
365. Holland, C.K., et al., Ultrasonics, Ferroelectrics and Frequency Control, IEEE Transactions on, 1992. 39(1): p. 95-101.
366. Bouakaz, A., et al., Ultrasound in medicine & biology, 2005. 31(3): p. 391-399.
367. Dayton, P.A., et al., Ultrasonics, Ferroelectrics and Frequency Control, IEEE Transactions on, 1999. 46(1): p. 220-232.
368. Borden, M.A., et al., Ultrasonics, Ferroelectrics and Frequency Control, IEEE Transactions on, 2005. 52(11): p. 1992-2002.
369. Thomas, D., et al., Applied Physics Letters, 2012. 101(7): p. 071601.
370. Paradossi, G., et al., Biomacromolecules, 2002. 3(6): p. 1255-1262.
371. Grishenkov, D., et al., Ultrasound in medicine & biology, 2009. 35(7): p. 1127-1138.
372. Cavalieri, F., et al., Chemistry of Materials, 2008. 20(10): p. 3254-3258.
373. Brismar, T.B., et al., Biomacromolecules, 2012. 13(5): p. 1390-1399.
374. Pecorari, C. and Grishenkov, D., The Journal of the Acoustical Society of America, 2007. 122(4): p. 2425-2430.
375. Grishenkov, D., et al., Ultrasound in medicine & biology, 2009. 35(7): p. 1139-1147.
376. Chin, C.T., et al., Review of scientific instruments, 2003. 74(12): p. 5026-5034.
377. Poehlmann, M., et al., Soft Matter, 2014. 10(1): p. 214-226.
378. Wells, P., Ultrasound in medicine & biology, 1975. 1(4): p. 369-376.
379. Banihashemi, B., et al., Cancer Research., 2008. 68(20): p. 8590-8596.
380. Lensen, D., et al., Soft Matter, 2011. 7(11): p. 5417-5422.
381. Postema, M., et al., Ultrasonics, Ferroelectrics and Frequency Control, IEEE Transactions on, 2005. 52(6): p. 1035-1041.
382. Marmottant, P., et al., The Journal of the Acoustical Society of America, 2011. 129(3): p. 1231-1239.
383. Marmottant, P., et al., The Journal of the Acoustical Society of America, 2005. 118(6): p. 3499-3505.
384. Tzvetkov, G., et al., Soft Matter, 2008. 4(3): p. 510-514.
385. Porter, T.R. and Xie, F., JACC: Cardiovascular Imaging, 2010. 3(2): p. 176-187.
386. Bevan, P.D., et al., Ultrasound in medicine & biology, 2007. 33(11): p. 1777-1786.
387. Tang, Y., et al., Theranostics, 2013. 3(2): p. 85-92.
388. Liu, J., et al., Physics in Medicine and Biology, 2007. 52(16): p. 4739-47.
389. Liu, J., et al., Physics in Medicine and Biology, 2006. 51(9): p. 2179-89.
390. Verweij, M.D., et al., The Journal of the Acoustical Society of America, 2013. 134(5): p. 4049-4049.

391. Reznik, N., et al., Ultrasound in Medicine & Biology, 2014. 40(6): p. 1379-1384.
392. Reznik, N., et al., Ultrasonics, 2013. 53(7): p. 1368-1376.
393. Shpak, O., et al., Proceedings of the National Academy of Sciences, 2014. 111(5): p. 1697-1702.
394. Sheeran, P.S. and Dayton, P.A., Scientifica, 2014. 2014: p. 24.
395. Williams, R., et al., Ultrasound in Medicine & Biology, 2013. 39(3): p. 475-489.
396. de Jong, M., et al., Nature Reviews Cancer, 2014. 14(7): p. 481-493.
397. Konantz, M., et al., Annals of the New York Academy of Sciences, 2012.
398. Leong, H.S., et al., Methods in Molecular Biology, 2012. 872: p. 1-14.
399. Mimeault, M. and Batra, S.K., Drug Discov Today, 2013. 18(3-4): p. 128-40.
400. Durupt, F., et al., Cancer Gene Therapy, 2012. 19(1): p. 58-68.
401. Walsby, A.E., Microbiol Rev, 1994. 58(1): p. 94-144.
402. Pfeifer, F., Nature Reviews Microbiology, 2012. 10(10): p. 705-715.
403. Shapiro, M.G., et al., Nature Nanotechnology, 2014. 9(4): p. 311-316.
404. Jun Hui Ho, C., et al. Biomedical Optics 2014.
405. Jokerst, J.V., et al., SPIE Photons Plus Ultrasound: Imaging and Sensing 2014, 894366: p. 894366-894366-11
406. Kim, S., et al., IEEE Trans Ultrason Ferroelectr Freq Control. 2014, 61(5): p. 891-7.
407. Luke, G.P. and Emelianov, S.Y., Optics Letters, 2014. 39(7): p. 2214-7.
408. Qu, M., et al., Photoacoustics, 2014. 2(2): p. 55-62.
409. Bouchard, R., et al., IEEE Trans Ultrason Ferroelectr Freq Control, 2014. 61(3): p. 450-66.
410. Heuchel, R., et al., Pancreatology. 13(3): p. S19.
411. Jansen, K., et al., Ultrasound in Medicine & Biology, 2014. 40(6): p. 1037-1048.
412. Zhang, J., et al., Journal of the American College of Cardiology, 2014. 64(4): p. 385-390.
413. Rouleau, L., et al., Contrast Media & Molecular Imaging, 2013. 8(1): p. 27-39.
414. Wilson, K., et al., Nature Communications, 2012. 3: p. 618.
415. Hannah, A., et al., ACS Nano, 2013. 8(1): p. 250-259.

Summary

Molecular imaging visualizes biological processes at the cellular and molecular level in living systems. Molecular imaging can be performed with different imaging modalities, such as ultrasound. Ultrasound molecular imaging (UMI) makes use of special targeted ultrasound contrast agents (tUCA) consisting of microbubbles with specific ligands bound to the shell, referred to as targeted microbubbles (tMBs). UMI can image and quantify biomarkers associated with diseases and has significantly contributed to understanding of pathological processes in cancer and cardiovascular diseases, especially atherosclerosis and neovascularization. In this research we focused on angiogenesis biomarkers, $\alpha_v\beta_3$ integrin, to quantify atherosclerotic plaque neovascularization using tMBs in apolipoprotein E-deficient ($ApoE^{-/-}$) mouse model. For preclinical imaging in small animals, high-frequency ultrasound is used (>15MHz), but the microbubbles are not ideal for imaging at such high frequencies. This research aims to investigate and improve a number of crucial components needed for high-frequency ultrasound molecular imaging. After a general introduction in the **first chapter** giving a broad overview of diagnostic ultrasound, contrast agents and targeted contrast imaging, the state-of-the-art for UMI and therapy is extensively reviewed in the **second chapter**. In this review, recent achievements with tUCA in the field of molecular imaging, evaluation of therapy, drug delivery, and therapeutic applications are discussed. We present the different coating materials and aspects that have to be considered when manufacturing tUCAs. Next to tUCA design and the choice of ligands for specific biomarkers, additional techniques are discussed that are applied to improve binding of the tMBs to their target and to quantify the strength of this bond. As imaging techniques rely on the specific behavior of tUCAs in an ultrasound field, it is crucial to understand the characteristics of both free and adhered tUCAs. To image and quantify the adhered tMBs, the state-of-the-art techniques used for ultrasound molecular imaging and quantification are presented. This review concludes with the potential of tUCAs for drug delivery and therapeutic applications.

The need for ultrasound images with higher resolution (micro-ultrasound) and the technological development in the manufacturing of ultrasound arrays have pushed the frequencies to above 15 MHz. Established contrast-specific imaging methods however, showed a disappointing sensitivity and specificity when applied to micro-ultrasound imaging. This posed the first challenge we had to solve before going further with micro-UMI. As one possible solution, the use

of the self-demodulation (S-D) signal is proposed as a means to enhance the subharmonic (SH) response of the MBs. In the **third and the fourth chapters**, we extensively discuss how the envelope of an excitation signal generates S-D signals with different frequency content and how this can be applied for enhanced SH imaging of the ultrasound contrast agent (UCA). We show that among the most commonly used excitation envelopes in the UMI (Gaussian, rectangular and an intermediate envelope), a rectangular envelope excitation can significantly enhance the SH response of the UCA compared to a Gaussian envelope excitation. We hypothesize that the reason for the observed enhancement was the broadband S-D signal with most of its energy at half the transmitted (subharmonic) frequency. However, care should be taken when exploiting this feature of a rectangular envelope, since an increase in the amplitude of the excitation can rapidly increase the low frequency S-D signal. A strong S-D signal in turn results in strong artifacts at the SH frequency, therefore degrading the contrast to tissue ratio (CTR) in SH images, as described in the fifth chapter.

In **chapter five**, using the most frequently used micro-ultrasound system in preclinical applications (Vevo 2100, VisualSonics Inc.) we systematically compare the SH imaging with nonlinear fundamental (NF) and ultraharmonic (UH) imaging. SH imaging with rectangular envelope excitation performs very well with high sensitivity and specificity in media with low attenuation such as in a chicken embryo model. However, NF imaging is a more suitable approach for deeper and more attenuating media such as a mouse model. The largest CTR and contrast-to-artifact ratios for the SH images are achieved when pulse inversion is applied and for the NF images when amplitude modulation is used. The results of this comprehensive investigation, not unexpectedly suggest that optimal nonlinear processing will depend on the application and required depth of imaging.

With these optimized imaging parameters for SH imaging of UCA at high frequencies, in the **sixth chapter**, SH response of MicroMarker UCA and four homemade UCAs with DSPC or DPPC as main lipid and different size distributions are compared *in vitro*. This was inspired by recent studies which have shown that the size distribution, manufacturing mechanism and microstructure on the lipid shell can influence the MBs SH response. Our results show that DPPC MBs have higher SH response than DSPC ones. At high concentration of the UCA, smaller MBs such as MicroMarker and our ‘C’ type UCAs produce the most homogeneous SH responses and are less affected by attenuation. Acknowledging the fact that the concentration of the UCA for UMI applications is very low, our

findings suggest that our 'B' type MBs (main lipid DPPC, mean diameter of 1.95 μm) and the commercially available MicroMarker UCA are suitable choices for micro-ultrasound SH imaging.

Our research challenge in the **seventh chapter** is to develop an accurate and reliable method to quantify the bound tMBs in an *in vivo* environment. We present a new quantification method which benefits from motion compensation and individual contrast spot detection, and is capable of distinguishing the bound MBs from unbound MBs based on their displacement. Our quantification method can be applied in studies performed with different imaging settings because it is less sensitive to imaging parameters. Moreover, it is more robust to tissue motion artifacts. Another advantage of our technique is that it can be applied without changing the widely used for ultrasound molecular imaging protocols.

After improving the various steps involved in UMI, in the **eighth chapter**, we provide *in vitro* and *in vivo* proof-of-concept for UMI of $\alpha_v\beta_3$ integrin in carotid artery lesions and expanded vasa vasorum neovessels in an animal model of atherosclerosis (ApoE$^{-/-}$ mice). This study thus not only provides an excellent test of the contrast detection approaches we have developed but does so in a relevant biological context. Also notable in this study is the use of $\alpha_v\beta_3$-tMBs binding in the mouse salivary gland as positive control for binding and a convenient reference for relative expression of $\alpha_v\beta_3$ integrin. We show that UMI allows noninvasive assessment of the expression levels of $\alpha_v\beta_3$ on the vascular endothelium and may provide insights into early atherosclerotic plaque detection and treatment monitoring. Moreover, during the *in vivo* study, symptoms suggesting plaque disruption in the right brachiocephalic artery were observed in one of the animals. Histological analysis of the affected carotid artery and brachiocephalic trunk confirm presence of intraplaque haemorrhage in advanced atherosclerotic lesions in the brachiocephalic trunk, with dissections and even cap rupture, pointing towards plaque rupture as the cause of the observed event. Although features suggestive of plaque rupture in ApoE$^{-/-}$ mice have been reported, whether plaque disruption actually occurs in mice has been a matter of debate in the past decade. For the first time, we observed possible spontaneous plaque disruption in the right brachiocephalic artery of an ApoE$^{-/-}$ mouse in real-time with contrast enhanced ultrasonography. This observation is briefly documented in the **ninth chapter**.

In the **tenth chapter**, a new PVA MB is investigated using the ultra-high-speed Brandaris 128 camera and an acoustical setup. Its unique fracturing mechanism and the pumping-out of gas through the shell is investigated optically and

acoustically. Local delivery of therapeutic gas is of great clinical interest and the subject of new researches. The new PVA-shell microbubbles are capable of encapsulating gas in between their crosslinks, and we hypothesize that the observed fracturing mechanism can be further utilized to deliver therapeutic gases such as nitric oxide (NO) or anesthetic gases such as nitrogen dioxide (NO_2).
Finally, in the last chapter (chapter eleven) contributions of this thesis to improve the three major steps in high frequency ultrasound molecular imaging are discussed and summarized. Moreover, the possible future directions and outlooks for the field are reviewed briefly.

Samenvatting

Met moleculaire beeldvorming is het mogelijk om biologische processen in levende organismen op cellulaire of moleculaire schaal in beeld te brengen. Moleculaire beeldvorming kan uitgevoerd worden met verschillende beeldvormende modaliteiten, waaronder ultrageluid of echo. Ultrageluid moleculaire beeldvorming (UMB) maakt gebruik van speciale ultrageluid contrastmiddelen, bestaande uit microbellen (MB), die met behulp van specifieke moleculen gericht kunnen binden aan een biomarker in het lichaam. Deze MB worden ook wel gefuctionaliseerde microbellen (fMB) genoemd. Met gebruik van UMB kunnen fMB in beeld gebracht worden en kan het aantal biomarkers waaraan ze zich gebonden hebben kwantitatief bepaald worden. Doordat deze biomarkers specifiek zijn voor bepaalde ziekteprocessen, kunnen bijvoorbeeld de vorming van nieuwe bloedvaten in tumoren (angiogenese) en het ontstaan van aderverkalking beter begrepen worden. In dit proefschrift ligt de focus op een biomarker voor angiogenese, $\alpha_v\beta_3$ integrine, om kwantitatief de nieuw gevormde bloedvaten in atherosclerotische plaques in beeld te kunnen brengen. Hiervoor gebruiken we fMB in muizen met een uitgeschakeld gen voor apolipoproteïne E ($ApoE^{-/-}$). In het pre-klinisch stadium van UMB worden kleine dieren gebruikt, zoals muizen, waardoor ultrageluid met hoge frequenties nodig is (> 15 MHz). Omdat het gebruik van fMB in combinatie met hoge frequenties niet ideaal is, hebben wij ons gericht op het verbeteren van een aantal cruciale factoren die nodig zijn om hoog-frequente moleculaire beeldvorming mogelijk te maken.

In het **eerste hoofdstuk** wordt een overzicht gegeven van ultrageluid in de diagnostiek en het gebruik van contrastmiddelen voor o.a. moleculaire beeldvorming. Het **tweede hoofdstuk** geeft een overzicht van de huidige stand van de techniek en lopende ontwikkelingen op het gebied van ultrageluid moleculaire beeldvorming, evaluatie van therapie, lokale medicijnafgifte en therapeutische toepassingen. In het kader van contrastmiddelontwikkeling beschrijven we de belangrijkste overwegingen betreffende de schil van de microbellen en andere aspecten die bepalend zijn voor goede contrasteigenschappen, een goede binding aan de biomarker, en de kwantificering hiervan. Omdat ultrageluid moleculaire beeldvorming berust op het vermogen om gebonden van ongebonden MB te kunnen onderscheiden, is het cruciaal om de karakteristieken in kaart te brengen van zowel MB die vastzitten aan de biomarker, als van de MB die zich nog vrij in het bloed bevinden. Voor het afbeelden en kwantificeren van de bellen die vastzitten aan hun biomarker laten we zien welke state-of-the-art technieken gebruikt kunnen worden voor moleculaire beeldvorming met ultrageluid.

We sluiten dit hoofdstuk af met de laatste ontwikkeling op het gebied van lokale medicijnafgifte en therapeutische toepassingen met het gebruik van fMB.
De behoefte aan ultrageluidbeelden met een hoger oplossend vermogen (micro-ultrageluid) en de technologische vooruitgang in de ontwikkeling van ultrageluid-arrays zorgen ervoor dat nu frequenties boven de 15 MHz gebruikt worden. Helaas heeft de bestaande contrastmodus van ultrageluidscanners een teleurstellende sensitiviteit en specificiteit wanneer deze gebruikt wordt voor micro-ultrageluid; dit is de eerste te nemen horde. Een mogelijke oplossing hiervoor is het gebruik van het zelfdemodulatie-effect (ZD) van het uitgezonden signaal om de subharmonische (SH) activiteit van de microbellen te verhogen. In de **hoofdstukken drie en vier** bediscussiëren we uitgebreid hoe de omhullende van het uitgezonden signaal ZD-signalen genereert met verschillende frequentie-inhoud en hoe we dit kunnen gebruiken om meer SH responsie op te wekken in de MB. Tevens laten we zien dat van de meest gebruikte excitatie-omhullenden voor moleculaire beeldvorming met ultrageluid (Gaussisch, rechthoekig, of een tussenvorm) een rechthoekige omhullende een significant hoger SH signaal geeft dan een Gaussische. Onze hypothese is dat dit veroorzaakt wordt door een breedbandig ZD signaal met de meeste energieinhoud op de halve excitatiefrequentie, ofwel de SH frequentie. Men moet echter prudent omgaan met het gebruik van een rechthoekige omhullende, omdat een hogere excitatie-amplitude kan leiden tot een flinke verhoging in het laagfrequente ZD signaal. Dit sterke ZD signaal veroorzaakt aanzienlijke artefacten op de SH frequentie, wat weer zorgt voor een slechtere verhouding tussen het signaal van het contrast en van het weefsel (CTR) in SH beelden.
In **hoofdstuk vijf** gebruken we het meest toegepaste micro-ultrageluidsysteem in preklinisch onderzoek, de Vevo 2100 (VisualSonics Inc.) om SH beeldvorming systematisch te vergelijken met niet-lineare beeldvorming op de fundamentale frequentie (NF) en met ultraharmonische (UH) beeldvorming. Hier laten we zien dat SH beeldvorming met een rechthoekige omhullende van het excitatiesignaal een goede sensitiviteit en specificiteit heeft in media met een lage verzwakking, zoals bijvoorbeeld het kippenembryomodel. NF beeldvorming is daarentegen bruikbaarder voor dieper gelegen media met meer verzwakking zoals het muismodel. De hoogste CTR en de beste verhouding tussen contrast en artefacten voor SH beeldvorming verkregen we met pulsinversie en voor NF beeldvorming met amplitudemodulatie. De resultaten van deze vergelijking laten, niet geheel onverwacht, zien dat de optimale keus voor niet-lineare beeldvorming afhangt van de toepassing en van de diepte van het af te beelden weefsel.
Deze geoptimaliseerde parameters voor SH beeldvorming gebruiken we in **hoofdstuk zes** om SH responsie van MicroMarker en vier eigen formuleringen

van MB (gebaseerd op DSPC of DPPC) met verschillende grootteverdelingen *in vitro* te vergelijken. Uit recente studies is gebleken dat de grootteverdeling, het productieproces en de microstructuur van de lipidenschil invloed kunnen hebben op het SH gedrag van de MB. Onze resultaten laten zien dat MB die gebaseerd zijn op DPPC een hogere SH responsie hebben dan de MB gebaseerd op DSPC. Bij hoge microbelconcentraties is de SH responsie van kleinere MB zoals MicroMarker en ons C-type MB het meest homogeen en de invloed van de verzwakking het laagst. Wanneer we kijken naar de toepassing van MB voor UMB, waarbij de concentratie MB erg laag is, volgt uit onze resultaten dat ons B-type bellen (DPPC, gemiddelde diameter 1.95 µm) en het commercieel verkrijgbare MicroMarker geschikte keuzes zijn voor micro-ultrageluid SH beeldvorming.
In **hoofdstuk zeven** zijn we de uitdaging aangegaan om een betrouwbare en accurate methode te ontwikkelen om het signaal van MB gebonden aan hun biomarker *in vivo* te kwantificeren. De door ons ontwikkelde methode maakt gebruik van bewegingscompensatie en de detectie van individuele contrastlocaties, waarbij het mogelijk is om vrije en gebonden bellen van elkaar te onderscheiden op basis van hun beweging. Doordat onze kwantificatiemethode minder gevoelig is voor de instellingen die gekozen worden bij het maken van de beelden, kan deze gebruikt worden in studies waar zulke instellingen niet gelijk gehouden kunnen worden. Ook is onze methode beter bestand tegen artefacten die veroorzaakt worden door beweging van het weefsel kunnen de ingeburgerde protocollen voor UMB gebruikt blijven worden.
Na de verschillende stappen verbeterd te hebben om micro-UMB mogelijk te maken, leveren we in **hoofdstuk acht** het *in vitro* en *in vivo* bewijs dat de techniek ook in een biologische context goed werkt. Hiervoor hebben we MB gebruikt die binden aan $\alpha_v\beta_3$ integrine in laesies in de halsslagaders en vasa vasorum vaten bij een atherosclerotisch diermodel ($ApoE^{-/-}$ muizen). Als positieve controle hebben we gebruik gemaakt van MB die binden aan $\alpha_v\beta_3$ integrine in de speekselklieren van de muizen, waardoor we een betrouwbare referentie hebben voor de relatieve expressie van $\alpha_v\beta_3$ integrine. Dit hoofdstuk laat zien dat UMB het mogelijk maakt om niet-invasief de expressie van $\alpha_v\beta_3$ integrine in het endotheel van de bloedvaten in beeld te brengen, wat het mogelijk kan maken om atherosclerotische plaques in een vroeger stadium op te sporen en de behandeling ervan te volgen. Gedurende de *in vivo* studie vertoonde één van de muizen symptomen die overeenkomen met die van een gescheurde plaque in de rechter truncus brachiocephalicus. Uit histologische analyse van de betreffende rechter carotide en truncus brachiocephalicus bleek dat het ging om een bloeding in een vergevorderde plaque in de truncus brachiocephalicus, met dissecties en zelfs scheuring van de kap. Dit alles wijst er inderdaad op dat de symptomen

veroorzaakt werden door een ruptuur van de plaque. Ondanks dat meerdere observaties in het verleden suggereerden dat ruptuur van plaques voorkomt in ApoE$^{-/-}$ muizen, is hier in het afgelopen decennium veel discussie over geweest. In onze studie laten we met real-time UMB voor het eerst zien dat spontane ruptuur van plaques in de rechter truncus brachiocephalicus plaats kan vinden. Dit beschrijven we kort in **hoofdstuk negen**.

In het **tiende hoofdstuk** beschrijven we een nieuw type PVA MB die we bestudeerd hebben met de ultrahogesnelheidscamera Brandaris 128 gecombineerd met een akoestische opstelling. Het unieke mechanisme achter het breken van de schil en het gas dat door de schil naar buiten gepompt wordt konden we daarmee optisch en akoestisch bestuderen. Klinisch gezien is de lokale afgifte van therapeutische gassen van groot belang en hier wordt op dit moment veel onderzoek naar gedaan. Deze nieuwe PVA MB kunnen efficiënt het gas inkapselen door de kruisverbindingen tussen de moleculen, en daarom stellen wij dat het mechanisme achter het breken van de schil verder gebruikt kan worden om therapeutische gassen zoals stikstofoxide (NO), of anesthetica zoals stikstofdioxide (NO_2), beter af te geven.

In het laatste hoofdstuk (**hoofdstuk elf**) vatten we de bijdragen van dit proefschrift samen en bediscussiëren we de verbeteringen van de drie belangrijkste stappen die nodig zijn om hoogfrequent UMB mogelijk te maken. We sluiten af met mogelijke richtingen voor vervolgonderzoek en geven onze visie op de mogelijkheden die nog voor deze techniek in het verschiet liggen.

Acknowledgments

Living in the very moment, respect, devotion and royalty with no expectation were the lessons I was given day by day since I remember. Whether, I have learned my lessons still remains a question. Having said this, I can't put it in words how grateful and thankful I am to be part of my always supporting family: My mother, Marziyeh, my father, Jahanbakhsh and little sister and brother, Sheyda and Shahin, I love you. I also feel so privileged to have you, Sara, in my life with all your generosity in love, kindness and patience.

Ton, Nico and Hans, this coalition is seamless. This thesis would have never had a chance to be done without the precision and patience of you, Hans. Kind Nico, it was your keen and always smart hints which fueled this research. And Ton, thank you for your trust and your remarkable way of running the BME family.

Telli, Guillaum, David and Krista, the older cool dudes with whom I had the chance to share some times, desks and labs. Beside your always helpful scientific contributions, with you around, it was very easy to establish a social life immediately after my arrival in Rotterdam. Thank you for being there and I hope this friendship will never fade out. Klazina and Ilya, your significance in this thesis is obvious in almost every chapter, thank you for sharing your knowledge and skills with me. Nobody can deny your endless generosity Ilya, I'll always remember that. Tom van Roij, now that I am writing these lines you are perhaps translating my summary into Dutch, hartstikke bedankt for being so kind. Alex, no matter how hard you try to run away but you are somehow very close to me, it must be your eastern German blood. Pieter I'll always remember you my friend, together with: Bolle Jan, Queen Beatrix with her orange niqab, Feyenoord shining in neon Christmas lights and loud chansons scattered through the heavy smoke of cigarettes. Ying, thank you for being always helpful and all the amazing foods your mom cooked for us. Zeynetting, thank you for being an amazing trench mate and all the time we spent together. Tom Kokhuis, my very-Dutch and not-Ducth-at-all friend, it was a pleasure knowing you. Robert, when I become a famous musician I'll tell the world how awesome you are. Frites, thanks for always having a solution for my problems on your desk or in your computer. Jacopo and Deep, I do not feel sad at all to leave my trench behind, because you are taking care of it perfectly. I hope to see you soon becoming climbing masters. Thank you Gerard, Hans, Geert, Michiel, Jan and Charles for all the time you had for me.

Mieke, Gracia and Rita, you are so wonderful, without you I would have a PhD in Dutch bureaucracy. Thank you for being always available and kind.

Frank, Rik, Kim& Kim, Lambert, Ruoyu and all the folks on the other side of the corridor I am so thankful for the time you took to help with my project and the

fun we had in all the Labuitje. Thank you guys.
Gijs, thank you for bearing me all this time I was sitting behind you and still working on my thesis, I hope to make that up some day. Tianshi, Min, Muthu, Sophinese and Jovana, the insider crew, it was and it is a great fun sharing an office/lab with you guys and I hope for a lot more fun to come. Thank you for the good vibe.
I would like to address special thanks to:
Stuart Foster, for his very constructive comments
Mat Daemen, for his valuable knowledge and sharing some of it with me.
Judith Sluymmer, for her hospitality in her lab and all the facilities she generiously provided for my research.
Ben Janssen, Peter Leenders, Agnieszka Strzelecka, and Jacques Debets, Thomas Theelen and Anique Janssen from Maastricht University medical Center, for their help and support.
And William and sara in the human resource department at Erasmus MC who arranged everything for me at my arrival.

Once more I would like to thank you all, the members of the BME family at Erasmus MC, I feel honored to be part of this family.

Hans Bosch climbing in mission trails after an SPIE conference in San diego.
© Verya Daeichin

Curriculum Vitale

Verya Daeichin was born in Kermanshah, Iran, in 1984. He did his secondary, high school and pre-university school at National Organization for Development of Exceptional Talents (NODET) in Kermanshah and Tehran. He received his Bachelor degree in Bioelectric Engineering from the Biomedical Engineering department at Amirkabir University of Technology (Tehran Polytechnic) in 2008. Then he moved to Sweden and in 2009, he finished his first Master degree in Biomedical Signal Processing and Pattern Recognition from university of Boras. He completed his first master's thesis, entitled " Development of an intraoperative visualization tool for electrode placement in deep brain stimulation", at Institute for Medical and Analytical Technologies, University of Applied Sciences Northwestern Switzerland.
His second Master degree was from Chalmers University of Technology in Biomedical Image Processing with a thesis, entitled "Ultrasound Contrast Agent Detection". He is a Ph.D. candidate from 2010 at Erasmus MC, Rotterdam, the Netherlands. His research area is Molecular Imaging.

Publications

Articles

V. Daeichin, T. Faez, G. Renaud, J. G. Bosch, A. F. van der Steen, and N. de Jong, "Effect of self-demodulation on the subharmonic response of contrast agent microbubbles," Phys Med Biol, vol. 57, pp. 3675-91, 2012.

V. Daeichin, J.G. Bosch, A. Needles, F. S. Foster, A.F.W. van der Steen, and N. de Jong, "Subharmonic, nonlinear fundamental, and ultraharmonic imaging of microbubble contrast at high frequencies," Ultrasound in Medicnice and Biology, 2014 (in press).

V. Daeichin, Z. Akkus, I. Skachkov, K. Kooiman, A. Needles, J. Sluimer, M.J.A.P. Daemen, A. F.W. van der Steen Fellow, N. de Jong, and J.G. Bosch, "Quantification of bound microbubbles in ultrasound molecular imaging," IEEE Trans Ultrason Ferroelectr Freq Control, 2014 (in press).

V. Daeichin*, T. van Rooija*, I. Skachkova, N. de Jonga, and K. Kooiman," Targeted ultrasound contrast agents for ultrasound molecular imaging and therapy," International Journal of Hyperthermia (in press). * contributed equally.

V. Daeichin, J. C. Sluimer, K. Van der Heiden, I. Skachkov, K. Kooiman, A. Janssen, B. Janssen, J.G. Bosch, N. de Jong, M.J.A.P. Daemen, and A. F.W. van der Steen, "Live observation of atherosclerotic plaque disruption in apolipoprotein E-deficient mouse," submitted, 2014.

S. V. V. N. Kothapalli, **V. Daeichin**, F. Mastik, L. Åke Brodin, B. Janerot-Sjoberg, G. Paradossi, N. de Jong, and D. Grishenkov," Unique "pumping-out" fracturing mechanism of a polymer-shelled contrast agent: an acoustic characterization and optical visualization," submitted , 2014.

Conference papers

V. Daeichin, A. Needles, I. Skachkov, K. Kooiman, J. G. Bosch, A. F. W. van der Steen, and N. de Jong, "Optimized high frequency nonlinear contrast imaging using self-demodulation,". Ultrasonics Symposium (IUS), 2012 IEEE International, 2012, pp. 1110-1113.

V. Daeichin, T. Faez, A. Needles, G. Renaud, J. G. Bosch, A. F. W. van der Steen, and N. de Jong, "Self-demodulation effect on subharmonic response of ultrasound contrast agent," SPIE Proceedings, 2012, pp. 83200W-83200W-9.
V. Daeichin, A. Needles, I. Skachkov, K. Kooiman, J. G. Bosch, A. F. W. van der Steen, and N. de Jong, " Real time high frequency subharmonic imaging using self-demodulation,". 17th European Ultrasound Contrast Imaging symposium, 2012.

V. Daeichin, G. Renaud, J. G. Bosch, A. F. W. van der Steen, and N. de Jong, "Effect of excitation envelope on volumetric subharmonic vibrations of single contrast agent microbubbles using an acoustical camera," Ultrasonics Symposium (IUS), 2013 IEEE International, 2013, pp. 537-540.

V. Daeichin, Z. Akkus, A. Hoogi, J. G. Bosch, A. Needles, K. Kooiman, I. Skachkov, J. Sluimer, B. Janssen, M. J. A. P. Daemen, A. F. W. van der Steen, and N. de Jong, "Quantification of targeted microbubbles in contrast enhanced ultrasound," Ultrasonics Symposium (IUS), 2013 IEEE International, 2013, pp. 1825-1828.

V. Daeichin, K. Kooiman, I. Skachkov, J. G. Bosch, A. F. W. van der Steen, and N. de Jong, "Optimization of ultrasound contrast agent for high frequency ultrasound molecular imaging using subharmonic oscillation," in Ultrasonics Symposium (IUS), 2014 IEEE International, 2014, pp. 1766-1769.

V. Daeichin, K. Kooiman, I. Skachkov, J. Sluimer, B. Janssen, M. J. A. P. Daemen, W. van Cappellen, A. F. W. van der Steen, J. G. Bosch, and N. de Jong, " Ultrasound molecular imaging: overcoming pitfalls in crucial steps," 19th European Ultrasound Contrast Imaging symposium, 2014.

PhD portfolio

Courses

Contrast agent: theory and experiments (IEEE, Orlando, USA)	2011	0.15 ECTs
Quantitative Ultrasound, Theory and Practice (IEEE, Orlando, USA)	2011	0.15 ECTs
Ultrafast Ultrasound Imaging (IEEE, Dresden, Germany)	2012	0.15 ECTs
English Biomedical writing and communication	2012	4.00 ECTs
Animal Experimentation article 9 Wod	2013	4.00 ECTs
Animal Imaging Workshop by AMIE (MolMed)	2011	1.40 ECTs

International conferences

European Ultrasound Contrast Imaging symposium, Rotterdam the Netherlands (Oral)	2011	1.60 ECTs
European Ultrasound Contrast Imaging symposium, Rotterdam the Netherlands (Poster)	2012	1.10 ECTs
European Ultrasound Contrast Imaging symposium, Rotterdam the Netherlands (Oral)	2013	1.60 ECTs
European Ultrasound Contrast Imaging symposium, Rotterdam the Netherlands (Oral)	2014	1.60 ECTs
IEEE International Ultrasonics Symposium, Dresden, Germany (Oral)	2012	2.00 ECTs
IEEE International Ultrasonics Symposium, Prague, Czech republic (two Orals)	2013	3.00 ECTs
IEEE International Ultrasonics Symposium, Prague, Czech republic (poster)	2013	1.60 ECTs
SPIE Medical Imaging, Dan Diego, USA (Oral)	2012	2.00 ECTs
Leeds Microbubble Consortium, Leeds, UK, (Oral)	2011	2.00 ECTs
Leeds Microbubble Consortium, Leeds, UK, (Poster)	2013	1.50 ECTs
Ultrasonic Biomedical Microscanning, Canada, (Oral)	2012	2.00 ECTs
Ultrasonic Biomedical Microscanning, Scotland, (Oral)	2014	2.00 ECTs

Seminars and workshops

Photoacoustic (Visualsonics Inc, Amsterdam, the Netherlands)	2011	0,40 ECTs
Dutch Society for Medical Ultrasound meetings	2010-2014	1.80 ECTs
CTMM and ParisK semiannual and annual meetings (posters and orals)	2010-2014	8.00 ECTs
COEUR research seminar- Imaging of Atherosclerosis	2010	0.40 ECTs
COEUR research seminar- Biomarkers of Risk	2010	0.40 ECTs
COEUR research seminar- Detection of Early	2011	0,4 ECTs
COEUR research seminar- New imaging strategies for the detection of atherosclerosis	2014	0,20 ECTs

Total ECTs: 43.45